Periodic driving and nonreciprocity in cavity optomechanics

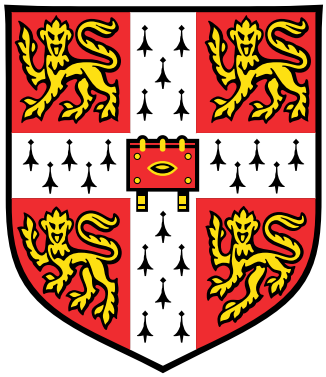

Daniel Hendrik Malz

Trinity College
University of Cambridge

Submitted: August 2018

This dissertation is submitted for the degree of Doctor of Philosophy

TO MY FAMILY.

Declaration

I hereby declare that except where specific reference is made to the work of others, the contents of this dissertation are original and have not been submitted in whole or in part for consideration for any other degree or qualification in this or any other institution. This dissertation is my own work and contains nothing which is the outcome of work done in collaboration with others, except as detailed in the text and specified below. This dissertation contains fewer than 60,000 words including appendices, bibliography, footnotes, tables, and equations, and has fewer than 150 figures.

Chapters 2 through 6 contain material published in

- Ref. 1; D. Malz and A. Nunnenkamp, "Floquet approach to bichromatically driven cavity-optomechanical systems," Physical Review A 94, 023803 (2016).
- Ref. 2; D. Malz and A. Nunnenkamp, "Optomechanical dual-beam backaction-evading measurement beyond the rotating-wave approximation," Physical Review A 94, 053820 (2016).
- Ref. 3; N. R. Bernier, L. D. Tóth, A. Koottandavida, M. A. Ioannou, D. Malz, A. Nunnenkamp, A. K. Feofanov, and T. J. Kippenberg, "Nonreciprocal reconfigurable microwave optomechanical circuit," Nature Communications 8, 604 (2017).
- Ref. 4; D. Malz, L. D. Tóth, N. R. Bernier, A. K. Feofanov, T. J. Kippenberg, and A. Nunnenkamp, "Quantum-Limited Directional Amplifiers with Optomechanics," Physical Review Letters 120, 023601 (2018).
- Ref. 5; D. Malz and A. Nunnenkamp, "Current rectification in a double quantum dot through fermionic reservoir engineering," Physical Review B 97, 165308 (2018).

Daniel Hendrik Malz
August 2018

Acknowledgments

I am grateful that there are many people who have made my graduate life a great pleasure, and for all the help and guidance I have received over the years.

Andreas, it was an extraordinary privilege to have you as my supervisor and mentor. You have managed to strike the perfect balance between supporting me and leaving me with the liberty to make my own choices. Thank you for asking the right questions, and having the patience to wait until I learn from trying to answer them. In countless inspiring conversations with you I have learned what independent research in physics means. Through your guidance and encouragement, I have managed produced some work that I am proud of and feel well prepared for the future.

I have also learned immense amounts from my collaborators over the years, especially Nathan Bernier, Alexey Feofanov, Tobias Kippenberg, Itay Shomroni, Daniel Tóth, and Liu Qiu at EPFL in Lausanne, Erika Aranas and Tania Monteiro at UCL in London, and most recently Johannes Knolle, now at Imperial College. There are countless others I have learned from over the course of the years and naming all of them would be excessive. However, I am particularly grateful to my colleagues in the Theory of Condensed Matter group at the Cavendish Laboratory, especially Nigel Cooper for his advice on many topics, members of the Collective Phenomena group for discussions, my office mates Beñat "Comilón" Mencia, Chris "Max" Parmee-san, and Adam Smith for countless conversations about wacky ideas and silly questions as well as Adam's selfless provision of hobnobs, Michael Rutter for his excellent computer support, and all the others who have helped produce an inspiring and welcoming atmosphere in TCM, making it a place I have always enjoyed coming to. Particular thanks also go to Matteo Brunelli and Nathan Bernier for proofreading parts of this thesis.

Outside of academia I am thankful to my house mates in Portugal Street 4, who have turned our house into a home: Thank you Draško for your endless supply of inappropriate jokes, Lasagna, and sass, Lydia, for your unwavering support for my questionable dinner choices (cereal), Ruth, for teaching us all how to be cool, Sam, for great squash rallies and in general anything that happens after normal people go to sleep, and of course Konrad,

for countless hours of rehearsals, superb concerts, as well as your (the following has to be said in Received Pronunciation) really rather marvellous company, advice, and generally for being such a lovable person.

I feel tremendously lucky to have met so many amazing people in this beautiful place that is Cambridge, who have made me feel at home, given me support when I needed it, and have left me many unforgettable memories. Leah, I am incredibly grateful to have met you and thank you for everything. Sven, I have had so much fun in the many hours in which we have listened to, played, or sang music together, hiked, fooled around, at your legendary parties, in your piano lessons – thank you for bringing joy and energy to every occasion. To the whole Trinity family – Marius, for being such a good sport, Veronika, for lots of climbing sessions and conversations, Kasia, for being such a sunshine, Nelson, for being my choir buddy, Anton, for introducing me to Carlo's, Sofia, Olimpia, Christoph, and all the others – thank you for bringing joy to my life in Cambridge. To my friends from undergraduate, Ognjen, Patrick, Christina, Will, Pavol, George, Carl, Satchee, Shan, to las ciclistas, to my friends from school, who still put up with me – Jan, Emanuel, Emmanuel, Timon, Julz, Leo, Karla, Nina, David, Clara – it is always such a pleasure to see you all again. I feel privileged to have met so many outstanding musicians during my time in Cambridge from whom I have learned so much, in CU(C)O – especially my fellow clarinettists Chloe, Helen, Alex, and Holly – as well as in Pembroke Chapel Choir and all the other temporary ensembles and orchestras. I would like to thank my chamber music partners over the years, in particular Richard for Sforzando and some awesome hiking holidays over the years, vierimpuls – Miriam, Charlotte, Konrad & Minh –, the Musikakademie crew – Vanessa, Annika, Hannah, Liya, Mirjam, Julian, Tobias, Anna, Viola, Fabio, Hanna, Max, Almuth, . . . –, and the Kammermusikkreis Unterwachingen, especially the main organisers Thomas, Judith, and Marlene, but also the Rettich(/Pilz)sekte Dschuud, Silkiii, Lucie, Andrea.

Zum Abschluss geht mein ganz besonderer Dank an meine Familie. Sonja, Gert, Hansi, Matthias, und Carolin, durch euch wird der Wengert immer ein Stück Heimat für mich sein. Opa, ich bin dankbar für jedes Stück Fleiß, Großzügigkeit und Liebenswürdigkeit ich von dir geerbt habe. Elena, ich erzähle allen stets mit größtem Stolz von meiner großen Schwester. Mama, Papa, nur durch eure Hingabe und Liebe bin ich soweit gekommen. Danke, dass ihr immer an mich glaubt und für mich kämpft.

Abstract

Part I of this thesis is concerned with cavity optomechanical systems subject to periodic driving. We develop a Floquet approach to solve time-periodic quantum Langevin equations in the steady state, show that two-time correlation functions of system operators can be expanded in a Fourier series, and derive a generalized Wiener-Khinchin theorem that relates the Fourier transform of the autocorrelator to the noise spectrum.

We apply our framework to optomechanical systems driven with two tones. In a setting used to prepare mechanical resonators in quantum squeezed states, we find and study the general solution in the rotating-wave approximation. In the following chapter, we show that our technique reveals an exact analytical solution of the explicitly time-periodic quantum Langevin equation describing the dual-tone backaction-evading measurement of a single mechanical oscillator quadrature due to Braginsky, Vorontsov, and Thorne [Science 209, 547 (1980)] beyond the commonly used rotating-wave approximation and show that our solution can be generalized to a wide class of systems, including to dissipatively or parametrically squeezed oscillators, as well as recent two-mode backaction-evading measurements.

In Part II, we study nonreciprocal optomechanical systems with several optical and mechanical modes. We show that an optomechanical plaquette with two cavity modes coupled to two mechanical modes is a versatile system in which isolators, quantum-limited phase-preserving, and phase-sensitive directional amplifiers for microwave signals can be realized. We discuss the noise added by such devices, and derive isolation bandwidth, gain bandwidth, and gain-bandwidth product, paving the way toward flexible, integrated nonreciprocal microwave amplifiers.

Finally, we show that similar techniques can be exploited for current rectification in double quantum dots, thereby introducing fermionic reservoir engineering. We verify our prediction with a weak-coupling quantum master equation and the exact solution. Directionality is attained through the interference of coherent and dissipative coupling. The relative phase is tuned with an external magnetic field, such that directionality can be reversed, as well as turned on and off dynamically.

Contents

1 | Introduction

Quantum mechanics had its beginnings in 1900, when Max Planck postulated the existence of a smallest "energy element" (German: "Energieelement") in order to explain black-body radiation [6]. In his original article, he considered a large collection of resonators in a "medium enclosed by reflecting walls". Introducing Planck's constant h, he posited that the energy in every resonator and every light mode be quantized in units of $h \cdot \nu$, where ν is the frequency of that mode. It would be a stretch to call such a system *cavity optomechanics*, but now, more than a hundred years after this discovery, there is renewed interest in the interaction of electromagnetic modes in a cavity with (mechanical) resonators, as evidenced by this thesis.

What is new about this revival of interest in basic quantum-mechanical systems is the unprecedented level of control over the quantum states of such systems that we have today. In the early days, physicists believed that quantum theory was only a valid description of statistical ensembles containing many particles. The implications of their theory for individual particles made many physicists of the time uncomfortable. This is perhaps best illustrated with Schrödinger's thought experiment of a cat in a box that is prepared in a superposition of dead and alive [7], which he conceived to prove is own theory *ad absurdum*.

Despite early ridicule, the stranger predictions of quantum mechanics such as superpositions and entanglement have since been verified experimentally many times over and their existence is no longer up to debate, although the question remains how large systems can potentially be while still exhibiting detectable quantum effects. The mechanisms that limits the size of objects that exhibit quantum effects is the interaction of a system with its environment, leading to *decoherence* [8–10], which is perhaps best illustrated via example.

Let us consider a particle prepared in a spatial superposition of being at two positions, A and B, in contact with a gas. Such a state can be written $|\Phi\rangle = (|A\rangle + |B\rangle)\,|\text{gas}\rangle\,/\sqrt{2}$. If a gas molecule passes through A, it will either scatter or not, depending on the state of the particle, leading to the entangled state $|\tilde{\Phi}\rangle = (|A\rangle\,|\text{scattered}\rangle + |B\rangle\,|\text{not-scattered}\rangle)/\sqrt{2}$. If we were able to determine the state of all gas molecules before and after, we would find

out whether the particle is at A or B. For a macroscopic number of gas molecules, this is clearly impossible, and the information is lost instead. Without further measurements we remain ignorant of the state of the gas, such that the correct description of the particle is a *mixed state*, captured by the reduced density matrix $\hat{\rho}_S = \mathrm{Tr}_{\mathrm{gas}}[|\tilde{\Phi}\rangle\langle\tilde{\Phi}|] = (|A\rangle\langle A| + |B\rangle\langle B|)/2$, where $\mathrm{Tr}_{\mathrm{gas}}$ denotes the trace over the Hilbert space of the gas. Before the decoherence occurred, the particle was in a known state, $|\psi\rangle = (|A\rangle + |B\rangle)/\sqrt{2}$, that could be manipulated, but afterwards, we have lost the information about the state of the particle. This is evidenced by a density matrix that is proportional to the identity and thus invariant under all similarity transformations. Pure states can interfere, whereas particles in a statistical mixture do not interfere, having lost their *coherence*.

As described above, the environment is commonly believed to always be detrimental to quantum coherence. In the example above this is true because the gas couples to the position of the particle, such that it acts to suppress spatial superpositions. Zurek argues that in general, decoherence affects quantum states with clear classical analogue (so-called *pointer states* [11]) the least, thus explaining why we only ever observe robust classical states in everyday life. In recent years it has become clear, however, that specifically engineered environments *can* lead to quantum coherence. Akin to a body assuming the temperature of its surroundings, a quantum state can adopt properties of its environment (we will meet an example where a squeezed environment induces a squeezed motional state in a mechanical resonator in Part I, Sec. 3.2). Or consider a typical tube station, in which passengers are directed by signs, escalators, and walls, leading to an efficient flow. Analogously, specific transport properties can be induced by connecting a system to a tailor-made reservoir, and Part II of this thesis will consider scenarios in which directional flow of particles is achieved in this way. Overall, this paradigm is known as *reservoir engineering* [12], and it might become an invaluable tool in the quest for viable quantum technologies.

While of great fundamental importance, decoherence is also encountered every day in the lab, and presents one of the biggest hurdles for the design of *quantum devices*. Such devices aim to use quantum mechanical effects such as coherence and entanglement for technological applications. One could contest that quantum physics already underpins virtually all of modern technology, illustrated best by the example of the the transistor that powers computers. In fact the majority of 20^{th} century's key insights and technologies – understanding the periodic table, modern material science, solar cells, lasers, MRI scanners – hinge on quantum physics. But while last century's inventions rely on quantum mechanics as description of materials and light, the next generation of quantum devices will be designed to *manipulate* quantum states of matter. This is captured perhaps best in the European Quantum Manifesto [`http://qurope.eu/manifesto`], which is an

attempt to describe what the *second quantum revolution* might look like. The manifesto highlights four core fields in which quantum technologies promise far-reaching advances.

1. Communication. Technologies that use entanglement to make it impossible to eavesdrop.

2. Simulators. Clean, controllable quantum systems that can be used to simulate systems inaccessible to classical computers.

3. Sensors. More accurate sensors that use coherence to suppress noise.

4. Computers. Special- or general-purpose quantum computers that solve certain exponentially hard problems in polynomial time.

The underlying resource in those technologies is quantum coherence, and thus understanding the interaction of quantum systems with their environment is of key importance.

Optomechanics is concerned with the interaction between mechanical motion and light. As most thoughts, the idea that light could affect motion goes back to ancient Greece. Then, however, it was just a potential implication of the atomistic postulate – that everything is made up of particles, which are indivisible at some scale. One of the first reported experimental observation of the effect of light on matter is Kepler's observation that comet tails point away from the sun. That electromagnetic radiation exerts a force on matter, which fundamentally is made up of charged particles, has been clear since Maxwell's theory of electromagnetism, but it took until 1901 when Lebedev [13] and Nichols and Hull [14] measured the radiation pressure force – as it came to be known – experimentally. The invention of the laser made systematic exploration and exploitation of this force possible, which led to the discovery of optical tweezers [15], laser-trapped atoms [16, 17], laser cooling [18], and Bose-Einstein condensates [19, 20].

In cavity optomechanics, a cavity is used to enhance the interaction between the light and mechanical motion. Cavity optomechanics is a young field of research that has attracted a lot of attention due to its variety of potential applications in quantum technology and the possibility of probing quantum mechanics in a new parameter regime [21–24]. In particular, it is demonstrably important in force, acceleration, mass, and charge sensing [25–29], can be used to catch and release photons a.k.a. "flying qubits" [30–32] – a necessary component of quantum networks [33, 34], – and can serve as a transducer between different quantum systems [28, 35, 36].

Broadly speaking, cavity optomechanics is concerned with the interaction of light in a cavity with mechanical systems, typically through radiation pressure force, i.e., the momentum transfer due to photons reflected from a mechanical object. Even though

typically the force exerted by photons on objects is negligible, there exists a plethora of systems where this interaction is important [24], ranging from trapped atoms, which are so light that the momentum of individual photons is clearly important [37], to the Laser Interferometer Gravitational-Wave Observatory (LIGO) [29, 38], a kilometre-sized interferometer with mirrors weighing several kilograms, where laser light crucially influences the motion of the mirror [39, 40] and quantum effects are used to reach higher sensitivities [41]. About half-way in between (on a logarithmic scale) are superconducting LC circuits with drum-capacitors, which, in the past few years, have been put into their quantum ground state [42] (related [43]), in a quantum squeezed state [44–46], been used to store quantum information and retrieve it with high fidelity [32], and have been entangled with each other [47], to name just a few remarkable demonstrations of quantum mechanics in such devices. This list is even more remarkable considering that the mechanical oscillators in these latter experiments weigh tens of picograms ($\sim 10^{-11}\,\mathrm{g}$), and are just about visible to the naked eye.

Mechanical oscillators have mass and inertia and are therefore well-suited to form gravitational wave detectors and acceleration sensors. Reaching the ground state and generating squeezed states are important steps toward enhancing the precision of such sensors beyond standard quantum bounds. The above-mentioned demonstration that quantum information can be faithfully stored on mechanical resonators [32] also establishes them as a viable quantum memory. Finally, the fact that excitations can coherently travel in between electromagnetic and mechanical modes implies that optomechanical systems can be used as frequency transducers [48], amplifiers [49–51], isolators [3, 52, 53], circulators [54], and directional amplifiers [4].

Looking back at the four core fields for quantum technologies, we see that cavity optomechanics is a platform to realize quantum sensors (item #3), but its capacity to store, relay, direct, and amplify information at the quantum level makes it directly useful for quantum communication (#1) and quantum computers (#4) as well. Breaking ground on the way to macroscopic quantum systems, it also promises a table-top experimental platform to explore quantum gravitational effects [55, 56] and the quantum-to-classical transition.

The remainder of this thesis is divided into two parts: Part I is concerned with modulated optomechanical systems. Those are understood as systems where the coherent intracavity field oscillates at a certain frequency, such that the Hamiltonian in the linearized picture becomes periodic in time. This is a very common situation in optomechanics, and while by means of a rotating-wave approximation a time-independent frame can usually be found, this is not always the case. We develop a method to calculate the noise property of linear, periodically modulated systems (Chapter 2), and apply it to a few important

cases (Chapter 3). These include squeezing the mechanical oscillator Sec. 3.2), performing quantum nondemolition measurements of resonator quadratures (Sec. 3.3) – all techniques or measurements where precision is of prime importance, which is why counter-rotating terms ought to be included for highest precision. We address how a power spectral density can be defined in situations where the Wiener-Khinchin theorem does not hold.

In Part II we go beyond the "standard model" of optomechanics containing a single cavity mode and single mechanical mode to multi-mode systems. In particular, we consider systems with two cavity modes and two intermediate mechanical modes, all coupled via radiation, in an arrangement dubbed *optomechanical plaquette*. We show how such a system lends itself to engineering non-reciprocal scattering of photons and phonons. In particular, we study an isolator for microwave photons (Chapter 4) and directional phase-preserving and phase-sensitive amplifiers (Chapter 5). These systems require multiple pumps on each cavity mode and thus always contain modulated intracavity fields, and indeed the theory developed in Part I will find another application in these systems. The examples above use reservoir engineering to achieve directional flow of bosons (photons and phonons). In Chapter 6 we show that reservoir engineering in a double dot can also yield directional flow of electrons, thus extending these concepts to fermions.

Finally, the remainder of this chapter introduces some cavity optomechanics fundamentals and standard techniques.

1.1 The damped harmonic oscillator

1.1.1 Response

As has been alluded to above, cavity optomechanical systems are open systems, which means they are not isolated from their environment. This brings about physical phenomena such as mechanical damping, dephasing of the mechanical state, decay of cavity photons, as well as thermal and quantum noise. These effects are crucial to our understanding of optomechanics and in fact a large part of this thesis is concerned with determining the *noise spectral density*, defined later in this section. The simplest system to study in this context, and also the one we are ultimately interested in, is the damped driven harmonic oscillator, governed by the differential equation

$$\ddot{x} + \omega_0^2 x + \Gamma_{\mathrm{m}} \dot{x} = f(t)/m. \tag{1.1.1}$$

Equation (1.1.1) is solved by introducing its *(retarded) Green function* or *response function* [57]

$$\chi(t) = \Theta(t)\frac{1}{m\omega_{\mathrm{m}}}\sin(\omega_{\mathrm{m}}t)\exp[-\Gamma_{\mathrm{m}}t/2], \tag{1.1.2}$$

where $\Theta(t)$ is the Heaviside step function and $\omega_{\mathrm{m}} \equiv \sqrt{\omega_0^2 - \Gamma_{\mathrm{m}}^2/4}$. The position as a function of time can then be found as the convolution of the response $\chi(t)$ with the driving $f(t)$.

Another way to go about solving Eq. (1.1.1) is by transforming into Fourier space

$$(-\omega^2 + \omega_0^2 - i\Gamma_{\mathrm{m}}\omega)\tilde{x}(\omega) = \tilde{f}(\omega)/m, \tag{1.1.3}$$

which yields the response function in Fourier space (the Fourier transform of $\chi(t)$)

$$\tilde{\chi}(\omega) = \frac{1}{m[(\omega_0^2 - \omega^2) - i\Gamma_{\mathrm{m}}\omega]}. \tag{1.1.4}$$

Here, and in the remainder of this thesis, the Fourier transform is defined as

$$\tilde{f}(\omega) \equiv \int_{-\infty}^{\infty} dt\, e^{i\omega t} f(t), \tag{1.1.5}$$

except when stated otherwise. We will also drop the tilde from now on, and instead distinguish the functions by their argument; frequency ω and time t. The complex function $\chi(\omega)$, shown in Fig. 1.1, gives the response of the oscillator to a force oscillating at a given frequency. It is often referred to as *susceptibility*. The fact that the response is causal (the oscillation occurs after the force is applied) is encoded in the fact that χ is analytic in the upper half plane, which ensures that the inverse Fourier transform (1.1.2) is zero for $t < 0$).[†] The *dissipative* imaginary part of χ arises from the part of $\chi(t)$ that is odd under time-reversal and is proportional to the power dissipated, whereas the *reactive* real part is proportional to the energy shift due to driving.[‡] They are related via the Kramers-Kronig relation, since χ is analytic in the upper half plane. In particular, it allows us to write the susceptibility $\chi(\omega)$ in terms of its imaginary part[*]

$$\chi(\omega) = \int_{-\infty}^{\infty} \frac{d\omega'}{\pi}\frac{\mathrm{Im}[\chi(\omega')]}{\omega' - \omega - i\varepsilon}. \tag{1.1.6}$$

[†]A harmonic oscillator with $\Gamma_{\mathrm{m}} < 0$ therefore seems to violate causality. But the real problem in this case is that the amplitude of oscillations grows exponentially, such that the Fourier transform is not defined. Equation (1.1.2) still makes sense though.

[‡]This interpretation comes from the Hamiltonian of the system where the applied force appears as $-f(t)x(t)$. If $f(t) = f_0\cos(\omega_d t)$, we have $E_{\mathrm{shift}} = -\,\mathrm{Re}[\chi(\omega_d)]f_0^2/2$.

[*]See for example David Tong's lecture notes on kinetic theory for more details, available on its web page: `http://www.damtp.cam.ac.uk/user/tong/kinetic.html`.

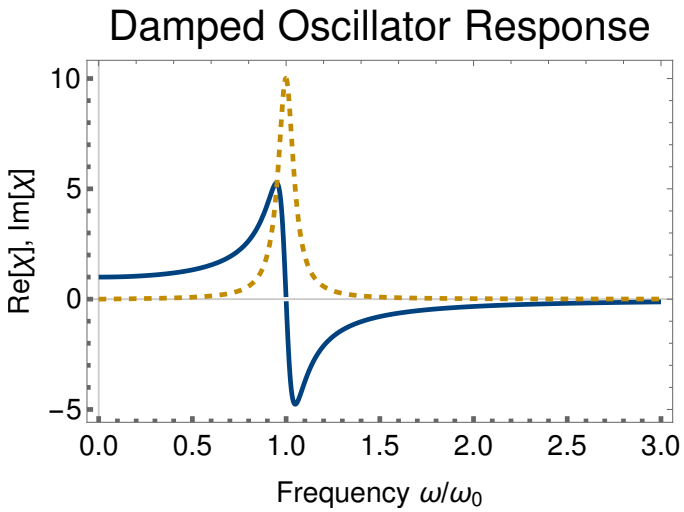

Figure 1.1: Response function for a damped harmonic oscillator. The real part $\mathrm{Re}[\chi(\omega)]$ is shown in blue (solid), the imaginary part in yellow (dashed). Parameters $\Gamma_\mathrm{m} = 0.1\omega_0$, $m = 1$.

1.1.2 Fluctuations

If the harmonic oscillator is in contact with a thermal bath, we expect the oscillator to reach a steady state at the bath temperature. According to statistical mechanics, a collection of such harmonic oscillators is described by a *canonical ensemble* with partition function

$$Z = \frac{1}{h}\int e^{-\beta H(x,p)}dx\,dp = \frac{2\pi}{h\beta\omega_0}\exp\left(\frac{\beta f_0^2}{2m\omega_0^2}\right). \tag{1.1.7}$$

In order to make the partition function dimensionless we have divided by h, which may be chosen to be the Planck constant.[†] The Hamiltonian $H(x,p) = p^2/2m + m\omega_0^2x^2/2 - f(t)x$ appearing in Eq. (1.1.7) describes a harmonic oscillator subject to a constant force f_0. From the partition function Z, we can straightforwardly calculate average position and variance[‡]

$$\langle x\rangle = \beta^{-1}\left.\frac{\partial}{\partial f_0}\right|_{f_0=0}\ln Z = 0, \qquad (\Delta x)^2 = \beta^{-2}\left.\frac{\partial}{\partial f_0}\right|_{f_0=0}\ln Z = \frac{1}{2\beta m\omega_0^2}. \tag{1.1.8}$$

The nonzero variance (1.1.8) arises as a result of thermal fluctuations. As we will see below, damping can be modelled as a coupling to a large number of modes, which together

[†]One can interpret h as an area element in phase space. One can then imagine coarse-graining phase space into little chunks of area h, reflecting our inability to distinguish states below the resolution of measurement instruments, which turns the integral in Eq. (1.1.7) into a sum. Mathematically, however, h can take any value, as multiplying the partition function Z by a number has no effect.

[‡]A faster way to derive this result is to assume equipartition, and thus $\langle H\rangle = \frac{1}{2}k_BT = \langle p^2\rangle/2m + m\omega_0^2\langle x^2\rangle/2$, which also gives Eq. (1.1.7) and additionally yields $\langle p^2\rangle/2m = \frac{1}{4}k_BT$.

form a *bath*. The bath modes have an average, incoherent thermal population and therefore produce a stochastic force on the oscillator. Their shared origin implies that fluctuations and dissipation are closely related, which is captured by the *fluctuation-dissipation theorem* [Eq. (1.1.14)].

In order to account for the fluctuations, we can manually add a stochastic forcing term $f(t) = \xi(t)$ to Eq. (1.1.1). As $\langle x \rangle = 0$, the stochastic force has to have zero mean $\langle \xi(t) \rangle = 0$. If the memory time of the bath is much smaller than the response time of the system, which is often a very good approximation, we can assume delta-correlated (white) noise $\langle \xi(t)\xi(t') \rangle = m^2\Gamma_{\mathrm{m}}^2 D\delta(t-t')$, where D is the diffusion parameter, and the other constants have been inserted for convenience. The resulting *stochastic differential equation* is also known as *Langevin equation*

$$\ddot{x} + \omega_0^2 x + \Gamma_{\mathrm{m}}\dot{x} = \xi(t)/m. \tag{1.1.9}$$

In order to derive the properties of this system, we solve the Langevin equations using the oscillator response function $\chi(t)$, e.g., in Fourier space $x(\omega) = \chi(\omega)\xi(\omega)$. However, since $\xi(t)$ is stochastic, only its expectation values are known. By construction, and in agreement with Eq. (1.1.8), the mean displacement evaluates to $\langle x(t) \rangle = \langle x(\omega) \rangle = 0$. More interesting than the mean is the *autocorrelation function*

$$G(t, t_0) \equiv \langle x(t+t_0)x(t_0) \rangle = \frac{\Gamma_{\mathrm{m}} D}{4\omega_0^2}\left[2\cos(\omega_{\mathrm{m}} t) + \frac{\Gamma_{\mathrm{m}}}{\omega_{\mathrm{m}}}\sin(\omega_{\mathrm{m}} t)\right] e^{-\Gamma_{\mathrm{m}} t/2}. \tag{1.1.10}$$

For a *stationary system*, in which the parameters are independent of time and the noise correlation function only depends on relative time, the autocorrelation function is independent of the centre-of-mass time t_0, $G(t, t_0) = G(t)$. In this case, the *Wiener-Khinchin theorem* states that the Fourier transform of the autocorrelator is the noise spectral density

$$S_x(\omega) = \int_{-\infty}^{\infty} dt\, e^{i\omega t} G(t) = \int_{-\infty}^{\infty} dt\, e^{i\omega t} \langle x(t)x(0) \rangle, \tag{1.1.11}$$

where the noise spectral density is defined as

$$S_x(\omega) \equiv \lim_{T\to\infty} \frac{1}{T} \langle x_T(\omega) x_T(-\omega) \rangle, \tag{1.1.12}$$

where $x_T(\omega) = \int_{-T/2}^{T/2} dt\, \exp(i\omega t) x(t)$ is the windowed Fourier transform. The noise spectral density of a stochastic variable tells us how much power there is at a certain frequency, and is a useful characterization of noise processes. For example, the delta-correlated noise process $\xi(t)$ has a flat noise spectral density $S_\xi(\omega) = m^2\Gamma_{\mathrm{m}}^2 D$, which is

why it is called white noise.[†] In contrast, the oscillator has a response peaked around its effective resonance frequency ω_{m} and filters the white noise, which yields a Lorentzian noise spectral density. It has the noise spectral density (displayed in Fig. 1.2)

$$S_x(\omega) = m^2\Gamma_{\mathrm{m}}^2 D|\chi(\omega)|^2. \tag{1.1.13}$$

The integral over $S_x(\omega)$ yields the total variance, which coincides with $G(0)$, and also

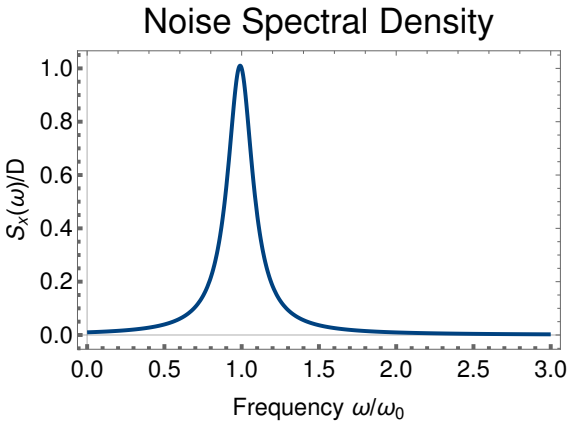

Figure 1.2: Noise spectral density of a damped harmonic oscillator driven by white noise. The noise spectral density is scaled by D [Eq. (1.1.14)] such that this plot is independent of temperature and the mass of the oscillator. Parameter: $\Gamma_{\mathrm{m}} = 0.1\omega_{\mathrm{m}}$.

with Eq. (1.1.8). Comparing the two expressions, we find

$$D = \frac{k_B T}{m\Gamma_{\mathrm{m}}}. \tag{1.1.14}$$

This is a fluctuation-dissipation theorem, as it relates the fluctuations, parametrized by D, and the dissipation (as well as temperature).[‡]

[†] In reality, what we perceive as white light or white noise does not actually have a flat spectral density. Nevertheless, it is an apt name, because no realistic noise process has a flat spectral density anyway (at least there always is a cutoff at some large frequency). Rather, what is important is whether it is approximately flat over the frequency range where the system has an appreciable response, such as the visible range of electromagnetic radiation for eyes.

[‡] The form of D is arbitrary to some extent, as it relies on our definition for the noise correlator. Importantly though, Eq. (1.1.14) relates something that parametrizes the noise strength to temperature and damping rate, as a fluctuation-dissipation theorem should. For more details and examples we refer to Kubo [58].

1.1.3 Rotating-wave approximation

Instead of the second-order differential equation for position x [Eq. (1.1.1)] we can write two coupled first-order differential equations, by introducing the momentum $p \equiv m\dot{x}$

$$\dot{x} = p/m, \tag{1.1.15a}$$

$$\dot{p} = -m\omega_0^2 x - \Gamma_\mathrm{m} p + mf(t). \tag{1.1.15b}$$

These two equations govern the evolution in phase space. An often more convenient form can be obtained by rewriting these equations in terms of the complex amplitude

$$a(t) = \sqrt{\frac{m\omega_0}{2\hbar}}\left[x(t) + \frac{ip(t)}{m\omega_0}\right]. \tag{1.1.16}$$

Note that the prefactor is needed to make the amplitude a dimensionless. The scale is in principle arbitrary, but we have chosen it to match the definitions of the quantum mechanical ladder operators. The complex amplitude has the equation of motion

$$\dot{a} = -i\omega_0 a - \frac{\Gamma_\mathrm{m}}{2}(a - a^*) + \frac{if(t)}{\sqrt{2m\omega_0\hbar}}. \tag{1.1.17}$$

We can pretend we do not already know the solution to the damped harmonic oscillator and solve it again. This time we go straight into Fourier space

$$\left[\frac{\Gamma_\mathrm{m}}{2} - i(\omega - \omega_0)\right] a(\omega) \equiv \chi_\mathrm{m}^{-1}(\omega)a(\omega) = +\frac{\Gamma_\mathrm{m}}{2}a^*(\omega) + \frac{if(\omega)}{\sqrt{2m\omega_0\hbar}}, \tag{1.1.18}$$

where we have defined the mechanical susceptibility

$$\chi_\mathrm{m}(\omega) = \left[\frac{\Gamma_\mathrm{m}}{2} - i(\omega - \omega_0)\right]^{-1} \tag{1.1.19}$$

and Fourier transforms through

$$a(\omega) = \int dt\, e^{i\omega t} a(t), \qquad a^*(\omega) = \int dt\, e^{i\omega t} a^*(t). \tag{1.1.20}$$

This convention is slightly odd, as it implies that $a(\omega)$ and $a^*(\omega)$ are not complex conjugates. Rather, we have $[a(\omega)]^* = a^*(-\omega)$. Overall, it turns out that this convention, whilst initially a bit perplexing, has more advantages than disadvantages.

For mechanical resonators with a high quality factor, $\Gamma_\mathrm{m} \ll \omega_0$, the susceptibility (1.1.19) is strongly peaked around the resonance frequency, and we have $\omega_\mathrm{m} \approx \omega_0$. As

a result, the a^* on the right-hand side of Eq. (1.1.17) is akin to a far off-resonant drive and has little influence on the time-evolution of $a(t)$. In the *rotating-wave approximation* we neglect this term. We can better understand where this expression comes from by transforming into a rotating reference frame $\tilde{a}(t) = e^{i\omega_{\rm m}t}\tilde{a}(t)$, in which Eq. (1.1.17) transforms to

$$\dot{a} = -\frac{\Gamma_{\rm m}}{2}\left(a - e^{2i\omega_{\rm m}t}a^*\right) + \frac{if(t)e^{i\omega_{\rm m}t}}{\sqrt{2m\omega_{\rm m}\hbar}}. \tag{1.1.21}$$

In the frame rotating with the natural frequency of the mode, the RWA can be understood as neglecting terms that rotate quickly. In real time, such terms rotate many times in the complex plane during the natural response time of the mode, $\tau_{\rm resp} = 1/\Gamma_{\rm m}$, and thus they average out. In frequency, they can be understood as far off-resonant drives suppressed by a narrow linewidth. Either way, the upshot is that we can write

$$a(\omega) = \chi_{\rm m}(\omega)\frac{if(\omega)}{\sqrt{2m\omega_{\rm m}\hbar}}. \tag{1.1.22}$$

Computationally, this is easier to deal with than Eq. (1.1.3), and we will use the RWA extensively in this thesis. The quality of the approximation can be determined by comparing the response in the RWA (1.1.19) with the full response (1.1.4). The parameter that controls the size of the corrections is clearly $\Delta\omega/\Gamma_{\rm m}$, where $\Delta\omega$ stands for the detuning of the input from resonance.

1.2 Quantum Langevin equation for damped oscillator

We quantize the harmonic oscillator by introducing the commutation relations analogous to the Poisson bracket in Hamiltonian mechanics [59]. In the case of the harmonic oscillator, this implies

$$[\hat{x}, \hat{p}] = i\hbar, \qquad [\hat{a}, \hat{a}^\dagger] = 1. \tag{1.2.1}$$

However, if we just take the equations of motion in the rotating frame that we derived earlier for the complex amplitude [Eq. (1.1.21)] and turn it into an operator equation, we have (in the absence of driving, and at zero temperature to make the Langevin force disappear)

$$\dot{\hat{a}} \stackrel{?}{=} \left(-i\omega_{\rm m} - \frac{\Gamma_{\rm m}}{2}\right)\hat{a}, \tag{1.2.2}$$

which yields $\hat{a}(t) = \exp[-(i\omega_{\rm m} + \Gamma_{\rm m}/2)t]\hat{a}(0)$. Classically, we expect a harmonic oscillator to come to rest in the absence of driving and at zero temperature. However, Eq. (1.2.2) would imply that the commutation relation decays exponentially $[\hat{a}(t), \hat{a}^\dagger(t)] = \exp(-\Gamma_{\rm m}t)$. It turns out we are missing a crucial ingredient for the description of open

quantum systems[†]: *quantum noise* (or *vacuum noise*).

We have already stated above that damping originates from coupling the system to a bath, which therefore implies the presence of thermal fluctuations. This is still true in quantum mechanics, but a quantum description of the bath reveals that the stochastic force gains an additional contribution responsible for preserving the commutation relations. Such quantum noise does not vanish at zero temperature.

The microscopic model we will study is closely related to the seminal *Caldeira-Leggett model* [60] of a particle coupled to an infinite bath of harmonic oscillators, and is a subset of the general class of systems linearly coupled to a collection of harmonic modes, as introduced by Feynman and Vernon [61]. Quantum Langevin equations were first obtained by Ford *et al.* [62]. Caves [63] was the first to introduce inputs and outputs to study the noise properties of quantum amplifiers, whereas Yurke and Denker [64] have applied quantum Langevin equations to quantum microwave systems. Finally, Gardiner and Collett [65] first wrote down the input-output relations Eq. (1.2.16). The discussion here is inspired by Ref. 66, but very similar derivations can be found in many textbooks [67–69].

Why do we need an infinite set of modes? If there is a finite set of modes, it is straightforward to prove a *quantum recurrence theorem* [70] (in analogy to Poincaré's recurrence theorem), which says that for each $\varepsilon > 0$ and initial state $|\psi(0)\rangle$ there is a finite time τ for which $\langle\psi(\tau)|\psi(0)\rangle > 1 - \varepsilon$. In fact, in order to obtain proper dissipation, we not only need infinitely many modes, they also have to be continuously distributed. This can be appreciated by thinking about a waveguide attached to a cavity. If the waveguide is finite, it will have a discrete (though in theory infinite) spectrum, and our expectation is that a photon emitted into the waveguide will be reflected at the end and subsequently return. On the other hand, if the waveguide is infinite, it has a continuous spectrum, and photons can radiate away for good.

The following derivation holds for both mechanical oscillators coupled to a bath of phonons and cavities coupled to an infinite set of electromagnetic modes outside the cavity. Since the model describes most closely the latter situation, we will talk about a driven damped cavity mode from now on.

1.2.1 Cavity coupled to waveguide

While in principle we would not have to specify a physical situation corresponding to our microscopic model, it is helpful to think of the example of a 1D waveguide terminated by a cavity at $x = 0$. Almost all elements of this discussion will generalize straightforwardly

[†]Though note that Eq. (1.2.2) correctly describes the evolution of the expectation value $\langle a\rangle$.

to different geometries or systems. Let us take x to be the coordinate parallel to the waveguide, such that the electromagnetic field is confined in the y and z direction. Solving the Laplace equation perpendicular to the waveguide yields a set of modes, and we will only consider the state with the lowest energy, such that what is left over is a free wave equation along x. We can therefore write the amplitude of the field as (neglecting polarization, the dependence on y, z, and some overall proportionality constants)

$$\hat{\phi}(x,t) = \int \frac{dk}{2\pi} \left(\hat{b}_k(0) e^{ikx - i\omega t} + \hat{b}_k^\dagger(0) e^{i\omega t - ikx} \right), \tag{1.2.3}$$

where $\omega_k = kc$, where c is the speed of light (in whichever medium the waveguide is in). Adding a perfectly reflecting wall in at $x = 0$ turns this into a semi-infinite waveguide, which supports only those modes that have a node at $x = 0$, which are exactly half as many. In contrast to this perfectly reflecting wall, a cavity allows a small portion of light to pass through. As a result, the waveguide modes couple into the cavity. In the interaction picture, this is represented by the Hamiltonian[†]

$$\hat{H}_{\text{int}}/\hbar = -\lambda \hat{\phi}(x=0,t) \left[\hat{a}(t) e^{-i\omega_c t} + \hat{a}^\dagger(t) e^{i\omega_c t} \right]. \tag{1.2.4}$$

Equation (1.2.4) has been written in the interaction picture (or rotating frame) with respect to the bare Hamiltonian of all modes, in order to make the frequency dependence clear. Note that the uniform coupling λ (independent of mode) and the assumption that the dispersion relation is linear together form the *Markov approximation*, as a result of which the memory-time of the bath is zero. These might appear as stringent conditions, but in the end, for low-loss cavities, they only need to be valid over the small range of frequencies that is the linewidth of the cavity.

For the following discussion it will be useful to have a time-independent Hamiltonian, so we apply the RWA (i.e., neglect the terms $\hat{a}\hat{b}_k + \text{H.c.}$) and instead choose the interaction picture with respect to the Hamiltonian $\hat{H}_0 = \omega_c(\hat{a}^\dagger \hat{a} + \sum_k \hat{b}_k^\dagger \hat{b}_k)$, such that the full Hamiltonian reads

$$\hat{H}/\hbar = \int dk \left[\tilde{\omega}_k \hat{b}_k^\dagger \hat{b}_k - \lambda(\hat{a}^\dagger \hat{b}_k + \hat{b}_k^\dagger \hat{a}) \right], \tag{1.2.5}$$

where $\tilde{\omega}_k = \omega_k - \omega_c$ is the frequency difference of the kth bath mode to the cavity mode. The coupling λ depends on some overlap integral and is therefore mode-dependent. Over the narrow range of frequency we are concerned with, it can be taken to be approximately

[†]Here we assume there is just one single cavity mode. In reality there are of course many, but they are well separated in frequency. Despite writing sums and integrals over all frequencies, we are only interested in a frequency range much smaller than the mode spacing in the cavity (the *free spectral range*), which is true if the cavity is designed in a way to make this true. There could be an issue if there are degenerate modes with differing polarization, but they can be filtered out if necessary.

constant. Given the Hamiltonian (1.2.5) we can now proceed by deriving the Heisenberg equations of motion. For the bath modes, we have

$$\dot{\hat{b}}_k = -i\tilde{\omega}_k \hat{b}_k + i\lambda \hat{a}, \tag{1.2.6}$$

which can readily be solved

$$\hat{b}_k(t) = e^{-i\tilde{\omega}_k t}\hat{b}_k(0) + i\lambda \int_0^t d\tau\, e^{-i\tilde{\omega}_k(t-\tau)}\hat{a}(\tau), \tag{1.2.7}$$

where we have chosen the origin of time to lie at $t = 0$ without loss of generality. Given this, the equation of motion for the cavity annihilation operators becomes

$$\dot{\hat{a}}(t) = i\lambda \int dk\, \hat{b}_k(t) \quad = i\lambda \int dk\, e^{-i\tilde{\omega}_k t}\hat{b}_k(0) - |\lambda|^2 \int dk \int_0^t d\tau\, e^{-i\tilde{\omega}_k(t-\tau)}\hat{a}(\tau). \tag{1.2.8}$$

The first term on the right hand side of Eq. (1.2.8) contains the bath operators at time zero, which therefore encode the initial state of the bath. These bath operators evolve according to their bare (non-interacting) time evolution and then interact with the bath at time t. In the frequency range we are interested in, we can assume a linear dispersion $\tilde{\omega}_k = kc + \text{const.}$ such that, using Eq. (1.2.3), we can interpret the bath field that interacts with the cavity at time t as the right-moving portion of the waveguide field (1.2.3) that at time $t = 0$ was a distance ct away from the cavity

$$\int dk\, e^{-i\tilde{\omega}_k t} i\hat{b}_k(0) = i\hat{\phi}^{\rightarrow}(x = 0, t) = i\hat{\phi}^{\rightarrow}(x = -ct, 0) = \sqrt{c}\hat{a}_{\text{in}}(t). \tag{1.2.9}$$

The second term in Eq. (1.2.8) is the self-energy due to the coupling to the bath modes. It can be evaluated to yield

$$\begin{aligned} &- \int dk\, |\lambda|^2 \int_0^t d\tau\, e^{-i\tilde{\omega}_k(t-\tau)}\hat{a}(\tau) \\ =& - \int_0^t d\tau |\lambda|^2 \int \frac{c}{2\pi} d\omega\, e^{-i\omega(t-\tau)}\hat{a}(\tau) \\ =& - c|\lambda|^2 \int_0^t d\tau\, \delta(t-\tau)\hat{a}(\tau) = -\frac{\kappa}{2}\hat{a}(t). \end{aligned} \tag{1.2.10}$$

In the second equality we used $\omega_k = kc + \text{const.}$ and in last equality we have defined the dissipation rate $\kappa = c|\lambda|^2$.[†] As a result, we can write the equation of motion for the cavity

[†] c does not necessarily have to be the speed of light, it can be modified to absorb constants.

annihilation operator as the *quantum Langevin equation*

$$\dot{\hat{a}}(t) = -\frac{\kappa}{2}\hat{a}(t) + \sqrt{\kappa}\hat{a}_{\mathrm{in}}(t). \tag{1.2.11}$$

It is closely related to the classical Langevin equation [Eq. (1.1.9)], but with the important difference that the noise input $\hat{a}_{\mathrm{in}}(t)$ is an operator. In general, $\hat{a}_{\mathrm{in}}$ provides both thermal and quantum noise. This can be shown directly from the properties of the bath operators that make it up, which have commutation relations

$$\langle \hat{b}_k^\dagger(0)\hat{b}_q(0)\rangle = \delta(k-q)n(\hbar\omega_k), \qquad [\hat{b}_q(0), \hat{b}_k^\dagger(0)] = \delta(k-q), \tag{1.2.12}$$

where $n(\varepsilon) = [\exp(\varepsilon/k_BT) - 1]^{-1}$ is the Bose-Einstein distribution. As a result, the input field obeys

$$\langle \hat{a}_{\mathrm{in}}^\dagger(t)\hat{a}_{\mathrm{in}}(t')\rangle = 2\pi\delta(t-t')n(\hbar\omega_k), \qquad [\hat{a}_{\mathrm{in}}(t), \hat{a}_{\mathrm{in}}^\dagger(t')] = 2\pi\delta(t-t'), \tag{1.2.13}$$

and has zero mean $\langle \hat{a}_{\mathrm{in}}(t)\rangle = 0$. At the same time, it has operator character, such that even in the absence of thermal excitations there is some quantum noise. While classically, at zero temperature there exists neither fluctuations nor dissipation, this is not true in quantum mechanics, where a photon can just as well decay into vacuum (spontaneous emission). The associated fluctuations are the vacuum fluctuations of the field, which supply the quantum noise.

1.2.2 Input-output relation

The input field $\hat{a}_{\mathrm{in}}(t)$ interacts with the cavity during a short amount of time, after which it travels back to $-\infty$, this is the *output field*. At late times, the outgoing field in the waveguide is therefore a record of some linear combination of the input field and whatever has left the cavity. In order to determine its form, we can repeat our derivation of the quantum Langevin equation, except setting the origin of time at a large t_1 which lies in the future of whichever time we are interested in. We then have

$$\hat{b}_k(t) = e^{-i\tilde{\omega}_k(t-t_1)}\hat{b}_k(t_1) + i\lambda\int_t^{t_1} d\tau\, e^{-i\tilde{\omega}_k(t-\tau)}\hat{a}(\tau). \tag{1.2.14}$$

Plugging into the equation of motion for $\hat{a}$ and introducing the output field, this yields the quantum Langevin equation

$$\dot{\hat{a}}(t) = \frac{\kappa}{2}\hat{a}(t) + \sqrt{\kappa}\hat{a}_{\mathrm{out}}(t). \tag{1.2.15}$$

Subtracting Eq. (1.2.15) from Eq. (1.2.11), we arrive at the *input-output relation* [65]

$$\hat{a}_{\mathrm{out}}(t) = \hat{a}_{\mathrm{in}}(t) - \sqrt{\kappa}\hat{a}(t). \tag{1.2.16}$$

This equation is equally valid in Fourier space. Solving the quantum Langevin equation, we can determine the intracavity field $\hat{a}(\omega)$ in terms of the input field $\hat{a}_{\mathrm{in}}(\omega)$, such that the input-output relation can be used to find the *scattering matrix* of the system. This is done several times below. The scattering matrix is the central quantity of interest in linear system, as it predicts the response for any input (as long as the approximations that made the system linear in the first place still hold true).

Finally, note that the above analysis can equivalently be carried out for a mechanical oscillator clamped to some substrate. In that case, the mechanical oscillator can be thought of being attached to many other oscillators via springs, which introduces a coupling of the form $f_k\hat{x}\hat{x}_k$, if $\hat{x}$ is the position operator for the mechanical oscillators and $\hat{x}_k$ are the position operators for the bulk phonon modes. In the RWA, this interaction gives rise to the same Hamiltonian as above (1.2.5), as long as we are allowed to make the same approximations, namely that the spectrum is approximately linear and the coupling approximately constant over the frequency range of interest. If these assumptions are invalid, the environment is said to be *non-Markovian*, in which case much more care has to be taken to analyze the system.

1.3 The optomechanical Hamiltonian

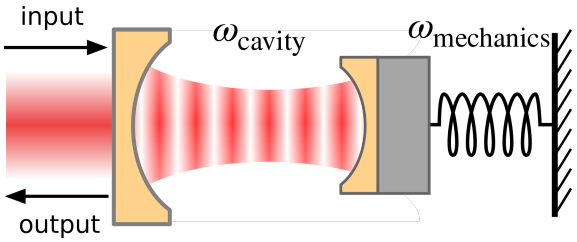

Figure 1.3: Cavity optomechanical system in the optical regime. The cavity is formed by two mirrors (blue). The left mirror is intentionally made less reflective, such that the cavity's principal decay channel is into the vacuum to its left (in other geometries it more common to couple a cavity from both sides). This allows for efficient pumping and readout. The mechanical oscillator is depicted schematically as a mass (grey) on a spring, which has its own resonance frequency $\omega_{\mathrm{mechanics}}$. Photons in the cavity cycle back and forth $\mathcal{F}$-times, which defines the finesse $\mathcal{F}$. On each round trip, a small momentum is imparted on the mechanical resonator. The collection of momentum transfers average to a force, the radiation pressure force.

In cavity optomechanics, an electromagnetic mode confined in a cavity interacts with a mechanical mode via radiation pressure. One way in which this interaction can come about is shown in Fig. 1.3: a Fabry-Pérot cavity is formed by two mirrors (blue), one of which is compliant and acts as mechanical resonator. Photons in the cavity are reflected back and forth many times and impart a small impulse onto the mirror during each round-trip. Taken together, these impulses average to a force proportional to the number of photons in the cavity, the *radiation pressure force*[†], which leads to the optomechanical interaction

$$\hat{H}_{\mathrm{int}}/\hbar = -x_{\mathrm{zpf}}\hat{F}\cdot\hat{x} = -g_0\hat{a}^\dagger\hat{a}(\hat{b}+\hat{b}^\dagger), \tag{1.3.1}$$

where g_0 is the *single-photon optomechanical coupling* and we have introduced the zero-point fluctuations of the mechanical resonator $x_{\mathrm{zpf}} = \sqrt{\hbar/(2m\omega_{\mathrm{m}})}$, with m being the mass of the mechanical resonator, such that $\hat{x}$ is a dimensionless operator

$$\hat{x} = \hat{b} + \hat{b}^\dagger. \tag{1.3.2}$$

Here, we have used bosonic annihilation and creation operators for one cavity mode $\hat{a}$ and one mechanical mode $\hat{b}$. There is an interesting asymmetry in the coupling between light and mechanics in that photons enter through their number or intensity, and phonons only through the amplitude. This nonlinearity could in principle lead to the generation of nonclassical quantum states [71, 72], but unfortunately it is very weak in present-day experiments. In practice, this means that it has to be *coherently enhanced* (or *pumped*) by driving the cavity, which we explain in more detail in Sec. 1.5.

Naturally, there is not just one cavity resonance or one vibrational mode but essentially infinitely many, and all cavity modes couple to all mechanical modes. However, as long as the spacing of cavity modes – the *free spectral range* – is larger than the other energies in the problem, we can safely ignore all other cavity modes. Similarly, if there is no resonant process exciting other mechanical modes, we can ignore them as well. Sometimes it is desirable to use more than one mechanical mode, and one such situation is discussed in Part II.

Another equivalent way to think about the interaction between cavity and mechanical modes is by considering the energy of the photons in the cavity. The energy of each photon in a certain cavity mode is $\hbar\omega_{\mathrm{cav}}$. However, the cavity resonance frequency depends on mirror position, such that to first order in displacements $\hat{x}$ around the equilibrium value,

[†]Radiation pressure force is certainly an awkward name – is it a force or a pressure?

we have [73]

$$\hat{H}_{\text{photons}}/\hbar = \omega_{\text{cav}}(\hat{x})\hat{a}^\dagger\hat{a} = [\omega_{\text{cav}}(0) - g_0\hat{x} + \mathcal{O}(\hat{x}^2)]\hat{a}^\dagger\hat{a}. \tag{1.3.3}$$

It is perhaps not obvious that Eqs. (1.3.1) and (1.3.3) describe the same coupling. In order to establish their equivalence, we assume that $\omega_{\text{cav}}(\hat{x}) = \omega_{\text{cav}}(0)[1 - x_{\text{zpf}}\hat{x}/L + \mathcal{O}(\hat{x}^2)]$, where L is the length of the cavity. On the other hand, the momentum imparted by photon on a mirror is $\hbar\omega_{\text{cav}}/c$ and the rate at which it reflects off the mirror is the inverse of the round-trip time of the photon, c/L. Together this yields a force per photon $\hbar\omega_{\text{cav}}/L$, in agreement with the previous consideration. It also provides us with an estimate of the order of magnitude of the optomechanical coupling. Since the length of the cavity $L \sim c/\omega_{\text{cav}}$, we have $g_0 \sim x_{\text{zpf}}F \sim x_{\text{zpf}}\hbar\omega_{\text{cav}}^2/c$.

Physically, even for very good mirrors there is a finite chance for photons to be transmitted through the mirror, at some rate κ_{ex}. Once outside the cavity, the photons can be detected (see Sec. 1.7), which allows us to infer the state of the system. In reality though, there are many ways a photon could decay. It could for example leave the cavity in the other direction, or be absorbed somewhere. The information encoded in the photons dissipated through these other channels is lost to the experimenter. Therefore, cavities should ideally be *overcoupled*. In experiments, one mirror is usually made slightly less reflective, so that it becomes the dominant decay channel. As a result, the total cavity decay rate $\kappa \approx \kappa_{\text{ex}}$. In Fig. 1.3, the dominant channel is assumed to be tunnelling through the left mirror. Especially in the microwave architecture described below it is not uncommon to have two main ports to the cavity, but the theory can be adapted straightforwardly to this case as well, so we will not discuss this further.

We have drawn the mechanical oscillator as a mass on a spring, which is merely an abstraction. In reality, the "mechanical resonator" could be one of the low-lying modes of a suspended mirror [74], a trampoline [75], or a membrane [76], but very different physical implementations that do not directly implement the paradigm in Fig. 1.3 have been conceived, too. They may hold distinct advantages, such as higher mechanical frequencies, lower dissipation, stronger optomechanical coupling, or better integrability. Among the most important are

- microtoroidal resonators [77], which couple optical whispering-gallery modes in silicon-nitride microtoroids with radial breathing modes that modulate the circumference of the toroid,

- photonic and phononic crystals, which are periodically patterned dielectrics, in which a defect can be introduced that supports localized optical and mechanical

modes [43],

- levitated spheres or rods [78],
- waves in liquids, such as superfluid ^{4}He [79–81], or water [82].

One of the crucial properties of the mechanical oscillators typically used in experiments is their *quality factor* $Q = \omega_{\mathrm{m}}/\Gamma_{\mathrm{m}}$, i.e., the mechanical frequency divided by its bandwidth. It is a measure of the interaction with the environment during one period of oscillation. A large effort is being dedicated in engineering solid state mechanical resonators with large quality factors, be it through phononic band shields [83], improving clamping [84], or strain engineering [85, 86], which has led to tremendous achievements, with current technology achieving $Q > 10^8$ at room temperature [84, 86].

1.4 Microwave optomechanics

So far we have only discussed optomechanics in the optical domain. However, it has already become clear that there are many alternative implementations of the same Hamiltonian, and we have mentioned a few systems with a great variety of mechanical oscillators in the penultimate paragraph of Sec. 1.3 above. At optical frequencies, the electromagnetic field is naturally in its ground state, as even room temperature is much smaller than the energy of an optical photon $k_B T \ll \hbar\omega$. Furthermore, there exists a raft of clever experimental tools to manipulate laser fields, making this platform very versatile. Finally, atoms and ions have transitions in the optical range, and thus optomechanical systems in the optical regimes could be coupled to atoms in cavities [87], ion-trap quantum computers [88, 89], and quantum simulators based on ultracold atoms [90, 91].

There is, however, another popular platform for optomechanics, often referred to as *electromechanics*. Whereas before we have quantized the electromagnetic field in vacuum, we now quantize the electromagnetic field in an LC circuit with frequencies in the microwave range.

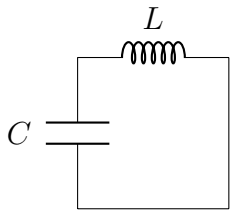

Figure 1.4: LC circuit. It comprises a capacitor C and inductor L. Its resonance frequency is $\omega_{\mathrm{cav}} = 1/\sqrt{LC}$.

The LC circuit is governed by the following equation of motion

$$\dot{Q} = -I, \quad Q = CV = CL\dot{I} \quad \Longrightarrow \quad \ddot{Q} + \omega_{\text{cav}}^2 Q = 0, \tag{1.4.1}$$

where Q is the charge on the capacitor, V is the voltage across the inductor, and $\omega_{\text{cav}}^2 = 1/(LC)$. The implementations we are interested in are superconducting circuits, which is why we can safely neglect dissipation via resistance here. Instead, dissipation will enter later in the form of radiation loss. Overcoupled cavities can again be engineered by evanescent coupling to a transmission line, such that a picture very alike the optical cavity above emerges.

Formally, the LC circuit can be quantized by introducing its Lagrangian [92]

$$\mathcal{L} = \frac{C\dot{\Phi}^2}{2} - \frac{\Phi^2}{2L}, \tag{1.4.2}$$

which reproduces the equations of motion Eq. (1.4.1). Here we have introduced the coordinate $\Phi = LI$, which is the magnetic flux in the coil (note $\dot{\Phi} = \dot{Q}/C$). Φ has the canonical momentum $P = \partial\mathcal{L}/\partial\dot{\Phi} = C\dot{\Phi} = Q$, such that the Hamiltonian is

$$H = P\dot{\Phi} - \mathcal{L} = \frac{\Phi^2}{2L} + \frac{Q^2}{2C}. \tag{1.4.3}$$

To quantize, we take the canonically conjugate coordinates and promote them to operators with commutation relation [59]

$$[\hat{\Phi}, \hat{Q}] = i\hbar. \tag{1.4.4}$$

The operators $\hat{\Phi}$ and $\hat{Q}$ behave like position and momentum of a harmonic oscillator and can be written in terms of ladder operators that create and destroy photons in the LC circuit

$$\hat{\Phi} = \Phi_{\text{zpf}}(\hat{a} + \hat{a}^\dagger), \quad \hat{Q} = -iQ_{\text{zpf}}(\hat{a} - \hat{a}^\dagger), \quad \hat{H} = \hbar\omega_{\text{cav}}(\hat{a}^\dagger\hat{a} + 1/2). \tag{1.4.5}$$

In order to turn the LC circuit into an electromechanical system, we need to introduce a mechanical element. This is commonly done by shaping a parallel-plate capacitor like a drum, with a fixed lower plate and a suspended upper plate [93], as is shown in Fig. 1.5. Displacing the upper plate alters the capacitance and thus the resonance frequency of the LC circuit, leading to the same optomechanical coupling described above.

Comparing the properties of optomechanical and electromechanical systems (see Table 1.1), it seems like electromechanical systems are at a severe disadvantage. In particular, microwave fields are not in vacuum at room temperature, and instead require cryogenic temperature to be noise-free. At the same time, their long wavelength means that

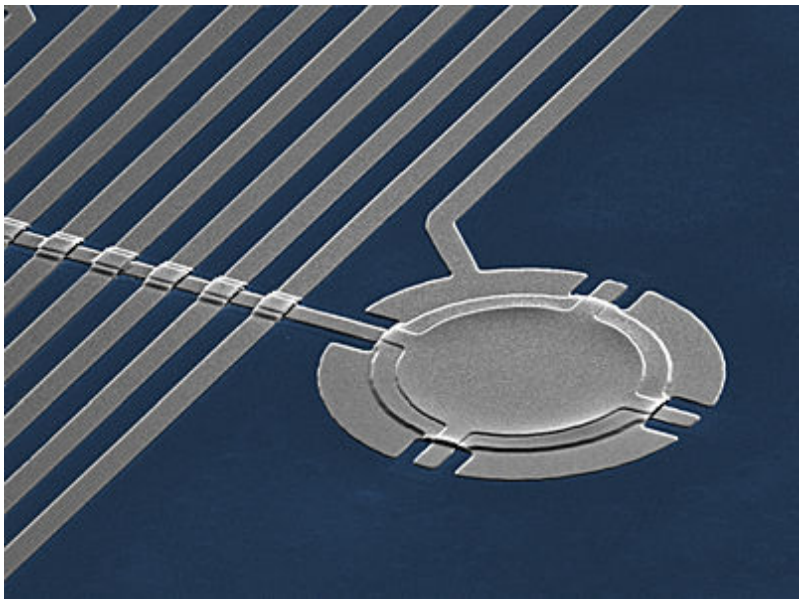

Figure 1.5: Drum capacitor as introduced in Ref. 93. The upper plate is suspended and free to vibrate, which modulates the resonance frequency of the LC circuit. The latter is not shown completely, but a part of the waveguide that forms the inductor is visible. Credit: Teufel/NIST.

cavities will be large, and larger mode volumes imply smaller optomechanical coupling. Finally, it is a formidable task to detect single microwave photons, whereas this does not constitute a problem for optical photons.

Property	**Optomechanics**	**Electromechanics**
Photon frequency	300 THz	30 GHz
Wavelength	1 μm	1 cm
Photon vacuum temperature	15,000 K	1.5 K
Can detect single photons	Yes	Very difficult
Momentum per photon	6.6×10^{-28}kg·m/s	6.6×10^{-32}kg·m/s

Table 1.1: A comparison of some important parameters for optomechanical and electromechanical systems

Many of these limitations, however, can be overcome. As we have already seen above, instead of using vacuum cavities, microwave transmission lines can be used to confine the electromagnetic fields, thus increasing the coupling by orders of magnitude [94]. In order to prevent thermal excitation of photons, circuits can be put in advanced refrigerators, and indeed electromechanical systems are often operated in dilution refrigerators at temperatures of the order of 50 mK in order to reduce the thermal occupancy of the mechanical resonator.

Once these problems have been addressed, electromechanics is attractive for a variety

of reasons. Electromechanical systems are usually printed directly onto superconducting circuits and can directly couple to superconducting qubits, enabling readout via the qubit [95, 96], or control of the phonon number via the qubit, which can be used to produce mechanical Fock states or superpositions thereof [97, 98]. As circuit QED is a strong contender to become the primary platform for quantum computers, electromechanics might become a cornerstone of this development. As we have mentioned above, it has already been demonstrated that electromechanics can be used to catch, store, and release photons at will [30–32]. Another important advantage is that experimentally, microwaves are less fickle than optical photons: albeit more noisy, there is off-the-shelf technology both for producing arbitrarily shaped microwave tones, and for readout.

In the rest of this thesis, we use *optomechanics* to denote cavity optomechanical systems both in the optical and in the microwave regime. Where necessary we will explicitly refer to microwave and optical photons.

1.5 Phenomenology of the optomechanical interaction

As written in Eq. (1.3.1), the optomechanical interaction Hamiltonian actually contains two distinct terms, $\hat{a}^\dagger\hat{a}\hat{b}$ and $\hat{a}^\dagger\hat{a}\hat{b}^\dagger$. Each of them scatters a photon into another one, but the former does so while lowering the occupation of the mechanical resonator, and the latter while raising it. If these processes involve real photons, in the first case the photon gains an energy $\hbar\omega_\mathrm{m}$ (anti-Stokes scattering) and in the second loses this energy (Stokes scattering). Apart from a recent work [99], optomechanical experiments have involved very weak optomechanical nonlinearities, $g_0 \ll \sqrt{\kappa\Gamma_\mathrm{m}}$. Consequently, the most important regime for optomechanics is the one where the cavity is pumped by applying a drive. The drive generates a large coherent field in the cavity, around which the interaction is linearized. With the exception of a few important early works [71, 72, 100], the linearized regime features in most theoretical descriptions of optomechanics.

We can include a coherent drive into the Hamiltonian by writing

$$\hat{H} = \hat{H}_0 + \hat{H}_\mathrm{int} + (\hat{a} + \hat{a}^\dagger)[\varepsilon \exp(-i\omega_L t) + \varepsilon^* \exp(i\omega_L t)], \tag{1.5.1}$$

where $\hat{H}_0 = \hbar(\omega_\mathrm{cav}\hat{a}^\dagger\hat{a} + \omega_\mathrm{m}\hat{b}^\dagger\hat{b})$, and $\hat{H}_\mathrm{int}$ is given through Eq. (1.3.1). The quantum Langevin equation for the cavity mode given this Hamiltonian and damping at rate κ reads (in a rotating frame with respect to $\hbar\omega_L\hat{a}^\dagger\hat{a}$)

$$\dot{\hat{a}} = \left(i\Delta - \frac{\kappa}{2}\right)\hat{a} - ig_0\hat{a}(\hat{b} + \hat{b}^\dagger) - i(\varepsilon + \varepsilon^* e^{2i\omega_L t}) + \sqrt{\kappa}\hat{a}_\mathrm{in}, \tag{1.5.2}$$

where $\Delta = \omega_L - \omega_{\rm cav}$. For an underdamped cavity, we have $\omega_L \gg \kappa$, such that we can neglect the rotating term in the RWA. Neglecting further the weak optomechanical coupling g_0[†], and considering only the expectation value, $\langle \hat{a} \rangle = \alpha$, we have

$$\dot{\alpha} = (i\Delta - \kappa/2)\alpha - i\varepsilon \quad \Longrightarrow \quad \alpha_0 = \frac{i\varepsilon}{i\Delta - \kappa/2}. \tag{1.5.3}$$

Note that this result is simply an application of Eq. (1.1.22). Knowing the steady state amplitude α_0 of the coherent field, we can study fluctuations around this steady state. We thus expand the intracavity field in terms of coherent amplitude plus fluctuations

$$\hat{a} = \alpha_0 + \delta\hat{a}. \tag{1.5.4}$$

The relevant terms in the Hamiltonian appear to second order, which yields the *linearized Hamiltonian*[‡]

$$\hat{H} = -\hbar\Delta\hat{a}^\dagger\hat{a} + \hbar\omega_{\rm m}\hat{b}^\dagger\hat{b} - \hbar g(\delta\hat{a} + \delta\hat{a}^\dagger)(\hat{b} + \hat{b}^\dagger). \tag{1.5.5}$$

Here we have taken the cavity field-enhanced optomechanical coupling $g \equiv g_0\alpha$ to be real without loss of generality. Note that in the rest of this thesis we will consider the linearized case and rename

$$\delta\hat{a} \to \hat{a} \tag{1.5.6}$$

for simplicity. In the context of optomechanics there rarely exists any ambiguity, and in particular this thesis will only be concerned with fluctuations around the mean field.

Initial studies of the effects of radiation pressure on a cavity mirror were focused on cooling its motion using the anti-Stokes process. This is done via so-called *sideband cooling*, where the system is driven with a laser with a frequency around $\omega_{\rm cav} - \omega_{\rm m}$. Since the cavity acts like a filter around its mode frequency $\omega_{\rm cav}$, with a linewidth equal to its dissipation rate κ, anti-Stokes scatting of the incoming photons is enhanced, whereas Stokes scatting is strongly suppressed, at least in the limit where $\kappa \ll \omega_{\rm m}$, also known as *good cavity limit*. A constant influx of photons therefore continuously extracts phonons from the mechanical oscillator and thus cools it. In terms of the linearized Hamiltonian we

[†]This assumption is not necessary to find a closed form solution. The full non-linear equations can be used to find a multistable regime at very strong driving [100], but for intermediate driving strengths all we are missing is a slight change of the cavity detuning

$$\Delta \to \Delta - \frac{2g_0^2\alpha^2}{\alpha_m},$$

and a small modification of α itself [69].

[‡]The Hamiltonian is bilinear, but because the equations of motion derived from the Hamiltonian are going to be linear, this is often called the linearized regime of optomechanics, and the Hamiltonian is therefore the *linearized Hamiltonian.*

have presented above (1.5.5), sideband cooling corresponds to $\Delta = -\omega_{\mathrm{m}}$, in which case we can go into a rotating frame with respect to $\hat{H}_0 = \hbar\omega_{\mathrm{m}}(\hat{a}^\dagger\hat{a} + \hat{b}^\dagger\hat{b})$, which turns it into

$$\hat{H}_{\mathrm{int}} = -\hbar g(\hat{a}^\dagger\hat{b} + \hat{a}\hat{b}e^{2i\omega_{\mathrm{m}}t} + \mathrm{H.c.}) \simeq -\hbar g(\hat{a}^\dagger\hat{b} + \mathrm{H.c.}), \tag{1.5.7}$$

where in the second step we have again used the RWA, which is valid in the good cavity limit mentioned above. Note that we have now started to use $\hat{a}$ to denote fluctuations as described in Eq. (1.5.6). The final Hamiltonian (1.5.7) is sometimes referred to as *beam-splitter Hamiltonian* [24], but one can also think of it as hopping between the two modes. Either way, the implication is that excitations are exchanged between the cavity mode and the mechanical mode. If the cavity mode has a vanishing or very low thermal occupancy, and thermalizes quickly to its bath (as is usually the case), it acts as a cold reservoir to the mechanical resonator and cools it.

A complete theoretical study of the mechanism can be found in Refs 100 and 101. The power of this effect has been demonstrated in many experiments (see, e.g., Refs 76 and 102) and has become a standard tool. Note that we do not necessarily have to refer to quanta to explain this effect, cooling can also be understood as classical dynamical backaction [103, 104].

In the opposite regime, $\Delta = \omega_{\mathrm{m}}$, where the incoming photons have a frequency $\omega_{\mathrm{cav}} + \omega_{\mathrm{m}}$, a pump photon instead resonantly excites both a cavity photon and an oscillator phonon. The resulting Hamiltonian [again note we are talking about fluctuations here, cf. Eq. (1.5.6)]

$$\hat{H}_{\mathrm{int}} = -\hbar g\left(\hat{a}^\dagger\hat{b}^\dagger + \hat{a}\hat{b}\right), \tag{1.5.8}$$

is that of a non-degenerate parametric amplifier, which is why this Hamiltonian may be called *amplification Hamiltonian*. Another important aspect of this Hamiltonian is that it produces only pairs of photons and phonons. This means that the generated photons and phonons are correlated – if one is observed, the other one must exist as well (but could have decayed already) – or in other words, entangled [105–109]. Hence Eq. (1.5.8) may also be referred to as *entangling Hamiltonian*. Finally, this process naturally leads to a two-mode squeezed state, so it may also be called *two-mode squeezing Hamiltonian*.

More details about the entanglement produced are discussed in Ref. 69.

1.6 Input-output theory for linear coupled modes

Having introduced input-output theory for a single cavity mode or a single mechanical oscillator, we can ask the question how to calculate the scattering matrix and noise spectral

densities in more complicated systems that are made out of many modes. If the system is linear and weakly coupled to baths fulfilling the Markov conditions above, we can write down a generic quantum Langevin equation

$$\dot{\hat{\mathbf{x}}}(t) = \mathsf{A} \cdot \hat{\mathbf{x}}(t) + \mathsf{L} \cdot \hat{\mathbf{x}}_{\rm in}(t), \tag{1.6.1}$$

where we have introduced a vector of system operators $\hat{\mathbf{x}} = (\hat{a}_1, \cdots, \hat{a}_N, \hat{a}_1^\dagger, \cdots, \hat{a}_N^\dagger)^T$, a similarly structured vector of input operators $\hat{\mathbf{x}}_{\rm in}$, which are multiplied by the diagonal matrix $\mathsf{L} = \mathrm{diag}(\sqrt{\kappa_1}, \cdots, \sqrt{\kappa_N}, \sqrt{\kappa_1}, \cdots, \sqrt{\kappa_N})$, and finally the *dynamical matrix* A, which contains both the coupling in between the modes and dissipation

$$\mathsf{A} = i[\hat{H}, \hat{\mathbf{x}}] - \mathsf{L}^2. \tag{1.6.2}$$

This notation is a little glib, as evaluating the commutator $[\hat{H}, \hat{\mathbf{x}}]$ returns a vector with elements $[\hat{H}, \hat{x}_i]$ instead of a matrix. Instead we mean by this notation a matrix, where in the ith column is the vector $\mathbf{v}_i$ that obeys $\mathbf{v}_i \cdot \hat{\mathbf{x}} = [\hat{H}, \hat{\mathbf{x}}_i]$.

For a time-independent bilinear Hamiltonian $\hat{H}$, as we have assumed here, the set of Langevin equations (1.6.1) can be solved via a standard Fourier transform.[†] We obtain

$$\hat{\mathbf{x}}(\omega) = (-i\omega\mathbb{1} - \mathsf{A})^{-1} \cdot \mathsf{L} \cdot \hat{\mathbf{x}}_{\rm in}(\omega). \tag{1.6.3}$$

The output operators can be found by the general input-output relation $\hat{\mathbf{x}}_{\rm out} = \hat{\mathbf{x}}_{\rm in} - \mathsf{L}\hat{\mathbf{x}}$.[‡] We finally arrive at the scattering matrix defined through $\hat{\mathbf{x}}_{\rm out}(\omega) = \mathsf{S}(\omega)\hat{\mathbf{x}}_{\rm in}(\omega)$,

$$\mathsf{S}(\omega) = 1 - \mathsf{L}\,(-i\omega\mathbb{1} - \mathsf{A})^{-1}\,\mathsf{L}. \tag{1.6.4}$$

In Part I of this thesis we will encounter a common situation where the above analysis breaks down: when the Hamiltonian of the system is a periodic function of time. This arises commonly in cavity optomechanics in situations when the cavity is driven by multiple tones.

1.7 Detection of output fields

In the previous section we presented the general recipe to solve linear quantum Langevin equations, at least as long as the parameters in it are all time-independent. In order to verify these predictions, we need to compare them to experiment. The natural way to analyze

[†] Recall we are using a slightly unusual convention, displayed in Eq. (1.1.20)

[‡] We have suppressed the argument because this holds both in real time and in frequency space.

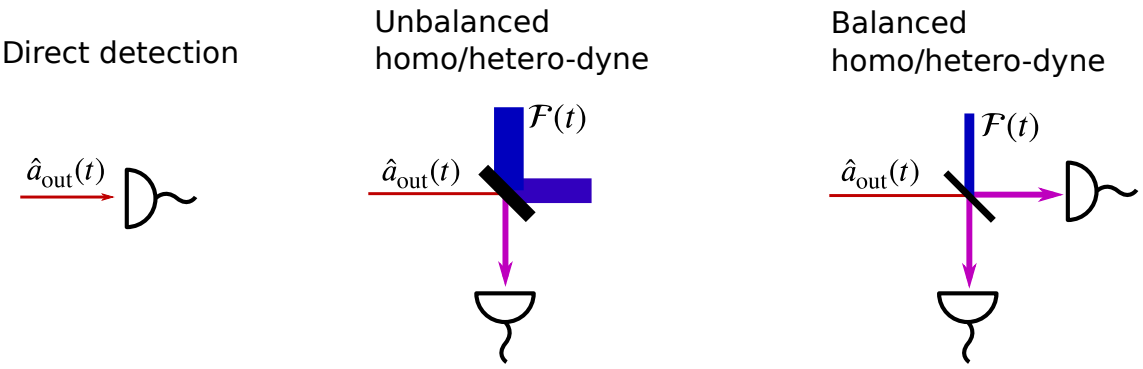

Figure 1.6: Three versions of photo detection. The linear detection schemes are subdivided into homo- and heterodyne, which depends on the frequency of the local oscillator relative to the signal.

properties of the quantum system we are dealing with is to monitor its baths (such as any waveguides connected to it) and use the obtained data to infer the state of the system. The simplest and by far most common way to do this is by observing the photons leaving the cavity, or in other words, the cavity output field $\hat{a}_{\mathrm{out}}(t)$, as introduced above (Sec. 1.2). For the purpose of this section we will generalize the input-output relation (1.2.16) slightly to read

$$\hat{a}_{\mathrm{out}}(t) = \hat{a}_{\mathrm{in}}(t) - \sqrt{\kappa_{\mathrm{ex}}}\hat{a}(t). \tag{1.7.1}$$

Here, we have introduced the external coupling rate $\kappa_{\mathrm{ex}} < \kappa$, which describes the decay rate for photons into the observed output channel. This rate is complemented by other internal cavity decay channels that are not monitored to form the total cavity decay rate $\kappa = \kappa_{\mathrm{ex}} + \kappa_{\mathrm{in}}$. Altogether, this leads us the define the overall detection efficiency $\eta = \eta_{\mathrm{meas}} \cdot \kappa_{\mathrm{ex}}/\kappa$ (where η_{meas} characterizes the rest of the measurement setup), which is the overall efficiency with which the signal can be detected. If $\kappa_{\mathrm{ex}} \approx \kappa$, the cavity is *overcoupled*. This regime is of experimental significance as some protocols rely on detection efficiencies near unity.

There are two fundamentally different ways how the output field can be detected. An obvious possibility is to place a photodetector at the other end of the waveguide, which ideally measures $\hat{n}_{\mathrm{out}}(t) = \hat{a}^{\dagger}_{\mathrm{out}}(t)\hat{a}_{\mathrm{out}}(t)$. This method is called *direct photodetection*. It is a useful tool, because this measurement introduces a non-linearity in the system. In otherwise linear cavity optomechanical systems, this important resource can be used to herald non-classical mechanical states [110–116] and entanglement [117].

While perfectly viable[†], it only gives access to the intensity of the output field, and loses information contained in the quadratures. As a result, a second method is usually

[†]Perfectly viable for optical photons at least. At microwave frequencies it is easy to measure quadratures of the field (such as the voltage), but difficult to resolve single photons, as their energy is very low.

employed in optomechanics that goes by the name of *linear detection*. In order to access information about the quadratures of the output field, it is mixed with a much stronger coherent field $\mathcal{F}(t) = F\exp(-i\omega_{\mathrm{LO}}t - i\varphi_{\mathrm{LO}})$ (a.k.a. *local oscillator*) at either the same (*homodyne*) or different (*heterodyne*) frequency on beam splitter of reflectivity r. The resulting field has the amplitude

$$\hat{f}(t) = r[\mathcal{F}(t) + \hat{v}(t)] + t\hat{a}_{\mathrm{out}}(t), \tag{1.7.2}$$

where $r^2 + t^2 = 1$.

This field is measured via photodetection, which returns the total photocurrent, represented by the operator

$$\begin{aligned}\hat{n}_{\mathrm{det}} = \hat{f}^\dagger(t)\hat{f}(t) = r^2|\mathcal{F}(t)|^2 + r\left\{\mathcal{F}^*(t)\left[r\hat{v}(t) + \hat{a}_{\mathrm{out}}(t)\right] + \mathrm{H.c.}\right\} \\ + \left[r\hat{v}^\dagger(t) + \hat{a}^\dagger_{\mathrm{out}}(t)\right]\left[r\hat{v}(t) + \hat{a}_{\mathrm{out}}(t)\right].\end{aligned} \tag{1.7.3}$$

While the first part, $|\mathcal{F}(t)|^2$, is just a constant, the third describes fluctuations that are negligible for sufficiently large $\mathcal{F}$. This leaves us with the second term in curly brackets, which is the sum of output field $\hat{a}_{\mathrm{out}}$ and local oscillator noise $\hat{v}$, enhanced and demixed by the local oscillator. There are two ways to get rid of this undesirably contribution. We can either choose $r \ll 1$, but keep $r\mathcal{F} \gg 1$, which requires a very strong local oscillator tone, or we can used balanced detection, where $r = 1/2$ and both sides of the beamsplitter are observed, as shown in Fig. 1.6. The latter yields two photocurrents. As it turns out, the laser noise appears with opposite sign relative to the cavity output in the two currents, such that again it is possible to remove the laser noise [67].

We find the resulting photocurrent is proportional to

$$\hat{I}_{\mathrm{out}}(t) = \hat{a}_{\mathrm{out}}(t)e^{i\omega_{\mathrm{LO}}t + i\varphi_{\mathrm{LO}}} + \mathrm{H.c.} \tag{1.7.4}$$

If $\hat{a}_{\mathrm{out}}(t)$ contains a coherent part (as would be the case for small coherent inputs to our linear system), say $\hat{a}_{\mathrm{out}}(t) = \alpha\exp(-i\omega_{\mathrm{sig}}t) + \delta\hat{a}_{\mathrm{out}}(t)$, we could average the photon number reading to obtain $\langle\hat{I}_{\mathrm{out}}(t)\rangle = 2\,\mathrm{Re}[\alpha\exp(i\Delta_{\mathrm{LO}}t + i\varphi_{\mathrm{LO}})]$, where we have introduced the detuning of the local oscillator from the signal $\Delta_{\mathrm{LO}} = \omega_{\mathrm{LO}} - \omega_{\mathrm{sig}}$ in this case. If $\Delta_{\mathrm{LO}} = 0$, we call this *homodyne detection*, where we observe only one quadrature of the signal [namely $\alpha\exp(i\varphi_{\mathrm{LO}}) + \alpha^*\exp(-i\varphi_{\mathrm{LO}})$]. Conversely, if $\Delta_{\mathrm{LO}} \neq 0$, there will be two peaks at $\pm\Delta_{\mathrm{LO}}$ of equal height (classically) proportional to $|\alpha|$. This means that a signal would be detected regardless of phase, but also that correlations get lost, and that the signal-to-noise ratio decreases.

More commonly, we are interested in the noise spectral density in the output, in which

case averaging the photocurrent would just return zero. Instead we are interested in the noise correlations. This involves the two-time correlator of detection events

$$\begin{aligned} C_{\mathrm{pc}}(\tau) &= \langle \overline{\hat{f}^\dagger(t+\tau)\hat{f}^\dagger(t)\hat{f}(t+\tau)\hat{f}(t)} \rangle \\ &= \frac{1}{2}\langle \overline{\{\hat{n}_{\mathrm{det}}(t+\tau), \hat{n}_{\mathrm{det}}(t)\}} \rangle - \delta(\tau)\langle \overline{\hat{n}_{\mathrm{det}}(t)} \rangle, \end{aligned} \tag{1.7.5}$$

where the overline denotes time-average with respect to t. The second term in Eq. (1.7.5) only contributes at equal times, $\tau = 0$, and arises because the first term contains a contribution from counting the same photon twice at equal times and can therefore be neglected. Plugging in our expression for the photocurrent (1.7.3), we find

$$C_{\mathrm{pc}}(\tau) = (rF)^4 + \frac{(rF)^2}{2}\langle \overline{\{\hat{I}_{\mathrm{out}}(t+\tau), \hat{I}_{\mathrm{out}}(t)\}} \rangle. \tag{1.7.6}$$

Through a Fourier transform, we obtain the spectrum [67, 69]

$$\begin{aligned} \bar{S}_I(\omega) &= \int_{-\infty}^{\infty} d\tau\, e^{i\omega\tau} C_{\mathrm{pt}}(t) \\ &= (rF)^4\delta(\omega) + \frac{(rF)^2}{2}\int_{-\infty}^{\infty} d\tau\, e^{i\omega\tau} \langle \overline{\left\{\hat{I}_{\mathrm{out}}(t+\tau), \hat{I}_{\mathrm{out}}(t)\right\}} \rangle. \end{aligned} \tag{1.7.7}$$

Homodyne and heterodyne detection are distinguished by the frequency of the local oscillator, which can either coincide with the frequency of the signal or not. This means that in homodyne detection $\hat{I}_{\mathrm{out}}(t) = \hat{X}_{\mathrm{out}}^{\varphi_{\mathrm{LO}}}(t)$ is a slow variable, whereas in heterodyne it rotates at the difference frequency Δ_{LO}. Here, $\hat{X}_{\mathrm{out}}^{\varphi_{\mathrm{LO}}}(t) = \hat{a}_{\mathrm{out}}(t)e^{i\varphi_{\mathrm{LO}}} + \hat{a}_{\mathrm{out}}^\dagger(t)e^{-i\varphi_{\mathrm{LO}}}$ is a quadrature of the optical output field. As a result, we have

$$\bar{S}_I^{\mathrm{hom}}(\omega) = \bar{S}_{X_{\mathrm{out}}^{\varphi_{\mathrm{LO}}}}(\omega). \tag{1.7.8}$$

On the other hand, during heterodyne detection the detected quadrature $\hat{I}_{\mathrm{out}}$ rotates with respect to the stationary quadrature with frequency Δ_{LO}, which means that both quadratures appear in the output spectrum. Phase-sensitive correlations that, for example, are responsible for squeezing, are lost. We find

$$S_I^{\mathrm{het}}(\omega) = \frac{1}{4}\left[S_X(\omega+\Delta_{\mathrm{LO}}) + S_Y(\omega+\Delta_{\mathrm{LO}}) + S_X(\omega-\Delta_{\mathrm{LO}}) + S_Y(\omega-\Delta_{\mathrm{LO}})\right]. \tag{1.7.9}$$

The full heterodyne spectrum contains two copies of the spectrum, once around Δ_{LO} and once around $-\Delta_{\mathrm{LO}}$. Usually, Δ_{LO} is chosen to be large such that one side (say the negative frequency side) can be omitted and we can simply quote a *one-sided heterodyne spectrum*, denoted by an overline. In this case we can simplify Eq. (1.7.9) by omitting quickly

rotating anomalous terms and normal-ordering the creation and annihilation operators such that it reads (normalized to the shot noise floor, which is the 1 out front)

$$\bar{S}_I^{\rm het}(\omega) = 1 + \eta_{\rm meas} S^N_{a_{\rm out}}(\omega - \Delta_{\rm LO}), \tag{1.7.10}$$

where we have reintroduced the measurement efficiency η and defined the normal-ordered spectrum

$$S^N_{a_{\rm out}}(\omega) = \int_{-\infty}^{\infty} d\tau \, \langle \overline{\hat{a}^\dagger_{\rm out}(t+\tau)\hat{a}_{\rm out}(t)} \rangle e^{i\omega\tau}. \tag{1.7.11}$$

For a waveguide otherwise in vacuum, we can go another step further and use the input-output relation (1.2.16) to write the spectrum in terms of cavity operators, rather than output operators. For the heterodyne spectrum, we obtain

$$\bar{S}_I^{\rm het}(\omega) = 1 + \kappa\eta S^N_a(\omega - \Delta_{\rm LO}), \tag{1.7.12}$$

where $\eta = \eta_{\rm meas}\kappa_{\rm ex}/\kappa$.

For the homodyne spectrum the situation is similar, as we can write $\hat{X}^{\varphi_{\rm LO}}_{\rm out}(t) = \hat{X}^{\varphi_{\rm LO}}_{\rm in}(t) + \sqrt{\kappa_{\rm ex}}\hat{X}^{\varphi_{\rm LO}}(t)$. In the simplest case, $\hat{X}^{\varphi_{\rm LO}}$ and $\hat{X}^{\varphi_{\rm LO}}_{\rm in}$ are uncorrelated, in which case

$$\bar{S}_I^{\rm hom}(\omega) = 1 + \eta\kappa\bar{S}_{X^{\varphi_{\rm LO}}}(\omega). \tag{1.7.13}$$

Given an optomechanical system, we can use the method presented in Sec. 1.6 to find the form of the output operators in terms of the inputs (whose correlators are known) and proceed to calculate the spectra presented in this section.

Additional details or different derivations can be found in Refs [66, 67, 69, 118, 119].

1.8 The quantum limit of amplification

Linear detection as discussed in the previous section is a way of amplifying a signal. We have found that it is always associated with some shot-noise floor [Eqs. (1.7.12) and (1.7.13)]. This means that in these kinds of detection, there will always be some noise added to the signal. Natural questions to ask are whether noiseless amplification is possible in principle, how it could be obtained, or whether there is a lower limit of some sort, and where it could come from. We can go a long way toward answering this question with relatively simple arguments, but for more details on this topic we refer to the original articles by Haus and Mullen [120], Caves [63] and the review by Clerk *et al.* [66], which inspired the discussion in this section.

Generically, a linear amplifier has an input described by some variable

$$\hat{x}(t) = [\hat{a}(t)e^{-i\omega t} + \hat{a}^\dagger(t)e^{i\omega t}]/\sqrt{2} = \cos(\omega t)\hat{X}(t) + \sin(\omega t)\hat{P}(t), \tag{1.8.1}$$

often the voltage or electric field amplitude at its input port, and delivers an amplified version of the signal at its output. A signal can then be encoded in the slow variables $\langle\hat{a}(t)\rangle$ or a linear combination of $\langle\hat{X}(t)\rangle$ and $\langle\hat{P}(t)\rangle$. The latter two variables, $\hat{X}, \hat{P}$ are the *quadratures* of the signal. Amplifying a linear combination of those is called *phase-sensitive amplification*. However, it might mean that certain signals are missed, for example when $\hat{X}$ is amplified, but the signal is contained in P. For this reason, it usually makes more sense to amplify the complex amplitude $\hat{a} = (\hat{X} + i\hat{P})/\sqrt{2}$, as it contains both quadratures of the signal. Since the amplification captures the signal regardless of phase this is often referred to as *phase-preserving* or *phase-insensitive amplification*. Given this terminology, heterodyne detection is phase-preserving, whereas homodyne detection is phase-sensitive.

Defining the input and output modes at each port of the amplifier as above, $\hat{a}_{i,\mathrm{in}}$, $i = 1, 2$, we can ask what sort of transformations are allowed on the input mode. Ideally, we would like that $\hat{a}_{2,\mathrm{out}} = \sqrt{\mathcal{G}}\hat{a}_{1,\mathrm{in}}$, but it is straightforward to see that if both input and output operators need to have bosonic commutation relations, $\mathcal{G}$ has to be 1. We conclude that the above equation is incomplete, and we instead have

$$\hat{a}_{2,\mathrm{out}} = \sqrt{\mathcal{G}}\hat{a}_{1,\mathrm{in}} + \hat{F}. \tag{1.8.2}$$

In principle, $\mathcal{G} \in \mathbb{C}$, but at the moment the phase imparted by the device is unimportant and well set $\mathcal{G} \in \mathbb{R}$ and $\mathcal{G} > 0$. In this case, $[\hat{F}, \hat{F}^\dagger] = 1 - \mathcal{G} < 0$, which is easiest to fulfil with $\hat{F} = (\mathcal{G} - 1)\hat{c}$, some extra bosonic mode. This additional mode, the *idler*, adds noise to the signal. The variance of the output mode thus is given through

$$\langle\Delta\hat{a}_{2,\mathrm{out}}\rangle^2 = \mathcal{G}\langle\Delta\hat{a}_{1,\mathrm{in}}\rangle^2 + \frac{1}{2}\left\langle\left\{\hat{F}, \hat{F}^\dagger\right\}\right\rangle \geq \mathcal{G}\langle\Delta\hat{a}_{1,\mathrm{in}}\rangle + \frac{1}{2}(\mathcal{G} - 1). \tag{1.8.3}$$

In the limit of large gain, $\mathcal{G} \gg 1$, we see that the variance of the output mode has increased by at least "half a quantum" (relative to the signal, which is also amplified by a factor of $\mathcal{G}$), where the equality is reached for an idler in vacuum. This is therefore the *quantum limit* for an amplifier of this class, and an amplifier that saturates this bound is called *quantum-limited*.

One can trace the quantum limit back to the fact that a phase-preserving amplifier amplifies both quadratures of the signal. Those are non-commuting variables, such that perfect knowledge cannot be attained. In contrast, in phase-sensitive amplification only one

quadrature of the signal is amplified. The reason is that one can amplify $\hat{X}$, and de-amplify $\hat{P}$ by the same amount, without violating the commutation relations,[†]

$$\begin{pmatrix} \hat{X}_{2,\mathrm{out}} \\ \hat{P}_{2,\mathrm{out}} \end{pmatrix} = \begin{pmatrix} \sqrt{\mathcal{G}} & 0 \\ 0 & 1/\sqrt{\mathcal{G}} \end{pmatrix} \begin{pmatrix} \hat{X}_{1,\mathrm{in}} \\ \hat{P}_{1,\mathrm{in}} \end{pmatrix}. \tag{1.8.4}$$

As can be easily checked, $[\hat{X}_{2,\mathrm{out}}, \hat{P}_{2,\mathrm{out}}] = [\hat{X}_{1,\mathrm{in}}, \hat{P}_{1,\mathrm{in}}]$, such that this transformation preserves the commutation relations without the need for introducing additional modes. As a result, phase-sensitive amplification can be *noiseless*. It comes with the disadvantages that if the signal arrives in $\hat{P}_{1,\mathrm{in}}$, it is deamplified, such that this method is only useful if the phase of the signal is known.

In Part II of this thesis we study both phase-preserving and phase-sensitive directional amplifiers implemented in an optomechanical system. Squeezing and the closely related backaction-evading measurement of an oscillator quadrature are the main topics in Part I.

1.9 Our work

The research contained in this thesis can be divided into two main parts. In Part I, we study optomechanical systems with periodically modulated parameters. Such situations arise naturally when multiple tones are applied to the cavity, but can also be due to other external factors that lead to a periodic excursion of system parameters. This results in a Hamiltonian and consequentially quantum Langevin equations that are explicitly periodic in time, for which the methods described in Sections 1.6 and 1.7 are not directly applicable.

In Chapter 2, we therefore develop a new theoretical tool to calculate noise spectral densities in periodically modulated linear systems, work that has been published as Ref. 1. We show that two-time correlation functions of system operators can be expanded in a Fourier series and that a generalized Wiener-Khinchin theorem relates the Fourier transform of their zeroth Fourier component to the measured noise spectral density.

We apply our method to a standard optomechanical setup driven by two tones detuned from the cavity resonance by $\pm\omega_{\mathrm{m}}$, the mechanical frequency (Chapter 3). Such a setup was proposed in Ref. 121 as a way to generate quantum squeezing in a mechanical oscillator, which was subsequently realized experimentally [44–46, 122]. We then apply this method to other systems, finding an exact solution beyond the RWA in the case of balanced tones, a situation in which a backaction-evading measurement of the mechanical oscillator quadrature is performed, which has been published as another article [2].

In Part II we study optomechanical systems with more modes, in particular studying

[†]This transformation is known as *squeezing*.

the *optomechanical plaquette*, which is a system where two cavities are coupled via two intermediate mechanical oscillators. In Chapter 4 we show theoretically and experimentally that such a system can exhibit *nonreciprocity*, where light may be transmitted through the system in one way only, forming an *isolator*. This research was published as Ref. 3. In Chapter 5 we also show how this system can be generalized to form *directional amplifiers* that isolate in one direction and amplify photons in the other, published as Ref. 4. Finally, we find that the mechanism underlying this directional transport can not only be implemented in bosonic system, but also in fermionic systems. Along those lines we propose a novel double quantum dot architecture that achieves current rectification through the interference of dissipative and coherent coupling, which has been published as Ref. 5 and forms Chapter 6.

Part I

Periodic driving in optomechanics

2 | Theory

We develop a Floquet approach to solve time-periodic quantum Langevin equations in the steady state. We show that two-time correlation functions of system operators can be expanded in a Fourier series and that a generalized Wiener-Khinchin theorem relates the Fourier transform of their zeroth Fourier component to the measured spectrum. We apply our framework to periodically driven cavity optomechanical systems, a setting in which mechanical oscillators have recently been prepared in quantum-squeezed states. For balanced tones placed symmetrically around the cavity resonance we derive the spectral density without resorting to the rotating-wave approximation (RWA), which constitutes an exact solution of explicitly time-dependent quantum Langevin equations. Our method provides an intuitive and practical way to calculate the power spectral densities for time-periodic quantum Langevin equations in arbitrary rotating frames. Most of the results in this chapter have been published in Ref. 1.

2.1 Introduction

In a recent breakthrough, quantum squeezing of a mechanical oscillator has been demonstrated experimentally [44–46]. It was achieved in a standard optomechanical setup, in which the cavity is driven by two tones placed symmetrically around the cavity resonance frequency, with a detuning equal to the mechanical resonance frequency, i.e., at frequencies $\omega_{\mathrm{cav}} \pm \omega_{\mathrm{m}}$. This method, commonly referred to as *dissipative squeezing*[†] has been analyzed first in Ref. 124, but its full potential was realized later [121]. Driving the cavity with two coherent tones results in a Hamiltonian and consequentially quantum Langevin equations that have an explicit periodic time-dependence. The techniques presented in the previous chapter do not apply directly, as the Fourier transform of a Langevin equation with time dependence in general involves a convolution of frequencies, and in the specific case of

[†]This name was established in Ref. 121. It should be contrasted with *parametric squeezing*, where squeezing arises as a result of a term $\hat{H}_{\mathrm{squeeze}} = \lambda(\hat{a}^\dagger\hat{a}^\dagger + \hat{a}\hat{a})$ in the Hamiltonian, which however leads to only 3 dB of squeezing before an instability is encountered. Though note that strong squeezing could be obtained if the instability is prevented by additional sideband cooling [123].

periodic time dependence a sum over frequencies shifted from each other by multiples of the modulation frequency. As a result, solving such Langevin equations is more difficult than solving stationary ones. In addition, once the solution is obtained, the typical formulae for noise spectral densities presented in Sec. 1.7 do not apply.

In this chapter, we develop a simple, yet powerful approach to find the steady state of the periodically driven optomechanical system based on Floquet theory. In effect, we split up system operators into Fourier components, which individually obey stationary quantum Langevin equations. Any two-time correlation function of system operators such as $C_{AB}(\tau, t) = \langle \hat{A}(t+\tau)\hat{B}(t)\rangle$ is periodic in t and thus can also be expressed in Fourier components, a property that carries over to the Fourier transform with respect to the relative coordinate τ. The resulting quantity, $S_{AB}(\omega, t)$, is closely related to experimentally observed noise spectral densities. We find below that a typical measurement returns its time average, i.e., the zeroth Fourier component $S^{(0)}_{AB}(\omega) = \overline{S_{AB}(\omega, t)}$, but sometimes the rotating components may carry important information, as is the case in dissipative squeezing [44–46, 121] discussed further in Chapter 3.

We note that the covariance matrix for a cavity optomechanical system with periodically modulated coupling strength has been obtained by similar means [124], which is briefly described in Sec. 2.9, and that periodic quantum master equations have been studied, for example, in the context of cavity quantum electrodynamics [125]. Finally, input-output theory for periodically modulated linear systems is already an established field for classical systems [126–130].

Since the publication of our first article [1], time-dependent Langevin equations were found to describe levitated nanospheres [131], which led to another investigation of modulated optomechanical systems [132]. It can be shown that the methods introduced there can be brought into agreement with ours, a finding further corroborated by numerical simulations and experimental data [133]. Later, non-resonant terms (and thus Langevin equations with periodic time dependence) were found to play an important role in nonreciprocal optomechanical devices such as isolators [3, 53] and directional amplifiers [4]—the subject of Part II of this thesis,—as well as thermometry experiments [134]. Thus, our Floquet approach is rapidly becoming a valuable tool in the investigation of optomechanical devices.

The remainder of this chapter contains a detailed description of our framework. The theory contained in the chapter has been introduced in Ref. 1, however this chapter includes new results on the formulation of input-output theory and the scattering matrix to complete the description of periodically driven linear optomechanical systems. We generalize Sec. 1.7 to encompass the modulated case, keeping with the language established above. In Chapter 3 we present results obtained by applying this framework to a range of systems.

2.2 Floquet ansatz

In Sec. 1.5 we derived the linearized Hamiltonian for optomechanical systems by considering fluctuations around the cavity field. Regularly situations arise when the cavity mode is pumped with multiple tones, such that the intracavity field becomes time-dependent. As a consequence it is no longer possible (without further approximations) to find a rotating frame in which the Hamiltonian is time-independent. This situation is generically described by a set of quantum Langevin equations

$$\dot{\hat{\mathbf{x}}}(t) = \mathsf{A}(t)\hat{\mathbf{x}}(t) + \mathsf{L}\hat{\mathbf{x}}_{\mathrm{in}}(t), \tag{2.2.1}$$

which are a generalization of Eqs. (1.6.1) and (1.6.2), and where now $\mathsf{A}(t+T) = \mathsf{A}(t)$ for some period T. Equation (2.2.1) is no longer straightforwardly solvable via a Fourier transform, as the first term on the right-hand side leads to a convolution in frequency space. However, if the *dynamical matrix* (or *Langevin matrix* [135]) $\mathsf{A}(t)$ is periodic as assumed, we can write it as

$$\mathsf{A}(t) = \sum_n \mathsf{A}^{(n)} e^{in\delta t}, \tag{2.2.2}$$

where $\delta = 2\pi/T$ is the fundamental frequency. We can similarly expand the vector of operators in terms of *Fourier operators*, such that

$$\hat{\mathbf{x}}(t) = \sum_n \hat{\mathbf{x}}^{(n)}(t) e^{in\delta t}. \tag{2.2.3}$$

The Fourier operators $\hat{\mathbf{x}}^{(n)}(t)$ are not unique. Given a solution $\{\hat{\mathbf{x}}^{(n)}\}$, transformations such as $\hat{\mathbf{x}}^{(n)}(t) \to \hat{\mathbf{x}}^{(n)}(t) + e^{ik\delta t}\hat{\mathbf{y}}(t)$ and $\hat{\mathbf{x}}^{(n+k)}(t) \to \hat{\mathbf{x}}^{(n+k)}(t) - \hat{\mathbf{y}}(t)$ lead to other solutions. However, these transformations leave the (physical) system operators $\hat{\mathbf{x}}(t) = \sum_n e^{in\delta t}\hat{\mathbf{x}}^{(n)}(t)$ invariant and we can show that the Fourier components of the spectra are also unchanged. In Eq. (2.2.5) we choose to put the noise operators entirely in the zeroth component equation. The quantum Langevin equation is a first order ordinary differential equation, which guarantees the uniqueness of its solution. For a more mathematical discussion, we refer to established literature [126–130].

This ansatz allows us to rewrite the quantum Langevin equation as

$$\sum_n e^{in\delta t}\left[\left(\frac{d}{dt}+in\delta\right)\hat{\mathbf{x}}^{(n)}(t)\right] = \sum_{n,m} e^{i(n+m)\delta t}\mathsf{A}^{(m)}\hat{\mathbf{x}}^{(n)}(t) + \mathsf{L}\hat{\mathbf{x}}_{\mathrm{in}}(t)$$
$$= \sum_n e^{in\delta t}\left[\sum_m \mathsf{A}^{(n-m)}\hat{\mathbf{x}}^{(m)}(t) + \delta_{n,0}\mathsf{L}\hat{\mathbf{x}}_{\mathrm{in}}(t)\right]. \tag{2.2.4}$$

One solution to this set of equation is obtained when the square brackets equal each other, i.e.,

$$\left(\frac{d}{dt}+in\delta\right)\hat{\mathbf{x}}^{(n)}(t) = \sum_m \mathsf{A}^{(n-m)}\hat{\mathbf{x}}^{(m)}(t) + \delta_{n,0}\mathsf{L}\hat{\mathbf{x}}_{\mathrm{in}}(t). \tag{2.2.5}$$

With this transformation we have achieved to obtain a set of stationary Langevin equation (i.e., without explicit time-dependence), which means we can again solve it via a Fourier transform. However, the drawback of Eq. (2.2.5) is that it is an infinite set of coupled equations. Transforming Eq. (2.2.5) first into Fourier space [using convention Eq. (1.1.20) for the components of $\hat{\mathbf{x}}$]

$$(-i\omega+in\delta)\,\hat{\mathbf{x}}^{(n)}(\omega) = \sum_m \mathsf{A}^{(n-m)}\hat{\mathbf{x}}^{(m)}(\omega) + \delta_{n,0}\mathsf{L}\hat{\mathbf{x}}_{\mathrm{in}}(\omega), \tag{2.2.6}$$

we can cast the infinite set of equations into a matrix equation

$$\begin{pmatrix} \ddots & \vdots & \vdots & \vdots & \iddots \\ \cdots & i(\omega+\delta)+\mathsf{A}^{(0)} & \mathsf{A}^{(-1)} & \mathsf{A}^{(-2)} & \cdots \\ \cdots & \mathsf{A}^{(1)} & i\omega+\mathsf{A}^{(0)} & \mathsf{A}^{(-1)} & \cdots \\ \cdots & \mathsf{A}^{(2)} & \mathsf{A}^{(1)} & i(\omega-\delta)+\mathsf{A}^{(0)} & \cdots \\ \iddots & \vdots & \vdots & \vdots & \ddots \end{pmatrix} \begin{pmatrix} \vdots \\ \hat{\mathbf{x}}^{(-1)} \\ \hat{\mathbf{x}}^{(0)} \\ \hat{\mathbf{x}}^{(1)} \\ \vdots \end{pmatrix} = \begin{pmatrix} \vdots \\ 0 \\ -\mathsf{L}\hat{\mathbf{x}}_{\mathrm{in}} \\ 0 \\ \vdots \end{pmatrix}. \tag{2.2.7}$$

The inverse of this matrix is also referred to as *harmonic transfer function* [126]. In most cases, a solution requires an approximation that takes the Fourier modes above a certain index to be zero. One such approximation is the RWA, which neglects non-resonant terms, such that different Fourier modes are decoupled (in the basis where resonant terms are all contained in $\mathsf{A}^{(0)}$). This renders Eq. (2.2.7) block-diagonal. An example of this situation is dissipative squeezing (Sec. 3.2.2). Special cases exist in which the infinite matrix becomes block-diagonal due to fortuitous cancellation even without the RWA, an example of which is the backaction-evading measurement presented in Sec. 3.3.

Using Eq. (2.2.5), it is straightforward to go beyond the RWA, including perturbations up to a certain number of non-resonant terms. Truncating the infinite matrix (2.2.7) above

a certain Fourier index $n_{\max}$ and inverting gives an approximation to the full solution that is good if $n_{\max}\delta$ is much bigger than the relevant dissipation rates, which define the width of the response of the system in frequency space. This condition should be critically reviewed depending on system and driving, as one can find counter-examples, in particular when dealing with signals far off resonance, or strong coupling causing normal-mode splitting. Stringent mathematical definitions and conditions can be found in Ref. 126.

Equation (2.2.7) provides a visual tool for analyzing how the blocks in each entry of the matrix are coupled to each other, which can be exploited to design new driving schemes. For example, a block such as $\mathsf{A}^{(n)}$ can be "activated" by either having an anharmonic drive with a nonzero nth Fourier component, or by adding a laser with frequency $\omega_- + n\delta$. For details on how these matrices look like in optomechanics, see Appendix 3.A.

2.3 Floquet lattice

There is another picture in which we can understand the infinite matrix (2.2.7). It is best explained by example. Therefore, let us consider the standard optomechanical system where one cavity mode is coupled to one mechanical mode via radiation pressure, as introduced in Sections 1.3 and 1.5. As a result of a periodic external driving, a coherent state with the same period is produced in the cavity, $\langle \hat{a}(t) \rangle = \alpha(t)$. This means that the enhanced optomechanical coupling inherits this time dependence, viz.,

$$g(t) = g_0 \alpha(t) = \sum_n e^{in\delta t} g^{(n)}. \tag{2.3.1}$$

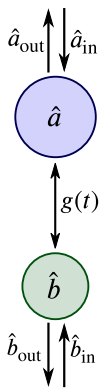

Figure 2.1: Two mode optomechanical system. This figure schematically represents the linearized quantum Langevin equations (2.3.2) governing a standard two-mode optomechanical system with periodic coupling between the cavity and the mechanical mode.

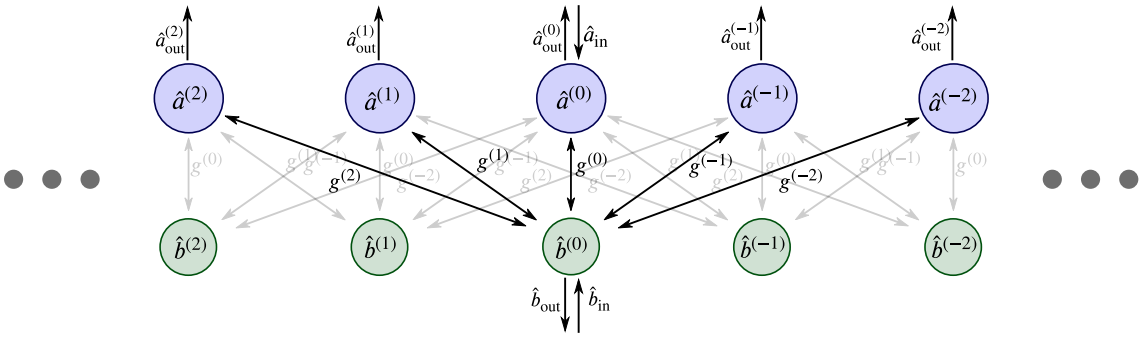

Figure 2.2: The Floquet lattice. A representation of the Langevin equations for the Fourier modes describing an optomechanical system with one cavity and one mechanical mode with periodic coupling. We have drawn one set of couplings (depicted by arrows) in bold colour. This pattern repeats for all modes, as shown in faint colour. $g^{(n)}$ is the Fourier decomposition of the periodic coupling.

The resulting linearized quantum Langevin equations for the fluctuations around the coherent field may be written

$$\dot{\hat{a}}(t) = -\frac{\kappa}{2}\hat{a}(t) + ig(t)[\hat{b}(t) + \hat{b}^\dagger(t)] + \sqrt{\kappa}\hat{a}_{\rm in}(t), \tag{2.3.2a}$$

$$\dot{\hat{b}}(t) = -\frac{\Gamma_{\rm m}}{2}\hat{b}(t) + i[g^*(t)\hat{a}(t) + g(t)\hat{a}^\dagger(t)] + \sqrt{\Gamma_{\rm m}}\hat{b}_{\rm in}(t). \tag{2.3.2b}$$

Pictorially, this is represented as two coupled modes, each coupled to input and output modes, as shown in Fig. 2.1. Performing the map to Fourier operators, this system of equations turns into (suppressing the time argument)

$$\dot{\hat{a}}^{(n)} = \left(-in\delta - \frac{\kappa}{2}\right)\hat{a} + i\sum_m g^{(m)}\left(\hat{b}^{(n-m)} + \hat{b}^{(n-m)\dagger}\right) + \delta_{n,0}\sqrt{\kappa}\hat{a}_{\rm in}, \tag{2.3.3a}$$

$$\dot{\hat{b}}^{(n)} = \left(-in\delta - \frac{\Gamma_{\rm m}}{2}\right)\hat{b}^{(n)} + i\sum_m \left(g^{(-m)*}\hat{a}^{(n-m)} + g^{(m)}\hat{a}^{(n-m)\dagger}\right) + \delta_{n,0}\sqrt{\Gamma_{\rm m}}\hat{b}_{\rm in}. \tag{2.3.3b}$$

Now we have an infinite set of Fourier modes, with linear (time-independent) coupling between them, which could be represented as an infinite lattice as shown in Fig. 2.2.

2.4 Scattering matrix for modulated optomechanics

We have derived the input-output relation for a single damped harmonic oscillator in Sec. 1.2. While the calculation was performed for a single mode connected to a single bath, it can equally well be repeated for a generic class of system Hamiltonians. In particular, there is no restriction for the Hamiltonian to be time-independent. Thus, repeating the

calculation of Sec. 1.2 returns exactly the same input-output relation as before (1.2.16). It can be generalized to many modes, as we have done in Sec. 1.6, such that it reads in Fourier space

$$\hat{\mathbf{x}}_{\mathrm{out}}(\omega) = \hat{\mathbf{x}}_{\mathrm{in}}(\omega) - \mathsf{L}\hat{\mathbf{x}}(\omega). \tag{2.4.1}$$

Writing the solution to Eq. (2.2.6) as

$$\hat{\mathbf{x}}^{(n)}(\omega) = \sum_{m=-\infty}^{\infty} \chi^{(n-m)}(\omega - n\delta)\mathsf{L}\hat{\mathbf{x}}_{\mathrm{in}}^{(m)}(\omega), \tag{2.4.2}$$

where we have introduced the susceptibility $\chi^{(n)}(\omega)$ that contains the response of the system at $\omega + n\delta$ to a signal at ω, we can write down the elements of the scattering matrix in terms of the susceptibility matrix

$$\mathsf{S}^{(n,m)}(\omega) = \mathsf{S}^{(n-m)}(\omega - n\delta) = \delta_{n,m}\mathbb{1} - \mathsf{L}\chi^{(n)}(\omega - n\delta)\mathsf{L}, \tag{2.4.3}$$

which can be used to calculate the output fields

$$\begin{aligned}\hat{\mathbf{x}}_{\mathrm{out}}^{(n)}(\omega) &= \sum_m \mathsf{S}^{(n,m)}(\omega)\hat{\mathbf{x}}_{\mathrm{in}}^{(m)}(\omega) \\ &= \hat{\mathbf{x}}_{\mathrm{in}}^{(n)}(\omega) - \sum_m \mathsf{L}\chi^{(n-m)}(\omega - n\delta)\mathsf{L}\hat{\mathbf{x}}_{\mathrm{in}}^{(m)}(\omega).\end{aligned} \tag{2.4.4}$$

If we further assume that the input is only non-zero in the zeroth Fourier component, and reconstructing $\hat{\mathbf{x}}_{\mathrm{in/out}}(\omega) = \sum_n \hat{\mathbf{x}}_{\mathrm{in/out}}^{(n)}(\omega + n\delta)$, we find

$$\hat{\mathbf{x}}_{\mathrm{out}}(\omega) = \hat{\mathbf{x}}_{\mathrm{in}}(\omega) - \sum_n \mathsf{L}\chi^{(n)}(\omega)\mathsf{L}\hat{\mathbf{x}}_{\mathrm{in}}(\omega + n\delta). \tag{2.4.5}$$

This implies that in principle a photon with frequency ω may be scattered to any of the frequencies $\omega + n\delta$, $n \in \mathbb{Z}$. The same is obviously true for noise, which leads to the emergence of higher-order sidebands.

2.5 Spectrum Fourier components

One might ask what implications the time-periodicity of the quantum Langevin Eq. (2.2.1) has on the properties of the measured spectra, which are derived from correlators of the form

$$C_{AB}(t_1, t_2) = \langle \hat{A}(t_1)\hat{B}(t_2)\rangle. \tag{2.5.1}$$

First of all, if $\mathsf{A}(t) = \mathrm{const}$, there exists a response function (matrix) $\chi(t)$, such that $\hat{\mathbf{x}}(t) = \int_{-\infty}^{t} d\tau\, \chi(t-\tau)\hat{\mathbf{x}}_{\mathrm{in}}(\tau)$. If the input noise is stationary (i.e., its moments are independent of time), then any correlator is translation invariant and can be written just in terms of time difference

$$C_{AB}(t_1, t_2) = C_{AB}(t_1 - t_2), \quad \forall A, B \in \hat{\mathbf{x}}. \tag{2.5.2}$$

In other words, the stochastic process that the operators describe is *stationary*. This is no longer true if $\mathsf{A}(t)$ varies in time, as in this case the response of the system depends on the time that a signal is applied. Thus, even if the noise in the input is stationary, the noise described by the system operators or output operators is not.

As the system is invariant under translations by multiples of its period, the response function, defined through

$$\hat{\mathbf{x}}(t) = \int_{-\infty}^{t} d\tau\, \chi(t,\tau)\hat{\mathbf{x}}_{\mathrm{in}}(\tau), \tag{2.5.3}$$

has the periodicity property

$$\chi(t,\tau) = \chi(t - nT, \tau - nT), \qquad \forall n \in \mathbb{Z}, \tag{2.5.4}$$

which is inherited by the correlators (again only if inputs are stationary)

$$\begin{aligned} C_{x_i x_j}(t_1, t_2) = \langle \hat{x}_i(t_1)\hat{x}_j(t_2)\rangle &= \int_{-\infty}^{t_1}\int_{-\infty}^{t_2} d\tau_1\, d\tau_2\, \chi_{ik}(t_1,\tau_1)\chi_{jl}(t_2,\tau_2)\langle \hat{x}_{\mathrm{in},k}(\tau_1)\hat{x}_{\mathrm{in},l}(\tau_2)\rangle \\ &= \int_{-\infty}^{t_1} d\tau_1\, \chi_{ik}(t_1,\tau_1)\chi_{jl}(t_2,\tau_1)2\pi n_{kl} \\ &= \int_{-\infty}^{t_1-nT} d\tau_1\, \chi_{ik}(t_1,\tau_1+nT)\chi_{jl}(t_2,\tau_1+nT)2\pi n_{kl} \\ &= \int_{-\infty}^{t_1-nT} d\tau_1\, \chi_{ik}(t_1-nT,\tau_1)\chi_{jl}(t_2-nT,\tau_1)2\pi n_{kl} \\ &= C_{x_i x_j}(t_1 - nT, t_2 - nT). \end{aligned} \tag{2.5.5}$$

In the proof we implicitly sum k, l over the components of x_{in}, assume delta-correlated input noise parametrized as $\langle \hat{x}_{\mathrm{in},k}(t_l)\hat{x}_{\mathrm{in},l}(t_l)\rangle = 2\pi\delta(t_k - t_l)n_{kl}$, and took $t_1 > t_2$ without loss of generality. From the third to the fourth line we had to use the periodicity property Eq. (2.5.4).

The periodic time-dependence therefore appears in the Fourier transform of the relative coordinate of any correlator. We define the *spectrum* as well as *spectrum Fourier*

components through

$$S_{AB}(\omega,t) \equiv \int_{-\infty}^{\infty} d\tau\, e^{i\omega\tau} C_{AA}(t+\tau,t) = \sum_n S_{AB}^{(n)}(\omega) e^{in\delta t} \tag{2.5.6}$$

where the spectrum Fourier are explicitly given through

$$S_{AB}^{(m)}(\omega) = \sum_{n=-\infty}^{\infty} \int \frac{d\omega'}{2\pi} \langle \hat{A}^{(n)}(\omega+n\delta) \hat{B}^{(m-n)}(\omega') \rangle. \tag{2.5.7}$$

By construction, the spectrum Fourier components encode all information about the autocorrelator $C_{AA}(\tau,t)$. We will often refer to $S_{A^\dagger A}(\omega,t)$ as "spectrum" although technically it is not a power spectrum in general. As we show in Sec. 2.6, in any given frame, the stationary part $S_{A^\dagger A}^{(0)}(\omega)$ is the physical power spectrum whereas other Fourier components $S_{A^\dagger A}^{(m\neq 0)}(\omega)$ average out for long measurement times. This generalization of the Wiener-Khinchin theorem is consistent with the stationary case, where all Fourier components apart from the zeroth one vanish. In one special rotating frame the rotating components become stationary and can be directly measured (see Sec. 3.2.8). Moreover, we can show that (proof in Sec. 2.8)

$$\left[S_{A^\dagger B}^{(n)}(\omega) \right]^\dagger = S_{B^\dagger A}^{(-n)}(\omega+n\delta). \tag{2.5.8}$$

The stationary spectrum $S_{A^\dagger A}^{(0)}(\omega)$ is thus real, but the other spectrum Fourier components are complex in general.

Finally, we would like to mention that one can regard $S_{A^\dagger A}(\omega,t)$ as a distribution of energy in time and frequency. Its marginal distributions are the stationary part

$$S_{A^\dagger A}^{(0)}(\omega) = \lim_{T\to\infty} \left[\frac{1}{T} \int_0^T dt\, S_{A^\dagger A}(\omega,t) \right], \tag{2.5.9}$$

and the variance as a function of time[†]

$$\langle \hat{A}^\dagger(t) \hat{A}(t) \rangle = \int_{-\infty}^{\infty} \frac{d\omega}{2\pi} S_{A^\dagger A}(\omega,t), \tag{2.5.10}$$

both of which are guaranteed to be real and positive.

[†]Note that we do not have to subtract $\langle \hat{A}(t) \rangle^2$, as all operators discussed here describe fluctuations with zero mean.

2.6 Real spectra in modulated optomechanics

The advantage of splitting system operators up into Fourier components is that these are governed by stationary quantum Langevin equations and thus have time-independent expectation values and time-translation invariant correlation functions. Therefore, any combination of Fourier components has a well-defined spectral density, from which the measured spectra can be obtained in any rotating frame. The remaining question is how the experimentally measured spectrum emerges from this description.

Starting from the definition for spectral density from Ref. 66,[†]

$$\begin{aligned} S^{\mathrm{power}}_{A^\dagger A}[\omega] &\equiv \lim_{T\to\infty} \langle |A_T[\omega]|^2 \rangle \\ &= \lim_{T\to\infty} \frac{1}{T} \int_0^T \int_0^T dt\, dt'\, e^{i\omega(t'-t)} \sum_{n,m} e^{in\delta t' + im\delta t} \langle \hat{A}^{(n)\dagger}(t') \hat{A}^{(m)}(t) \rangle \\ &= \lim_{T\to\infty} \frac{1}{T} \int_0^T dt \int_{-t}^{T-t} d\tau\, e^{i\omega\tau} \sum_{n,m} e^{i\delta[(n+m)t+n\tau]} \langle \hat{A}^{(n)\dagger}(t+\tau) \hat{A}^{(m)}(t) \rangle. \end{aligned} \tag{2.6.1}$$

The expectation value in the last line is in fact time-translation invariant and hence independent of t. Furthermore, as $T \to \infty$, the second integral becomes $\int_{-\infty}^{\infty}$. Therefore, the expression splits into two parts

$$\begin{aligned} S^{\mathrm{power}}_{A^\dagger A}[\omega] &= \sum_n \left(\lim_{T\to\infty} \frac{1}{T} \int_0^T dt \sum_m e^{i\delta(n+m)t} \right) \left(\int_{-\infty}^{\infty} d\tau\, e^{i\delta n\tau + i\omega\tau} \langle \hat{A}^{(n)\dagger}(\tau) \hat{A}^{(m)}(0) \rangle \right) \\ &= S^{(0)}_{A^\dagger A}(\omega), \end{aligned} \tag{2.6.2}$$

where the last line follows because the expression in the first round brackets acts like a Kronecker delta $\delta_{n,-m}$. Where it is helpful to be more precise, we note that the visibility of rotating terms at frequency ω decreases as $\mathrm{sinc}(\omega T/2)$, where T is the total time over which fluctuations are recorded.

Another option is to consider the experimental observation procedure that was discussed in detail in Sec. 1.7. We found that in linear detection, the observed spectrum is the time-averaged correlator of the output current [Eq. (1.7.7)]. Taking for example Eq. (1.7.11)

[†]We assume a specific operator ordering here. In general, the fluctuation power spectrum depends on detection method, some of which have been discussed in Sec. 1.7. However, for individual bosonic annihilation or creation operators, the difference between different orderings amounts to at most a constant.

and expressing it in terms of Fourier modes, we find

$$\begin{aligned} S^N_{a_{\rm out}}(\omega) &= \int_{-\infty}^{\infty} \overline{\langle \hat{a}^\dagger_{\rm out}(t+t_0)\hat{a}_{\rm out}(t_0)\rangle} e^{i\omega t} dt \\ &= \overline{S^{(n)}_{a^\dagger_{\rm out}a_{\rm out}}(\omega) e^{in\delta t_0}} \\ &= S^{(0)}_{a^\dagger_{\rm out}a_{\rm out}}(\omega) \end{aligned} \tag{2.6.3}$$

where the overline denotes averaging with respect to t_0. Note, however, that Eqs. (2.6.2) and (2.6.3) are different statements: one pertains to the power fluctuation spectrum of an observable, the other to a specific measurement process of the cavity output field.

2.7 The spectrum in a rotating frame

Although the rotating components of the spectrum do not appear in the lab frame, they can be observed in a special rotating frame, i.e., through a reference system rotating at the same frequency[†]. In this section we show how rotating frames and spectra are expressed in our framework.

Let us start by defining a quadrature rotating at frequency ν and with an additional phase ϑ

$$\hat{X}^\vartheta_\nu(t) \equiv \hat{b}(t)e^{i\nu t+i\vartheta} + \hat{b}^\dagger(t)e^{-i\nu t-i\vartheta} = \sum_n e^{in\delta t}\left(\hat{b}^{(n)}(t)e^{i\nu t+i\vartheta} + \hat{b}^{(n)\dagger}(t)e^{-i\nu t-i\vartheta}\right). \tag{2.7.1}$$

The autocorrelator of the rotating quadrature contains components rotating at $n\delta$ and $n\delta \pm 2\nu$ in general

$$\begin{aligned} S_{X^\vartheta_\nu X^\vartheta_\nu}(\omega,t) = \sum_{n,m} e^{i(n+m)\delta t}\Big[& f_{bb}(n,m,\omega+n\delta+\nu)e^{2i(\nu t+\vartheta)} \\ + f_{b^\dagger b^\dagger}(n,m,\omega+n\delta-\nu)e^{-2i(\nu t+\vartheta)} & + f_{bb^\dagger}(n,m,\omega+n\delta+\nu) + f_{b^\dagger b}(n,m,\omega+n\delta-\nu)\Big], \end{aligned} \tag{2.7.2}$$

where we have introduced the shorthand

$$f_{A^\dagger B}(n,m,\omega) \equiv \int d\tau\ \exp(i\omega\tau)\langle \hat{A}^{(n)\dagger}(t+\tau)\hat{B}^{(m)}(t)\rangle. \tag{2.7.3}$$

[†]With "measuring a rotating quadrature" and "measuring in a rotating frame" we mean that the cavity mode is coupled to a rotating quadrature of the mechanical oscillator, such that linear detection of the cavity output field Sec. 1.7 effectively performs a measurement of a rotating quadrature.

Note that the RHS of Eq. (2.7.3) does *not* depend on the time t. The Fourier operators $\hat{A}^{(n)}, \hat{B}^{(m)}$ are governed by Langevin equations without explicit time-dependence and thus their correlator is time-translation invariant. Note that the sum $n+m$ tells us which lab frame spectrum component $f(n,m,\omega)$ belongs to, as per Eq. (2.5.7).

Equation (2.7.2) makes it clear that the case $\nu = \delta/2$ is special, since in that case the terms $f_{bb}(n,-n-1,\omega+n\delta+\nu)$ and $f_{b^\dagger b^\dagger}(n,-n+1,\omega+n\delta-\nu)$ are part of the stationary spectrum. This is analogous to the relation between homodyne and heterodyne spectra. We obtain

$$\begin{aligned} S^{(0)}_{X^\vartheta_{\delta/2}X^\vartheta_{\delta/2}}(\omega) = S^{(0)}_{bb^\dagger}(\omega+\delta/2) + S^{(0)}_{b^\dagger b}(\omega-\delta/2) \\ + \cos(2\vartheta)\left[S^{(-1)}_{bb}(\omega+\delta/2) + S^{(1)}_{b^\dagger b^\dagger}(\omega-\delta/2)\right]. \end{aligned} \tag{2.7.4}$$

Equation (2.7.4) is real and positive. In particular, condition (2.5.8) ensures that $S^{(-1)}_{bb}(\omega+\delta/2) = [S^{(1)}_{b^\dagger b^\dagger}(\omega-\delta/2)]^*$.

The utility of these concepts will become clear in Sec. 3.2.4 where we contrast spectra for dissipative squeezing in the lab frame with those in the special rotating frame.

2.8 Properties of the spectrum Fourier components

Let $\hat{A}$ be governed by a time-periodic Langevin equation. Each of its Fourier components $\hat{A}^{(n)}$ obeys a Langevin equation without explicit time-dependence. If the system assumes a stationary state (which it does if all eigenvalues of the Langevin matrix have negative real part), we can write the Fourier transformed Fourier components as a linear combination of the N input operators $\{\hat{F}_{i,\mathrm{in}}(\omega)\}$ (this set contains input operators and their Hermitian conjugates)

$$\hat{A}^{(n)}(\omega) = \sum_i K^{(n)}_i(\omega)\hat{F}_{i,\mathrm{in}}(\omega), \tag{2.8.1}$$

where $\mathbf{K}^{(n)}(\omega)$ is an N-component vector (for each Fourier component n) containing the appropriate functions. In the convention for Fourier transforms described in the main text [Eq. (3.2.5)], the Hermitian conjugate of this equation gives

$$\hat{A}^{(n)\dagger}(\omega) = \sum_i K^{(-n)*}_i(-\omega)\hat{F}^\dagger_{i,\mathrm{in}}(\omega). \tag{2.8.2}$$

The stationary part of the spectrum is [cf. Eq. (2.5.7)]

$$\begin{aligned} S^{(0)}_{A^\dagger A}(\omega) &= \sum_n \int \frac{d\omega'}{2\pi} \langle \hat{A}^{(n)\dagger}(\omega + n\delta) \hat{A}^{(-n)}(\omega') \rangle \\ &= \sum_{n,i,j} \int \frac{d\omega'}{2\pi} K_i^{(-n)*}(-\omega - n\delta) K_j^{(-n)}(\omega') \langle \hat{F}^\dagger_{i,\mathrm{in}}(\omega + n\delta) \hat{F}_{j,\mathrm{in}}(\omega') \rangle \\ &= \sum_{n,i} n_i K_i^{(-n)*}(-\omega - n\delta) K_i^{(-n)}(-\omega - n\delta) \\ &= \sum_{n,i} n_i \left| K_i^{(-n)}(-\omega - n\delta) \right|^2, \end{aligned} \tag{2.8.3}$$

where we had to assume the noise correlators

$$\langle \hat{F}^\dagger_{i,\mathrm{in}}(\omega) \hat{F}_{j,\mathrm{in}}(\omega') \rangle = 2\pi n_i \delta_{ij} \delta(\omega + \omega'), \tag{2.8.4}$$

with thermal occupations $n_i \geq 0$. Thus the stationary part is real and positive.

Another property is $[S^{(n)}_{A^\dagger B}(\omega)]^\dagger = S^{(-n)}_{B^\dagger A}(\omega + n\delta)$. The proof is by expansion

$$\begin{aligned} \left[S^{(n)}_{A^\dagger B}(\omega) \right]^\dagger &= \left[\sum_m \int \frac{d\omega'}{2\pi} \langle \hat{A}^{(m)\dagger}(\omega + m\delta) \hat{B}^{(n-m)}(\omega') \rangle \right]^\dagger \\ &= \sum_m \int \frac{d\omega'}{2\pi} \langle \hat{B}^{(m-n)\dagger}(-\omega') \hat{A}^{(-m)}(-\omega - m\delta) \rangle \\ &= \sum_m \int \frac{d\omega'}{2\pi} 2\pi \delta(-\omega - m\delta - \omega') f_{B^\dagger A}(m - n, -m, -\omega - m\delta) \\ &= \sum_m \int \frac{d\omega'}{2\pi} 2\pi \delta(\omega' + \omega + (m + n)\delta) f_{B^\dagger A}(m, -m - n, \omega') \\ &= \sum_m \int \frac{d\omega'}{2\pi} \langle \hat{B}^{(m)\dagger}(\omega + (m + n)\delta) \hat{A}^{(-m-n)}(\omega') \rangle \\ &= S^{(-n)}_{B^\dagger A}(\omega + n\delta), \end{aligned} \tag{2.8.5}$$

where for convenience we have again used the shorthand (2.7.3)

$$f_{A^\dagger B}(n, m, \omega) \equiv \int \frac{d\omega'}{2\pi} \langle \hat{A}^{(n)\dagger}(\omega) \hat{B}^{(m)}(\omega') \rangle, \tag{2.8.6}$$

which assumes noise correlators of the form (2.8.4).

2.9 Periodic covariance matrix

If we are not interested in the noise spectral density, but exclusively in the variances and covariances of the variables, a more direct approach is to calculate the *covariance matrix*. In order to calculate it in time-periodic systems, we can use again a sort of Floquet ansatz. This has been done in perturbation theory in Ref. 124.

Given the vector of operators $\hat{\mathbf{x}}$, we define the covariance matrix through

$$\mathsf{V}(t) \equiv \langle \hat{\mathbf{x}}(t)\hat{\mathbf{x}}^T(t)\rangle. \tag{2.9.1}$$

Its equation of motion can readily be derived from the quantum Langevin equations (2.2.1)

$$\dot{\mathsf{V}}(t) = \mathsf{A}(t)\mathsf{V}(t) + \mathsf{V}(t)\mathsf{A}^T(t) + \mathsf{L}\mathsf{N}\mathsf{L}^T, \tag{2.9.2}$$

where N is defined through

$$\langle \hat{\mathbf{x}}_{\rm in}(t)\hat{\mathbf{x}}_{\rm in}^T(t')\rangle = \delta(t-t')\mathsf{N}. \tag{2.9.3}$$

The covariance matrix V evolves deterministically [there are no stochastic terms in Eq. (2.9.2)]. The last term in Eq. (2.9.2) is usually identified as diffusion matrix $\mathsf{D} = \mathsf{L}\mathsf{N}\mathsf{L}^T$. For a periodic dynamic matrix $\mathsf{A}(t)$, $\mathsf{V}(t)$ inherits the same periodicity (if the system is stable). Writing $\mathsf{V}(t) = \sum_n \exp(in\delta t)\mathsf{V}^{(n)}$, we obtain (in the steady state)

$$\sum_n e^{in\delta t} in\delta \mathsf{V}^{(n)} = \sum_n e^{in\delta t}\left[\sum_m \left(\mathsf{M}^{(n-m)}\mathsf{V}^{(m)} + \mathsf{V}^{(m)}\mathsf{M}^{(n-m)T}\right) + \delta_{n,0}\mathsf{L}\mathsf{N}\mathsf{L}^T\right]. \tag{2.9.4}$$

Integrating this equation over t, we isolate each Fourier component, so we are left with the system of coupled equations

$$in\delta \mathsf{V}^{(n)} - \sum_m \left(\mathsf{M}^{(n-m)}\mathsf{V}^{(m)} + \mathsf{V}^{(m)}\mathsf{M}^{(n-m)T}\right) - \delta_{n,0}\mathsf{L}\mathsf{N}\mathsf{L}^T = 0. \tag{2.9.5}$$

The entries of $\mathsf{V}^{(0)}$ contain the stationary part of the variance. Note that it is well possible for the variance to vary periodically [124], and then the state with (say) lowest variance occurs at some point during the periodic evolution. Higher Fourier components $\mathsf{V}^{(n)}$ reveal whether that is the case.

2.10 Conclusion

In this chapter, we presented a framework to deal with linear, time-periodic quantum Langevin equations that builds on Floquet theory. In its generic formulation, it can be used to derive the scattering matrix of the system, which has the property that signals at a given frequency ω can be scattered to $\omega + 2\pi n/T$, where $n \in \mathbb{Z}$ and T is the periodicity. The central element of the framework is the map from a finite set of coupled, linear equations of motion to an infinite set of stationary equations of motion. After truncation, the latter can be solved via standard techniques. Occasionally solutions are possible without truncation, an example of which is given in Chapter 3. The map proceeds by splitting system operators up into their Fourier components (3.2.5). The spectrum Fourier components (Sec. 2.5) can be used to calculate power spectra in any rotating frame. This opens a new perspective to understand the relation between the measured spectra and rotating frames, as discussed in Sec. 2.7.

Looking ahead, the presented framework can be used to map time-periodic quantum Langevin equations to familiar, coupled, stationary ones, albeit—as usual for Floquet techniques—infinitely many such equations. Where an exact analytical solution is not feasible, an approximation can be found by truncating the infinite matrix (2.2.7). We would like to point out Ref. 135 as a graphical tool to approximate the inverses of matrices such as Eq. (2.2.7), to any desired order in the coupling. Furthermore, it may prove beneficial to identify conditions under which exact solutions can be found.

3 | Applications

3.1 Introduction

In this chapter, we make use of the framework presented in the previous chapter, and apply it to optomechanical systems driven by two tones. In particular, we analyze the case when the drives are detuned from the cavity resonance by $\pm\omega_{\mathrm{m}}$, which has been shown to cause squeezing of the mechanical resonator for a range of drive strengths [121]. We derive analytic expressions for the mechanical and optical spectrum within the rotating-wave approximation (RWA) for general drive strengths and detunings. With the expressions for the Fourier components of system operators we provide, it is straightforward to construct the spectrum in an arbitrary rotating frame. This enables us to understand dynamical effects that occur when the drives are not exactly on the sidebands, for example, how squeezing generation can fail or fail to be detected. The method also elucidates how information about the system can be extracted through a second, periodically driven "readout" mode, an approach used in the experiments reported in Ref. 46. This part of this chapter has been published in Ref. 1.

The case of two balanced pumps is an important special case, as it realizes a *backaction-evading* (BAE) measurement. A continuous measurement of the position of a harmonic oscillator is subject to the *standard quantum limit* (SQL), a limit directly imposed by Heisenberg's uncertainty relation [66, 136]. An observable that can be monitored without precision limit is called *quantum non-demolition* (QND) variable, such that its continuous measurement can avoid the measurement backaction (BA) [137] and thus open the way to the detection of weak forces, such as those due to gravitational waves [29].

There has been continued interest in implementing BAE measurements [138]. Following a detailed theoretical proposal [139], the first demonstration with a sensitivity beyond the SQL was in optomechanics [140], and they have since proven useful [46, 50, 122, 141]. Despite the importance of such measurements, Ref. 139 discusses only lowest-order corrections to the RWA.

In Sec. 3.3, using our Floquet approach, we are able to go beyond the RWA and in

fact derive the exact solution to the equations describing a BAE measurement. Due to the presence of counterrotating (CR) terms, this constitutes a solution to genuinely explicitly time-dependent quantum Langevin equations, as there is no frame in which they become stationary. The solution is possible because even beyond the RWA, the quadrature of the light that imparts the measurement backaction is orthogonal to the quadrature that receives the signal. This work was published in Ref. 2.

3.2 Dissipative squeezing

3.2.1 Model

For the most part we consider a standard optomechanical system comprising one cavity mode and one mechanical mode. In Sec. 3.2.8 we include a second periodically driven cavity mode to use as readout, which is shown schematically in Fig. 3.1. Finally, in Sec. 3.3 we consider the case of equal pump strengths.

Without the second optical mode, the full Hamiltonian is

$$\hat{H} = \hat{H}_{\mathrm{OM}} + \hat{H}_{\mathrm{drive}} + \hat{H}_{\mathrm{baths}}, \tag{3.2.1}$$

where ($\hbar = 1$)

$$\hat{H}_{\mathrm{OM}} = \omega_{\mathrm{cav}}\hat{a}^\dagger\hat{a} + \omega_{\mathrm{m}}\hat{b}^\dagger\hat{b} - g_0\hat{a}^\dagger\hat{a}(\hat{b}^\dagger + \hat{b}), \tag{3.2.2a}$$

$$\hat{H}_{\mathrm{drive}} = (\alpha_+ e^{-i\omega_+ t} + \alpha_- e^{-i\omega_- t})\hat{a}^\dagger + \mathrm{H.c.} \tag{3.2.2b}$$

a, b are the bosonic annihilation operators of the cavity mode and the mechanical oscillator, respectively. The cavity mode frequency is ω_{cav}, the mechanical frequency ω_{m}, the coupling strength via radiation pressure g_0, and the driving strengths $\alpha_\pm$, which are associated with the drives with frequencies $\omega_\pm$. For an introduction to the optomechanical Hamiltonian we refer to Sec. 1.3, or Ref. 24, 69.

To proceed, we split the light field into a coherent part and fluctuations, move to a frame rotating with the frequency of the lower frequency laser, split the cavity annihilation operator into coherent part and fluctuations, $\hat{a} \to e^{-i\omega_- t}(\bar{a}_- + \bar{a}_+ e^{-i\delta t} + \hat{a})$, and linearize the Hamiltonian, as in Sections 1.2 and 1.5. With the usual assumptions of Markovian baths, the resulting Hamiltonian

$$\hat{H} = -\Delta\hat{a}^\dagger\hat{a} + \omega_{\mathrm{m}}\hat{b}^\dagger\hat{b} - \left[\hat{a}\left(G_+ e^{i\delta t} + G_-\right)(\hat{b}^\dagger + \hat{b}) + \mathrm{H.c.}\right] \tag{3.2.3}$$

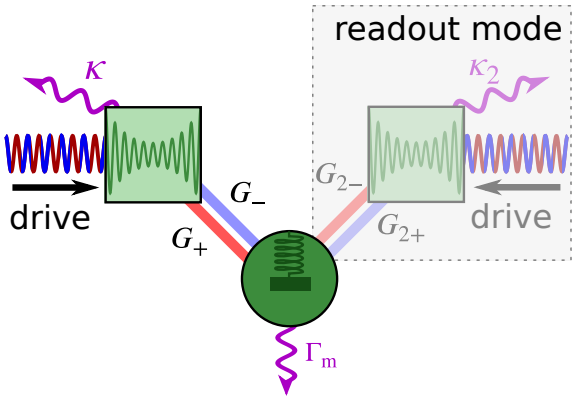

Figure 3.1: Schematic of linearized quantum Langevin equations (3.2.4a) **and** (3.2.4b). The dark green circle represents a mechanical resonator mode with annihilation operator $\hat{b}$, whereas the light green squares represent cavity modes $\hat{a}$ and $\hat{a}_2$, respectively. Both optical modes are driven by two tones placed close to $\omega_{\rm cav} \pm \omega_{\rm m}$, which leads to enhanced optomechanical beamsplitter interaction (G_+, G_{2+}, in red) and amplification interaction (G_-, G_{2-}, in blue). The optical modes are also coupled to independent zero-temperature baths (purple) with rate κ and κ_2, respectively, whereas the mechanical mode has a finite temperature bath at rate $\Gamma_{\rm m}$, leading to an average thermal occupation $n_{\rm th}$. We do not consider the readout mode until Sec. 3.2.8.

gives rise to Langevin equations [66, 67] with explicit periodic time dependence

$$\dot{\hat{a}} = \left(i\Delta - \frac{\kappa}{2}\right)\hat{a} + \sqrt{\kappa}\hat{a}_{\rm in} + i\left(G_+ e^{-i\delta t} + G_-\right)(\hat{b}^\dagger + \hat{b}), \tag{3.2.4a}$$

$$\dot{\hat{b}} = \left(-i\omega_{\rm m} - \frac{\Gamma_{\rm m}}{2}\right)\hat{b} + \sqrt{\Gamma_{\rm m}}\hat{b}_{\rm in} + i\left[\hat{a}\left(G_- + G_+ e^{i\delta t}\right) + \text{H.c.}\right]. \tag{3.2.4b}$$

Here, we have defined the enhanced optomechanical coupling constants $G_\pm = g_0\bar{a}_\pm$, the detuning of the laser from the cavity mode $\Delta = \omega_- - \omega_{\rm cav}$, and the difference between the two laser frequencies $\delta = \omega_+ - \omega_-$. Since we choose the frame of the lower frequency laser, $\delta > 0$ always. $\hat{b}_{\rm in}, \hat{a}_{\rm in}$ are input noise operators with $\langle \hat{a}_{\rm in}(t)\hat{a}^\dagger_{\rm in}(t')\rangle = \delta(t-t')$, $\langle \hat{a}^\dagger_{\rm in}(t)\hat{a}_{\rm in}(t')\rangle = 0$, $\langle \hat{b}_{\rm in}(t)\hat{b}^\dagger_{\rm in}(t')\rangle = (n_{\rm th}+1)\delta(t-t')$, and $\langle \hat{b}^\dagger_{\rm in}(t)\hat{b}_{\rm in}(t')\rangle = n_{\rm th}\delta(t-t')$.

In order to solve Eqs. (3.2.4a) and (3.2.4b), we express them in terms of Fourier components as described in Sec. 2.2 above, using the same convention [Eqs. (1.1.20) and (2.2.3)]

$$\hat{a}(t) = \sum_{n=-\infty}^{\infty} e^{in\delta t}\hat{a}^{(n)}(t), \qquad \hat{a}^\dagger(t) = \sum_{n=-\infty}^{\infty} e^{in\delta t}\hat{a}^{(n)\dagger}(t), \tag{3.2.5}$$

$$\hat{a}^{(n)}(\omega) = \int_{-\infty}^{\infty} dt\, e^{i\omega t}\hat{a}^{(n)}(t), \qquad \hat{a}^{(n)\dagger}(\omega) = \int_{-\infty}^{\infty} dt\, e^{i\omega t}\hat{a}^{(n)\dagger}(t). \tag{3.2.6}$$

Note that these choices imply $[a^{(n)}(\omega)]^\dagger = a^{(-n)\dagger}(-\omega)$. This map yields the generic form

Eq. (2.2.6), with

$$\hat{\mathbf{x}}^{(n)} = \left(\hat{a}^{(n)}, \hat{b}^{(n)}, \hat{a}^{(n)\dagger}, \hat{b}^{(n)\dagger}\right)^T, \quad \hat{\mathbf{x}}_{\mathrm{in}} = \left(\hat{a}_{\mathrm{in}}, \hat{b}_{\mathrm{in}}, \hat{a}_{\mathrm{in}}^\dagger, \hat{b}_{\mathrm{in}}^\dagger\right)^T, \tag{3.2.7}$$

and thus $\mathsf{L} = \mathrm{diag}(\sqrt{\kappa}, \sqrt{\Gamma_{\mathrm{m}}}, \sqrt{\kappa}, \sqrt{\Gamma_{\mathrm{m}}})$. The non-zero 4-by-4 matrices $\mathsf{A}^{(n)}$ are given by

$$\begin{aligned}
\mathsf{A}^{(0)} &= \begin{pmatrix} i\Delta - \frac{\kappa}{2} & iG_- & 0 & i\lambda G_- \\ iG_- & -i\omega_{\mathrm{m}} - \frac{\Gamma_{\mathrm{m}}}{2} & i\lambda G_- & 0 \\ 0 & -i\lambda G_- & -i\Delta - \frac{\kappa}{2} & -iG_- \\ -i\lambda G_- & 0 & -iG_- & i\omega_{\mathrm{m}} - \frac{\Gamma_{\mathrm{m}}}{2} \end{pmatrix}, \\
\mathsf{A}^{(-1)} &= iG_+ \left(\begin{array}{cc|cc} & \lambda & & 1 \\ & & 1 & \\ \hline & & & \\ & & & -\lambda \end{array}\right), \qquad \mathsf{A}^{(1)} = iG_+ \left(\begin{array}{cc|cc} \lambda & & & \\ & & & \\ \hline & & -1 & -\lambda \\ -1 & & & \end{array}\right).
\end{aligned} \tag{3.2.8}$$

Here, we have introduced λ to label the counterrotating terms. In the RWA $\lambda = 0$, else $\lambda = 1$. As discussed in Chapter 2, we can arrange the equations of motion as an infinite matrix Eq. (2.2.7). In RWA the infinite set of equations decouples in sets of four, making the problem tractable analytically, see Sec. 3.2.2. For a backaction-evading measurement, where $G_+ = G_-$, a solution can be found even without the RWA, as is discussed in Sec. 3.3.

3.2.2 Dissipative squeezing in the rotating-wave approximation

In this section we derive analytic expressions for the system operator Fourier components, which enables a detailed study of dissipative squeezing and simultaneously serves to illustrate the advantages of our new framework.

To obtain an analytical solution, we neglect counterrotating terms in Eqs. (3.2.4a) and (3.2.4b) (i.e., perform the RWA), which results in

$$\begin{aligned}
\dot{\hat{a}} &= \left(i\Delta - \frac{\kappa}{2}\right)\hat{a} + \sqrt{\kappa}\hat{a}_{\mathrm{in}} + i\left(G_+ e^{-i\delta t}\hat{b}^\dagger + G_-\hat{b}\right), \\
\dot{\hat{b}} &= \left(-i\omega_{\mathrm{m}} - \frac{\Gamma_{\mathrm{m}}}{2}\right)\hat{b} + \sqrt{\Gamma_{\mathrm{m}}}\hat{b}_{\mathrm{in}} + i\left(G_-\hat{a} + G_+ e^{-i\delta t}\hat{a}^\dagger\right).
\end{aligned} \tag{3.2.9}$$

Note that by defining $\tilde{\hat{a}} = e^{i\delta t/2}\hat{a}$ and $\tilde{\hat{b}} = e^{i\delta t/2}\hat{b}$ it is possible to write Eqs. (3.2.9) in a frame where they become stationary, which is done in Ref. 121 and Sec. 3.3.

Within RWA ($\lambda = 0$), we can make Eq. (2.2.7) block-diagonal through a rearrangement of rows. The blocks disconnected from input operators decay and vanish in the steady

state. Thus, only two blocks (mutually Hermitian conjugates) contribute. The problem reduces to solving

$$\begin{pmatrix} \chi_{\rm c}^{-1}(\omega) & -iG_- & 0 & -iG_+ \\ -iG_- & \chi_{\rm m}^{-1}(\omega) & -iG_+ & 0 \\ 0 & iG_+ & \chi_{\rm c}^{-1*}(-\omega+\delta) & iG_- \\ iG_+ & 0 & iG_- & \chi_{\rm m}^{-1*}(-\omega+\delta) \end{pmatrix} \begin{pmatrix} \hat{a}^{(0)} \\ \hat{b}^{(0)} \\ \hat{a}^{(1)\dagger} \\ \hat{b}^{(1)\dagger} \end{pmatrix} = \begin{pmatrix} \sqrt{\kappa}\hat{a}_{\rm in}(\omega) \\ \sqrt{\Gamma_{\rm m}}\hat{b}_{\rm in}(\omega) \\ 0 \\ 0 \end{pmatrix}, \tag{3.2.10}$$

with the cavity and mechanical response functions $\chi_{\rm c}^{-1}(\omega) = \kappa/2 - i(\omega+\Delta)$ and $\chi_{\rm m}^{-1}(\omega) = \Gamma_{\rm m}/2 - i(\omega-\omega_{\rm m})$, respectively.

Inverting the matrix on the left-hand side, we can write the system operators in terms of input operators. Specifically for the mechanical Fourier modes, we have

$$\begin{pmatrix} \hat{b}^{(0)}(\omega) \\ \hat{b}^{(1)\dagger}(\omega) \end{pmatrix} = \begin{pmatrix} a(\omega) & c(\omega) \\ f(\omega) & g(\omega) \end{pmatrix} \begin{pmatrix} \hat{b}_{\rm in}(\omega) \\ \hat{a}_{\rm in}(\omega) \end{pmatrix}. \tag{3.2.11}$$

Analytic expressions for the auxiliary functions can be found in Appendix 3.B. Much of the physics can be understood by separating weak-coupling and strong-coupling effects, discussed in turns below.

3.2.3 Weak-coupling approximation

We can gain more insight when the coupling $G_\pm$ is small, such that second-order perturbation theory captures the main effects.

If $\Delta = -\omega_{\rm m}$ and writing $\delta = 2\omega_{\rm m} + \varepsilon$, we obtain to second order in $G_\pm$ (see Appendix 3.C)

$$\dot{\hat{b}}^{(0)} = \left(-i\tilde{\omega}_{\rm m} - \frac{\tilde{\Gamma}_{\rm m}}{2}\right)\hat{b}^{(0)} + \frac{2iG_-}{\sqrt{\kappa}}\hat{a}_{\rm in} + \sqrt{\Gamma_{\rm m}}\hat{b}_{\rm in}, \tag{3.2.12a}$$

$$\dot{\hat{b}}^{(1)\dagger} = \left(i\tilde{\omega}_{\rm m} - i\delta - \frac{\tilde{\Gamma}_{\rm m}}{2}\right)\hat{b}^{(1)\dagger} - \frac{2iG_+}{\sqrt{\kappa}}\hat{a}_{\rm in}, \tag{3.2.12b}$$

where

$$\tilde{\Gamma}_{\rm m} = \Gamma_{\rm m} + \frac{4}{\kappa}\left(G_-^2 - \frac{G_+^2}{1+4\varepsilon^2/\kappa^2}\right), \tag{3.2.13a}$$

$$\tilde{\omega}_{\rm m} = \omega_{\rm m} + \frac{G_+^2\varepsilon}{(\kappa/2)^2+\varepsilon^2}. \tag{3.2.13b}$$

These equations provide several insights. First, in addition to the intrinsic mechanical damping, $b^{(0)}$ is subject to *optical damping* [24]. At $\varepsilon = 0$, this occurs with a rate $4\mathcal{G}^2/\kappa$, where $\mathcal{G}^2 \equiv G_-^2 - G_+^2$. Since we are treating the problem in a frame where the red-detuned drive is stationary, it couples to the zeroth Fourier component with strength G_-. Crucially, the optical input noise $a_{\rm in}$ has opposite signs in the two equations. The implications of that sign become clear if we consider the rotating quadrature (2.7.1)

$$\hat{X}^0_\nu(t) = e^{i\nu t}\left(\hat{b}^{(0)} + e^{-i\delta t}\hat{b}^{(-1)}\right) + e^{-i\nu t}\left(\hat{b}^{(0)\dagger} + e^{i\delta t}\hat{b}^{(1)\dagger}\right). \tag{3.2.14}$$

If $\delta = 2\nu$, $\hat{b}^{(0)}$ and $\hat{b}^{(1)\dagger}$ have the same phase factor

$$\hat{X}^0_{\delta/2}(t) = e^{i\delta t/2}\left(\hat{b}^{(0)} + \hat{b}^{(1)\dagger}\right) + \text{H.c.}, \tag{3.2.15}$$

and Eq. (3.2.12a) gives

$$\dot{\hat{X}}^0_{\delta/2} = -\frac{\tilde{\Gamma}_{\rm m}}{2}\hat{X}^0_{\delta/2} + \left(\frac{\delta}{2} - \tilde{\omega}_{\rm m}\right)\hat{X}^{\pi/2}_{\delta/2} + \left\{e^{i\delta t/2}\left[\frac{2i}{\sqrt{\kappa}}(G_- - G_+)\hat{a}_{\rm in} + \sqrt{\Gamma_{\rm m}}\hat{b}_{\rm in}\right] + \text{H.c.}\right\}. \tag{3.2.16}$$

First, as is the case for all quadratures, the effective mechanical damping has an optical contribution. Second, we see that in this particular rotating quadrature the optical noise is reduced, which is also a feature of the exact equations of motion [see minus sign on RHS of Eq. (3.B.1) in Appendix 3.B], and $\hat{X}^0_{\delta/2} = \hat{X}_-$ is the squeezed quadrature. If $\hat{b}^{(0)}$ and $\hat{b}^{(1)\dagger}$ do not have the same phase factor (for $\nu \neq \delta/2$), then as time t evolves, their relative phase changes, such that sometimes the noises add and at other times they subtract, i.e., the quadrature we consider rotates relative to the squeezed and antisqueezed quadratures. Third, note that the noises only subtract because both lasers are driving the same mode and thus are subject to the same vacuum fluctuations. If in addition $G_- = G_+$, this setup performs a backaction-evading (BAE) measurement of the rotating mechanical quadrature [139], evidenced by the disappearance of $\hat{a}_{\rm in}$ from Eq. (3.2.16). In (3.2.14) we could set $\vartheta = \pi/2$, which would introduce a relative minus sign between the two square brackets, such that the noises add, to give the antisqueezed quadrature X_+. Fourth, we note that the second term in (3.2.16) contains the conjugate quadrature. It is only non-zero if $\delta \neq 2\omega_{\rm m}$. Essentially, the mechanical quadratures naturally rotate at the mechanical frequency $\omega_{\rm m}$, so the faster $\hat{X}^0_{\delta/2}$ rotates relative to $\hat{X}_{\omega_{\rm m}}$ the quicker it catches up with the quadrature $\pi/2$ ahead. The resulting continuous mixing plays an important role in squeezing loss and heating, as discussed in Sections 3.2.6 and 3.2.7.

We Fourier transform Eq. (3.2.12a) to obtain an approximation to Eq. (3.2.11)

$$\begin{aligned} a(\omega) &\approx \sqrt{\Gamma_{\rm m}}\tilde{\chi}_{\rm m}(\omega), \\ c(\omega) &\approx 2iG_{-}\tilde{\chi}_{\rm m}(\omega)/\sqrt{\kappa}, \\ f(\omega) &\approx 0, \\ g(\omega) &\approx -2iG_{+}\tilde{\chi}^{*}_{\rm m}(-\omega+\delta)/\sqrt{\kappa}, \end{aligned} \tag{3.2.17}$$

where we have defined $\tilde{\chi}_{\rm m}^{-1}(\omega) = \tilde{\Gamma}_{\rm m}/2 - i(\omega - \tilde{\omega}_{\rm m})$ and again have neglected terms $\mathcal{O}(G_{\pm}^3)$. For details see Appendix 3.C, where we also write down an effective master equation that treats the cavity as an extra bath.

Using Eqs. (2.5.7) and (3.2.17) we write down the components that make up the mechanical spectrum for general detuning δ

$$S^{(0)}_{b^\dagger b}(\omega) = |\tilde{\chi}_{\rm m}(-\omega)|^2\left(\Gamma_{\rm m} n_{\rm th} + \frac{4G_{+}^2}{\kappa}\right), \tag{3.2.18a}$$

$$S^{(0)}_{bb^\dagger}(\omega) = |\tilde{\chi}_{\rm m}(\omega)|^2\left[\Gamma_{\rm m}(n_{\rm th}+1) + \frac{4G_{-}^2}{\kappa}\right], \tag{3.2.18b}$$

$$S^{(-1)}_{bb}(\omega) = -\frac{4G_{-}G_{+}}{\kappa}\tilde{\chi}_{\rm m}(\omega)\tilde{\chi}_{\rm m}(-\omega+\delta), \tag{3.2.18c}$$

$$S^{(1)}_{b^\dagger b^\dagger}(\omega) = -\frac{4G_{-}G_{+}}{\kappa}\tilde{\chi}^{*}_{\rm m}(\omega+\delta)\tilde{\chi}^{*}_{\rm m}(-\omega). \tag{3.2.18d}$$

Integrating over the frequency ω, we arrive at

$$\int_{-\infty}^{\infty}\frac{d\omega}{2\pi}S^{(0)}_{b^\dagger b}(\omega) = \frac{\Gamma_{\rm m} n_{\rm th} + 4G_{+}^2/\kappa}{\tilde{\Gamma}_{\rm m}}, \tag{3.2.19a}$$

$$\int_{-\infty}^{\infty}\frac{d\omega}{2\pi}S^{(0)}_{bb^\dagger}(\omega) = \frac{\Gamma_{\rm m}(n_{\rm th}+1) + 4G_{-}^2/\kappa}{\tilde{\Gamma}_{\rm m}}, \tag{3.2.19b}$$

$$\int_{-\infty}^{\infty}\frac{d\omega}{2\pi}S^{(-1)}_{bb}(\omega) = -\frac{4G_{-}G_{+}/\kappa}{\tilde{\Gamma}_{\rm m} - i\varepsilon}, \tag{3.2.19c}$$

$$\int_{-\infty}^{\infty}\frac{d\omega}{2\pi}S^{(1)}_{b^\dagger b^\dagger}(\omega) = -\frac{4G_{-}G_{+}/\kappa}{\tilde{\Gamma}_{\rm m} + i\varepsilon}, \tag{3.2.19d}$$

and we obtain the variance in the squeezed and antisqueezed quadratures (which are rotating at the frequency $\delta/2$)

$$\langle \hat{X}_{\pm}^2\rangle = \frac{\Gamma_{\rm m}}{\tilde{\Gamma}_{\rm m}}(2n_{\rm th}+1) + \frac{4}{\kappa\tilde{\Gamma}_{\rm m}}(G_{+}^2+G_{-}^2) \pm \frac{8G_{-}G_{+}}{\kappa\tilde{\Gamma}_{\rm m}}\left(\frac{1}{1+\varepsilon^2/\tilde{\Gamma}_{\rm m}^2}\right), \tag{3.2.20}$$

where we have defined the detuning of the higher-frequency laser from the upper mechanical sideband as $\varepsilon \equiv \delta - 2\omega_{\rm m}$. Term-by-term, the variance contains a reduced (if $\mathcal{G}^2 > 0$)

occupancy due to the extra optical damping, a positive term due to the noise added by the drives, and a term that can be negative due to the aforementioned noise cancelling effect of the two drives in one of the quadratures, see Eqs. (3.2.12a) and (3.2.12b). In the antisqueezed quadrature, the noises add. The optically enhanced damping rate $\tilde{\Gamma}_{\rm m}$ reduces to the one for sideband cooling for $\varepsilon \gtrsim \kappa$. In that limit the last term on the RHS of Eq. (3.2.20) vanishes and the two quadratures have equal variances. Equation (3.2.20) is then very close to the expected result, apart from the extra noise term $4G_+^2/\kappa\tilde{\Gamma}_{\rm m}$, which at this level of approximation does not depend of the detuning ε.

3.2.4 Variance in the squeezed and antisqueezed quadratures

In Sec. 3.2.3 we found that the quadrature in which the optical noises cancel most is the one rotating at half the laser frequency difference $\delta/2$. With the solution at hand, we can go a more direct way and ask which phase ϑ has the smallest (or largest) quadrature variance. In agreement to what we found above, ϑ will have to depend on time with angular velocity $\delta/2$.

Let us consider a lab frame quadrature $X^{\vartheta}_{\nu=0}$, with variance

$$\langle (\hat{X}_0^{\vartheta})^2 \rangle = 1 + 2\sum_n e^{in\delta t}\Xi^{(n)}_{bb} + 2\,\mathrm{Re}\left[e^{2i\vartheta}\sum_n e^{in\delta t}\Xi^{(n)}_{b^\dagger b}\right], \tag{3.2.21}$$

where

$$\Xi^{(n)}_{AB} \equiv \int S^{(n)}_{A^\dagger B}(\omega)\frac{d\omega}{2\pi}. \tag{3.2.22}$$

Note that by Eq. (2.5.8) the second term on the RHS of Eq. (3.2.21) is always real. The variance is minimal for

$$\vartheta = \frac{\pi}{2} - \frac{1}{2}\arg\left[\sum_n e^{in\delta t}\Xi^{(n)}_{b^\dagger b}\right]. \tag{3.2.23}$$

In RWA, the only non-zero $\Xi^{(n)}_{b^\dagger b}$ is the one with $n = -1$, which turns out to be real and negative. This results in $\vartheta(t) = \delta t/2$, the squeezed quadrature is rotating. So, even though we started off not knowing that we would have to consider a rotating quadrature, the result emerged naturally.

We can calculate the maximum and minimum variance

$$\langle \hat{X}_\pm^2 \rangle = 1 + 2\sum_n e^{in\delta t}\Xi^{(n)}_{bb} \pm 2\left|\sum_n e^{in\delta t}\Xi^{(n)}_{b^\dagger b}\right|. \tag{3.2.24}$$

For the position quadrature $x = X_0^{\vartheta=0}$ and in RWA, we obtain

$$\langle \hat{x}(t)^2 \rangle = 1 + 2\Xi_{bb}^{(0)} + 2|\Xi_{b^\dagger b}^{(-1)}| \cos(\delta t - \phi), \tag{3.2.25}$$

where we have written the complex number $\Xi_{b^\dagger b}^{(-1)}$ in terms of its absolute value and phase ϕ[†]. Note that Eq. (3.2.25) is the squared width in x-direction of an ellipse with major and minor axis $\langle \hat{X}_\pm^2 \rangle^{1/2}$, rotating at frequency $\delta/2$, with an initial tilt of $\phi/2$. This is no coincidence—the Wigner density of a squeezed state is an ellipse. There is one frame in which it is stationary, whereas in all other frames, the ellipse is rotating, and thus a measurement of the variance returns an average over both quadratures. Note that rotating the ellipse by π maps it onto itself, so we can take $\vartheta \in [0, \pi)$.

The conclusion is that in order to detect the squeezing we have to follow the quadrature and make the measurement in a special rotating frame. The necessity to "follow" the quadrature has been mentioned in the discussion of QND measurements in Ref. 66. The fact that we need to measure the rotating spectrum components to observe squeezing substantiates the claim that essential information can be hidden in rotating components of the spectra. In the literature, this special case is what characterizes a so-called *phase-sensitive* detector, also called *phase nonpreserving amplifier* in Ref. 66. Such a detector requires an external clock (here the beating of the laser drives) in order to keep track of the rotating quadrature, as noted in Ref. 137.

In Fig. 3.2 we illustrate how these concepts take form on the level of the mechanical spectra and plot the physical spectrum $S^{(0)}_{X_\nu^\vartheta X_\nu^\vartheta}(\omega)$ in the three most relevant cases. The first panel corresponds to $\nu = 0 = \vartheta$, i.e. the spectrum of the lab frame position quadrature $\hat{X}_0^0 = x = \hat{b} + \hat{b}^\dagger$. The left and right peak correspond to contributions of $\langle \hat{b}^\dagger \hat{b} \rangle$ and $\langle \hat{b} \hat{b}^\dagger \rangle$, respectively. The absolute value of the rotating terms is shown as well. In general, they are complex, with a phase depending on t and ϑ.

Panel (b) and (c) in Fig. 3.2 are the spectra in the special rotating frame $\nu = \delta/2$. The first consequence of going into a rotating frame is that the peaks are displaced [in opposite directions, as $\hat{b}$ and $\hat{b}^\dagger$ get opposite phases, see Eq. (2.7.2)]. In this particular frame, the peaks end up on top of each other. Equation (2.5.8) ensures that the imaginary parts of the rotating Fourier components cancel each other. In the two cases in which they (individually) are entirely real, $\vartheta = 0, \pi/2$, they contribute the most, yielding spectra with the smallest and largest variance, which are thus the squeezed and antisqueezed quadratures $\hat{X}_\mp$ [(b) and (c) panel], respectively.

[†]The phase ϕ is primarily set by the relative phase of the lasers. In terms of their intensity beating, the squeezed quadrature can be found at or near the maximum intensity. They do not coincide if $\delta \neq 2\omega_\mathrm{m}$, in which case the squeezed quadrature lags slightly behind. The assumption that the coherent amplitudes $\bar{a}_\pm$ are real leads to $\phi \approx \pi$ (equality if $\delta = 2\omega_\mathrm{m}$).

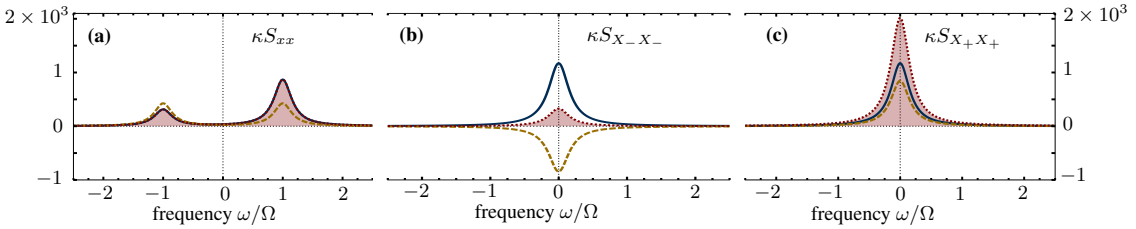

Figure 3.2: Mechanical spectrum in the lab frame and the special rotating frame. (a) Lab frame. The stationary part $S^{(0)}_{xx}$ (3.2.28) is plotted in blue (solid) and has two peaks that stem from $S^{(0)}_{b^\dagger b}$ (left) and $S^{(0)}_{bb^\dagger}$ (right peak). $S^{(0)}_{xx}$ coincides with the measured spectrum for the position quadrature $\hat{x} = \hat{b} + \hat{b}^\dagger$ (red, filled). The yellow (dashed) curve is the absolute value of the sum of the rotating components $S^{(1)}_{b^\dagger b^\dagger}$ (left peak) and $S^{(-1)}_{bb}$ (right peak), and does not contribute to the lab frame spectrum. **(b), (c) Special rotating frame.** The previously rotating spectrum components (still yellow and dashed) become stationary and thus part of the measured spectrum for the quadrature $\hat{X}^{\vartheta}_{\delta/2}$ (red, dotted and filled), see Eq. (2.7.4). Their phase relation (encoded in ϑ) determines whether they add to the stationary part (still blue and solid) to give the antisqueezed quadrature $\hat{X}_+$ in (c), at $\vartheta = \pi/2$, or subtract from it to yield the squeezed quadrature $\hat{X}_-$ in (b), at $\vartheta = 0$. Parameters are $\Gamma_\mathrm{m}/\kappa = 10^{-4}, n_\mathrm{th} = 10, \mathcal{C} = 10^2, \Delta = -\omega_\mathrm{m}, \delta = 2\omega_\mathrm{m}$. In RWA, the only effect of $\omega_\mathrm{m}/\kappa = .02$ is to determine the position of the peaks.

3.2.5 Squeezing for exact sideband driving

Reference [121] considered the case where the drives are on the sidebands, i.e., $\delta = 2\omega_\mathrm{m}$ and $\Delta = -\omega_\mathrm{m}$. Within RWA, the physical spectrum [cf. Eq. (2.7.4)] of the squeezed quadrature in a frame rotating with the mechanical frequency ω_m is given by

$$S_{X^0_{\omega_\mathrm{m}} X^0_{\omega_\mathrm{m}}}(\omega) = \frac{\kappa|\chi_\mathrm{c}(\omega+\omega_\mathrm{m})|^2(G_- - G_+)^2 + \Gamma_\mathrm{m}(2n_\mathrm{th}+1)}{|\chi_\mathrm{m}^{-1}(\omega+\omega_\mathrm{m}) + \chi_\mathrm{c}(\omega+\omega_\mathrm{m})\mathcal{G}^2|^2}. \tag{3.2.26}$$

This is a roundabout way to arrive at the desired result, as in this case it is easier to directly solve Eqs. (3.2.4a) and (3.2.4b) in a rotating frame, but our method is more general, enabling general detunings, rotating frames, and even beyond-RWA numerics.

Integrating Eq. (3.2.26) over frequency, we obtain the variance of the squeezed and antisqueezed quadratures

$$\langle \hat{X}^2_\pm \rangle = \frac{1}{\kappa + \Gamma_\mathrm{m}} \left[(2n_\mathrm{th}+1)\Gamma_\mathrm{m} \left(1 + \frac{\kappa}{\Gamma_\mathrm{m} + 4\mathcal{G}^2/\kappa} \right) + \frac{4(G_- \pm G_+)^2}{\Gamma_\mathrm{m} + 4\mathcal{G}^2/\kappa} \right], \tag{3.2.27}$$

where $\hat{X}_- = \hat{X}^{\vartheta=0}_{\nu=\omega_\mathrm{m}}$ and $\hat{X}_+ = \hat{X}^{\vartheta=\pi/2}_{\nu=\omega_\mathrm{m}}$. The result agrees with Ref. 44, where $(\kappa + \Gamma_\mathrm{m})^{-1} \approx \kappa^{-1}$ was approximated.

Within our framework it is straightforward to find out how squeezing looks like in

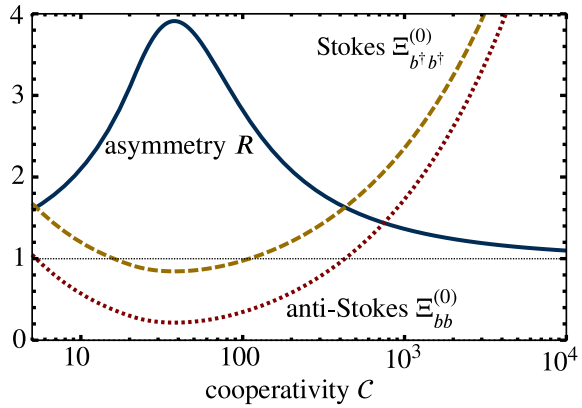

Figure 3.3: Sideband asymmetry. Weights of the left and the right peak of the mechanical spectrum $S^{(0)}_{xx}$ in the lab frame as a function of cooperativity $\mathcal{C}$. Left peak weight $\Xi^{(0)}_{bb}$ is labelled anti-Stokes (red dotted), right peak weight $\Xi^{(0)}_{b^\dagger b^\dagger}$ is labelled Stokes (yellow dashed). Blue (solid) is their ratio $R = \Xi^{(0)}_{b^\dagger b^\dagger}/\Xi^{(0)}_{bb}$. Parameters are $\Gamma_\mathrm{m}/\kappa = 10^{-4}, n_\mathrm{th} = 10, \Delta = -\omega_\mathrm{m}, \delta = 2\omega_\mathrm{m}$. The sideband parameter ω_m/κ is irrelevant in RWA.

the lab frame. In Fig. 3.2(a) we plot the spectrum of the lab frame position operator $\hat{X}^0_0 = \hat{x} = \hat{b} + \hat{b}^\dagger$, given through

$$S^{(0)}_{xx}(\omega) = \frac{(n_\mathrm{th}+1)\Gamma_\mathrm{m} + \kappa G_-^2|\chi_\mathrm{c}(\omega)|^2}{|\chi_\mathrm{m}^{-1}(\omega) + \chi_\mathrm{c}(\omega)\mathcal{G}^2|^2} + \frac{\Gamma_\mathrm{m} n_\mathrm{th} + \kappa G_+^2|\chi_\mathrm{c}(-\omega)|^2}{|\chi_\mathrm{m}^{-1}(-\omega) + \chi_\mathrm{c}(-\omega)\mathcal{G}^2|^2}. \tag{3.2.28}$$

It has two peaks as long as we do not consider the strong-coupling regime, where normal-mode splitting occurs. We call them Stokes ($\omega = \omega_\mathrm{m}$) and anti-Stokes ($\omega = -\omega_\mathrm{m}$) [24]. As we have discussed, the squeezing terms are not present.

The weights of the left and right (anti-Stokes and Stokes) peak are the integrals $\Xi^{(0)}_{bb}$ and $\Xi^{(0)}_{b^\dagger b^\dagger}$, respectively. Ξ is defined in Eq. (3.2.22). The ratio of Stokes to anti-Stokes is the asymmetry $R = \Xi^{(0)}_{b^\dagger b^\dagger}/\Xi^{(0)}_{bb}$. In Fig. 3.3 we plot the weights as a function of cooperativity $\mathcal{C}$ for the "optimal driving strength" as defined in Ref. 121

$$G_- = \sqrt{\frac{\mathcal{C}\kappa\Gamma_\mathrm{m}}{4}}, \qquad G_+ = G_-\left(1 - \sqrt{\frac{1+2n_\mathrm{th}}{\mathcal{C}}}\right). \tag{3.2.29}$$

At low cooperativities, the asymmetry increases with cooperativity. Physically, this is because the system is cooled. However, as the coupling strength is increased further, the asymmetry decreases and approaches unity. This is due to the fact that dissipative squeezing leads to a squeezed, thermal state with an effective temperature that increases with the degree of squeezing. In the lab frame, the squeezing terms are not a part of the spectrum, so we expect that the quadrature variance and the weight of both peaks increase.

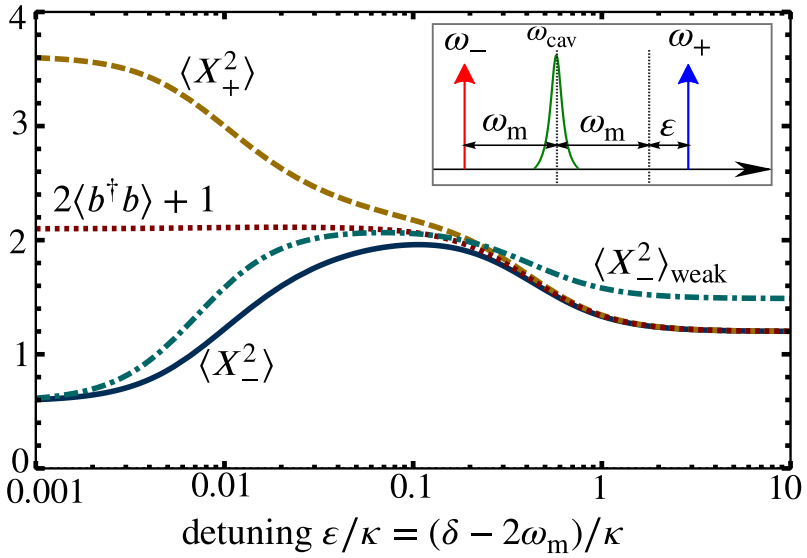

Figure 3.4: Squeezing loss due to detuning. Blue (solid) is the variance of the squeezed quadrature $\langle \hat{X}_-^2 \rangle$, orange (dashed) the antisqueezed quadrature $\langle \hat{X}_+^2 \rangle$, and red (dotted) is $2\langle b^\dagger b\rangle + 1$ as a function of detuning of the blue drive $\varepsilon = \delta - 2\omega_{\rm m}$. They have been obtained from Eq. (3.2.24). We also show the weak-coupling result Eq. (3.2.20) for the squeezed quadrature in turquoise (dash-dotted). The inset shows the driving scheme with the two driving frequencies $\omega_\pm$ relative to the cavity frequency $\omega_{\rm cav}$. Parameters are $\Gamma_{\rm m}/\kappa = 10^{-4}, n_{\rm th} = 10, \mathcal{C} = 10^2, \Delta = -\omega_{\rm m}$, so that $\tilde{\Gamma}_{\rm m} \approx 0.02\kappa$. The sideband parameter $\omega_{\rm m}/\kappa$ is irrelevant in RWA.

This leads to a decrease in the asymmetry R as a function of cooperativity $\mathcal{C}$.

3.2.6 Squeezing loss due to detuning

Instead of having both drives exactly on the sidebands as in Sec. 3.2.5, in this section we will study the behaviour of the system when the drives are detuned from the sidebands. Here, we only analyze the case $\Delta = -\omega_{\rm m}, \delta = 2\omega_{\rm m} + \varepsilon$, i.e., the red drive remains on the sideband. Changing the detuning of the cooling drive leads to an instability for $G_+ > \Gamma_{\rm m}$.

In Fig. 3.4, we plot the variance of the two quadratures, their average $2\langle \hat{b}^\dagger \hat{b}\rangle + 1$, and the weak-coupling result for the variance of the squeezed quadrature $\langle \hat{X}_-\rangle$ as a function of the detuning ε. There are two scales on which effects occur[†]. The larger scale is the cavity mode dissipation rate κ. Detunings on this scale render the detuned drive ineffective such that only cooling remains. In particular, we see that the occupation and the variance of both quadratures decreases, as the influence of the blue drive becomes weaker. Note that

[†]The lag of the squeezed quadrature behind the laser beating mentioned in Sec. 3.2.4 is negligible for the physics that we would like to discuss. In addition, we assume that the time scale on which the measurement is performed is large compared to any other time scale in the problem. If that were not the case, we could observe rotating spectrum components that decay as $\mathrm{sinc}(\nu T)$ for their respective frequency ν and measurement time T.

by this point both quadrature variances are already almost equal. The smaller scale is the effective mechanical damping $\tilde{\Gamma}_{\mathrm{m}} = \Gamma_{\mathrm{m}} + 4\mathcal{G}^2/\kappa$, introduced in Sec. 3.2.3. For $\varepsilon \sim \tilde{\Gamma}_{\mathrm{m}}$, squeezing has disappeared and for strong driving an instability occurs, see Sec. 3.2.7. In Fig. 3.4 the loss of squeezing is evidenced by the two quadrature variances becoming equal. On this scale it does not matter whether we move the blue drive away or the red, as long as $\varepsilon \ll \kappa$, as these effects are due to the mismatch between the beating frequency of the two lasers δ and the mechanical frequency ω_{m}. The beating can be thought of as a stroboscopic measurement of one of the quadratures every half period, akin to the scheme in Ref. 142. For finite detuning ε the measured quadrature starts to rotate at frequency $\varepsilon/2$ with respect to mechanical quadrature, so $2/\varepsilon$ is the timescale on which the squeezed and antisqueezed quadratures mix and interchange, see Eq. (3.2.16). In this sense, we are probing dynamical effects: they only become visible if their timescale is comparable to ε^{-1}. The mixing eventually mitigates squeezing entirely at $\varepsilon \sim \tilde{\Gamma}_{\mathrm{m}}$, i.e., when the mixing rate balances the squeezing rate as predicted in the weak-coupling approximation (3.2.20). The weak-coupling approximation (3.2.20) does not correctly capture the sideband cooling limit, the noise added by the blue-detuned drive does not vanish in the limit $\varepsilon \to \infty$, as discussed below Eq. (3.2.20).

3.2.7 Heating and parametric instability

We now turn to the strong-coupling effects. If the system is coupled more strongly, with $\mathcal{G}$ approaching κ, the minimum variance of the squeezed quadrature saturates at the lower bound $\langle \hat{X}_-^2 \rangle \to \Gamma_{\mathrm{m}}(1 + 2n_{\mathrm{th}})/(\kappa + \Gamma_{\mathrm{m}})$, see Eq. (3.2.27) or Ref. 121. In this regime, moving one of the lasers away from the sidebands, i.e., $\delta \neq 2\omega_{\mathrm{m}}$, results in a heating effect, and an instability for very strong coupling, see Fig. 3.5 and Sec. 3.D.

In Fig. 3.5, we plot the squeezed quadrature variance $\langle \hat{X}_-^2 \rangle$ as a function of the detuning of the blue laser ε for cooperativities $\mathcal{C} = 50,\ 500,\ 2000$. As we couple more strongly, heating occurs in addition to squeezing loss. From $\varepsilon = 0$, and for large enough $\mathcal{C}$, the squeezed quadrature variance first increases steeply, reaches a peak, and then decreases. The peak corresponds to the point where the system is closest to instability, whereas on a scale $\varepsilon \sim \kappa$ the driving becomes usual sideband cooling, as mentioned before. The heating effect has been mentioned in Ref. 45, where it was used to tune the lasers to the mechanical sidebands. Again, we find the separation of time scales: squeezing loss and heating for $\varepsilon \sim \tilde{\Gamma}_{\mathrm{m}}$, and cooling for $\varepsilon \sim \kappa$. We analyze the instability further in Appendix 3.D.

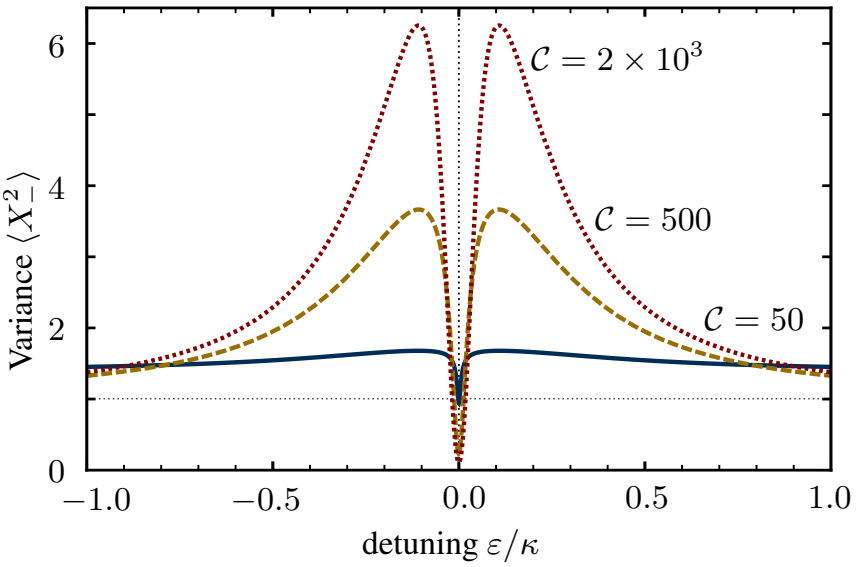

Figure 3.5: Heating due to detuning. Blue (solid), yellow (dashed), and red (dotted) are the squeezed quadrature variances $\langle \hat{X}_-^2 \rangle$ for cooperativities $\mathcal{C} = 50, 500, 2000$ as a function of detuning ε/κ. Here, $\Gamma_\mathrm{m}/\kappa = 10^{-4}, n_\mathrm{th} = 10, \Delta = -\omega_\mathrm{m}$. The sideband parameter ω_m/κ is irrelevant in RWA.

3.2.8 Measurement with second cavity mode

The ideas introduced above can be nicely illustrated if we study how the mechanical spectrum can be observed through a second, weakly coupled "readout" mode. Our approach will be the same as above, with two lasers pumping a single cavity mode, except that in this section the mechanical oscillator is a black box with a fixed, unknown spectrum that we would like to measure. We neglect the measurement backaction on the mechanical oscillator, an assumption that is excellent for QND measurements and reasonable for weak coupling.

Analogous to the first cavity mode $\hat{a}$, the linearized quantum Langevin equation for the second cavity mode $\hat{a}_2$ is

$$\dot{\hat{a}}_2 = \left(i\Delta_2 - \frac{\kappa_2}{2}\right)\hat{a}_2 + \sqrt{\kappa_2}\hat{a}_\mathrm{2in} + i\left(G_{2+}e^{-i\delta_2 t} + G_{2-}\right)(\hat{b}^\dagger + \hat{b}), \tag{3.2.30}$$

where $\Delta_2 = \omega_{2-} - \omega_{\mathrm{cav},2}$ is the detuning of the lower frequency laser from the frequency of the second cavity mode, $\delta_2 = \omega_{2+} - \omega_{2-}$ is the frequency difference between the blue and the red drive on the second cavity mode, κ_2 the dissipation rate of the second cavity mode, and $G_{2\pm}$ are the enhanced optomechanical couplings, see Fig. 3.1.

We can apply an analysis as above to find the most general spectra measured through

the second cavity mode. For details, we refer to Appendix 3.F. We split Eq. (3.2.30) up into Fourier components of the two frequencies present

$$\hat{a}_2(t) = \sum_{n,m} e^{in\delta t + im\delta_2 t} \hat{a}_2^{(m,n)}(t). \tag{3.2.31}$$

Generalized to two frequencies, the stationary spectrum is

$$S^{(0)}_{a_2^\dagger a_2}(\omega) = \sum_{n,m} \int \frac{d\omega'}{2\pi} \langle \hat{a}_2^{(n,m)\dagger}(\omega + n\delta + m\delta_2) \hat{a}_2^{(-n,-m)}(\omega') \rangle. \tag{3.2.32}$$

If $\delta \neq \delta_2$ (and are not multiples of each other), b does not have any components commensurate with δ_2, and hence

$$\hat{b}^{(n,m)} = 0, \quad \forall m \neq 0. \tag{3.2.33}$$

The stationary part simplifies to

$$S^{(0)}_{\hat{a}_2^\dagger \hat{a}_2}(\omega) = |\chi_{\mathrm{c},2}(-\omega)|^2 \left[G_{2-}^2 S_{xx}^{(0)}(\omega) + G_{2+}^2 S_{xx}^{(0)}(\omega + \delta_2) \right]. \tag{3.2.34}$$

$\hat{x} = \hat{X}_0^0$ here, as always, refers to the non-rotating position quadrature in the lab frame. Therefore, the only effect of having a second drive is that now there are two copies of the mechanical spectrum superposed with a different weights and shifted by δ_2 relative to each other. Furthermore, both are filtered by the response function of the cavity mode $\chi_{\mathrm{c},2}(\omega) = [\kappa_2/2 - i(\omega + \Delta_2)]^{-1}$. This case corresponds to the "non-QND" measurement in Ref. 46. It is an average over the squeezed and antisqueezed quadrature, see Sec. 3.2.4 and Fig. 3.2.

A special case is $\delta_2 = \delta$, in which Eq. (3.2.33) does not hold. Instead, we find for the stationary part of the noise spectrum of cavity 2

$$\begin{aligned} S^{(0)}_{a_2^\dagger a_2}(\omega) = |\chi_{\mathrm{c},2}(-\omega)|^2 \big\{ & G_{2-}^2 S_{xx}^{(0)}(\omega) + G_{2+}^2 S_{xx}^{(0)}(\omega + \delta) \\ & + G_{2-} G_{2+} \left[S_{xx}^{(-1)}(\omega + \delta) + S_{xx}^{(1)}(\omega) \right] \big\}. \end{aligned} \tag{3.2.35}$$

Note that here the rotating parts of S_{xx} contribute to $S^{(0)}_{a_2^\dagger a_2}$.

In RWA, only $\hat{b}^{(0)}, \hat{b}^{(0)\dagger}, \hat{b}^{(-1)}, \hat{b}^{(1)\dagger}$ are non-zero. Depending on the cavity linewidth κ_2, the prefactor $|\chi_{\mathrm{c},2}(-\omega)|^2$ more or less sharply picks out the contribution at $\omega = -\Delta_2$. This causes a suppression of counterrotating terms. So, if we make the readout mode a good cavity with $\kappa_2 \ll \omega_{\mathrm{m}}$ and choose $\Delta_2 = -\delta/2$, then we can make a second RWA (this

time for the second optical mode) and we are left with

$$\begin{aligned} S^{(0)}_{a_2^\dagger a_2}(\omega) &= |\chi_{\mathrm{c},2}(-\omega)|^2 \left[G_{2-}^2 S^{(0)}_{b^\dagger b}(\omega) + G_{2+}^2 S^{(0)}_{bb^\dagger}(\omega+\delta) + G_{2+}G_{2-}(S^{(-1)}_{bb}(\omega+\delta) + S^{(1)}_{b^\dagger b^\dagger}(\omega)) \right] \\ &= |\chi_{\mathrm{c},2}(-\omega)|^2 G_2^2 S_{X^0_{\delta/2}X^0_{\delta/2}}(\omega+\delta/2), \end{aligned} \tag{3.2.36}$$

where in the last line we have chosen $G_{2+} = G_{2-} \equiv G_2$, and identified the physical spectrum (2.7.4). Thus, this is a measurement of a rotating quadrature. In order to find out which terms contribute in (3.2.36), it is helpful to refer to the plot of spectrum Fourier components in RWA shown in Fig. 3.2, and remember that $|\chi_{\mathrm{c},2}(-\omega)|^2$ picks out contributions around $\omega = -\delta/2$. If additionally $\delta = 2\omega_{\mathrm{m}}$, this measurement is QND, as in Ref. 46.

3.3 Optomechanical backaction-evading measurement beyond the RWA

In this section, we present the exact analytical solution of the explicitly time-periodic quantum Langevin equation describing the dual-beam backaction-evasion measurement of a single mechanical oscillator beyond the commonly used rotating-wave approximation (RWA). The technique was introduced in seminal work by Braginsky, Vorontsov and Thorne [137]. We show that counterrotating terms lead to extra sidebands in the optical and mechanical spectra and to a modification of the main peak. Physically, the backaction of the measurement is due to periodic coupling of the mechanical resonator to a light field quadrature that only contains cavity-filtered shot noise. Since this fact is independent of other degrees of freedom the resonator might be coupled to, our solution can be generalized, including to dissipatively or parametrically squeezed oscillators, as well as recent two-mode backaction evasion measurements.

In optomechanics, a BAE measurement of one of the quadratures of the oscillator can be implemented by applying two drives of equal strength at frequencies $\omega_{\mathrm{cav}} \pm \omega_{\mathrm{m}}$ (see Fig. 3.6) [139]. Here, $\omega_{\mathrm{cav}}(\omega_{\mathrm{m}})$ is the frequency of a cavity (mechanical) mode.

We consider the Hamiltonian of a standard cavity optomechanical system as above [Eq. (3.2.1)], but with an extra arbitrary term that may couple the mechanical resonator to further degrees of freedom, $\hat{H}_{\mathrm{rest}}$, with the only requirement that $[\hat{H}_{\mathrm{rest}}, \hat{a} + \hat{a}^\dagger] = 0$, i.e., that the other degrees of freedom do not couple to the measurement cavity quadrature. The complete Hamiltonian thus reads

$$\hat{H} = \hat{H}_{\mathrm{OM}} + \hat{H}_{\mathrm{rest}} + \hat{H}_{\mathrm{drives}} + \hat{H}_{\mathrm{baths}}, \tag{3.3.1}$$

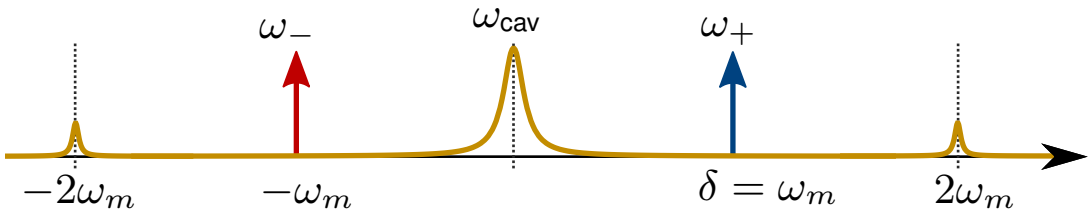

Figure 3.6: Dual-beam backaction-evading (BAE) measurement scheme proposed in Ref. 137, 139. Two lasers of equal strength drive the cavity at frequencies $\omega_\pm = \omega_{\mathrm{cav}} \pm \delta$, where $\delta = \omega_{\mathrm{m}}$ such that their sidebands overlap at the cavity frequency ω_{cav}. Counterrotating (CR) terms cause peaks at $\omega_{\mathrm{cav}} \pm 2\omega_{\mathrm{m}}$ to appear. The output light contains information of a rotating quadrature of the mechanical oscillator, the CR terms being responsible for the finite backaction.

where we have left δ unspecified for now (Fig. 3.6). The BAE measurement is realized for $\delta = \omega_{\mathrm{m}}$.

As above, we split the light field into a coherent part and fluctuations, go into a rotating frame, $\hat{a} \to e^{-i\omega_{\mathrm{cav}}t}[2\bar{a}\cos(\delta t) + \hat{a}]$, and linearize the Hamiltonian. Without loss of generality we take $\delta > 0$. Under the usual assumptions of Markovian baths and a one-sided cavity, we obtain Langevin equations very similar to the ones above, except now with an additional term due to $\hat{H}_{\mathrm{rest}}$ and equal drive strengths.

$$\dot{\hat{a}} = -\frac{\kappa}{2}\hat{a} + \sqrt{\kappa}\hat{a}_{\mathrm{in}} + 2iG\cos(\delta t)(\hat{b} + \hat{b}^\dagger), \tag{3.3.2a}$$

$$\dot{\hat{b}} = \left(-i\omega_{\mathrm{m}} - \frac{\Gamma_{\mathrm{m}}}{2}\right)\hat{b} + \sqrt{\Gamma_{\mathrm{m}}}\hat{b}_{\mathrm{in}} + 2iG\cos(\delta t)(\hat{a} + \hat{a}^\dagger) + i[\hat{H}_{\mathrm{rest}}, \hat{b}], \tag{3.3.2b}$$

where we have defined the enhanced optomechanical coupling constant $G = g_0\bar{a}$.

In Sec. 3.3.2, we solve Eqs. (3.3.2a) and (3.3.2b) without further approximations, in particular without the rotating wave approximation (RWA).

3.3.1 Backaction evasion in RWA

As a reminder, we first consider a BAE measurement within RWA. We define a quadrature rotating at frequency δ as

$$\hat{X}_\delta = \hat{b}e^{i\delta t} + \hat{b}^\dagger e^{-i\delta t}. \tag{3.3.3}$$

The cavity equation of motion is [cf. Eq. (3.3.2a)]

$$\dot{\hat{a}} = -\frac{\kappa}{2}\hat{a} + \sqrt{\kappa}\hat{a}_{\mathrm{in}} + iG\left(\hat{b}e^{i\delta t} + \hat{b}^\dagger e^{-i\delta t}\right). \tag{3.3.4}$$

The cavity couples only to one quadrature of the mechanical oscillator $\hat{X}_\delta$ (set by the phase relation of the external drives). The equation of motion for that quadrature can be obtained

from Eq. (3.2.4b) (here also in RWA)

$$\dot{\hat{X}}_\delta = -\frac{\Gamma_\mathrm{m}}{2}\hat{X}_\delta + \sqrt{\Gamma_\mathrm{m}}\hat{X}_{\delta,\mathrm{in}} + i[\hat{H}_\mathrm{rest}, \hat{X}_\delta] + iG\left\{\hat{a}\left[e^{i(\omega_\mathrm{m}-\delta)t} - e^{i(\delta-\omega_\mathrm{m})t}\right] - \mathrm{H.c.}\right\}. \tag{3.3.5}$$

If $\delta = \omega_\mathrm{m}$, the term in square brackets in the second line vanishes, and $\hat{X}_{\omega_\mathrm{m}}$ is entirely unaffected by the cavity. We can readily solve the equation of motion for $\hat{a}$, Eq. (3.3.4)

$$\hat{a}(\omega) = \chi_\mathrm{c}(\omega)\left[\sqrt{\kappa}\hat{a}_\mathrm{in}(\omega) + iG\hat{X}_\delta(\omega)\right], \tag{3.3.6}$$

with cavity response function $\chi_\mathrm{c}(\omega) = (\kappa/2 - i\omega)^{-1}$. Thus the optical spectrum is directly related to the quadrature spectrum

$$S_{a^\dagger a}(\omega) = |\chi_\mathrm{c}(\omega)|^2 G^2 S_{X_\delta X_\delta}(\omega), \tag{3.3.7}$$

The scheme corresponds to a true BAE measurement, if the mechanical quadrature rotating with frequency δ is a QND variable. Here, this is the case for $\delta = \omega_\mathrm{m}$ (or, if applicable, $\delta = \omega_\mathrm{m,eff}$, the effective mechanical frequency). Independent of RWA, the input-output relation $\hat{a}_\mathrm{out} = \hat{a}_\mathrm{in} - \sqrt{\kappa}\hat{a}$ can be used to the obtain the output spectrum $S_{a^\dagger_\mathrm{out}a_\mathrm{out}}(\omega) = \kappa S_{a^\dagger a}(\omega)$.

3.3.2 Solution beyond RWA

In terms of Fourier modes, Eqs. (3.3.2a) and (3.3.2b) read

$$\dot{\hat{a}}^{(n)} = \left(-in\delta - \frac{\kappa}{2}\right)\hat{a}^{(n)} + \delta_{n,0}\sqrt{\kappa}\hat{a}_\mathrm{in} + iG\left(\hat{b}^{(n-1)} + \hat{b}^{(n+1)\dagger} + \lambda\hat{b}^{(n+1)} + \lambda\hat{b}^{(n-1)\dagger}\right), \tag{3.3.8a}$$

$$\dot{\hat{b}}^{(n)} = \left(-i\omega_\mathrm{m} - in\delta - \frac{\Gamma_\mathrm{m}}{2}\right)\hat{b}^{(n)} + \delta_{n,0}\sqrt{\Gamma_\mathrm{m}}\hat{b}_\mathrm{in} + iG\left(\hat{I}^{(n+1)} + \lambda\hat{I}^{(n-1)}\right) + i[\hat{H}_\mathrm{rest}, \hat{b}]^{(n)}. \tag{3.3.8b}$$

where $\hat{x}^{(n)} \equiv \hat{b}^{(n)} + \hat{b}^{(n)\dagger}$, $\hat{I}^{(n)} \equiv \hat{a}^{(n)} + \hat{a}^{(n)\dagger}$, $\delta_{n,0}$ is the Kronecker delta, and $[\hat{H}_\mathrm{rest}, \hat{b}]^{(n)}$ denotes the nth Fourier component of the commutator. Where feasible, here and in the following, we will label counterrotating (i.e., off-resonance) terms by a λ (note that this only makes sense when δ is close to ω_m), such that RWA corresponds to $\lambda = 0$ and the full solution to $\lambda = 1$. To further guide the intuition, we remark that the second line of Eq. (3.3.8a) equals $iG(\hat{x}^{(n-1)} + \hat{x}^{(n+1)})$. One can think of the two laser drives to result in two separate couplings to the position x of the resonator.

To solve Eqs. (3.3.8a) and (3.3.8b), we define the optical quadratures $\hat{I} = \hat{a} + \hat{a}^\dagger$ and

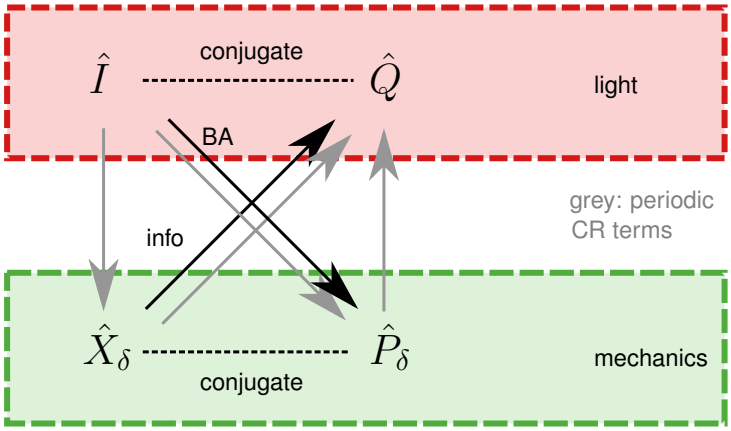

Figure 3.7: Coupling of quadratures. $\hat{Q}$ records the desired information (info) about $\hat{X}_\delta$. The measurement backaction (BA) is acting on $\hat{P}_\delta$. Depicted in grey are couplings due to counterrotating (CR) terms that are neglected in RWA.

$\hat{Q} = -i(\hat{a} - \hat{a}^\dagger)$. From Eq. (3.3.2a) we obtain

$$\dot{\hat{I}} = -\frac{\kappa}{2}\hat{I} + \sqrt{\kappa}\hat{I}_{\rm in}, \tag{3.3.9a}$$

$$\dot{\hat{Q}} = -\frac{\kappa}{2}\hat{Q} + \sqrt{\kappa}\hat{Q}_{\rm in} + 4G\cos(\delta t)\hat{x}. \tag{3.3.9b}$$

For an illustration how the mechanical and optical quadratures couple together, see Fig. 3.7. For example, the arrow from $\hat{X}_\delta$ to $\hat{Q}$ indicates that $\hat{X}_\delta$ appears in the equation of motion of $\hat{Q}$ and that the latter therefore is influenced by the former. Since $\hat{I}$ commutes with the system Hamiltonian, $[\hat{H}, \hat{I}] = 0$, there are no arrows pointing toward it in Fig. 3.7 and we can solve its equation of motion (3.3.9a) directly

$$\hat{I}(\omega) = \sqrt{\kappa}\chi_{\rm c}(\omega)\hat{I}_{\rm in}(\omega), \quad \text{and} \quad \hat{I}^{(n)}(\omega) = \delta_{n,0}\hat{I}(\omega). \tag{3.3.10}$$

Thus $\langle\hat{I}(\omega)\hat{I}(\omega')\rangle = 2\pi\delta(\omega+\omega')|\chi_{\rm c}(\omega)|^2$ and $\langle\hat{I}(\omega)\rangle = 0$. Equations (3.3.9a) and (3.3.10) imply that I is shot noise, filtered by the cavity, and is independent of the mechanics. Furthermore, this result does not depend on $\hat{H}_{\rm rest}$, as long as $[\hat{H}_{\rm rest}, \hat{I}] = 0$. The coupling to $\hat{I}$ is periodic [cf. Eq. (3.2.4b)], a consequence of amplitude beating of the coherent state in the cavity. Therefore, the measurement has the same effect on the mechanical resonator as a time-periodic coupling to filtered shot noise.

With Eq. (3.3.10) we can solve Eq. (3.3.8b) in the case $\hat{H}_{\rm rest} = 0$ by going into

frequency space

$$\hat{b}^{(n)}(\omega) = \chi_{\mathrm{m}}(\omega - n\delta)\left[\delta_{n,0}\sqrt{\Gamma_{\mathrm{m}}}\hat{b}_{\mathrm{in}} + 2\sqrt{\kappa}G\hat{f}_{\mathrm{in}}^{(n)}\right], \tag{3.3.11a}$$

$$\hat{b}^{(n)\dagger}(\omega) = \chi_{\mathrm{m}}^{*}(-\omega + n\delta)\left[\delta_{n,0}\sqrt{\Gamma_{\mathrm{m}}}\hat{b}_{\mathrm{in}}^{\dagger} - 2\sqrt{\kappa}G\hat{f}_{\mathrm{in}}^{(n)}\right], \tag{3.3.11b}$$

where the new bath noise operators

$$\hat{f}_{\mathrm{in}}^{(n)}(\omega) = i\chi_{\mathrm{c}}(\omega)(\delta_{n,1} + \lambda\delta_{n,-1})\hat{I}_{\mathrm{in}}(\omega)/2. \tag{3.3.12}$$

They obey $\hat{f}_{\mathrm{in}}^{(n)\dagger} = -\hat{f}_{\mathrm{in}}^{(n)}$, $\hat{f}_{\mathrm{in}}^{(-n)} = \hat{f}_{\mathrm{in}}^{(n)}$, and $\langle \hat{f}_{\mathrm{in}} \rangle = 0$. The time-dependence is best seen in the time domain, where

$$\hat{f}_{\mathrm{in}}(t) = i\cos(\delta t)\hat{I}(t)/\sqrt{\kappa}. \tag{3.3.13}$$

This expression explicitly contains the time-dependent coupling and the filtered shot noise $I(t)$. The correlator is

$$\langle \hat{f}_{\mathrm{in}}(t)\hat{f}_{\mathrm{in}}(t')\rangle = -e^{-\kappa|t-t'|/2}\cos(\delta t)\cos(\delta t'). \tag{3.3.14}$$

For stationary noise, the RHS of Eq. (3.3.14) would have to depend solely on the difference $t - t'$.

We can rewrite the equation of motion for $\hat{b}$ in terms of the new input $\hat{f}_{\mathrm{in}}$

$$\dot{\hat{b}} = \left(-i\omega_{\mathrm{m}} - \frac{\Gamma_{\mathrm{m}}}{2}\right)\hat{b} + \sqrt{\Gamma_{\mathrm{m}}}\hat{b}_{\mathrm{in}} + 2\sqrt{\kappa}G\hat{f}_{\mathrm{in}} + i[\hat{H}_{\mathrm{rest}}, \hat{b}]. \tag{3.3.15}$$

From this equation it is clear that we are always able to pass from the "unmeasured system" ($G = 0$) to the "measured" one ($G \neq 0$) by substituting

$$\sqrt{\Gamma_{\mathrm{m}}}\hat{b}_{\mathrm{in}} \to \sqrt{\Gamma_{\mathrm{m}}}\hat{b}_{\mathrm{in}} + 2\sqrt{\kappa}G\hat{f}_{\mathrm{in}}. \tag{3.3.16}$$

We use this to generalize the solution in Sec. 3.3.7.

3.3.3 Importance of Floquet framework

At this point it is useful to reflect on the advantage of the Floquet approach. It might appear as if it were unnecessary, since with Eqs. (3.3.9a) and (3.3.10), we can already write down

$$\dot{\hat{b}} = \left(-i\omega_{\mathrm{m}} - \frac{\Gamma_{\mathrm{m}}}{2}\right)\hat{b} + \sqrt{\Gamma_{\mathrm{m}}}\hat{b}_{\mathrm{in}} + 2iG\cos(\delta t)\hat{I}(t) + i[\hat{H}_{\mathrm{rest}}, \hat{b}], \tag{3.3.17}$$

which for $\hat{H}_{\rm rest} = 0$ has the solution

$$\hat{b}(\omega) = \chi_{\rm m}(\omega)\left\{\sqrt{\Gamma_{\rm m}}\hat{b}_{\rm in}(\omega) + iG\left[\hat{I}(\omega-\delta) + \hat{I}(\omega+\delta)\right]\right\}. \tag{3.3.18}$$

Since $\hat{x}(\omega) = \hat{b}(\omega) + \hat{b}^\dagger(\omega)$, this might prompt us to derive the "power spectrum"

$$S_{xx}(\omega) \stackrel{?}{=} \int \frac{d\omega'}{2\pi}\langle\hat{x}(\omega)\hat{x}(\omega')\rangle. \tag{3.3.19}$$

This, however, is *not* the correct power spectrum, since $\hat{x}(t)$ does not describe a stationary stochastic process. It is possible to remove the non-stationary terms manually (above they will be $\langle\hat{I}(\omega-\delta)\hat{I}(\omega'-\delta)\rangle$ and $\langle\hat{I}(\omega+\delta)\hat{I}(\omega'+\delta)\rangle$) and thus obtain the stationary part, which *is* the power spectrum (Sec. 2.6). In contrast, the systematic solution via Fourier components, which all obey stationary Langevin equations, is well-defined. In addition, the Fourier components are more versatile, and allow writing down the spectrum in arbitrary rotating frames (Sec. 2.7). They also provide more intuition, since different Fourier components tend to have different physical origins. Finally, if no exact solution is viable, they simplify the process of approximating to desired order.

3.3.4 Mechanical quadrature spectrum

We define a rotating quadrature as before [see Eq. (3.3.3)]. Its spectrum is (Sec. 2.7)

$$S^{(0)}_{X_\delta X_\delta}(\omega) = S^{(-2)}_{bb}(\omega+\delta) + S^{(0)}_{bb^\dagger}(\omega+\delta) + S^{(2)}_{b^\dagger b^\dagger}(\omega-\delta) + S^{(0)}_{b^\dagger b}(\omega-\delta), \tag{3.3.20}$$

where S_{AB} is defined through Eq. (2.5.7). We have only written down the zeroth Fourier component (the stationary part), because that is the part of the spectrum that is observed in experiment. We can split it up into two parts

$$S^{(0)}_{X_\delta X_\delta}(\omega) = S^{\rm RWA}_{X_\delta X_\delta}(\omega) + S^{\rm CR}_{X_\delta X_\delta}(\omega), \tag{3.3.21}$$

with $S^{\rm RWA}_{X_\delta X_\delta}$ being the result in RWA (dependent on $\hat{H}_{\rm rest}$), and $S^{\rm CR}_{X_\delta X_\delta}$ being due to CR terms. Note that $S^{\rm RWA}_{X_\delta X_\delta}$ is unchanged from the unmeasured case, since this is the essence of a BAE measurement. For $\hat{H}_{\rm rest} = 0$, we obtain our first major result, the correction to the RWA spectrum due to CR terms

$$S^{\rm CR}_{X_\delta X_\delta}(\omega) = \kappa\lambda^2 G^2\left(|\chi_{\rm m}(\omega+\delta)\chi_{\rm c}(\omega+2\delta)|^2 + |\chi_{\rm m}(-\omega+\delta)\chi_{\rm c}(-\omega+2\delta)|^2\right). \tag{3.3.22}$$

If $\hat{H}_{\rm rest}$ is nonzero, but couples weakly, such that its effect is well approximated

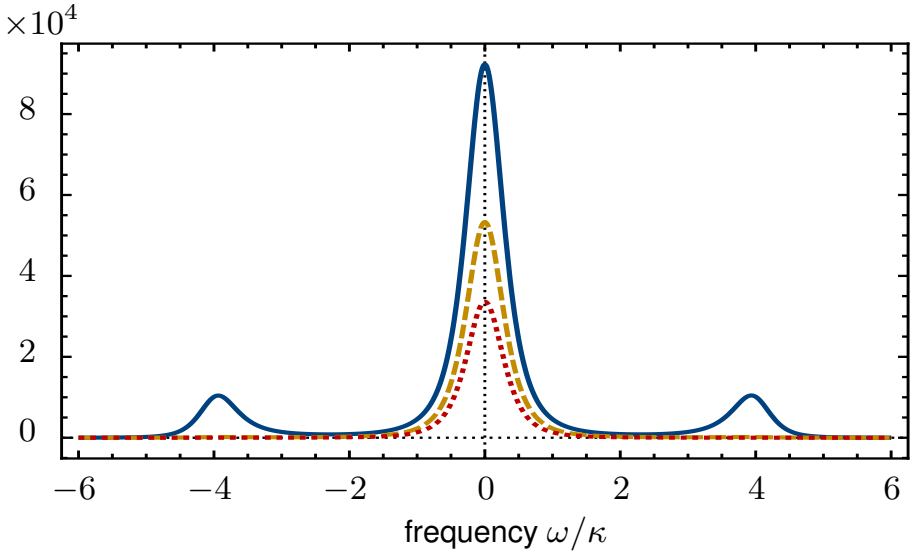

Figure 3.8: The optical spectrum. Exact optical output spectrum $\kappa S^{(0)}_{a^\dagger a}$ Eq. (3.3.24) (blue, solid) in comparison to a perfect BAE measurement of the modified mechanical spectrum (3.3.23) from Sec. 3.3.4 (yellow, dashed), and the RWA result Eq. (3.3.7) (red, dotted). The full spectrum (blue, solid) is calculated via Eq. (3.3.24), where additional terms due to the counterrotating quadrature $\hat{X}_{-\delta}$ appear. The sidepeaks in the modified mechanical spectrum do not show in the yellow curve, as they are suppressed by $|\chi_c(\omega)|^2$. Parameters $\Gamma_{\rm eff}/\kappa = 1, \omega_m/\kappa = 2, n_{\rm eff} = 10, G/\kappa = 10, \delta = \omega_m$ (thus $\mathcal{C} = 400$). Note that the large value of $\Gamma_{\rm eff}$ is chosen for visibility.

by introducing an effective damping constant and mechanical frequency, the analysis is unchanged, and the correction takes the same form

$$S^{\rm CR}_{X_\delta X_\delta}(\omega) = \kappa\lambda^2 G^2 \left\{ |\chi_{\rm m,eff}(\omega+\delta)\chi_c(\omega+2\delta)|^2 + |\chi_{\rm m,eff}(-\omega+\delta)\chi_c(-\omega+2\delta)|^2 \right\}, \tag{3.3.23}$$

but with an effective susceptibility $\chi_{\rm m,eff}(\omega) = [\Gamma_{\rm eff} - i(\omega - \omega_{\rm m,eff})]^{-1}$. Note that if $\delta \neq \omega_{\rm m,eff}$, the measured quadrature rotates at a different frequency than the natural oscillator quadratures and thus the measurement backaction (BA) will contaminate the measurement at later times, even in RWA. Only the case $\delta = \omega_{\rm m,eff}$ is backaction-evading (BAE). Since this is our main interest, we will fix $\delta = \omega_{\rm m,eff}$ in the following. For the general case $\delta \neq \omega_{\rm m,eff}$, see Eq. (3.L.1). The change in the spectrum Eq. (3.3.23) includes a modification of the main peak, and new peaks corresponding to the upper sideband of the blue drive and the lower sideband of the red drive.

3.3.5 Optical spectrum

As we have seen, CR terms modify the mechanical quadrature spectrum, which is reflected in the optical spectrum

$$\begin{aligned} S^{(0)}_{a^\dagger a}(\omega) &= G^2|\chi_\mathrm{c}(\omega)|^2\left[S^{(0)}_{xx}(\omega-\delta)+S^{(0)}_{xx}(\omega+\delta)+S^{(2)}_{xx}(\omega-\delta)+S^{(-2)}_{xx}(\omega+\delta)\right] \\ &= G^2|\chi_\mathrm{c}(\omega)|^2\left\{S^{(0)}_{X_\delta X_\delta}(\omega)+\lambda^2 S^{(0)}_{X_{-\delta}X_{-\delta}}(\omega)+\lambda\left[S^{(0)}_{X_\delta X_{-\delta}}(\omega)+S^{(0)}_{X_{-\delta}X_\delta}(\omega)\right]\right\}. \end{aligned} \tag{3.3.24}$$

Comparing the second line of Eq. (3.3.24) to Eq. (3.3.7), we notice that there are extra terms present, namely those with at least one λ out front. They are due to additional terms containing $\hat{X}_\delta$ and $\hat{P}_\delta$ on the RHS of the equation of motion for $\hat{Q}$. In Fig. 3.7, they are denoted by the two grey arrows pointing to $\hat{Q}$. Thus, this is an *imperfection* of the BAE measurement.

In fact, the additional contributions stem from the spectrum of the *counterrotating quadrature* $\hat{X}_{-\delta}$ (i.e., with frequency $-\delta$) and correlations of that quadrature with $\hat{X}_\delta$. That prompts a remarkably literal interpretation of "counterrotating terms". It also clarifies the origin of the measurement BA. The CR quadrature can be written

$$\hat{X}_{-\delta}(t) = \cos(2\delta t)\hat{X}_\delta(t) + \sin(2\delta t)\hat{P}_\delta(t), \tag{3.3.25}$$

which makes it apparent that the measurement picks up some information about $\hat{P}_\delta$, the quadrature conjugate to $\hat{X}_\delta$.

In contrast, the *measurement backaction*, as discussed in Sec. 3.3.4, arises from the grey arrows emanating from $\hat{I}$. This correction is contained within $S_{X_\delta X_\delta}$ in Eq. (3.3.24).

In order to distinguish the two contributions (the imperfection and BA), we plot three functions in Fig. 3.8. The full optical spectrum (3.3.24) in blue (solid) encompasses both contributions. A perfect BAE measurement of the modified mechanical spectrum Eqs. (3.3.7) and (3.3.23) is shown in yellow (dashed), it picks up the thermal contribution and the BA. Finally, the expected result in RWA is red (dotted), which corresponds to a perfect BAE measurement of an otherwise undriven mechanical oscillator. The sidepeaks of the modified mechanical spectrum do not show in the yellow curve, as they are suppressed by $|\chi_\mathrm{c}(\omega)|^2$.

3.3.6 Mechanical and optical variances

An important application of BAE measurements is determining the quadrature variance, necessary for the verification of quantum squeezing. The BA imperils this by increasing

the variance to

$$\langle \hat{X}_\delta^2 \rangle = \langle \hat{X}_{\mathrm{RWA}}^2 \rangle + 2n_{\mathrm{CR}}, \tag{3.3.26}$$

where $\langle \hat{X}_{\mathrm{RWA}}^2 \rangle = \langle \hat{X}_{\mathrm{unmeasured}}^2 \rangle$ is the result calculated without CR terms and [cf. Eq. (3.3.23)]

$$2n_{\mathrm{CR}} \equiv \int \frac{d\omega}{2\pi} S_{X_\delta X_\delta}^{\mathrm{CR}}(\omega) = \frac{8G^2(\kappa/\Gamma_{\mathrm{eff}} + 1)}{(\Gamma_{\mathrm{eff}} + \kappa)^2 + 16\omega_{\mathrm{m,eff}}^2}. \tag{3.3.27}$$

Perhaps the most surprising aspect about this result is that n_{CR} is independent of the temperature of the mechanical bath, whether it is squeezed or not, and what quadrature we measure. This fact is already realized on the level of the spectrum correction Eq. (3.3.23). The reason, as we have noted above, is that the optical quadrature I in the measurement cavity is independent of the mechanics and that the BA is solely due to this quadrature (see Fig. 3.7). Note that although we have written the change in terms of a number of phonons $2n_{\mathrm{CR}}$, it is not thermal heating that causes this effect, but rather the extraction of information about the conjugate quadrature.

In the optical spectrum, we saw that sidepeaks appear (cf. Fig. 3.8). To get an approximation to the variance of the measured mechanical quadrature, we integrate over the main peak of Eq. (3.3.24). Here, we calculate the error of this method, which can be used for underdamped oscillators $\Gamma_{\mathrm{eff}} \ll \omega_{\mathrm{m,eff}}$. The weight of the main peak is

$$\langle \hat{X}_{\mathrm{meas}}^2 \rangle = \langle \hat{X}_{\mathrm{RWA}}^2 \rangle + 2n_{\mathrm{CR}} \frac{16\omega_{\mathrm{m,eff}}^2(2\Gamma_{\mathrm{eff}} + \kappa)}{(\Gamma_{\mathrm{eff}} + \kappa)(\Gamma_{\mathrm{eff}}^2 + 16\omega_{\mathrm{m,eff}}^2)}, \tag{3.3.28}$$

with n_{CR} given by Eq. (3.3.27). Integrating $S^{(0)}_{a_{\mathrm{out}}^\dagger a_{\mathrm{out}}}(\omega)/(\kappa G^2|\chi_{\mathrm{c}}(\omega)|^2)$ from $-\omega_{\mathrm{m,eff}}$ to $\omega_{\mathrm{m,eff}}$ returns a good approximation to $\langle \hat{X}_{\mathrm{meas}}^2 \rangle$, as we show in Appendix 3.K. The second term is the BA. For example, if $\Gamma_{\mathrm{eff}}/\kappa = 10^{-4}$, $G/\kappa = 0.05$, and $\omega_{\mathrm{m}}/\kappa = 5$ (i.e., $\mathcal{C} = 10^6$), the variance increases by 0.5 (in units of the zero-point fluctuations of the mechanical oscillator). Since $n_{\mathrm{CR}} \propto G^2$, stronger driving quickly makes this effect noticeable. In typical experimental regimes, where $\Gamma_{\mathrm{eff}} \ll (\omega_{\mathrm{m}}, \kappa)$, the BA in Eq. (3.3.28) is well approximated by $2n_{\mathrm{CR}}$, such that $\langle \hat{X}_{\mathrm{meas}}^2 \rangle \approx \langle \hat{X}_\delta^2 \rangle$ (3.3.26), as desired.

Finally, we would like to gain some insights about the good and bad cavity limits of Eqs. (3.3.27) and (3.3.28). To give some intuition what these limits imply for the optical spectrum, consider the solution of Eq. (3.3.2a)

$$\hat{a}(t) = \int_{-\infty}^{t} d\tau\, e^{\frac{\kappa(\tau - t)}{2}} \left[2iG\cos(\omega_{\mathrm{m}}\tau)\hat{x}(\tau) + \hat{a}_{\mathrm{in}}(\tau)\right]. \tag{3.3.29}$$

In the good cavity limit ($\omega_{\mathrm{m}} \gg \kappa$), the exponential decay is negligible over a period

$2\pi/\omega_{\rm m}$. Thus

$$\int_0^{\frac{2\pi}{\omega_{\rm m}}} d\tau\ \cos(\omega_{\rm m}\tau)[\cos(\omega_{\rm m}\tau)\hat{X}_\delta(\tau)+\sin(\omega_{\rm m}\tau)\hat{P}_\delta(\tau)] \approx (1/2)\int_0^{\frac{2\pi}{\omega_{\rm m}}} d\tau\,\hat{X}_\delta(\tau), \tag{3.3.30}$$

since $\hat{X}_\delta(\omega)$ and $\hat{P}_\delta(\omega)$ are centred around $\omega=0$. On the other hand, in the bad cavity limit $\kappa > \omega_{\rm m}$ the photons leave the cavity faster than the change in coupling parameter, such that no averaging takes place. A simple argument then shows that the contribution from $\hat{X}_\delta$ is roughly three times as big as the contribution from $\hat{P}_\delta$.

These properties are reflected in the variances Eqs. (3.3.27) and (3.3.28). In the bad cavity limit, where $\kappa \gg \omega_{\rm m,eff}$, the number of added phonons is

$$2n_{\rm CR} \to \frac{8G^2}{\Gamma_{\rm eff}(\Gamma_{\rm eff}+\kappa)}. \tag{3.3.31}$$

In this regime the separation of the two drives is small compared to the bandwidth of the cavity, and therefore the BA becomes significant ($n_{\rm CR}\sim 1$) at a cooperativity $\mathcal{C}\sim 1$, where $\mathcal{C}\equiv 4G^2/\kappa\Gamma_{\rm eff}$. As we have seen, the reason is that resonant and CR terms couple with equal strength.

In contrast, the good cavity limit is $\kappa \gg \Gamma_{\rm eff}$ and $\omega_{\rm m,eff}\gg\kappa$, where Eq. (3.3.27) reduces to

$$2n_{\rm CR} \to \frac{\kappa G^2}{2\Gamma_{\rm eff}\omega_{\rm m,eff}^2}. \tag{3.3.32}$$

This agrees with the perturbative result in Ref. 139. Equation (3.3.32) tells us that the BA depends inversely on the effective mechanical dissipation rate. Physically, this is because $\Gamma_{\rm eff}$, the rate at which the mechanical oscillator relaxes to its steady state, competes with the BA rate due to CR terms, which is independent of $\Gamma_{\rm eff}$. The BA also decreases with increasing $\omega_{\rm m}$, as CR terms become less resonant. We find that the BA becomes significant ($n_{\rm CR}\sim 1$) for a cooperativity $\mathcal{C}\sim 16\omega_{\rm m}^2/\kappa^2$. Therefore, in the good cavity regime, the CR terms are suppressed by a factor $\sim 16\omega_{\rm m}^2/\kappa^2$ in comparison to resonant terms, due to the mechanism described above.

3.3.7 Generalization

Above, we have taken $\hat{H}_{\rm rest}=0$ for simplicity, but we can in fact take any $\hat{H}_{\rm rest}$ and write down the solution, as long as we know the steady state of $\hat{H}_{\rm OM}+\hat{H}_{\rm rest}+\hat{H}_{\rm baths}$, i.e., without the BAE measurement ($G=0$). Furthermore, we need

$$[\hat{H}_{\rm rest},\hat{I}]=0. \tag{3.3.33}$$

If the unmeasured solution is also periodic, the consideration in Sec. 2.7 applies: For incommensurate periods, only the stationary part will be picked up by the measurement, but if they are commensurate, some other Fourier components may enter the output spectrum.

To formulate a general theory, we collect all system (input) operators into a vector $\mathbf{x}$ ($\hat{\mathbf{x}}_{\mathrm{in}}$), such that the system is governed by Eq. (2.2.6). If this system of equations is solvable without the BAE measurement (i.e., for $G = 0$), this means we are able to find the scattering matrix Eq. (2.4.3). The upshot of our solution in Sec. 3.3 is that since in Eq. (2.2.6) we do not make any assumption about the noise $\hat{\mathbf{x}}_{\mathrm{in}}^{(n)}$, the replacement in Eq. (3.3.16) above will leave the scattering matrix unchanged and therefore we can calculate the measurement backaction for all systems with suitable $\hat{H}_{\mathrm{rest}}$.

For examples how $\chi^{(n)}$ can look like, see the detailed calculations in Appendices 3.H, 3.G, 3.I, and 3.J. Appendix 3.G contains the setup used to produce dissipative squeezing [1, 44–46, 121, 122, 124], Appendix 3.H discusses a weak-coupling version of the former, which is easily adapted to other weakly coupled systems, and Appendix 3.I contains the parametric squeezing case, which is an example with more than one independent, relevant component in χ. Last is Appendix 3.J, which extends the method here to two mechanical modes, and covers a recently developed two-mode BAE measurement [143, 144].

3.4 Conclusion

In this chapter we applied the Floquet framework from Chapter 2 to optomechanical systems driven by two tones. Such systems have garnered a large amount of interest recently, as they can be used to prepare a mechanical oscillator in a quantum-squeezed state [44–46, 121], or perform backaction-evading measurements [139]. Using the full analytical solution in the RWA, we shed light on the squeezing mechanism and provided some intuition for the behaviour of periodically driven systems (Sec. 3.2). When a second cavity is used for readout, the rotating readout quadrature has to match the frequency of the squeezed quadrature in order to detect squeezing. This conclusion has close parallels to the detection of squeezing in optical field, which has to be done via a homodyne (frequency-matched) measurement.

In a second part (Sec. 3.3), we derived the full solution of an optomechanical system subject to a dual-beam BAE measurement [46, 50, 122, 138, 140]. This enabled us to calculate the modification of the spectrum and quantify the measurement backaction precisely. Furthermore, we showed how to generalize our calculation to systems where the mechanical resonator is additionally coupled to other degrees of freedom and illustrate the

technique with several examples.

From the exposition in the previous Chapter 2 it is clear that our technique applies generally to linear time-periodic systems. This chapter illustrated this point by discussing some applications in some detail. As has been mentioned before, similar periodically driven optomechanical systems arise naturally in levitated optomechanics, where a mechanical oscillator may be trapped in a dipole trap [145]. A dipole trap has vanishing optomechanical coupling at the antinode, such that the particle has to be pushed away from its equilibrium position. The ensuing periodic oscillations lead not only to a periodically oscillating optomechanical coupling $g(t)$, but also to a periodic modulation of the mechanical frequency [131]. This can be described quantitatively with our technique [133].

Another situation arises when in addition to the optomechanical coupling there is some cavity nonlinearity. This commonly occurs in cavities with a small mode volume in which the per-photon field amplitude is large. Small optical mode volumes are generally desirable as they enhance the single-photon optomechanical coupling. However, at the same time this means that other nonlinearities are stronger as well [146–148]. In such a case, a periodically varying intracavity field causes both an oscillating optomechanical coupling as well as a periodic excursion of the cavity resonance frequency. This causes sidebands from different tones to couple, which again may be described within the framework presented here [134].

Appendix

3.A Floquet engineering

In the case studied in the main text, the infinite matrix (2.2.7) only contains $\mathsf{A}^{(0)}, \mathsf{A}^{(\pm 1)}$, the other elements being zero. We describe how to activate more blocks and their general structure below.

One can think of $\mathsf{A}^{(0)}$ as the fundamental building block and of $\mathsf{A}^{(\pm n)}$ for $n > 0$ as contributions that oscillate with $n\delta$ and therefore are capable of coupling fundamental blocks a distance n away from each other.

Any periodic driving with period $T = 2\pi/\delta$, either due to anharmonic drives or several harmonic ones, can be expressed as a Fourier series with fundamental frequency δ. Usually, the drive frequencies are offset by the cavity mode frequency and some detuning, i.e.,

$$\omega_n = \omega_{\text{cav}} + \Delta + in\delta. \tag{3.A.1}$$

It is useful to define the matrices

$$\mathsf{A}_+ \equiv \left(\begin{array}{cc|cc} & & & \\ 1 & & & \\ \hline & & -1 & -1 \\ -1 & & & \end{array}\right), \; \mathsf{A}_- \equiv \left(\begin{array}{cc|cc} & & 1 & 1 \\ & & & 1 \\ \hline & & & \\ & & -1 & \end{array}\right). \tag{3.A.2}$$

If we assume a driving Hamiltonian of the form

$$\hat{H}_{\text{drive}} = e^{-i(\omega_{\text{cav}}+\Delta)t}\left(\sum_n \alpha_n e^{-in\delta t}\right)\hat{a}^\dagger + \text{H.c.}, \tag{3.A.3}$$

we can linearize the Hamiltonian by a displacement operation like the one used in the main text, with

$$\hat{a} = e^{-i(\omega_{\text{cav}}+\Delta)t}\left(\sum_n \bar{a}_n e^{-in\delta t} + \delta\hat{a}\right). \tag{3.A.4}$$

Defining $J_n = \bar{a}_n g$, the enhanced optomechanical coupling strengths, we can write

$$\mathsf{A}^{(n)} = iJ_n\mathsf{A}_+ + iJ_{-n}\mathsf{A}_- - \delta_{n,0}\mathsf{M}_0, \tag{3.A.5}$$

where

$$\mathsf{M}_0 \equiv \begin{pmatrix} \frac{\kappa}{2} - i\Delta & & & \\ & \frac{\Gamma_\mathrm{m}}{2} + i\omega_\mathrm{m} & & \\ & & \frac{\kappa}{2} + i\Delta & \\ & & & \frac{\Gamma_\mathrm{m}}{2} - i\omega_\mathrm{m} \end{pmatrix}. \tag{3.A.6}$$

This includes the case discussed in the main text (3.2.8) and provides a simple recipe to couple any two blocks together and thus to engineer new types of driving schemes. Moreover, it is straightforward to adapt this to a different system, once the relevant matrices $\mathsf{M}_0, \mathsf{A}_\pm$ have been identified.

3.B Full solution to periodically driven optomechanical system in RWA

In RWA, the infinite set of differential equations (2.2.6) decouples into sets of four, as discussed above. Here we give the full solution to Eq. (3.2.10). Eliminating the light field we find

$$\begin{pmatrix} \chi_\mathrm{m}^{-1}(\omega) - i\Sigma_{00}(\omega) & -i\Sigma_{01}(\omega) \\ i\Sigma_{01}^*(-\omega+\delta) & \chi_\mathrm{m}^{-1*}(-\omega+\delta) + i\Sigma_{00}^*(-\omega+\delta) \end{pmatrix} \begin{pmatrix} \hat{b}^{(0)} \\ \hat{b}^{(1)\dagger} \end{pmatrix} = \begin{pmatrix} \sqrt{\Gamma_\mathrm{m}} & iG_-\sqrt{\kappa}\chi_\mathrm{c}(\omega) \\ 0 & -iG_+\sqrt{\kappa}\chi_\mathrm{c}(\omega) \end{pmatrix} \begin{pmatrix} \hat{b}_\mathrm{in} \\ \hat{a}_\mathrm{in} \end{pmatrix}, \tag{3.B.1}$$

with

$$\begin{aligned} \Sigma_{00}(\omega) &= i\left[G_-^2\chi_\mathrm{c}(\omega) - G_+^2\chi_\mathrm{c}^*(-\omega+\delta)\right], \\ \Sigma_{01}(\omega) &= iG_-G_+\left[\chi_\mathrm{c}(\omega) - \chi_\mathrm{c}^*(-\omega+\delta)\right]. \end{aligned} \tag{3.B.2}$$

This allows us to write the system operators in terms of input operators

$$\begin{pmatrix} \hat{b}^{(0)}(\omega) \\ \hat{b}^{(1)\dagger}(\omega) \end{pmatrix} = \begin{pmatrix} a(\omega) & c(\omega) \\ f(\omega) & g(\omega) \end{pmatrix} \begin{pmatrix} \hat{b}_\mathrm{in}(\omega) \\ \hat{a}_\mathrm{in}(\omega) \end{pmatrix}, \tag{3.B.3}$$

with

$$a(\omega) = A^{-1}(\omega)\sqrt{\Gamma_{\rm m}}\left[\chi_{\rm m}^{-1*}(-\omega+\delta) + i\Sigma_{00}^{*}(-\omega+\delta)\right], \tag{3.B.4a}$$
$$c(\omega) = iA^{-1}(\omega)\sqrt{\kappa}\chi_{\rm c}(\omega)G_{-}\left[\chi_{\rm m}^{-1*}(-\omega+\delta) + \mathcal{G}^2\chi_{\rm c}^{*}(-\omega+\delta)\right], \tag{3.B.4b}$$
$$f(\omega) = -iA^{-1}(\omega)\sqrt{\Gamma_{\rm m}}\Sigma_{01}(\omega), \tag{3.B.4c}$$
$$g(\omega) = -iA^{-1}(\omega)\sqrt{\kappa}\chi_{\rm c}(\omega)G_{+}\left[\chi_{\rm m}^{-1}(\omega) + \mathcal{G}^2\chi_{\rm c}^{*}(-\omega+\delta)\right], \tag{3.B.4d}$$

where $\mathcal{G}^2 \equiv G_{-}^2 - G_{+}^2$ and $A(\omega)$ is the determinant of the matrix on the left hand side of Eq. (3.B.1),

$$A(\omega) = \left[\chi_{\rm m}^{-1*}(-\omega+\delta) + i\Sigma_{00}^{*}(-\omega+\delta)\right]\left[\chi_{\rm m}^{-1}(\omega) - i\Sigma_{00}(\omega)\right] - \Sigma_{01}(\omega)\Sigma_{01}^{*}(-\omega+\delta). \tag{3.B.5}$$

The solution can be used to find spectrum Fourier components, employing Eq. (2.5.7),

$$S_{b^\dagger b}^{(0)}(\omega) = |a(-\omega)|^2 n_{\rm th} + |f(\omega+\delta)|^2(n_{\rm th}+1) + |g(\omega+\delta)|^2, \tag{3.B.6a}$$
$$S_{bb^\dagger}^{(0)}(\omega) = (n_{\rm th}+1)|a(\omega)|^2 + |c(\omega)|^2 + n_{\rm th}|f(-\omega+\delta)|^2, \tag{3.B.6b}$$
$$\begin{aligned} S_{xx}^{(0)}(\omega) &= (n_{\rm th}+1)\left(|a(\omega)|^2 + |f(\omega+\delta)|^2\right) + |c(\omega)|^2 \\ &\quad + n_{\rm th}\left(|a(-\omega)|^2 + |f(-\omega+\delta|^2\right) + |g(\omega+\delta)|^2, \end{aligned} \tag{3.B.6c}$$
$$S_{bb}^{(-1)}(\omega) = (n_{\rm th}+1)a(\omega)f^{*}(\omega) + c(\omega)g^{*}(\omega) + n_{\rm th}f^{*}(-\omega+\delta)a(-\omega+\delta) \tag{3.B.6d}$$
$$= [S_{b^\dagger b^\dagger}^{(1)}(\omega-\delta)]^\dagger. \tag{3.B.6e}$$

An important special case [45, 46] is the symmetric detuning $\delta = 2\omega_{\rm m} + \varepsilon$, $\Delta = -\omega_{\rm m} - \varepsilon/2 = -\delta/2$. Crucially, this leads to $\chi_{\rm c}^{*}(-\omega+\delta) = \chi_{\rm c}(\omega)$, which implies

$$\Sigma_{00} = i\chi_{\rm c}(\omega)\mathcal{G}^2, \qquad \Sigma_{01} = 0. \tag{3.B.7}$$

Thus, the determinant $A(\omega)$ takes a particularly simple form

$$A(\omega) = \left[\chi_{\rm m}^{-1}(\omega-\varepsilon) + \chi_{\rm c}(\omega)\mathcal{G}^2\right]\left[\chi_{\rm m}^{-1}(\omega) + \chi_{\rm c}(\omega)\mathcal{G}^2\right] \tag{3.B.8}$$

and so do the auxiliary functions

$$\begin{aligned} a(\omega) &= \sqrt{\Gamma_{\rm m}}/\left[\chi_{\rm m}^{-1}(\omega) + \chi_{\rm c}(\omega)\mathcal{G}^2\right], \\ c(\omega) &= i\sqrt{\kappa}G_{-}\chi_{\rm c}(\omega)/\left[\chi_{\rm m}^{-1}(\omega) + \chi_{\rm c}(\omega)\mathcal{G}^2\right], \\ f(\omega) &= 0, \\ g(\omega) &= -i\sqrt{\kappa}\chi_{\rm c}(\omega)G_{+}/\left[\chi_{\rm m}^{-1}(\omega-\varepsilon) + \mathcal{G}^2\chi_{\rm c}(\omega)\right]. \end{aligned} \tag{3.B.9}$$

The spectrum Fourier components are

$$S_{xx}^{(0)}(\omega) = \frac{(n_{\rm th}+1)\Gamma_{\rm m} + \kappa G_-^2|\chi_{\rm c}(\omega)|^2}{|\chi_{\rm m}^{-1}(\omega) + \chi_{\rm c}(\omega)\mathcal{G}^2|^2} + \frac{\Gamma_{\rm m} n_{\rm th} + \kappa G_+^2|\chi_{\rm c}(-\omega)|^2}{|\chi_{\rm m}^{-1}(-\omega) + \chi_{\rm c}(-\omega)\mathcal{G}^2|^2}, \tag{3.B.10a}$$

$$S_{xx}^{(1)}(\omega) = [S_{xx}^{(-1)}(-\omega)]^* = \frac{\kappa G_- G_+ \chi_{\rm c}(-\omega)}{\sigma^*(-\omega)\left[\chi_{\rm m}^{-1}(-\omega-\varepsilon) + \chi_{\rm c}(-\omega)\mathcal{G}^2\right]}, \tag{3.B.10b}$$

where we have introduced $\sigma(\omega) = \mathcal{G}^2 + \chi_{\rm m}^{-1}(\omega)\chi_{\rm c}^{-1}(\omega)$.

We can employ Eq. (2.7.4) for the physical spectrum in the special rotating frame. It has two parts. One is the previously stationary part, which corresponds to the radially symmetric contribution to the Wigner density (and therefore it remains stationary, despite going into a rotating frame)

$$\begin{aligned} U(\omega) &= S_{b^\dagger b}^{(0)}(\omega - \delta/2) + S_{bb^\dagger}^{(0)}(\omega + \delta/2) \\ &= \kappa\left[\frac{G_-^2}{|\sigma(\omega+\delta/2)|^2} + \frac{G_+^2}{|\sigma(-\omega+\delta/2)|^2}\right] \\ &+ \frac{\Gamma_{\rm m}}{|\chi_{\rm c}(\omega+\delta/2)|^2}\left[\frac{n_{\rm th}+1}{|\sigma(\omega+\delta/2)|^2} + \frac{n_{\rm th}}{|\sigma(-\omega+\delta/2)|^2}\right] \end{aligned} \tag{3.B.11}$$

The other one stems from the previously rotating parts

$$\begin{aligned} V(\omega) &= S_{b^\dagger b^\dagger}^{(1)}(\omega - \delta/2) + S_{bb}^{(-1)}(\omega + \delta/2) \\ &= -2\kappa G_- G_+ \,\mathrm{Re}\left\{\frac{1}{|\sigma(\omega+\delta/2)|^2 - i\varepsilon\chi_{\rm c}^{-1*}(\omega+\delta/2)\sigma(\omega+\delta/2)}\right\}. \end{aligned} \tag{3.B.12}$$

Finally,

$$S_{X_\mp X_\mp}(\omega) = U(\omega) \pm V(\omega). \tag{3.B.13}$$

3.C Weak-coupling approximation of periodically driven optomechanical system

Our approach in this section will be to perturb around the mechanical spectrum in the absence of coupling. We will do so up to second order in $G_\pm$.

The equations of motion in RWA (3.2.9), split up into Fourier components, are

$$\dot{\hat{a}}^{(n)} = \left(-in\delta + i\Delta - \frac{\kappa}{2}\right)a^{(n)} + \sqrt{\kappa}\delta_{n,0}\hat{a}_{\rm in} + i\left(G_+\hat{b}^{(n+1)\dagger} + G_-\hat{b}^{(n)}\right), \tag{3.C.1a}$$

$$\dot{\hat{b}}^{(n)} = \left(-in\delta - i\omega_{\rm m} - \frac{\Gamma_{\rm m}}{2}\right)\hat{b}^{(n)} + \sqrt{\Gamma_{\rm m}}\delta_{n,0}\hat{b}_{\rm in} + i\left(G_+\hat{a}^{(n+1)\dagger} + G_-\hat{a}^{(n)}\right). \tag{3.C.1b}$$

The unperturbed mechanical spectrum consists only of $\hat{b}^{(0)}$ and $\hat{b}^{(0)\dagger}$. Thus, to first order,

$$\hat{a}^{(0)}(\omega) = \chi_{\mathrm{c}}(\omega)\left[\sqrt{\kappa}\hat{a}_{\mathrm{in}}(\omega) + iG_{-}\hat{b}^{(0)}(\omega)\right], \tag{3.C.2a}$$

$$\hat{a}^{(-1)}(\omega) = \chi_{\mathrm{c}}(\omega+\delta)iG_{+}\hat{b}^{(0)\dagger}(\omega). \tag{3.C.2b}$$

We can now determine $\hat{b}^{(0)}$ without knowledge of $\hat{b}^{(-1)}$

$$\left[-i\omega + i\omega_{\mathrm{m}} + \frac{\Gamma_{\mathrm{m}}}{2} - G_{+}^{2}\chi_{\mathrm{c}}^{*}(-\omega+\delta) + G_{-}^{2}\chi_{\mathrm{c}}(\omega)\right]\hat{b}^{(0)}(\omega) = \sqrt{\Gamma_{\mathrm{m}}}\hat{b}_{\mathrm{in}}(\omega) + i\sqrt{\kappa}G_{-}\chi_{\mathrm{c}}(\omega)\hat{a}_{\mathrm{in}}(\omega) + \mathcal{O}(G_{\pm}^{3}). \tag{3.C.3}$$

The reason for this is that $\hat{b}^{(-1)} = \mathcal{O}(G_{\pm})$, such that the effect $\hat{b}^{(-1)}$ has on $\hat{b}^{(0)}$ (via the optical field) is at least $\mathcal{O}(G_{\pm}^{3})$. The LHS of (3.C.3) is the modified response function

$$\tilde{\chi}_{\mathrm{m}}(\omega) = \left\{\frac{\tilde{\Gamma}_{\mathrm{m}}(\omega)}{2} - i[\omega - \tilde{\omega}_{\mathrm{m}}(\omega)]\right\}^{-1} \tag{3.C.4}$$

with

$$\tilde{\Gamma}_{\mathrm{m}}(\omega) = \Gamma_{\mathrm{m}} + \kappa\left(|\chi_{\mathrm{c}}(\omega)|^{2}G_{-}^{2} - |\chi_{\mathrm{c}}(-\omega+\delta)|^{2}G_{+}^{2}\right), \tag{3.C.5a}$$

$$\tilde{\omega}_{\mathrm{m}}(\omega) = \omega_{\mathrm{m}} + |\chi_{\mathrm{c}}(\omega)|^{2}(\omega+\Delta)G_{-}^{2} + |\chi_{\mathrm{c}}(-\omega+\delta)|^{2}(-\omega+\delta+\Delta)G_{+}^{2}. \tag{3.C.5b}$$

The mechanical response function (3.C.4) strongly suppresses contributions away from $\omega = -\tilde{\omega}_{\mathrm{m}} \approx -\omega_{\mathrm{m}}$. In comparison to χ_{m}, χ_{c} is flat (if $\tilde{\Gamma}_{\mathrm{m}} \ll \kappa$), such that we can approximate $\chi_{\mathrm{c}}(\omega) \approx \chi_{\mathrm{c}}(-\omega_{\mathrm{m}})$. For $\Delta = -\omega_{\mathrm{m}}$ the corrections simplify to Eqs. (3.2.13a), and

$$\hat{b}^{(0)}(\omega) = \tilde{\chi}_{\mathrm{m}}(\omega)\sqrt{\Gamma_{\mathrm{m}}}\hat{b}_{\mathrm{in}} + \frac{2iG_{-}}{\sqrt{\kappa}}\chi_{\mathrm{m}}(\omega)\hat{a}_{\mathrm{in}}. \tag{3.C.6}$$

We would like the same accuracy for the rotating components, so we keep the next order in a

$$\begin{aligned}\hat{a}^{(0)}(\omega) &= \chi_{\mathrm{c}}(\omega)\left[\sqrt{\kappa}\hat{a}_{\mathrm{in}}(\omega) + iG_{-}\hat{b}^{(0)} + iG_{+}\hat{b}^{(1)\dagger}(\omega)\right],\\ \hat{a}^{(-1)}(\omega) &= i\chi_{\mathrm{c}}(\omega+\delta)\left[G_{+}\hat{b}^{(0)\dagger}(\omega) + G_{-}\hat{b}^{(-1)}(\omega)\right].\end{aligned} \tag{3.C.7}$$

Then

$$\chi_{\mathrm{m}}^{-1*}(-\omega+\delta)\hat{b}^{(1)\dagger}(\omega) = -i\left[G_{+}\hat{a}^{(0)}(\omega) + G_{-}\hat{a}^{(1)\dagger}(\omega)\right]. \tag{3.C.8}$$

We substitute for $\hat{a}$ with Eq. (3.C.7)

$$\hat{b}^{(1)\dagger}(\omega) = \chi_{\mathrm{m}}'^{*}(-\omega+\delta)\left\{-iG_{+}\chi_{\mathrm{c}}(\omega)\sqrt{\kappa}\hat{a}_{\mathrm{in}}(\omega) + G_{+}G_{-}\left[\chi_{\mathrm{c}}(\omega) - \chi_{\mathrm{c}}^{*}(-\omega+\delta)\right]\hat{b}^{(0)}(\omega)\right\}, \quad (3.C.9)$$

where $\hat{b}^{(0)} = \chi_{\mathrm{m}}(\omega)\sqrt{\Gamma_{\mathrm{m}}}\hat{b}_{\mathrm{in}}$ in the absence of driving (the second order corrections to $\hat{b}^{(0)}$ would be fourth order in this equation). With a differently modified response function $\chi_{\mathrm{m}}' = [\Gamma_{\mathrm{m}}'/2 - i(\omega - \omega_{\mathrm{m}}')]^{-1}$, with

$$\Gamma_{\mathrm{m}}'(\omega) = \Gamma_{\mathrm{m}} + \kappa\left(|\chi_{\mathrm{c}}(-\omega+\delta)|^2 G_{-}^2 - |\chi_{\mathrm{c}}(\omega)|^2 G_{+}^2\right), \quad (3.C.10a)$$

$$\omega_{\mathrm{m}}'(\omega) = \omega_{\mathrm{m}} + |\chi_{\mathrm{c}}(\omega)|^2(\omega+\Delta)G_{+}^2 + |\chi_{\mathrm{c}}(-\omega+\delta)|^2(-\omega+\delta+\Delta)G_{-}^2. \quad (3.C.10b)$$

Comparing with Eq. (3.C.5a), we see that the corrections have the same form, but with the frequencies interchanged. The reason that the picture is reversed is that $\hat{b}^{(1)\dagger}$ rotates in sync with the upper drive and not with the lower one as $\hat{b}^{(0)}$ does. In the case $\Delta = -\omega_{\mathrm{m}}, \omega = \omega_{\mathrm{m}}$, they are mirrored versions of Eq. (3.C.5a)

$$\Gamma_{\mathrm{m}}' = \Gamma_{\mathrm{m}} + \frac{4}{\kappa}\left(\frac{G_{-}^2}{1+4\varepsilon^2/\kappa^2} - G_{+}^2\right), \quad (3.C.11a)$$

$$\omega_{\mathrm{m}}' = \omega_{\mathrm{m}} + \frac{\varepsilon G_{-}^2}{\kappa^2/4+\varepsilon^2}. \quad (3.C.11b)$$

We can neglect the second-order perturbation on the first order quantities $\hat{b}^{(1)\dagger}, \hat{b}^{(-1)}$, because they appear to third order on the level of spectrum calculations, such that

$$\hat{b}^{(1)\dagger}(\omega) = -\chi_{\mathrm{m}}^{*}(-\omega+\delta)\frac{2iG_{+}}{\sqrt{\kappa}}\hat{a}_{\mathrm{in}}. \quad (3.C.12)$$

In the main text we use the modified parameters $\tilde{\Gamma}_{\mathrm{m}}, \tilde{\omega}_{\mathrm{m}}$ in (3.2.12b). With this replacement, Eqs. (3.C.6) and (3.C.12) yield Eq. (3.2.17) It might seems surprising to use $\tilde{\Gamma}_{\mathrm{m}}, \tilde{\omega}_{\mathrm{m}}$ instead of $\Gamma_{\mathrm{m}}', \omega_{\mathrm{m}}'$, but is allowed, as the corrections are third order. We mainly do that for convenience, because it makes the subsequent analysis more transparent. Comparing to the full solution and looking at Fig. 3.4, we see that our approximation is reasonable. In fact, we cannot use Γ_{m}', because it crosses zero for relatively small detunings $\varepsilon < \kappa$ when $\mathcal{C} > n_{\mathrm{th}}$, which leads to a divergence.

In order to derive a master equation, we define $\hat{\tilde{b}} \equiv e^{i\delta t/2}\hat{b}$, and assume $\delta = 2\omega_{\mathrm{m}}$. Then

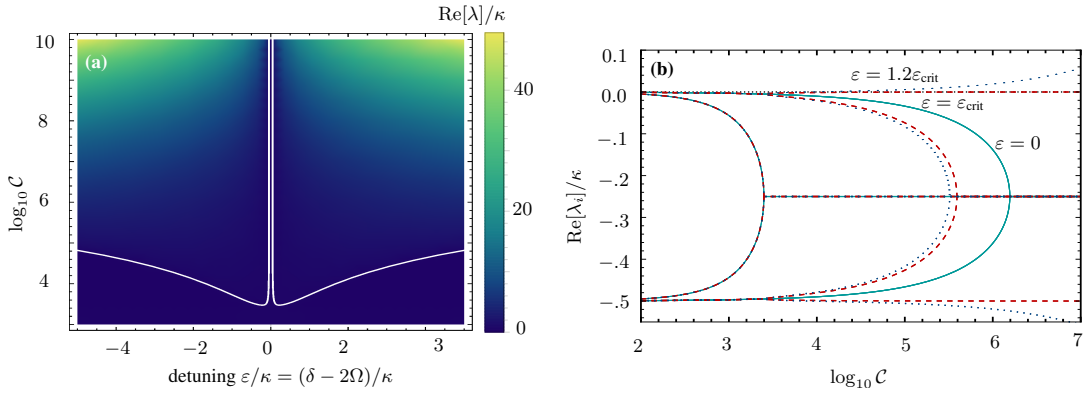

Figure 3.9: Analysis of instability within RWA. Parameters are $\Gamma_{\rm m}/\kappa = 10^{-4}, n_{\rm th} = 10, \mathcal{C} = 2 \times 10^3$, and $\Delta = -\omega_{\rm m}$. The sideband parameter $\omega_{\rm m}/\kappa$ is irrelevant in RWA. **(a) Boundary of stability.** The white curve is the analytical result for the boundary of stability (3.D.4). The colour scale gives the real part of the eigenvalue with the largest real part λ of the matrix (3.2.10). As $\mathcal{C} \to \infty$, a "stability corridor" remains, $\varepsilon_{\rm crit} = \pm\sqrt{\kappa\Gamma_{\rm m}(1+2n_{\rm th})}$. The corridor collapses without RWA. **(b) Eigenvalues as a function of cooperativity.** Real part of the eigenvalues of (3.2.10) as a function of cooperativity $\mathcal{C}$ for optimal driving Eq. (3.2.29), and detuning $\varepsilon = 0, \varepsilon_{\rm crit}, 1.2\varepsilon_{\rm crit}$, in dark blue (solid), red (dashed) and turquoise (dotted). In the strictly stable regime all eigenvalues converge to have the same real part $(\kappa + \Gamma_{\rm m})/4$ at large cooperativities $\mathcal{C}$. At the critical detuning two eigenvalues remain at $\Gamma_{\rm m}/2$ and two at $\kappa/2$ for all $\mathcal{C}$. Above the critical detuning, there exists a value of $\mathcal{C}$ above which the system is unstable.

$\hat{\beta} \equiv (G_- \hat{\tilde{b}} + G_+ \hat{\tilde{b}}^\dagger)/\mathcal{G}$ obeys

$$\dot{\hat{\beta}} = \left(-\frac{\Gamma_{\rm m}}{2} - \frac{2\mathcal{G}^2}{\kappa}\right)\hat{\beta} + \sqrt{\Gamma_{\rm m}}\hat{\beta}_{\rm in} + \frac{2i\mathcal{G}}{\sqrt{\kappa}}\hat{\tilde{a}}_{\rm in}, \tag{3.C.13}$$

where $\hat{\tilde{a}}_{\rm in} \equiv e^{i\omega_{\rm m}t}\hat{a}_{\rm in}$. The associated quantum master equation is (NB in frame rotating with the mechanical frequency $\omega_{\rm m}$)

$$\dot{\hat{\rho}} = \left\{\Gamma_{\rm m} n_{\rm th}\mathcal{D}[\hat{\tilde{b}}^\dagger] + \Gamma_{\rm m}(n_{\rm th}+1)\mathcal{D}[\hat{\tilde{b}}] + \frac{4\mathcal{G}^2}{\kappa}\mathcal{D}[\hat{\beta}]\right\}\hat{\rho}. \tag{3.C.14}$$

This agrees with Ref. 121. The physics here is that the drives cool the Bogoliubov mode $\hat{\beta}$ close to its ground state, which is a squeezed state for the rotating quadrature $\hat{\tilde{b}} + \hat{\tilde{b}}^\dagger$ [121].

3.D Analysis of instability within RWA

To study the instability we employ the Routh-Hurwitz criterion, according to which a system is unstable if the matrix M in $\dot{\mathbf{x}} = \mathsf{M}\mathbf{x}$ has an eigenvalue with positive real part.

Let us call the matrix on the LHS of (3.2.10) $\mathsf{K}(\omega)$. In our case, $\mathsf{K}(0) = -\mathsf{M}$. Thus we can write $\mathsf{K}(\omega) = -\mathsf{M} - i\omega\mathbb{1}_4$, where $\mathbb{1}_4$ is the 4×4 identity matrix. The eigenvalues of $\mathsf{K}(\omega)$ satisfy the secular equation

$$\det[-\mathsf{M} - (i\omega + \lambda)\mathbb{1}_4] = 0. \tag{3.D.1}$$

Thus, if λ is an eigenvalue of M, then $-\lambda + i\omega$ is an eigenvalue of $\mathsf{K}(\omega)$. We conclude that if $\mathrm{Re}[\lambda] = 0$, $\mathsf{K}(\mathrm{Im}[\lambda])$ is singular, and *vice versa*, which marks the onset of instability.

Assuming $\Delta = -\omega_\mathrm{m}$, it turns out that $\det[\mathsf{K}(\omega_\mathrm{m} + \varepsilon/2)]$ is purely real and

$$\det[\mathsf{K}(\omega_\mathrm{m} + \varepsilon/2)] = \sigma(\omega)\sigma(\omega - \varepsilon) - \varepsilon^2 G_+^2, \tag{3.D.2}$$

with $\sigma(\omega) = \mathcal{G}^2 + \chi_\mathrm{m}^{-1}(\omega)\chi_\mathrm{c}^{-1}(\omega)$ and $\delta = 2\omega_\mathrm{m} + \varepsilon$. Its imaginary part is zero at $\omega = \omega_\mathrm{m} + \varepsilon/2$, so we are left with

$$0 = \left(\mathcal{G}^2 + \frac{\Gamma_\mathrm{m}\kappa}{4} - \frac{\varepsilon^2}{4}\right)^2 + \frac{\varepsilon^2(\kappa + \Gamma_\mathrm{m})^2}{16} - \varepsilon^2 G_+^2, \tag{3.D.3}$$

which gives

$$\varepsilon_\pm^2 = 4(G_-^2 + G_+^2) - \frac{\kappa^2 + \Gamma_\mathrm{m}^2}{2} \pm \sqrt{\left[\frac{\kappa^2 + \Gamma_\mathrm{m}^2}{2} - 4(G_-^2 + G_+^2)\right]^2 - (4\mathcal{G}^2 + \Gamma_\mathrm{m}\kappa)^2}. \tag{3.D.4}$$

$\varepsilon_\pm$ is complex if the term under the root is negative, i.e., if

$$\mathcal{C} \leq \left(\frac{\kappa + \Gamma_\mathrm{m}}{2\sqrt{\kappa\Gamma_\mathrm{m}}} + \sqrt{1 + 2n_\mathrm{th}}\right)^2. \tag{3.D.5}$$

In Eq. (3.D.5) we have used the optimal driving strengths, see Eq. (3.2.29) or Ref. 121. We conclude that there is an instability for $\varepsilon_- < |\varepsilon| < \varepsilon_+$. Note that the stability regions are symmetric in ε with stability at $\varepsilon = 0$. Because of condition (3.D.5), we can only study large detuning for small cooperativities. As $\mathcal{C} \to \infty$, $\varepsilon_- \to \varepsilon_\mathrm{crit} = \pm\sqrt{\kappa\Gamma_\mathrm{m}(1 + 2n_\mathrm{th})}$, so there is a *stability corridor* in between $\pm\varepsilon_-$ even at largest cooperativities, which is shown in Fig. 3.9. Once we numerically include counterrotating terms, the stability corridor is lost. Note that we have assumed $\Delta = -\omega_\mathrm{m}$ and that if $G_+ > G_-$ the system may be unstable for all detunings δ.

3.E The optical spectrum $S_{a^\dagger a}$

Following the same steps as in the main text, we can write the optical system operators in terms of the input operators

$$\begin{pmatrix} \hat{a}^{(0)}(\omega) \\ \hat{a}^{(1)\dagger}(\omega) \end{pmatrix} = \begin{pmatrix} \hat{\tilde{a}}(\omega) & \hat{\tilde{c}}(\omega) \\ \hat{\tilde{f}}(\omega) & \hat{\tilde{g}}(\omega) \end{pmatrix} \begin{pmatrix} \hat{a}_{\rm in}(\omega) \\ \hat{b}_{\rm in}(\omega) \end{pmatrix}. \tag{3.E.1}$$

We obtain the functions in the matrix by a calculation analogous to the one in Appendix 3.B. Because of the symmetry of the equations of motion in the RWA, this amounts to swapping $\Gamma_{\rm m} \leftrightarrow \kappa, \chi_{\rm c} \leftrightarrow \chi_{\rm m}, \hat{b}_{\rm in} \leftrightarrow \hat{a}_{\rm in}$. Thus,

$$\begin{aligned}
\tilde{a}(\omega) &= \tilde{A}^{-1}(\omega)\sqrt{\kappa}\left[\chi_{\rm c}^{-1*}(-\omega+\delta) + i\tilde{\Sigma}_{00}^{*}(-\omega+\delta)\right], \\
\tilde{c}(\omega) &= i\tilde{A}^{-1}(\omega)\sqrt{\Gamma_{\rm m}}\chi_{\rm m}(\omega)G_{-}\left[\chi_{\rm c}^{-1*}(-\omega+\delta) + \mathcal{G}^2\chi_{\rm m}^{*}(-\omega+\delta)\right], \\
\tilde{f}(\omega) &= -i\tilde{A}^{-1}(\omega)\sqrt{\kappa}\tilde{\Sigma}_{01}(\omega), \\
\tilde{g}(\omega) &= -i\tilde{A}^{-1}(\omega)\sqrt{\Gamma_{\rm m}}\chi_{\rm m}(\omega)G_{+}\left[\chi_{\rm c}^{-1}(\omega) + \mathcal{G}^2\chi_{\rm m}^{*}(-\omega+\delta)\right],
\end{aligned} \tag{3.E.2}$$

with

$$\tilde{A}(\omega) = \left[\chi_{\rm c}^{-1*}(-\omega+\delta) + i\tilde{\Sigma}_{00}^{*}(-\omega+\delta)\right]\left[\chi_{\rm c}^{-1}(\omega) - i\tilde{\Sigma}_{00}(\omega)\right] - \tilde{\Sigma}_{01}(\omega)\tilde{\Sigma}_{01}^{*}(-\omega+\delta), \tag{3.E.3}$$

and

$$\begin{aligned}
\tilde{\Sigma}_{00}(\omega) &= i\left[G_{-}^2\chi_{\rm m}(\omega) - G_{+}^2\chi_{\rm m}^{*}(-\omega+\delta)\right], \\
\tilde{\Sigma}_{01}(\omega) &= iG_{-}G_{+}\left[\chi_{\rm m}(\omega) - \chi_{\rm m}^{*}(-\omega+\delta)\right].
\end{aligned} \tag{3.E.4}$$

The stationary part of the optical spectrum is

$$S_{a^\dagger a}^{(0)}(\omega) = |\tilde{c}(-\omega)|^2 n_{\rm th} + |\tilde{f}(\omega+\delta)|^2 + |\tilde{g}(\omega+\delta)|^2(n_{\rm th}+1). \tag{3.E.5}$$

Note that the same spectra can be obtained by employing the formulae in Sec. 3.2.8 for the case $\delta = \delta_2$. As the mechanical spectrum one has to use the one derived in Appendix 3.B, in particular Eq. (3.2.35). Further note that the output spectrum is trivially related to $S_{a^\dagger a}$. Using the input-output relation (1.2.16) we find

$$S_{a_{\rm out}^\dagger a_{\rm out}}^{(n)}(\omega) = \kappa S_{a^\dagger a}^{(n)}(\omega). \tag{3.E.6}$$

Note that this holds only if the optical input fields are in vacuum.

3.F Readout spectra in second mode

In this section we provide more details on the calculation of the readout spectrum. We split Eq. (3.2.30) into Fourier components

$$\sum_{n,m} e^{in\delta t+im\delta_2 t}\left[(in\delta+im\delta_2)\hat{a}_2^{(n,m)}+\dot{\hat{a}}_2^{(n,m)}\right]=\sum_{n,m} e^{in\delta t+im\delta_2 t} \times\left[\left(i\Delta_2-\frac{\kappa_2}{2}\right)\hat{a}_2^{(n,m)}+\sqrt{\kappa_2}\hat{a}_{2,\mathrm{in}}\delta_{n,0}\delta_{m,0}+i\left(G_{2+}\hat{x}^{(n,m+1)}+G_{2-}\hat{x}^{(n,m)}\right)\right]. \quad (3.F.1)$$

If $\delta\neq\delta_2$ (and they do not have a common multiple), we have $\hat{b}^{(n,m\neq 0)}=0$. Thus, with $\hat{x}^{(n,m)}\equiv\hat{b}^{(n,m)}+\hat{b}^{(n,m)\dagger}$,

$$\hat{a}_2^{(n,0)}=\chi_{\mathrm{c},2}(\omega-n\delta)\left(\sqrt{\kappa_2}\delta_{n,0}\hat{a}_{2,\mathrm{in}}+iG_{2-}\hat{x}^{(n,0)}\right) \quad (3.F.2a)$$

$$\hat{a}_2^{(n,0)\dagger}=\chi_{\mathrm{c},2}^*(-\omega+n\delta)\left(\sqrt{\kappa_2}\delta_{n,0}\hat{a}_{2,\mathrm{in}}^\dagger-iG_{2-}\hat{x}^{(n,0)}\right), \quad (3.F.2b)$$

$$\hat{a}_2^{(n,-1)}=\chi_{\mathrm{c},2}(\omega-n\delta+\delta_2)iG_{2+}\hat{x}^{(n,0)}, \quad (3.F.2c)$$

$$\hat{a}_2^{(n,1)\dagger}=-\chi_{\mathrm{c},2}^*(-\omega+n\delta+\delta_2)iG_{2+}\hat{x}^{(n,0)}. \quad (3.F.2d)$$

A substitution into Eq. (2.5.7) yields (3.2.34).

For the special choice $\delta_2=\delta$,

$$\hat{a}_2^{(n)}(\omega)=\chi_{\mathrm{c},2}(\omega-n\delta)\left[\sqrt{\kappa_2}\delta_{n,0}\hat{a}_{2,\mathrm{in}}+i\left(G_{2+}\hat{x}^{(n+1)}+G_{2-}\hat{x}^{(n)}\right)\right], \quad (3.F.3a)$$

$$\hat{a}_2^{(n)\dagger}(\omega)=\chi_{\mathrm{c},2}^*(-\omega+n\delta)\left[\sqrt{\kappa_2}\delta_{n,0}\hat{a}_{2,\mathrm{in}}^\dagger-i\left(G_{2+}\hat{x}^{(n-1)}+G_{2-}\hat{x}^{(n)}\right)\right]. \quad (3.F.3b)$$

Again we substitute into Eq. (2.5.7) to get (3.2.36).

3.G Dissipative dissipative squeezing

An important application of the type of BAE measurement discussed in this section is the verification of quantum squeezing in mechanical resonators, e.g., Ref. 46, 122. Here we generalize our method to this squeezing scheme, proposed in [121, 124], which has successfully produced quantum squeezing of the resonator [44–46, 122]. In this case

$$\hat{H}_{\mathrm{rest}}=-\Delta\hat{c}^\dagger\hat{c}-\left[\hat{c}\left(G_+e^{2i\delta t}\hat{b}+G_-\hat{b}^\dagger\right)+\mathrm{H.c.}\right], \quad (3.G.1)$$

where we have already displaced and linearized. $\hat{c}$ is the annihilation operator of another cavity in a frame rotating with the lower-frequency drive. Furthermore, we have applied

the RWA to $\hat{H}_{\mathrm{rest}}$. The governing Langevin equations are

$$\dot{\hat{c}} = \left(i\Delta - \frac{\kappa_2}{2}\right)\hat{c} + \sqrt{\kappa_2}\hat{c}_{\mathrm{in}} + i\left(G_-\hat{b} + G_+ e^{-2i\delta t}\hat{b}^\dagger\right), \tag{3.G.2a}$$

$$\dot{\hat{b}} = \left(-i\omega_{\mathrm{m}} - \frac{\Gamma_{\mathrm{m}}}{2}\right)\hat{b} + \sqrt{\Gamma_{\mathrm{m}}}\hat{b}_{\mathrm{in}} + i\left(G_-\hat{c} + G_+ e^{-2i\delta t}\hat{c}^\dagger\right), \tag{3.G.2b}$$

where $\hat{c}_{\mathrm{in}}$ corresponds to a vacuum (zero temperature) bath, and $\hat{b}_{\mathrm{in}}$ to a finite temperature bath with mean occupation n_{th}, so $\langle \hat{c}_{\mathrm{in}}(t)\hat{c}^\dagger_{\mathrm{in}}(t')\rangle = \delta(t-t')$, $\langle \hat{b}^\dagger_{\mathrm{in}}(t)\hat{b}_{\mathrm{in}}(t')\rangle = \delta(t-t')n_{\mathrm{th}}$, $\langle \hat{b}_{\mathrm{in}}(t)\hat{b}^\dagger_{\mathrm{in}}(t')\rangle = \delta(t-t')(1+n_{\mathrm{th}})$ (other correlators are zero).

In the Floquet ansatz, Eq. (3.G.2) can be expressed in terms of a block-diagonal infinite matrix (Sec. 2.2) with blocks

$$\begin{pmatrix} \chi_{\mathrm{opt}}^{-1}(\omega - n\delta) & -iG_- & 0 & -iG_+ \\ -iG_- & \chi_{\mathrm{m}}^{-1}(\omega - n\delta) & -iG_+ & 0 \\ 0 & iG_+ & \chi_{\mathrm{opt}}^{-1*}(-\omega + (n+2)\delta) & iG_- \\ iG_+ & 0 & iG_- & \chi_{\mathrm{m}}^{-1*}(-\omega + (n+2)\delta) \end{pmatrix} \times \begin{pmatrix} \hat{c}^{(n)}(\omega) \\ \hat{b}^{(n)}(\omega) \\ \hat{c}^{(n+2)\dagger}(\omega) \\ \hat{b}^{(n+2)\dagger}(\omega) \end{pmatrix} = \begin{pmatrix} \sqrt{\kappa}\hat{c}^{(n)}_{\mathrm{in}}(\omega) \\ \sqrt{\Gamma_{\mathrm{m}}}\hat{b}^{(n)}_{\mathrm{in}}(\omega) \\ \sqrt{\kappa}\hat{c}^{(n+2)\dagger}_{\mathrm{in}}(\omega) \\ \sqrt{\Gamma_{\mathrm{m}}}\hat{b}^{(n+2)\dagger}_{\mathrm{in}}(\omega) \end{pmatrix}, \tag{3.G.3}$$

where the cavity and mechanical response functions read $\chi_{\mathrm{opt}}(\omega) = [\kappa/2 - i(\omega+\Delta)]^{-1} \neq \chi_{\mathrm{c}}$ and $\chi_{\mathrm{m}}(\omega) = [\Gamma_{\mathrm{m}}/2 - i(\omega - \omega_{\mathrm{m}})]^{-1}$, respectively.

Blocks with zero input will vanish in the steady state. Since the noise resides entirely in the zeroth Fourier component (it describes a stationary process),

$$\hat{c}^{(n)}_{\mathrm{in}} = \hat{b}^{(n)}_{\mathrm{in}} = 0, \qquad \forall n \neq 0. \tag{3.G.4}$$

Although the result for general δ and Δ is available (cf. Appendix 3.B), we focus on the simple and relevant case $\delta = -\Delta = \omega_{\mathrm{m}}$, where

$$\begin{pmatrix} \hat{b}^{(0)}(\omega) \\ \hat{b}^{(2)\dagger}(\omega) \end{pmatrix} = J(\omega) \begin{pmatrix} 1 & iG_-\chi_{\mathrm{opt}}(\omega) \\ 0 & iG_+\chi_{\mathrm{opt}}(\omega) \end{pmatrix} \begin{pmatrix} \sqrt{\Gamma_{\mathrm{m}}}\hat{b}_{\mathrm{in}} \\ \sqrt{\kappa_2}\hat{c}_{\mathrm{in}} \end{pmatrix}, \tag{3.G.5}$$

with $J(\omega) = \left[\chi_{\mathrm{m}}^{-1}(\omega) + \mathcal{G}^2\chi_{\mathrm{opt}}(\omega)\right]^{-1}$.

Now we include the noise of a BAE measurement as per Sec. 3.3.7. The measurement

requires another cavity mode coupled to the mechanical oscillator. We define

$$\hat{\mathbf{x}} = (\hat{b}, \hat{b}^\dagger, \hat{c}, \hat{c}^\dagger)^T, \quad \hat{\mathbf{x}}_{\rm in} = (\hat{b}_{\rm in}, \hat{b}_{\rm in}^\dagger, \hat{c}_{\rm in}, \hat{c}_{\rm in}^\dagger)^T. \tag{3.G.6}$$

From Eq. (3.G.5), we can directly infer the elements

$$\begin{pmatrix} \chi_{11}^{(0)}(\omega) & \chi_{13}^{(0)}(\omega) \\ \chi_{21}^{(2)}(\omega - 2\delta) & \chi_{23}^{(2)}(\omega - 2\delta) \end{pmatrix} = J(\omega) \begin{pmatrix} 1 & iG_-\chi_{\rm opt}(\omega) \\ 0 & iG_+\chi_{\rm opt}(\omega) \end{pmatrix}. \tag{3.G.7}$$

Furthermore, the elements of χ are not all independent. In general,

$$\chi_{ij}^{(n)*}(\omega) = \chi_{\bar{i}\bar{j}}^{(-n)}(-\omega), \tag{3.G.8}$$

where $\bar{i}$ is the index for the operator that is the Hermitian conjugate of the operator indexed by i (so $\bar{1} = 2$, $\bar{3} = 4$, and *vice versa*).

We are only interested in the elements that connect the system operators with the mechanical bath, as those will determine the susceptibility to the measurement noise. Fortunately, the only non-zero ones are

$$\chi_{11}^{(0)}(\omega) = J(\omega) = \chi_{22}^{(0)*}(-\omega). \tag{3.G.9}$$

This gives the problem exactly the same structure as the case with $H_{\rm rest} = 0$, except that here $\chi_{\rm m}(\omega)$ is replaced by $J(\omega)$.

Nevertheless, we give the general formula for the added contribution due to the measurement

$$\hat{b}_{\rm add}^{(n)}(\omega) = 2\sqrt{\kappa}G \sum_m K^{(n-m)}(\omega - n\delta)\hat{f}_{\rm in}^{(m)}(\omega), \tag{3.G.10a}$$

$$\hat{b}_{\rm add}^{(n)\dagger}(\omega) = 2\sqrt{\kappa}G \sum_m K^{(-n+m)*}(-\omega + n\delta)\hat{f}_{\rm in}^{(m)}(\omega), \tag{3.G.10b}$$

where

$$K^{(n)}(\omega) \equiv \chi_{11}^{(n)}(\omega) - \chi_{12}^{(n)}(\omega). \tag{3.G.11}$$

This gives [note the similarity with Eq. (3.3.11)]

$$\hat{b}_{\rm add}^{(n)} = 2\sqrt{\kappa}GJ(\omega - n\delta)\hat{f}_{\rm in}^{(n)}(\omega). \tag{3.G.12}$$

and Hermitian conjugate. The CR correction can be calculated as before and looks very

familiar [cf. Eq. (3.3.23)]

$$S^{\mathrm{CR}}_{X_\delta X_\delta}(\omega) = \kappa\lambda^2 G^2 \left(|J(\omega+\delta)\chi_{\mathrm{c}}(\omega+2\delta)|^2 + |J(-\omega+\delta)\chi_{\mathrm{c}}(-\omega+2\delta)|^2\right). \quad \text{(3.G.13)}$$

The reason why it is so simple is that here $\hat{b}^{(0)}(\omega)$ only couples to $\hat{b}_{\mathrm{in}}$ and not to $\hat{b}^\dagger_{\mathrm{in}}$. This ceases to be the case for $\Delta \neq -\omega_{\mathrm{m}}$, or in parametric squeezing discussed in Appendix 3.I.

3.H Dissipative squeezing in the absence of strong-coupling effects

As a relevant example for how a weakly coupled $\hat{H}_{\mathrm{rest}}$ can lead to effective parameters in the mechanical susceptibility, we consider the weak-coupling version of Appendix 3.G. We place the red-detuned drive on the red sideband $\Delta = -\omega_{\mathrm{m}}$, but allow the other to vary. To second order in $G_\pm$, the effective quantum Langevin equation is (in a frame rotating with frequency δ)

$$\dot{\hat{b}} = -\left[i(\omega_{\mathrm{m,eff}} - \delta) + \frac{\Gamma_{\mathrm{eff}}}{2}\right]\hat{b} + \sqrt{\Gamma_{\mathrm{m}}}\hat{b}_{\mathrm{in}} + \frac{2i\mathcal{G}}{\sqrt{\kappa}}\hat{s}_{\mathrm{in}}, \quad \text{(3.H.1)}$$

with (see Sec. 3.2.3)

$$\Gamma_{\mathrm{eff}} = \Gamma_{\mathrm{m}} + \frac{4}{\kappa}\left(G_-^2 - \frac{G_+^2}{1+4\varepsilon^2/\kappa^2}\right), \quad \text{(3.H.2a)}$$

$$\omega_{\mathrm{m,eff}} = \omega_{\mathrm{m}} + \frac{G_+^2\varepsilon}{(\kappa/2)^2+\varepsilon^2}, \quad \text{(3.H.2b)}$$

$$s_{\mathrm{in}} = \frac{G_- a_{\mathrm{in}} + G_+ a^\dagger_{\mathrm{in}}}{\mathcal{G}}. \quad \text{(3.H.2c)}$$

Here, $\varepsilon \equiv 2(\delta - \omega_{\mathrm{m}})$ and $\mathcal{G} \equiv \sqrt{G_-^2 - G_+^2}$. $\hat{s}_{\mathrm{in}}$ is a Bogoliubov rotation of the original optical bath operators, and is therefore a squeezed vacuum bath with nonzero anomalous correlators, such as $\langle \hat{s}_{\mathrm{in}}(\omega)\hat{s}_{\mathrm{in}}(\omega')\rangle = -2\pi\delta(\omega+\omega')G_+G_-/\mathcal{G}^2$.

The equivalent master equation (generalization of Ref. 121 to general drive detuning δ) is

$$\dot{\hat{\rho}} = -i[(\omega_{\mathrm{m,eff}} - \delta)\hat{b}^\dagger\hat{b}, \hat{\rho}] + \left\{\Gamma_{\mathrm{eff}}(n_{\mathrm{eff}}+1)\mathcal{D}[\hat{b}] + \Gamma_{\mathrm{eff}}n_{\mathrm{eff}}\mathcal{D}[\hat{b}^\dagger] + \frac{4\mathcal{G}^2}{\kappa}\mathcal{D}[\hat{\beta}]\right\}\hat{\rho}, \quad \text{(3.H.3)}$$

where $\mathcal{D}[\hat{a}]\hat{\rho} \equiv \hat{a}\hat{\rho}\hat{a}^\dagger - \frac{1}{2}(\hat{a}^\dagger\hat{a}\hat{\rho} + \hat{\rho}\hat{a}^\dagger\hat{a})$ is the Lindblad superoperator.

In order to include the measurement noise, it is easier to work in the laboratory frame,

where

$$\dot{\hat{b}} = -\left(i\omega_{\mathrm{m,eff}} + \frac{\Gamma_{\mathrm{eff}}}{2}\right)\hat{b} + \sqrt{\Gamma_{\mathrm{m}}}\hat{b}_{\mathrm{in}} + 2\sqrt{\kappa}G\hat{f}_{\mathrm{in}} + \frac{2i\mathcal{G}}{\sqrt{\kappa}}\hat{s}_{\mathrm{in}}. \tag{3.H.4}$$

There is a subtlety here, as the anomalous averages of $\hat{s}_{\mathrm{in}}$, will become rotating in the transition from a rotating frame into the laboratory frame. We can ignore this difficulty, because we are only interested in the correction. Rewriting Eq. (3.H.4) in Fourier components, we find that the only independent nonzero element of the susceptibility matrix is

$$\chi_{11}^{(0)}(\omega) = \chi_{\mathrm{m,eff}}(\omega) \equiv [\Gamma_{\mathrm{eff}}/2 - i(\omega - \omega_{\mathrm{m,eff}})]^{-1}. \tag{3.H.5}$$

We could have obtained this from Eq. (3.G.9) by setting $\mathcal{G} = 0$ (weak coupling) and replacing ω_{m} and Γ_{m} by their modified values. Thus we can use the result Eq. (3.G.13) with $J \to \chi_{\mathrm{m,eff}}$. Therefore, the results in Sec. 3.3 also apply to dissipative squeezing in weak coupling as well, with $\Gamma_{\mathrm{m}} \to \Gamma_{\mathrm{eff}}$ and $\omega_{\mathrm{m}} \to \omega_{\mathrm{m,eff}}$.

Optionally, we can remain in a rotating frame, but that means we have to rotate the added measurement noise to $\hat{\tilde{f}}_{\mathrm{in}} \equiv e^{i\delta t}\hat{f}_{\mathrm{in}}$. This implies $\hat{\tilde{f}}_{\mathrm{in}}^{(n)} = \hat{f}_{\mathrm{in}}^{(n-1)}$. Solving the Langevin equation gives $\chi_{11}^{(0)}(\omega) = [\Gamma_{\mathrm{eff}}/2 - i(\omega - \omega_{\mathrm{m,eff}} + \delta)]^{-1}$. Consulting Eq. (3.G.10), we find that the new set of Fourier components $\hat{\tilde{b}}_{\mathrm{add}}^{(n)}(\omega) = \hat{b}_{\mathrm{add}}^{(n-1)}(\omega)$. It is straightforward to check that in the end $\hat{\tilde{b}}_{\mathrm{add}}(t) = e^{i\delta t}\hat{b}_{\mathrm{add}}(t)$.

This result can be adapted to a wide variety of cases, as long as they can be approximated by coupling the harmonic oscillators to baths only (and potentially modify its effective parameters).

3.I Parametric squeezing

Squeezing is induced naturally in a degenerate parametric amplifier [68]. Whilst it is limited to 3 dB of squeezing, it displays features that we have not seen in the previous Appendices. Here,

$$\hat{H}_{\mathrm{rest}} = \omega_{\mathrm{m}}\hat{b}^\dagger\hat{b} + (\mu\hat{b}^2 e^{2i\omega_{\mathrm{m}}t} + \mathrm{H.c.}), \tag{3.I.1}$$

where μ is the parametric driving strength. Without the BAE measurement ($G = 0$), the quantum Langevin equation is

$$\dot{\hat{b}} = -i\omega_{\mathrm{m}}\hat{b} - i\mu\hat{b}^\dagger e^{-2i\omega_{\mathrm{m}}t} - \frac{\Gamma_{\mathrm{m}}}{2}\hat{b} + \sqrt{\Gamma_{\mathrm{m}}}\hat{b}_{\mathrm{in}}. \tag{3.I.2}$$

In Fourier components,

$$\begin{pmatrix} \chi_{\mathrm{m}}^{-1}(\omega - n\omega_{\mathrm{m}}) & i\mu \\ -i\mu & \chi_{\mathrm{m}}^{-1}(\omega - n\omega_{\mathrm{m}}) \end{pmatrix} \begin{pmatrix} \hat{b}^{(n)}(\omega) \\ \hat{b}^{(n+2)\dagger}(\omega) \end{pmatrix} = \sqrt{\Gamma_{\mathrm{m}}} \begin{pmatrix} \delta_{n,0}\hat{b}_{\mathrm{in}} \\ \delta_{n,2}\hat{b}_{\mathrm{in}}^{\dagger} \end{pmatrix}, \tag{3.I.3}$$

where $\chi_{\mathrm{m}}(\omega) \equiv [\Gamma_{\mathrm{m}}/2 - i(\omega - \omega_{\mathrm{m}})]^{-1}$. Inverting leads to

$$\begin{pmatrix} \hat{b}^{(n)} \\ \hat{b}^{(n+2)\dagger} \end{pmatrix} = A(\omega - n\omega_{\mathrm{m}}) \begin{pmatrix} \chi_{\mathrm{m}}^{-1}(\omega - n\omega_{\mathrm{m}}) & -i\mu \\ i\mu & \chi_{\mathrm{m}}^{-1}(\omega - n\omega_{\mathrm{m}}) \end{pmatrix} \begin{pmatrix} \sqrt{\Gamma_{\mathrm{m}}}\delta_{n,0}\hat{b}_{\mathrm{in}} \\ \sqrt{\Gamma_{\mathrm{m}}}\delta_{n,2}\hat{b}_{\mathrm{in}}^{\dagger} \end{pmatrix}, \tag{3.I.4}$$

where

$$A(\omega) \equiv \left[\chi_{\mathrm{m}}^{-2}(\omega - n\omega_{\mathrm{m}}) - \mu^2\right]^{-1}. \tag{3.I.5}$$

It is again enough to consider only one block (the other nonzero block is the Hermitian conjugate)

$$\begin{pmatrix} \hat{b}^{(0)}(\omega) \\ \hat{b}^{(2)\dagger}(\omega) \end{pmatrix} = A(\omega) \begin{pmatrix} \chi_{\mathrm{m}}^{-1}(\omega) & -i\mu \\ i\mu & \chi_{\mathrm{m}}^{-1}(\omega) \end{pmatrix} \begin{pmatrix} \sqrt{\Gamma_{\mathrm{m}}}\hat{b}_{\mathrm{in}} \\ 0 \end{pmatrix}. \tag{3.I.6}$$

To make the discussion as simple as possible, we choose $\delta = \omega_{\mathrm{m}}$ for the measurement scheme. Then the same analysis as above can be applied to obtain

$$\chi_{11}^{(0)}(\omega) = A(\omega)\chi_{\mathrm{m}}^{-1}(\omega), \tag{3.I.7a}$$

$$\chi_{12}^{(2)}(\omega - 2\omega_{\mathrm{m}}) = -i\mu A(\omega), \tag{3.I.7b}$$

$$\chi_{12}^{(-2)*}(-\omega + 2\omega_{\mathrm{m}}) = i\mu A^*(\omega). \tag{3.I.7c}$$

In order to evaluate the added noise due to the BAE measurement, we have to add the noise Eq. (3.3.12) and use Eq. (3.G.10). We find (λ labels terms with CR origin)

$$\hat{b}_{\mathrm{add}}^{(n)}(\omega) = i\sqrt{\kappa}G\chi_{\mathrm{c}}(\omega)\hat{I}_{\mathrm{in}}(\omega) \begin{cases} i\mu A(\omega - \delta) & \text{if} n = 3 \\ i\mu\lambda A(\omega + \delta) + A(\omega - \delta)\chi_{\mathrm{m}}^{-1}(\omega - \delta) & \text{if} n = 1 \\ \lambda A(\omega + \delta)\chi_{\mathrm{m}}^{-1}(\omega + \delta) & \text{if} n = -1 \end{cases} \tag{3.I.8}$$

This reverts to Eq. (3.3.11) when we set $\mu = 0$. Using Eq. (3.3.20) with the spectra calculated from Eq. (3.I.8), we obtain the correction to the quadrature spectrum. The resulting spectra have terms rotating at multiples of δ. They could be measured by coupling to another suitably driven cavity mode (cf. Sec. 3.2.8), but tend to be very small.

3.J Two-mode BAE

In this section, we consider another recently experimentally demonstrated QND scheme [143, 144]. The goal here is to measure a collective quadrature of two mechanical oscillators, in order to eventually measure both quadratures of an external force with the same device. Whilst the overall theory is more general [149], in the specific experiment we consider here, both mechanical resonators couple to the same cavity and the problem has the Hamiltonian [143]

$$\begin{aligned}\hat{H} = &(\omega_{\mathrm{m}} + \Omega)\hat{b}_1^\dagger \hat{b}_1 + (\omega_{\mathrm{m}} - \Omega)\hat{b}_2^\dagger \hat{b}_2 + \omega_{\mathrm{cav}}\hat{a}^\dagger \hat{a} \\ &+ g_1(\hat{b}_1 + \hat{b}_1^\dagger)\hat{a}^\dagger \hat{a} + g_2(\hat{b}_2 + \hat{b}_2^\dagger)\hat{a}^\dagger \hat{a} + \hat{H}_{\mathrm{drive}} + \hat{H}_{\mathrm{diss}}\end{aligned} \tag{3.J.1}$$

Note that in Ref. 143 the mechanical oscillators have annihilation operators a and b, and the cavity $\hat{c}$, whereas here, they are $\hat{b}_1, \hat{b}_2$, and $\hat{a}$, respectively. As before, periodic driving leads to a coherent state

$$\hat{a} \to 2\cos(\omega_{\mathrm{m}} t)\bar{a} + \delta\hat{a}, \tag{3.J.2}$$

where $\bar{a}$ is a real number, and $\langle \delta\hat{a} \rangle = 0$ (and note we will again rename $\delta\hat{a} \to \hat{a}$ below).

Our generic solution is applicable, because Eq. (3.3.33) is fulfilled after linearizing, no matter which of the oscillators we put into H_{rest}. For example, we could chose

$$\hat{H}_{\mathrm{rest},1} = (\omega_{\mathrm{m}} + \Omega)\hat{b}_1^\dagger \hat{b}_1 + 2g_1 \cos(\omega_{\mathrm{m}} t)\bar{a}(\hat{b}_1 + \hat{b}_1^\dagger)(\hat{a} + \hat{a}^\dagger), \tag{3.J.3}$$

but the choice with $1 \to 2$ is equally valid. Our result for the backaction on the mechanical oscillators [all of Sec. 3.3, particularly Eq. (3.3.23)] thus applies to both resonators individually.

The correction to the cavity spectrum is slightly more tricky to find, since the fluctuations in the two resonators are correlated, leading to cross terms. Instead of Eq. (3.3.2a) we have

$$\dot{\hat{a}} = -\frac{\kappa}{2}\hat{a} + \sqrt{\kappa}\hat{a}_{\mathrm{in}} + 2i\cos(\omega_{\mathrm{m}} t)\left(G_1 \hat{x}_1 + G_2 \hat{x}_2\right), \tag{3.J.4}$$

where $\hat{x}_{1,2}$ are the position operators for the two oscillators, and $G_{1,2} \equiv g_{1,2}\bar{a}$. $\hat{x}_{1,2}$ are both given through Eq. (3.3.11), but with the respective parameters for each resonator.

To calculate the optical spectrum, first note that there is a cross correlation. For $m, n \in \{1, -1\}$, we have

$$\int \frac{d\omega'}{2\pi} \langle \hat{x}_1^{(m)}(\omega + m\delta)\hat{x}_2^{(n)}(\omega') \rangle = -\kappa G_1 G_2 |\chi_{\mathrm{c}}(\omega + m\delta)|^2 \chi_{x_1}(\omega)\chi_{x_2}(-\omega - (m+n)\delta), \tag{3.J.5}$$

with $\chi_{x_{1,2}}$ defined analogously to χ_x in Appendix 3.M. Then $S^{(0)}_{a^\dagger a}$ contains two copies of Eq. (3.3.24) (one for each resonator), in addition to

$$4G^2|\chi_\mathrm{c}(\omega)|^2 \,\mathrm{Re}\left[S^{(0)}_{x_1x_2}(\omega-\delta)+S^{(0)}_{x_1x_2}(\omega+\delta)+S^{(2)}_{x_1x_2}(\omega-\delta)+S^{(-2)}_{x_1x_2}(\omega+\delta)\right], \tag{3.J.6}$$

where $S_{x_1x_2}$ are given through Eqs. (2.5.7) and (3.J.5). Here, we used the property $[S^{(n)}_{AB}(\omega)]^\dagger = S^{(-n)}_{B^\dagger A^\dagger}(\omega+n\delta)$ derived in Eq. (2.8.5).

This demonstrates that our technique can also be applied for multiple modes coupled to the cavity, as long as $[\hat{H}_\mathrm{rest}, \hat{I}] = 0$.

3.K Integration of the main peak

One goal of a BAE measurement of a mechanical oscillator quadrature is to extract the quadrature variance. We show that the weight of the main peak of the optical spectrum

$$\frac{S^{(0)}_{a^\dagger a}(\omega)}{G^2|\chi_\mathrm{c}(\omega)|^2} = S^{(0)}_{xx}(\omega-\delta)+S^{(0)}_{xx}(\omega+\delta)+S^{(2)}_{xx}(\omega-\delta)+S^{(-2)}_{xx}(\omega+\delta) \tag{3.K.1}$$

is a good measure for the quadrature variance. The weight of its middle peak at $\omega = 0$ is

$$W = \int_{-\infty}^{\infty}\frac{d\omega}{2\pi}S^{(0)}_{xx}(\omega) + 2\,\mathrm{Re}[S^{(2)}_{xx}(\omega)]. \tag{3.K.2}$$

Equation (3.K.2) can be evaluated with the formulae in Appendix 3.M. Given the output spectrum $\kappa S^{(0)}_{a^\dagger a}(\omega)$, the weight can be approximated by integrating from $-\omega_\mathrm{m}$ to ω_m

$$W \approx \langle \hat{X}^2_\mathrm{meas}\rangle \equiv \int_{-\omega_\mathrm{m}}^{\omega_\mathrm{m}}\frac{d\omega}{2\pi}\frac{S^{(0)}_{a^\dagger_\mathrm{out}a_\mathrm{out}}(\omega)}{\kappa G^2|\chi_\mathrm{c}(\omega)|^2}. \tag{3.K.3}$$

3.L Full quadrature spectrum

Here we present the full expression for the spectrum of the rotating quadrature X_δ

$$\begin{aligned}
S^{(0)}_{X_\delta X_\delta}(\omega) = {}& \Gamma_\mathrm{m}\left(|\chi_\mathrm{m}(\omega+\delta)|^2(n_\mathrm{th}+1)+|\chi_\mathrm{m}(-\omega+\delta)|^2 n_\mathrm{th}\right)\\
&+\kappa G^2\left\{-2|\chi_\mathrm{c}(\omega)|^2\,\mathrm{Re}\left[\chi_\mathrm{m}(\omega+\delta)\chi_\mathrm{m}(-\omega+\delta)\right]\right.\\
&+|\chi_\mathrm{m}(\omega+\delta)|^2\left(|\chi_\mathrm{c}(\omega)|^2+|\chi_\mathrm{c}(\omega+2\delta)|^2\right)\\
&\left.+\,|\chi_\mathrm{m}(-\omega+\delta)|^2\left(|\chi_\mathrm{c}(\omega-2\delta)|^2+|\chi_\mathrm{c}(\omega)|^2\right)\right\}.
\end{aligned} \tag{3.L.1}$$

It contains a part due to the thermal bath of the oscillator (terms with a Γ_m) and an optical part (terms with κ). If $\delta = \omega_\mathrm{m}$, $\chi_\mathrm{m}(-\omega+\delta) = \chi_\mathrm{m}^*(\omega+\delta)$, and the negative term in the curly brackets cancels two resonant contributions in the third and fourth line. This cancellation makes the measurement BAE in RWA. The two terms left over make sidebands at $\pm 2\omega_\mathrm{m}$ appear. Inverting the sign of the first term in curly brackets would lead to the spectrum of the conjugate quadrature $S^{(0)}_{P_\delta P_\delta}(\omega)$, which gets all the BA in RWA. The BA due to CR terms is the same in both. If the oscillator is weakly coupled to other degrees of freedom, this formula is still approximately correct, using effective parameters Γ_eff, $\omega_\mathrm{m,eff}$ and n_eff.

3.M Optical spectrum

In this section we outline the derivation of the optical spectrum. We use the expression given in the main text (3.3.24). For $\hat{H}_\mathrm{rest} = 0$, the necessary correlators are

$$\int \frac{d\omega'}{2\pi} \langle \hat{x}^{(0)}(\omega)\hat{x}^{(0)}(\omega')\rangle = \Gamma_\mathrm{m}\left[|\chi_\mathrm{m}(-\omega)|^2 n_\mathrm{th} + |\chi_\mathrm{m}(\omega)|^2(n_\mathrm{th}+1)\right], \tag{3.M.1}$$

and for $m, n \in \{1, -1\}$

$$\int \frac{d\omega'}{2\pi} \langle \hat{x}^{(m)}(\omega+m\delta)\hat{x}^{(n)}(\omega')\rangle = -\kappa G^2 |\chi_\mathrm{c}(\omega+m\delta)|^2 \chi_x(\omega)\chi_x(-\omega-(m+n)\delta), \tag{3.M.2}$$

where $\chi_x(\omega) \equiv \chi_\mathrm{m}(\omega) - \lambda\chi_\mathrm{m}^*(-\omega)$. This gives

$$\begin{aligned} S^{(0)}_{xx}(\omega) &= \Gamma_\mathrm{m}\left[|\chi_\mathrm{m}(-\omega)|^2 n_\mathrm{th} + |\chi_\mathrm{m}(\omega)|^2(n_\mathrm{th}+1)\right] \\ &\quad + \kappa G^2\left(|\chi_x(-\omega)|^2|\chi_\mathrm{c}(\omega+\delta)|^2 + |\chi_x(\omega)|^2|\chi_\mathrm{c}(\omega-\delta)|^2\right), \end{aligned} \tag{3.M.3a}$$

$$S^{(2)}_{xx}(\omega) = -\kappa G^2 |\chi_\mathrm{c}(\omega+\delta)|^2 \chi_x^*(-\omega)\chi_x^*(\omega+2\delta), \tag{3.M.3b}$$

$$S^{(-2)}_{xx}(\omega) = -\kappa G^2 |\chi_\mathrm{c}(\omega-\delta)|^2 \chi_x(\omega)\chi_x(-\omega+2\delta), \tag{3.M.3c}$$

whence $S^{(0)}_{a^\dagger a}(\omega)$ can be constructed, using [cf. Eq. (3.3.24)]

$$\begin{aligned} S^{(n)}_{a^\dagger a}(\omega) &= G^2\chi_\mathrm{c}(\omega)\chi_\mathrm{c}^*(\omega+n\delta) \\ &\quad \times \left[S^{(n)}_{xx}(\omega-\delta) + S^{(n)}_{xx}(\omega+\delta) + S^{(n+2)}_{xx}(\omega-\delta) + S^{(n-2)}_{xx}(\omega+\delta)\right]. \end{aligned} \tag{3.M.4}$$

Part II

Nonreciprocity in optomechanics and beyond

4 | Optomechanical isolator

Nonreciprocal transmission and amplification of electromagnetic signals are essential to communication and signal processing, necessary to minimize the noise entering communication channels or sensitive devices [150], and generally useful to mitigate spurious reflections, interference, and interactions. Previous implementations of nonreciprocal devices have used the Faraday effect in ferrite materials [151–153], or other magneto-optical materials [154–157], optical nonlinearities [158–160], temporal modulation [161–166], Brillouin scattering [167, 168], or polarization-dependent scattering off an atom spin [169].

Taking a step back, we can contemplate the basic requirements for nonreciprocal transmission through a system. One of the most fundamental nonreciprocal devices is the *isolator*, a linear two-port device that allows signals to pass only in one direction. One can show on general grounds that this requires at least a broken *Lorentz symmetry* [170]. A putative isolator therefore has to either break time-reversal symmetry through magneto-optical effects [151–157], through nonlinearities [158–160, 167–169], or employ temporal modulation [161–166], although these classes are not mutually exclusive, and many of the cited examples fall in more than one category. For example, temporal modulation usually results from pumping some sort of nonlinearity. The optomechanical devices discussed here fall in the last class. The original optomechanical Hamiltonian is nonlinear, but as a result of the applied pumps, the effective description governing small fluctuations on top of the pumps are governed by time-dependent linear equations of motion.

Another distinction we can make is between *active* and *passive* devices. Using magneto-optical effects yields passive nonreciprocal devices, which do not consume energy during operation, while time-dependent Hamiltonians can only be implemented through some form of driving, which therefore yields active nonreciprocal devices. Both methods have advantages and disadvantages, as passive, magnetic materials tend to result in larger devices incompatible with superconducting chips, whereas active devices require drives and thus are prone to heat up. Conventional ferrite-based nonreciprocal devices have reached great maturity, but rely on magnetic fields and are challenging to integrate in superconducting circuits, which in recent years have been established as a promising platform for quantum

technologies [171]. Yet, isolation from noisy readout electronics is particularly problematic for quantum systems, providing strong incentive to find more suitable implementations of nonreciprocal devices [172–183].

Optomechanics can be used to generate synthetic magnetic fields for sound and light, which has led to an array of theoretical works predicting classical gauge fields [184] and topological phases [185–188] in optomechanical arrays. In recent theoretical work, Ranzani and Aumentado [135, 189] analyzed general conditions for nonreciprocity in parametrically coupled systems, and showed that nonreciprocity arises due to dissipation in ancillary modes and multi-path interference. Following this approach, nonreciprocity has recently been demonstrated in Josephson junction-based microwave circuits [183, 190]. Metelmann and Clerk [191] have shown that any coherent interaction (including the important subset of linear coupling) can be made directional by balancing it with a dissipative process. Indeed, this insight led to a demonstration of nonreciprocity using optomechanics in the optical domain [52], and theoretical investigations into minimal implementations of directional amplifiers [192].

Previous experimental realizations and theoretical proposals for nonreciprocity in multi-mode systems rely on a direct, coherent coupling between the electromagnetic input and output modes. While possible in the optical regime using optomechanical crystals [52], such a direct coupling has proven to be difficult to implement in the microwave regime, requiring alternative implementations, which are the subject of this chapter.

This chapter contains our work on an optomechanical isolator realized in the *optomechanical plaquette* [3], which is an optomechanical system comprising two cavity modes coupled via two intermediary mechanical resonator modes. Tian and Li [193] have studied a related system theoretically, whereas Peterson *et al.* [53] have independently come up with the same experimental design. The key innovation in the optomechanical plaquette is that the coupling of its modes is purely optomechanical, doing away with the requirement of directly coupled cavity modes. As there are two transmission paths between the cavity modes, interference occurs. As we will elucidate below, due to the driven-dissipative nature of the system, the interference generically happens in a nonreciprocal way and can be tuned to give complete isolation. The discussion in this chapter is based on our analysis in Refs 3 and 4, and is supported by the experimental data taken by Nathan Bernier, Daniel Tóth, and Alexey Feofanov originally published as Ref. 3.

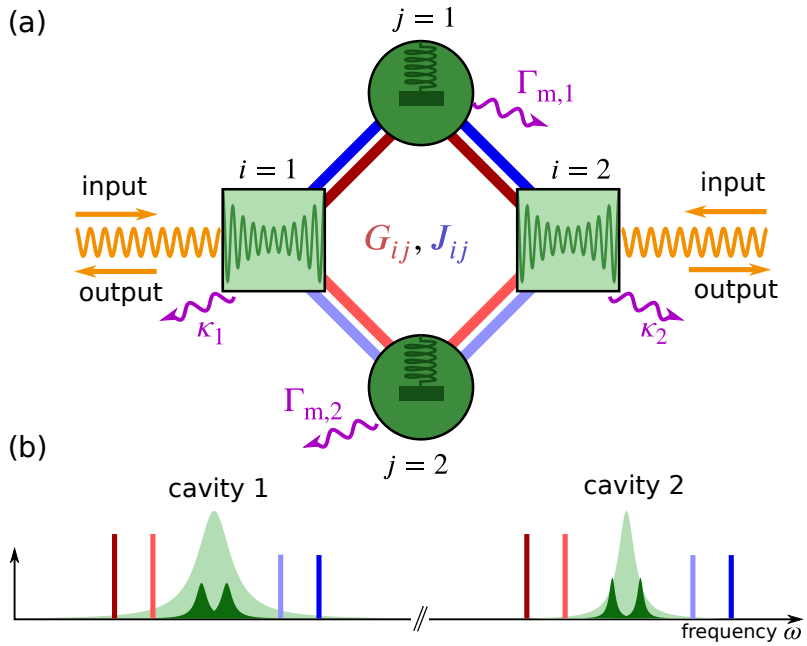

Figure 4.1: The optomechanical plaquette. (a) Schematic of all possible interactions in the optomechanical plaquette comprising two mechanical resonators (round, dark green) and two cavities (square, light green). The cavities [light green Lorentzians in (b)] are driven by up to eight tones, placed at frequencies $\omega_{c,i} \pm (\omega_{m,j} + \delta_j)$, as illustrated in (b). They induce hopping and two-mode squeezing interactions of strength G_{ij}, J_{ij} (cf. Sec. 1.5) denoted in (a) by red and blue lines connecting the modes, which is captured by the time-independent Hamiltonian (4.1.5).

4.1 The optomechanical plaquette

The optomechanical Hamiltonian for the plaquette (Fig. 4.1) is given by $(\hbar = 1)$

$$\hat{H}_{\rm OM} = \sum_{i=1}^{2} \left[\omega_{c,i} \hat{a}_i^\dagger \hat{a}_i + \omega_{m,i} \hat{b}_i^\dagger \hat{b}_i - \sum_{j=1}^{2} g_{0,ij} \hat{a}_i^\dagger \hat{a}_i (\hat{b}_j + \hat{b}_j^\dagger) \right], \tag{4.1.1}$$

where $g_{0,ij}$ denotes the bare, single-photon coupling between the ith cavity mode and the jth mechanical resonator mode. Each cavity is driven by up to four tones, at frequencies $\omega_{c,i} \pm (\omega_{m,j} + \delta_j)$, i.e., on the red and blue motional sidebands due to the mechanical resonators, as illustrated in Fig. 4.1(b). The drives generate coherent states in the cavities, such that the annihilation operators for the cavity modes can be written as a sum of coherent part $\bar{a}_i$ and fluctuations $\delta\hat{a}_i$

$$\hat{a}_i = e^{-i\omega_{c,i}t}[\bar{a}_i(t) + \delta\hat{a}_i], \tag{4.1.2}$$

where $\bar{a}_i(t)$ contains several coherent states corresponding to several drives, as detailed below, and $\delta\hat{a}_i$ are bosonic operator with zero mean describing the fluctuations around the

mean field. In the following, we will rename $\delta\hat{a}_i \to \hat{a}_i$ for a cleaner notation. Going into a rotating frame with respect to

$$\hat{H}_0 = \sum_j \left(\omega_{\mathrm{m},j} + \delta_j\right) \hat{b}_j^\dagger \hat{b}_j + \sum_i \omega_{\mathrm{c},i} \hat{a}_i^\dagger \hat{a}_i, \tag{4.1.3}$$

and using Eq. (4.1.2), we obtain the linearized Hamiltonian

$$\hat{H}_{\text{lin}} = -\sum_j \delta_j \hat{b}_j^\dagger \hat{b}_j - \sum_{ij} g_{0,ij} \left\{ \bar{a}_i^*(t) a_i \left[\hat{b}_j e^{-i(\omega_{\mathrm{m},j}+\delta_j)t} + \hat{b}_j^\dagger e^{i(\omega_{\mathrm{m},j}+\delta_j)t} \right] + \text{H.c.} \right\}. \tag{4.1.4}$$

Collecting only time-independent (resonant) terms, we arrive at the Hamiltonian

$$\hat{H}_{\text{sys}} = -\sum_{i=1}^{2} \delta_i \hat{b}_i^\dagger \hat{b}_i - \sum_{i,j=1}^{2} \hat{a}_i^\dagger (G_{ij} \hat{b}_j + J_{ij} \hat{b}_j^\dagger) + \text{H.c.}, \tag{4.1.5}$$

where $\hat{a}_i$ ($\hat{b}_i$) is the annihilation operator for the ith cavity mode (mechanical resonator), $G_{ij} = \bar{a}_{ij-} g_{0,ij}$ and $J_{ij} = \bar{a}_{ij+} g_{0,ij}$ are field-enhanced optomechanical coupling strengths, $\bar{a}_{ij\pm}$ is the amplitude of the coherent state produced in cavity i due to a pump at frequency $\omega_{\mathrm{c},i} \pm (\omega_{\mathrm{m},j} + \delta_j)$, and $g_{0,ij}$ are the vacuum optomechanical couplings. Since the couplings G, J depend on the pumps, their amplitude and phase can be controlled. The interactions are represented in Figs. 4.1(a), 5.1(a), 5.2(a) as red (G) and blue (J) lines. In the following, we will mainly discuss the time-independent Hamiltonian (4.1.5) for simplicity. The rotating terms present an important correction, which we will discuss later.

We describe the system with input-output theory (introduced in Sec. 1.2.2) and quantum Langevin equations (Sec. 1.2) [24, 65, 67]

$$\hat{b}_j(\omega) = \chi_{\mathrm{m},j}(\omega) \left\{ i \sum_{i=1}^{2} \left[\hat{a}_i(\omega) G_{ij}^* + \hat{a}_i^\dagger(\omega) J_{ij} \right] + \sqrt{\Gamma_{\mathrm{m},j}} \hat{b}_{j,\text{in}}(\omega) \right\}, \tag{4.1.6a}$$

$$\hat{a}_i(\omega) = \chi_{\mathrm{c},i}(\omega) \left\{ i \sum_{j=1}^{2} \left[G_{ij} \hat{b}_j(\omega) + J_{ij} b_j^\dagger(\omega) \right] + \sqrt{\kappa_i} \hat{a}_{i,\text{in}}(\omega) \right\} \tag{4.1.6b}$$

where the susceptibilities are given through

$$\chi_{\mathrm{m},j}(\omega) = [\Gamma_{\mathrm{m},j}/2 - i(\omega + \delta_j)]^{-1}, \quad \chi_{\mathrm{c},i}(\omega) = (\kappa_i/2 - i\omega)^{-1}, \tag{4.1.7}$$

with mechanical (cavity) dissipation rates $\Gamma_{\mathrm{m},j}$ (κ_i). The mechanical (cavity) input noise operators $\hat{b}_{j,\text{in}}$ ($\hat{a}_{i,\text{in}}$) are assumed to have bosonic commutation relations and delta-correlated noise $\langle \hat{b}_{i,\text{in}}^\dagger(t) \hat{b}_{j,\text{in}}(t') \rangle = \delta_{ij} n_{\mathrm{m},i} \delta(t - t')$, $\langle \hat{a}_{i,\text{in}}^\dagger(t) \hat{a}_{j,\text{in}}(t') \rangle = \delta_{ij} n_{\mathrm{c},i} \delta(t - t')$. In order to

obtain a description only in terms of the microwave modes, we eliminate the mechanical degrees of freedom in Eq. (4.1.6b) with Eq. (4.1.6a), which yields

$$\sum_{j=1}^{2}[\chi_{\mathrm{c},i}^{-1}(\omega)\delta_{ij} + i\mathsf{T}_{ij}(\omega)]\hat{\mathbf{A}}_j(\omega) = \sqrt{\kappa_i}\hat{\mathbf{A}}_{i,\mathrm{in}}(\omega), \tag{4.1.8}$$

where the susceptibility $\chi_{\mathrm{c},i}(\omega) = [\kappa_i/2 - i\omega]^{-1}$, $\hat{\mathbf{A}}_{j(,\mathrm{in})} = (\hat{a}_{j(,\mathrm{in})}, \hat{a}^\dagger_{j(,\mathrm{in})})^T$, and each $i\mathsf{T}_{ij}$ is a 2-by-2 matrix

$$i\mathsf{T}_{ij}(\omega) = \sum_{k=1}^{2}\sigma_z\left[\chi_{\mathrm{m},k}(\omega)\begin{pmatrix} G_{ik}G_{jk}^* & G_{ik}J_{jk} \\ J_{ik}^*G_{jk}^* & J_{ik}^*J_{jk}\end{pmatrix} - \chi_{\mathrm{m},k}^*(-\omega)\begin{pmatrix} J_{ik}J_{jk}^* & J_{ik}G_{jk} \\ G_{ik}^*J_{jk}^* & G_{ik}^*G_{jk}\end{pmatrix}\right], \tag{4.1.9}$$

where $\sigma_z = \mathrm{diag}(1,-1)$ and $\chi_{\mathrm{m},i}(\omega) = [\Gamma_{\mathrm{m},i}/2 - i(\omega+\delta_i)]^{-1}$. $i\mathsf{T}_{ii}$ is akin to a self-energy for mode $\hat{\mathbf{A}}_i$, whereas $i\mathsf{T}_{ij}$ for $i \neq j$ is a matrix of coupling strengths between the modes. Since the interaction is mediated by mechanical resonators, their susceptibility $\chi_{\mathrm{m},i}$ appears in the coupling matrix. The coupling matrices $i\mathsf{T}_{ij}$, defined in Eq. (4.1.9), exhibit the symmetry

$$\mathsf{T}_{ij}(\omega) = \sigma_1\mathsf{T}_{ij}^*(-\omega)\sigma_1, \tag{4.1.10}$$

which arises as we are using both annihilation operators and their Hermitian conjugates in the description of the system. The minus sign in the frequency is due to our choice of Fourier transform, $[\hat{a}_i(\omega)]^\dagger = \hat{a}_i^\dagger(-\omega)$. This is the only symmetry, since we know that there are 8 free complex parameters (the 8 driving amplitudes), and T has $4^2 = 16$ complex entries.

Using the input-output relation $\hat{a}_{i,\mathrm{out}} = \hat{a}_{i,\mathrm{in}} - \sqrt{\kappa_i}\hat{a}_i$ [Eq. (1.2.16)], the optical scattering matrix that relates the inputs $(\hat{a}_{1,\mathrm{in}}, \hat{a}^\dagger_{1,\mathrm{in}}, \hat{a}_{2,\mathrm{in}}, \hat{a}^\dagger_{2,\mathrm{in}})$ to the outputs $(\hat{a}_{1,\mathrm{out}}, \hat{a}^\dagger_{1,\mathrm{out}}, \hat{a}_{2,\mathrm{out}}, \hat{a}^\dagger_{2,\mathrm{out}})$ is given through

$$\mathsf{S}_{\mathrm{optical}}(\omega) = \mathbb{1}_4 - \mathsf{L}\chi(\omega)\mathsf{L}, \tag{4.1.11}$$

where $\mathsf{L} = \mathrm{diag}(\sqrt{\kappa_1}, \sqrt{\kappa_1}, \sqrt{\kappa_2}, \sqrt{\kappa_2})$, and

$$[\chi(\omega)]^{-1} = \begin{pmatrix} \chi_{\mathrm{c},1}^{-1}(\omega)\mathbb{1}_2 + i\mathsf{T}_{11}(\omega) & i\mathsf{T}_{12}(\omega) \\ i\mathsf{T}_{21}(\omega) & \chi_{\mathrm{c},2}^{-1}(\omega)\mathbb{1}_2 + i\mathsf{T}_{22}(\omega)\end{pmatrix}. \tag{4.1.12}$$

We say the system is nonreciprocal if the moduli of forward and reverse scattering amplitudes differ, which occurs if $|\mathsf{T}_{12}| \neq |\mathsf{T}_{21}|$.This definition is slightly unusual, as it neglects differences in phases. In electrical engineering, a gyrator, which is a two-port device with the scattering matrix $S = -i\sigma_y$, i.e., where $S_{12} = -S_{21} = 1$, is usually considered the basic building block for nonreciprocal devices. Here, in contrast, the phase difference

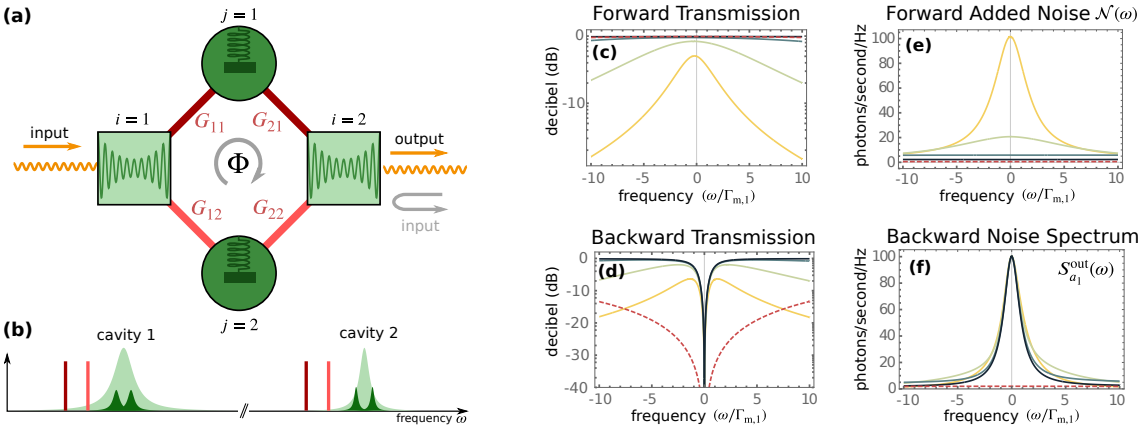

Figure 4.2: The isolator. (a) Model. Pumping an optomechanical system comprising two cavities and two mechanical resonators with four red-detuned tones gives rise to a bilinear Hamiltonian describing hopping around a plaquette with an overall phase Φ. **(b)** Pump setup. Both cavities are pumped by two tones, red-detuned by the mechanical resonator frequencies. In **(c-f)** we plot forward transmission, reverse transmission [obtained from Eq. (4.1.11)], added noise [defined in Eq. (5.1.11)], and the output noise fluctuation spectrum of cavity 1, all as functions of frequency in units of $\Gamma_{\mathrm{m},1}$, for cooperativities $\mathcal{C}_1 = \{1, 3, 10, 30\}$, $\mathcal{C}_2 = \mathcal{C}_1$ (yellow to black, or light to dark). Parameters are $\kappa_2/\kappa_1 = 0.7, \Gamma_{\mathrm{m},1}/\kappa_1 = 10^{-2}, \Gamma_{\mathrm{m},2}/\Gamma_{\mathrm{m},1} = 0.8$, thermal occupation of the mechanical resonators $n_{\mathrm{m},1} = n_{\mathrm{m},2} = 100$, and cavities $n_{\mathrm{c},1} = n_{\mathrm{c},2} = 0$. Depending on parameters, external sideband cooling with an auxiliary mode can achieve $n_{\mathrm{m},j} \approx 0$, without negatively affecting transmission or isolation properties, as discussed below. The red (dashed) curve in each plot illustrates this case, with $\mathcal{C}_1 = 30$ and effective parameters $n_{\mathrm{eff},i} = n_{\mathrm{m},i}(\Gamma_{\mathrm{m},i}/\Gamma_{\mathrm{eff},i}), \Gamma_{\mathrm{eff},i} = 50\Gamma_{\mathrm{m},i}$.

is not well defined, as the modes that are related via the scattering matrix have different frequencies. The time-independent description we use here is in a rotating frame with some arbitrary origin in time. Choosing a different origin in time changes the relative phase of forward and backward scattering element. In order to obtain an isolator, one has to add interference (the phase between two scattering paths is independent from the choice of origin of time) and dissipation [194].

Looking for instance at the top left elements $[iT_{12}]_{11}, [iT_{21}]_{11}$, we see that nonreciprocity arises because flipping direction $(1 \leftrightarrow 2)$ conjugates the complex couplings, but leaves the mechanical susceptibility unchanged. Nonreciprocity can also be understood in the framework presented in Ref. 191, which we discuss in Sec. 5.4 below.

4.2 The optomechanical isolator

In the absence of amplifier terms, $\mathsf{J} = 0$, the expressions in the previous section simplify substantially. In particular, the matrices $i\mathsf{T}_{ij}$ that connect the cavity modes become

diagonal, as there is no mixing of annihilation and creation operators. Thus, we can just consider the annihilation operators alone, which means that Eq. (4.1.8) turns into

$$\left[\begin{pmatrix}\chi_{\mathrm{c},1}^{-1}(\omega) & 0\\ 0 & \chi_{\mathrm{c},2}^{-1}(\omega)\end{pmatrix}+\sum_k \chi_{\mathrm{m},k}(\omega)\begin{pmatrix}G_{1k}G_{1k}^* & G_{1k}G_{2k}^*\\ G_{2k}G_{1k}^* & G_{2k}G_{2k}^*\end{pmatrix}\right]\begin{pmatrix}\hat{a}_1(\omega)\\ \hat{a}_2(\omega)\end{pmatrix}=\begin{pmatrix}\sqrt{\kappa_1}\hat{a}_{\mathrm{in},1}(\omega)\\ \sqrt{\kappa_2}\hat{a}_{\mathrm{in},2}(\omega)\end{pmatrix}. \tag{4.2.1}$$

From the scattering matrix Eq. (4.1.11), we can directly calculate the ratio of forward and backward transmission,

$$\frac{S_{12}(\omega)}{S_{21}(\omega)}=\frac{G_{11}\chi_{\mathrm{m},1}(\omega)G_{21}^*+G_{12}\chi_{\mathrm{m},2}(\omega)G_{22}^*}{G_{11}^*\chi_{\mathrm{m},1}(\omega)G_{21}+G_{12}^*\chi_{\mathrm{m},2}(\omega)G_{22}}=e^{-i\Phi}\frac{\Gamma_{\mathrm{m},1}\chi_{\mathrm{m},1}(\omega)+\Gamma_{\mathrm{m},2}\chi_{\mathrm{m},2}(\omega)e^{i\Phi}}{\Gamma_{\mathrm{m},1}\chi_{\mathrm{m},1}(\omega)+\Gamma_{\mathrm{m},2}\chi_{\mathrm{m},2}(\omega)e^{-i\Phi}}, \tag{4.2.2}$$

where in the second equality we chose to parametrize the coupling strengths G_{ij} in the following way

$$\mathsf{G}=\frac{1}{2}\begin{pmatrix}e^{-i\Phi/2}\sqrt{\mathcal{C}_1\Gamma_{\mathrm{m},1}\kappa_1} & e^{i\Phi/2}\sqrt{\mathcal{C}_1\Gamma_{\mathrm{m},2}\kappa_1}\\ \sqrt{\mathcal{C}_2\Gamma_{\mathrm{m},1}\kappa_2} & \sqrt{\mathcal{C}_2\Gamma_{\mathrm{m},2}\kappa_2}\end{pmatrix}, \tag{4.2.3}$$

introducing the cooperativities $\mathcal{C}_{1,2}$. In principle, there are four independent phases in the coupling $\theta_{ij}\equiv\arg(G_{1i})$. However, only the overall relative "plaquette phase" $\Phi\equiv\theta_{11}+\theta_{21}-\theta_{12}-\theta_{22}$ is physically relevant, which we chose to distribute onto G_{11} and G_{12}. We have also allowed for only two independent cooperativities $\mathcal{C}_{1,2}$ instead of one for each drive. While not strictly necessary, this condition makes the equations more symmetric and simplifies the calculation without affecting the result.

The nominator of Eq. (4.2.2) describes scattering from $2\to1$, whereas the denominator describes the reverse process. Equation (4.2.2) lends itself to a concrete interpretation of the physical origin of nonreciprocal transmission. From a comparison of nominator and denominator it is clear that the difference between forwards and backwards transmission is a conjugation of the coupling strengths G_{ij}, while the mechanical susceptibilities remain unchanged. The reason is that forward and backward scattering are related via time-reversal, which conjugates the phases associated to coherent evolution. In a more concrete picture, creating a photon and destroying a phonon is associated with absorbing a photon from the external drive, whereas in the reverse process a pump photon is created. When an excitation hops from one cavity to the other, this process occurs twice, "connecting" the two pumps, such that their phase relation becomes imprinted on the overall amplitude for this process. In contrast, the mechanical susceptibility depends only on the frequency ω, independent of the direction of the scattering process. In other words, the susceptibility is not affected by time-reversal.

If we demand isolation of cavity 1 from cavity 2 on resonance ($\omega=0$), a necessary requirement is that the two terms in the nominator have equal magnitude, which implies

$\delta_1^2\Gamma_{\mathrm{m},2}^2 = \delta_2^2\Gamma_{\mathrm{m},1}^2$. If this is fulfilled, the next requirement is that δ_1 and δ_2 have opposite signs, since otherwise $\Gamma_{\mathrm{m},1}\chi_{\mathrm{m},1}(0) = \Gamma_{\mathrm{m},2}\chi_{\mathrm{m},2}(0)$, such that Eq. (4.2.2) is always 1 (on resonance). Hence we choose $\delta_1 = \delta\Gamma_{\mathrm{m},1}/2$ and $\delta_2 = -\delta\Gamma_{\mathrm{m},2}/2$ (note that δ is dimensionless). We arrive at

$$\frac{S_{12}(0)}{S_{21}(0)} = e^{-i\Phi}\frac{(1+i\delta)^{-1} + (1-i\delta)^{-1}e^{i\Phi}}{(1+i\delta)^{-1} + (1-i\delta)^{-1}e^{-i\Phi}}, \tag{4.2.4}$$

such that the plaquette phase required for isolation becomes

$$\Phi = \pi - 2\tan^{-1}(\delta). \tag{4.2.5}$$

Note that inverting the plaquette phase $-\Phi$ leads to isolation in the opposite direction. In a second step, we demand vanishing reflection at the input ports, which translates to

$$\mathcal{C}_1 = \mathcal{C}_2 \equiv \mathcal{C} = \frac{1+\delta^2}{2} \iff \delta = \pm\sqrt{2\mathcal{C}-1}, \tag{4.2.6}$$

where either sign is permissible. Given these conditions, forward transmission becomes

$$|S_{21}(0)|^2 = \frac{\kappa_{\mathrm{ex},1}\kappa_{\mathrm{ex},2}}{\kappa_1\kappa_2}\left(1 - \frac{1}{2\mathcal{C}}\right), \tag{4.2.7}$$

where we have also introduced the external couplings $\kappa_{\mathrm{ex,i}}$ as discussed in Sections 1.3 and 1.7.

We have thus established that on resonance, the optomechanical plaquette serves as isolator with perfect isolation and an insertion loss limited by the intrinsic dissipation of the cavity modes. However, maximum isolation is only achieved at $\omega = 0$. On which frequency scale isolation is lost determines the *isolation bandwidth* of the isolator. Equation (4.2.2) indicates that this bandwidth is of order of the mechanical dissipation rate. This underscores that the mechanical dissipation rate is a crucial ingredient in this isolator, something that has already been recognized in Refs. 135 and 191. However, while this means that the optical damping induced by the resonant tones in Eq. (4.1.4) does not alter the bandwidth of the mechanical resonator, other dissipation channels that broaden the mechanical resonance do. In particular, this includes the cross damping due to non-resonant contributions in Eq. (4.1.4). This point will be discussed more extensively in Sec. 5.A.

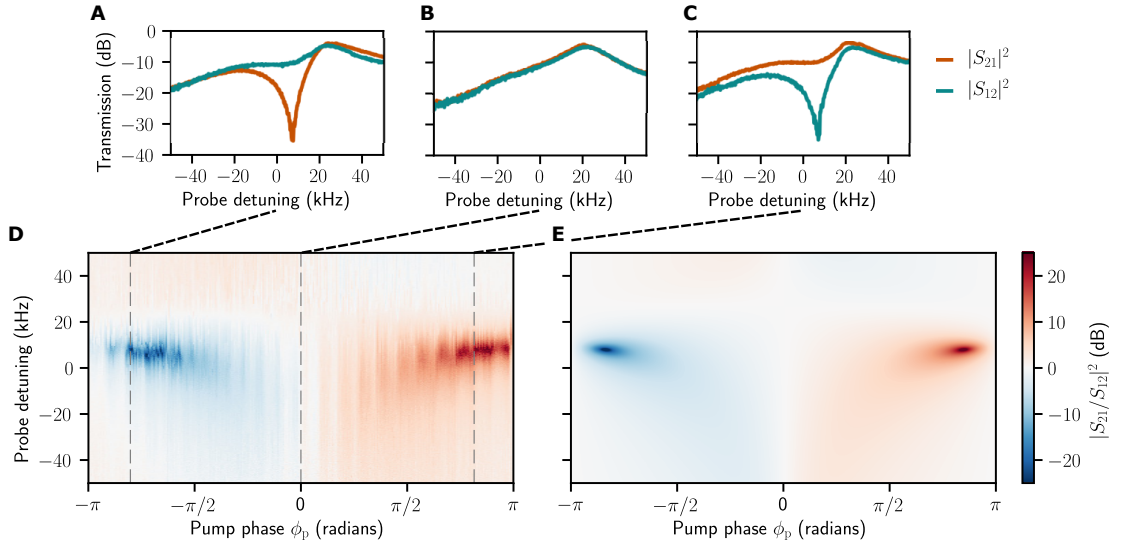

Figure 4.3: Experimental demonstration of nonreciprocity. (**A**-**B**) Scattering rates between cavity modes 1 and 2 as a function of probe detuning from resonance, for plaquette phases $\phi_p = -0.8\pi, 0, 0.8\pi$ radians (respectively **A**, **B** and **C**). Isolation of more than 20 dB in the forward (**C**) and backward (**A**) directions is demonstrated, as well as reciprocal behaviour (**B**). (**D**) The ratio of forward and backward scattering rates $|S_{21}/S_{12}|^2$, a measure of nonreciprocity, plotted as a function of pump phase ϕ_p and probe detuning. At $\pm 0.8\pi$ regions of strong nonreciprocity are situated. (**E**) Theoretical prediction for ratio of scattering rates from Eq. (4.2.2), calculated from independently measured experimental parameters. Due to the cross damping, the effective cooperativities are lowered compared to the values quoted. Figure reproduced from Ref. 3.

4.3 Experimental realization of optomechanical isolator

This section provides a brief account of the experiment done by Nathan Bernier, Daniel Tóth, and Alexey Feofanov at the École Fédérale Polytechnique de Lausanne, in the group of Prof. Tobias Kippenberg, work that has been published as Ref. 3, where more details on the experiment can be found.

The optomechanical plaquette is realized in a superconducting circuit featuring two coupled LC circuits, whose symmetric and antisymmetric eigenmodes [at $(\omega_{c,1}, \omega_{c,2}) = 2\pi \cdot (4.1, 5.2)$ GHz] are each coupled to the same transmission line and the same vacuum gap capacitor. Due to the coupling geometry, the symmetric mode couples much more strongly to the transmission line, such that the cavity decay rates differ by more than an order of magnitude [$(\kappa_1, \kappa_2) = 2\pi \cdot (0.2, 3.4)$ MHz]. Two radial modes of the vacuum-gap capacitor serve as mechanical modes. As described in detail in Sec. 1.4, such a setup is described by the standard optomechanical Hamiltonian, in this case featuring two cavity modes and two mechanical modes.

In the experiment, the mechanical resonance frequencies $(\omega_{\mathrm{m},1}, \omega_{\mathrm{m},2}) = 2\pi \cdot (6.5, 10.9)$ MHz, intrinsic energy decay rates $(\Gamma_{\mathrm{m},1}, \Gamma_{\mathrm{m},2}) = 2\pi \cdot (30, 10)$ Hz and optomechanical vacuum coupling strengths $(g_{0,11}, g_{0,12}) = 2\pi \cdot (91, 12)$ Hz, respectively (with $g_{0,11} \approx g_{0,21}$ and $g_{0,12} \approx g_{0,22}$, i.e., the two microwave cavities are symmetrically coupled to the mechanical modes). The device was placed at the mixing chamber of a dilution refrigerator at 200 mK and all four incoming pump tones are heavily filtered and attenuated to eliminate Johnson and phase noise as described in Ref. 51. Via the transmission line, the four pump tones are applied at frequencies $\omega_{\mathrm{c,i}} \pm \delta$, such that the fluctuations in this system are effectively described by Eq. (4.1.4). The individual cooperativities due to the coherent states were $\mathcal{C}_{11} = 520$, $\mathcal{C}_{21} = 450$, $\mathcal{C}_{12} = 1350$ and $\mathcal{C}_{22} = 1280$, when calculated with the bare mechanical dissipation rates. However, the fact that the bare coupling to the first mechanical mode was much stronger and the wide second cavity resonance $(\kappa_2/\omega_{\mathrm{m},1} \approx 0.5)$ meant that the pump at $\omega_{\mathrm{c},2} - \omega_{\mathrm{m},1}$ caused strong non-resonant damping, enhancing the mechanical linewidth by $\Gamma_{\mathrm{m},1}^{(\mathrm{cross})} \approx 2\pi \cdot 20$ kHz at the relevant parameters. This lowered the effective cooperativities to to $(\mathcal{C}_{11}, \mathcal{C}_{21}) \approx (0.78, 0.68)$. The stark discrepancy between cooperativities was responsible for significant insertion loss and asymmetric scattering rates seen in Fig. 4.3. Off-resonant damping was also measured in Ref. 53 and can be estimated by taking the off-resonant terms in Eq. (4.1.4) into account, as done in Sec. 5.A.

In the region of maximum isolation, the pumps were detuned from the cavity resonance by $\delta = 2\pi \cdot 18$ kHz. In the experiment, the plaquette phase was altered by varying the phase of one tone relative to the others ϕ_{p}, which directly corresponds the plaquette phase, except for some constant offset of approximately π.

An injected probe signal $\omega_{\mathrm{s1(s2)}}$ around the lower (higher) frequency microwave mode was measured in reflection using a vector network analyzer, producing the data shown in Fig. 4.3. This way, the scattering matrix elements $|S_{21}(\omega)|^2$ and $|S_{12}(\omega)|^2$ can be measured directly. They are plotted for forward isolation (A), backward isolation (C), and reciprocal transmission (B) in Fig. 4.3. The ratio of the forward and backward scattering rates $|S_{21}/S_{12}|^2$ is a measure of nonreciprocity. Figure 4.3D shows this measure as a function of probe detuning and the relative pump phase. Isolation of more than 20 dB was demonstrated in each direction. To compare the experiment to theory we use a model with effective parameters that account for cross-damping, which works well as can be seen from Fig. 4.3E.

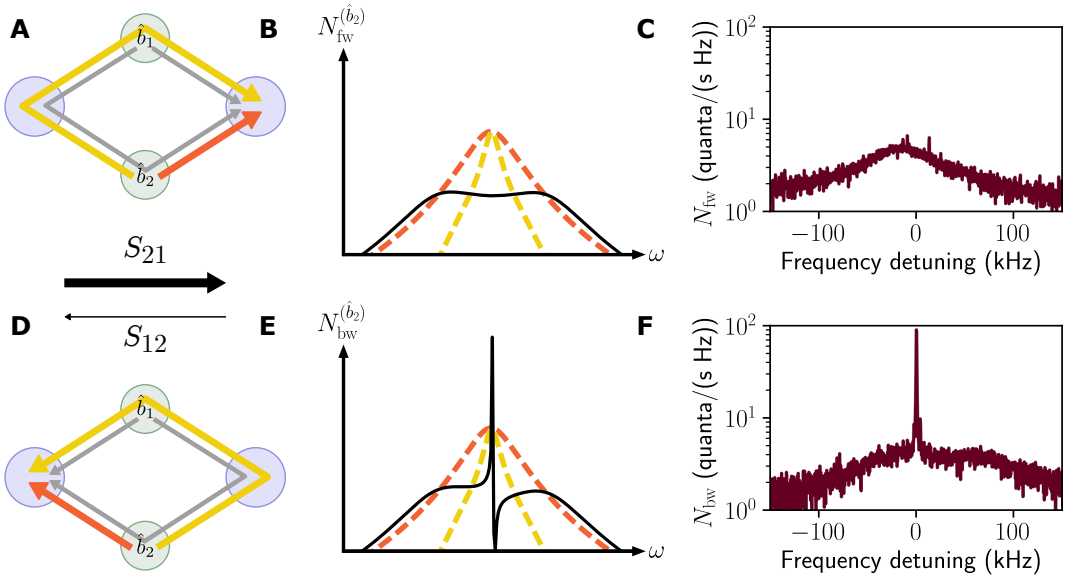

Figure 4.4: Asymmetric noise emission of the optomechanical isolator. The measured noise is predominantly mechanical thermal noise, that is converted through two paths to the microwave modes. The resulting interference creates a different noise pattern in the forward (**a-c**) and the backward (**d-f**) directions when the circuit is tuned as an isolator from mode $\hat{a}_1$ to $\hat{a}_2$, as has been discussed extensively in Sec. 4.4. (**a,d**) The two possible paths for the noise are shown for each mechanical mode. For $\hat{b}_2$, the direct path (orange) and the indirect path going through mode $\hat{b}_1$ (yellow) are highlighted (the corresponding paths for $\hat{b}_1$ are shown in grey). (**b,e**) Each path on its own would result in a wide noise spectrum that is equally divided between the two microwave cavities (dashed yellow and orange lines). When both paths are available, however, the noise interferes differently in each direction (solid lines). In the backward direction (**e**), a sharp interference peak appears, of much larger amplitude than the broad base. The theoretical curves (on a logarithmic scale) are shown for the symmetric case ($\Gamma_{\mathrm{m},1} = \Gamma_{\mathrm{m},2}$) and for the single mode $\hat{b}_2$. Note that for the mode $\hat{b}_1$, the shape of the asymmetric peak in the backward noise would be the mirror image. The Fano-like shape of the noise spectrum is a result of the interference of a direct path and one filtered by a mechanical resonator. (**c,f**) Measured output spectra of modes $\hat{a}_2$ (**c**) and $\hat{a}_1$ (**f**), calibrated to show the photon flux leaving the circuit. Because cross-damping provides extra cooling for the mode $\hat{b}_1$, the thermal noise of $\hat{b}_2$ is expected to dominate. Figure reproduced from Ref. 3.

4.4 Asymmetric noise properties of isolator

An isolator is not only characterized by its transmission properties, but also by the noise it emits and adds to the signal. This is particularly pertinent for quantum technologies, which are exceptionally sensitive to noise.

In the following, in order to understand the noise emitted by the isolator in the forward and backward direction, we adopt two different points of view. First, we derive the scattering amplitude from one mechanical resonator to one cavity, eliminating the other two modes. In this picture, the imbalance can be understood as an interference of the two paths the noise can take in the circuit, analogously to the interference in the microwave transmission. Second, we eliminate the mechanical resonators, but taking their input noise into account. This yields additional, effective noise input operators for the cavities, describing coloured (filtered) and correlated noise. In the second formulation we can use our knowledge of the microwave scattering matrix to deduce properties of the noise scattering. The conclusions in the following sections are supported by experiment, as shown in Fig. 4.4.

4.4.1 Noise interference in the scattering amplitude

Let us first consider the scattering from a mechanical resonator to cavities 1 and 2. Since in the experiment mechanical resonator 1 is strongly cross-damped due to off-resonant couplings, the noise emitted stems almost exclusively from resonator 2. If we are solely interested in the noise scattering from mechanical resonator 2 to cavity 2, we can eliminate the other two modes and drop their input noise. In frequency space, their equations of motion are

$$\begin{pmatrix} \chi_{\mathrm{c},1}^{-1}(\omega) & -iG_{11} \\ -iG_{11}^{*} & \chi_{\mathrm{m},1}^{-1}(\omega) \end{pmatrix} \begin{pmatrix} \hat{a}_1(\omega) \\ \hat{b}_1(\omega) \end{pmatrix} = \begin{pmatrix} iG_{12}\hat{b}_2(\omega) \\ iG_{21}^{*}\hat{a}_2(\omega) \end{pmatrix} + \text{noises}. \tag{4.4.1}$$

We drop the noise terms and solve for $\hat{a}_1, \hat{b}_1$

$$\begin{aligned} \begin{pmatrix} \hat{a}_1(\omega) \\ \hat{b}_1(\omega) \end{pmatrix} &= \frac{1}{\chi_{\mathrm{m},1}^{-1}(\omega)\chi_{\mathrm{c},1}^{-1}(\omega) + |G_{11}|^2} \begin{pmatrix} \chi_{\mathrm{m},1}^{-1}(\omega) & iG_{11} \\ iG_{11}^{*} & \chi_{\mathrm{c},1}^{-1}(\omega) \end{pmatrix} \begin{pmatrix} iG_{12}\hat{b}_2(\omega) \\ iG_{21}^{*}\hat{a}_2(\omega) \end{pmatrix} \\ &\equiv \chi_{\hat{a}_1\hat{b}_1}(\omega) \begin{pmatrix} iG_{12} & \\ & iG_{21}^{*} \end{pmatrix} \begin{pmatrix} \hat{b}_2(\omega) \\ \hat{a}_2(\omega) \end{pmatrix}, \end{aligned} \tag{4.4.2}$$

where single-mode susceptibilities are defined as above Eq. (4.1.7) and the susceptibility of the coupled system of modes $\hat{a}_1, \hat{b}_1$ is denoted by $\chi_{\hat{a}_1\hat{b}_1}(\omega)$. Equation (4.4.2) tells us

how to eliminate $\hat{a}_1, \hat{b}_1$ in favour of $\hat{a}_2, \hat{b}_2$. We turn to the other two modes, the ones that we are actually interested in. For those, we have a similar equation, which can be obtained from interchanging $1 \leftrightarrow 2$ in Eq. (4.4.1)

$$\begin{pmatrix} \chi_{\mathrm{m},2}^{-1}(\omega) & -iG_{22}^{*} \\ -iG_{22} & \chi_{\mathrm{c},2}^{-1}(\omega) \end{pmatrix} \begin{pmatrix} \hat{b}_2(\omega) \\ \hat{a}_2(\omega) \end{pmatrix} = \begin{pmatrix} iG_{12}^{*} & \\ & iG_{21} \end{pmatrix} \begin{pmatrix} \hat{a}_1(\omega) \\ \hat{b}_1(\omega) \end{pmatrix} + \begin{pmatrix} \sqrt{\Gamma_{\mathrm{m},2}}\hat{b}_{2,\mathrm{in}}(\omega) \\ \sqrt{\kappa_2}\hat{a}_{2,\mathrm{in}}(\omega) \end{pmatrix}. \tag{4.4.3}$$

Eliminating the modes $\hat{a}_1, \hat{b}_1$ with Eq. (4.4.2), we arrive at

$$\begin{aligned} &\left[\begin{pmatrix} \chi_{\mathrm{m},2}^{-1}(\omega) & -iG_{22}^{*} \\ -iG_{22} & \chi_{\mathrm{c},2}^{-1}(\omega) \end{pmatrix} - \frac{\begin{pmatrix} iG_{12}^{*} & \\ & iG_{21} \end{pmatrix} \begin{pmatrix} \chi_{\mathrm{m},1}^{-1}(\omega) & iG_{11} \\ iG_{11}^{*} & \chi_{\mathrm{c},1}^{-1}(\omega) \end{pmatrix} \begin{pmatrix} iG_{12} & \\ & iG_{21}^{*} \end{pmatrix}}{\chi_{\mathrm{m},1}^{-1}(\omega)\chi_{\mathrm{c},1}^{-1}(\omega) + |G_{11}|^2} \right] \begin{pmatrix} \hat{b}_2(\omega) \\ \hat{a}_2(\omega) \end{pmatrix} \\ &\equiv \left[\chi_{\hat{b}_2\hat{a}_2}^{-1}(\omega) - \begin{pmatrix} iG_{12}^{*} & \\ & iG_{21} \end{pmatrix} \chi_{\hat{a}_1\hat{b}_1}(\omega) \begin{pmatrix} iG_{12} & \\ & iG_{21}^{*} \end{pmatrix} \right] \begin{pmatrix} \hat{b}_2(\omega) \\ \hat{a}_2(\omega) \end{pmatrix} \\ &= \begin{pmatrix} \sqrt{\Gamma_{\mathrm{m},2}}\hat{b}_{2,\mathrm{in}}(\omega) \\ \sqrt{\kappa_2}\hat{a}_{2,\mathrm{in}}(\omega) \end{pmatrix}. \end{aligned} \tag{4.4.4}$$

In the second line, we have formulated the equation in terms of the susceptibilities of the two subsystems $(\hat{a}_1, \hat{b}_1)$ [cf. Eq. (4.4.2)] and $(\hat{a}_2, \hat{b}_2)$. This equation is a bit complicated, but we note that the coupling between $\hat{a}_2$ and $\hat{b}_2$ is

$$iT_{\hat{a}_2\hat{b}_2}(\omega) = -iG_{22}\left[1 - e^{-i\Phi}\frac{\mathcal{C}_{12}\mathcal{C}_{21}/(\mathcal{C}_{22}\mathcal{C}_{11})}{1 + (\chi_{\mathrm{c},1}(\omega)\chi_{\mathrm{m},1}(\omega)|G_{11}|^2)^{-1}}\right]. \tag{4.4.5}$$

Analogously, changing the indices referring to the cavity, we obtain the coupling between $\hat{a}_1$ and $\hat{b}_2$

$$iT_{\hat{a}_1\hat{b}_2}(\omega) = -iG_{12}\left[1 - e^{+i\Phi}\frac{\mathcal{C}_{11}\mathcal{C}_{22}/(\mathcal{C}_{12}\mathcal{C}_{21})}{1 + (\chi_{\mathrm{c},2}(\omega)\chi_{\mathrm{m},1}(\omega)|G_{21}|^2)^{-1}}\right], \tag{4.4.6}$$

The plaquette phase Φ appears as the relative phase between indirect and direct coupling path, as for the microwave signal transmission. Equations (4.4.5) and (4.4.6) demonstrate that the transmission of noise from the mechanical resonators to the microwave cavities is subject to interference, which ultimately leads to the difference in noise emitted in the forward versus the backward direction. The mechanical susceptibility that appears in the denominator in Eqs. (4.4.5) and (4.4.6) is responsible for the Fano-like lineshape seen in Fig. 4.4.

4.4.2 Noise interference as correlated noise in the cavity modes

In a second picture, we can also understand the mechanical noise interference in terms of the nonreciprocity in the scattering matrix for the microwave modes. In order to do so, we solve the equations of motion for the mechanical resonators (given in Eq. (4.1.6)), which leads to

$$\hat{b}_j(\omega) = \chi_{\mathrm{m},j}(\omega)\left[i\sum_i G_{ij}^*\hat{a}_i(\omega) + \sqrt{\Gamma_{\mathrm{m},j}}\hat{b}_{j,\mathrm{in}}(\omega)\right]. \tag{4.4.7}$$

We obtain equations that only relate the cavities

$$\begin{aligned}&\begin{pmatrix}\chi_{\mathrm{c},1}^{-1}(\omega)+iT_{11}(\omega) & iT_{12}(\omega)\\ iT_{21}(\omega) & \chi_{\mathrm{c},2}^{-1}(\omega)+iT_{22}(\omega)\end{pmatrix}\begin{pmatrix}\hat{a}_1(\omega)\\ \hat{a}_2(\omega)\end{pmatrix}\\ &= i\begin{pmatrix}G_{11} & G_{12}\\ G_{21} & G_{22}\end{pmatrix}\begin{pmatrix}\sqrt{\Gamma_{\mathrm{m},1}}\chi_{\mathrm{m},1}(\omega)\hat{b}_{1,\mathrm{in}}(\omega)\\ \sqrt{\Gamma_{\mathrm{m},2}}\chi_{\mathrm{m},2}(\omega)\hat{b}_{2,\mathrm{in}}(\omega)\end{pmatrix} + \begin{pmatrix}\sqrt{\kappa_1}\hat{a}_{1,\mathrm{in}}(\omega)\\ \sqrt{\kappa_2}\hat{a}_{2,\mathrm{in}}(\omega)\end{pmatrix},\end{aligned} \tag{4.4.8}$$

where

$$iT_{ij}(\omega) \equiv -i\sum_k \chi_{\mathrm{m},k}(\omega)G_{ik}G_{jk}^*. \tag{4.4.9}$$

We can think of mechanical noise as additional coloured and correlated noise in the optical inputs. That is, consider the replacement

$$\begin{pmatrix}\sqrt{\kappa_1}\hat{c}_{1,\mathrm{in}}(\omega)\\ \sqrt{\kappa_2}\hat{c}_{2,\mathrm{in}}(\omega)\end{pmatrix} \equiv i\begin{pmatrix}G_{11} & G_{12}\\ G_{21} & G_{22}\end{pmatrix}\begin{pmatrix}\sqrt{\Gamma_{\mathrm{m},1}}\chi_{\mathrm{m},1}(\omega)\hat{b}_{1,\mathrm{in}}(\omega)\\ \sqrt{\Gamma_{\mathrm{m},2}}\chi_{\mathrm{m},2}(\omega)\hat{b}_{2,\mathrm{in}}(\omega)\end{pmatrix}. \tag{4.4.10}$$

The effective noise $\hat{c}_{i,\mathrm{in}}$ is both coloured $\langle\hat{c}_{1,\mathrm{in}}^\dagger(\omega)\hat{c}_{1,\mathrm{in}}(\omega')\rangle \neq \delta(\omega+\omega')\bar{n}_{1,\mathrm{eff}}$ and correlated $\langle\hat{c}_{1,\mathrm{in}}^\dagger(\omega)\hat{c}_{2,\mathrm{in}}(\omega')\rangle \neq 0$.

Using the input-output relation $\hat{a}_{\mathrm{out}} = \hat{a}_{\mathrm{in}} - \sqrt{\kappa}\hat{a}$, the cavity output is given by

$$\begin{pmatrix}\hat{a}_{1,\mathrm{out}}(\omega)\\ \hat{a}_{2,\mathrm{out}}(\omega)\end{pmatrix} = S(\omega)\begin{pmatrix}\hat{a}_{1,\mathrm{in}}(\omega)\\ \hat{a}_{2,\mathrm{in}}(\omega)\end{pmatrix} + [S(\omega)-\mathbb{1}_2]\begin{pmatrix}\hat{c}_{1,\mathrm{in}}(\omega)\\ \hat{c}_{2,\mathrm{in}}(\omega)\end{pmatrix}, \tag{4.4.11}$$

where we have identified the 2-by-2 optical scattering matrix $S(\omega)$ that relates the cavity inputs to the outputs $\hat{a}_{i,\mathrm{out}}(\omega) = \sum_j S_{ij}(\omega)\hat{a}_{j,\mathrm{in}}(\omega)$. The fact that Eq. (4.4.11) contains mechanical noise as well, but can be written entirely in terms of the optical scattering matrix constitutes the central result here. Since the two effective input noises $\hat{c}_{i,\mathrm{in}}$ are coloured and correlated, they interfere.

In the ideal case, the circuit is impedance-matched to the signal and perfectly isolating. For simplicity, let us choose all cooperativities to be equal $\mathcal{C} = \mathcal{C}_{ij}$. For $\delta^2 = 2\mathcal{C}-1$ (impedance matching), the optical scattering matrix of the isolator is (up to some irrelevant

phase)

$$S(0) = \begin{pmatrix} 0 & 0 \\ \sqrt{1-1/(2\mathcal{C})} & 0 \end{pmatrix} \equiv T \begin{pmatrix} 0 & 0 \\ 1 & 0 \end{pmatrix}, \tag{4.4.12}$$

such that the cavity output on resonance is

$$\begin{pmatrix} \hat{a}_{1,\text{out}} \\ \hat{a}_{2,\text{out}} \end{pmatrix} = T \begin{pmatrix} 0 \\ \hat{a}_{1,\text{in}} \end{pmatrix} - \frac{i}{\sqrt{2}} \mathcal{C} \begin{pmatrix} e^{i\Phi} & 1 \\ 1 - Te^{i\Phi} & 1-T \end{pmatrix} \begin{pmatrix} \hat{b}_{1,\text{in}}(0) \\ \hat{b}_{2,\text{in}}(0) \end{pmatrix}. \tag{4.4.13}$$

As $\mathcal{C} \to \infty$, $T \to 1$ and $\Phi = \cos^{-1}(1 - 1/\mathcal{C}) \to 0$, such that the second cavity does not receive any noise, which is due to an interference of $\hat{c}_{1,\text{in}}$ with $\hat{c}_{2,\text{in}}$. In the backward direction, no interference can take place, since cavity 1 is isolated from cavity 2. As a consequence, the number of noise quanta emerging from cavity 1 on resonance is $N_{\text{bw}} = (\bar{n}_{\text{m},1} + \bar{n}_{\text{m},2} + 1)/2$.

4.4.3 General arguments for noise interference

One can argue on general grounds that in addition to the two modes connected to the two ports of the isolators, there always have to exist further auxiliary modes. The simplest way to appreciate this, is by considering the perfect isolator of the form

$$\begin{pmatrix} \hat{a}_{1,\text{out}} \\ \hat{a}_{2,\text{out}} \end{pmatrix} \stackrel{?}{=} \begin{pmatrix} 0 & 0 \\ 1 & 0 \end{pmatrix} \begin{pmatrix} \hat{a}_{1,\text{in}} \\ \hat{a}_{2,\text{in}} \end{pmatrix}. \tag{4.4.14}$$

One can immediately conclude that there is something missing from this equation, as it predicts a vanishing commutation relation for $\hat{a}_{1,\text{out}}$. Indeed, with only two modes, the field entering through $\hat{a}_{2,\text{in}}$ cannot be dissipated. As a consequence, there has to be at least one other bosonic mode (or potentially many) that serves to dissipate the signal in $\hat{a}_{2,\text{in}}$, and supplies quantum fluctuations to $\hat{a}_{1,\text{out}}$ such that its bosonic commutation relations are upheld.[†] In the case discussed here, this role is played by the mechanical oscillators.

The thermal occupation of the mechanical oscillators which appears in the noise emitted in the backward direction can be hundreds of quanta even at cryogenic millikelvin temperatures, due to the low mechanical frequencies, such that in addition to quantum fluctuations, there are large thermal fluctuations. A practical low-noise design therefore requires a scheme to externally cool the mechanical modes, e.g., via sideband cooling using an additional auxiliary microwave mode. Another alternative are circulators where the fluctuations stem from a third cavity mode.

[†]If this argument sounds familiar, it is because we have used almost the same line of reasoning to obtain the quantum limit for the phase-preserving amplifier in Sec. 1.8.

4.4.4 Noise interference in experiment

The noise asymmetry was demonstrated experimentally by detecting the output spectra at each microwave mode while the device isolates the mode $\hat{a}_1$ from $\hat{a}_2$ by more than 25 dB (Fig. 4.3C,F). The cooperativities are here set to $(\mathcal{C}_{11}, \mathcal{C}_{21}, \mathcal{C}_{12}, \mathcal{C}_{22}) = (20.0, 14.2, 106, 89)$ with a cross-damping $\Gamma_{\mathrm{m},1}^{(\mathrm{cross})} \approx 2\pi \cdot 2.6$ kHz, in order to optimize the circuit for a lower insertion loss and increase the noise visibility. As there is additional cooling from the off-resonant pump on mode $\hat{b}_1$, we expect noise from $\hat{b}_2$ to dominate.

4.5 Conclusion

In conclusion, we described and experimentally demonstrated a new scheme for reconfigurable nonreciprocal transmission in the microwave domain using a superconducting optomechanical circuit. This scheme is based purely on optomechanical couplings, thus it alleviates the need for coherent microwave cavity-cavity (or direct phonon-phonon) interactions, and significantly facilitates the experimental realization, in contrast to recently used approaches of optomechanical nonreciprocity in the optical domain [52]. Nonreciprocity arises due to interference in the two mechanical modes, which mediate the microwave cavity-cavity coupling. This interference also manifests itself in the asymmetric noise output of the circuit. This scheme can be readily extended to implement quantum-limited phase-preserving and phase-sensitive directional amplifiers [4]. Moreover, an additional microwave mode enables quantum-limited microwave circulators on-chip with large bandwidth, limited only by the energy decay rate of the microwave modes.

Since the original publication of our article [3], optomechanical circulators have been realized [54, 195–197], as well as directional amplifiers [197]. Another frontier is achieving larger bandwidth, for which Brillouin scattering has shown to be promising [198]. A lot of the progress has recently been reviewed [194, 199, 200]. Finally, it would be desirable to integrate all the advantages of on-chip, tunable circulator designs into a passive device that does not consume energy. Very recently, a theoretical proposal has pointed to the possibility of such devices [201].

5 | Directional amplifiers in optomechanics

As we have discussed in Chapter 4 above, there is an ongoing effort to find on-chip integrable nonreciprocal devices compatible with superconducting quantum architecture [3, 52, 53, 135, 174, 183, 189–193, 202–206]. We have already encountered the optomechanical plaquette, a novel type of optomechanical circuit that was used to demonstrate optomechanical isolation of microwaves, marking a major advance toward this goal. Isolators are necessary to protect quantum systems from the large amount of thermal noise present in microwave devices warmer than a few tens of millikelvin. However, noise should not only be prevented from entering the quantum system, it should also not be added to the signal during or before the amplification stage. Indeed, as we found in Sec. 1.8, specifically Eq. (1.8.3), (near) quantum-limited amplification requires an idler (close to) in vacuum, which requires cryogenic temperatures. This is why signals from superconducting circuits are ideally first sent through a *quantum-limited*[†] preamplification stage that resides in the dilution refrigerator, which greatly reduces the total noise added in the amplification process [207, 208].

As it turns out, superconducting circuits are well suited to build quantum-limited microwave amplifiers. For example, the strong Josephson nonlinearity has been used to build a near quantum-limited travelling-wave amplifier [207], and in optomechanics, both phase-preserving amplifiers [49, 51, 144, 209, 210], as well as phase-sensitive amplifiers [44, 45, 50, 122] have been proposed and realized.

A natural question to ask is whether isolation and amplification could occur in the same step, leading to further integration, potentially realizing devices with a smaller footprint and less added noise. A recent article studies minimal models for directional amplification [192], but these models again require a direct cavity-cavity coupling, which has proven difficult to implement in microwave superconducting circuits, at least while coupling both modes also to a mechanical mode. In this chapter, we show that the

[†]We have introduced the quantum limit for amplification above (Sec. 1.8).

optomechanical plaquette is capable of achieving integrated, reconfigurable, quantum-limited, directional amplifiers, research that has been published as Ref. 4.

In the optomechanical plaquette, microwave tones on the red and blue sidebands enable so-called beam-splitter and two-mode squeezing interactions (cf. Fig. 4.1), leading to a total of eight controllable terms in the Hamiltonian, which has already been derived above [Eq. (4.1.4)]. We identify and analyze a simple directional phase-preserving amplifier that uses four tones and a directional phase-sensitive amplifier using six tones. While the gain-bandwidth product of the phase-preserving amplifier is limited to the cavity decay rate, the phase-sensitive amplifier has an unlimited gain-bandwidth product. The isolation bandwidth in each is of the order of the mechanical linewidth divided by the amplitude gain. We show that both amplifiers can reach their quantum limits of a half and zero added quanta, respectively, and, like the isolator, emit thermal noise from the mechanical resonators in the reverse direction, a necessary consequence of impedance matching and directionality. We show how the reverse noise can be reduced through additional sideband cooling without interfering with directionality or amplification, a crucial aspect for technological applications. Our concrete proposal bridges the gap between previous theoretical studies and experimental realization and therefore represents an important step toward on-chip integrated nonreciprocal amplifiers of microwave signals.

5.1 Directional phase-preserving amplifier (DPPA)

As above, the optomechanical plaquette is described by the linearized Hamiltonian [Eq. (4.1.4), repeated here for convenience]

$$\hat{H}_{\text{lin}} = -\sum_j \delta_j \hat{b}_j^\dagger \hat{b}_j - \sum_{ij} g_{0,ij} \left\{ \bar{a}_i^*(t)\hat{a}_i \left[\hat{b}_j e^{-i(\omega_{\text{m},j}+\delta_j)t} + \hat{b}_j^\dagger e^{i(\omega_{\text{m},j}+\delta_j)t} \right] + \text{H.c.} \right\}. \tag{5.1.1}$$

In order to obtain a directional, phase-preserving amplifier, we consider the coupling strengths [cf. Fig. 5.1(a)]

$$\begin{aligned} \mathsf{G} &= \frac{1}{2} \begin{pmatrix} e^{\frac{i\Phi}{2}} \sqrt{\mathcal{C}_1 \Gamma_{\text{m},1} \kappa_1} & e^{-\frac{i\Phi}{2}} \sqrt{\mathcal{C}_1 \Gamma_{\text{m},2} \kappa_1} \\ 0 & 0 \end{pmatrix}, \\ \mathsf{J} &= \frac{1}{2} \begin{pmatrix} 0 & 0 \\ \sqrt{\mathcal{C}_2 \Gamma_{\text{m},1} \kappa_2} & \sqrt{\mathcal{C}_2 \Gamma_{\text{m},2} \kappa_2} \end{pmatrix}, \end{aligned} \tag{5.1.2}$$

that is, the first (second) cavity has two drives, close to the red (blue) motional sidebands corresponding to the mechanical resonators [cf. Fig. 5.1(a-b)]. Here, we have written the amplitudes in terms of cooperativities $\mathcal{C}_{1i} = 4|G_{1i}|^2/(\kappa_1 \Gamma_{\text{m},i})$, $\mathcal{C}_{2i} = 4|J_{2i}|^2/(\kappa_2 \Gamma_{\text{m},i})$, and

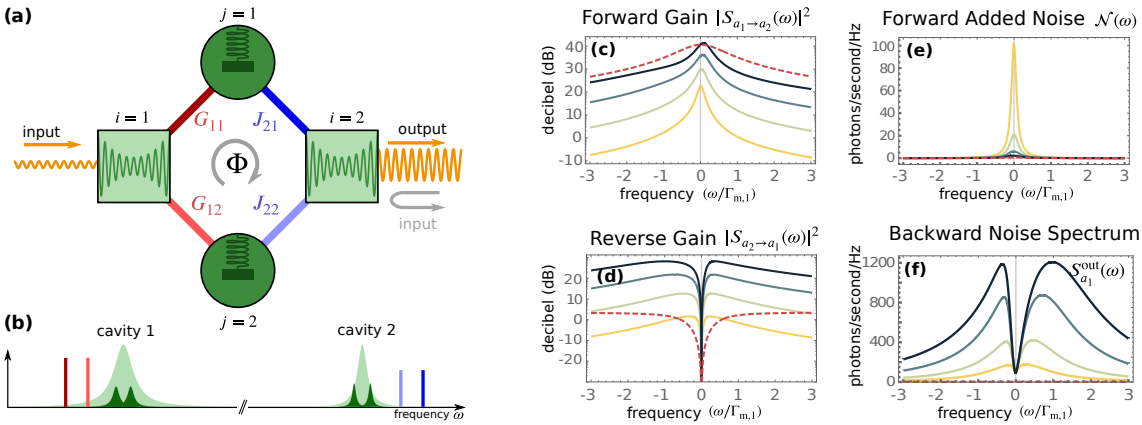

Figure 5.1: The directional phase-preserving amplifier (DPPA). (a) Model. Red hopping interactions are impedance matched, blue provide amplification. **(b)** Pump setup. Cavity 1 (cavity 2) is pumped on the red (blue) sidebands of the mechanical resonators. In **(c-f)** we plot forward gain, reverse gain [Eq. (5.1.9)], added noise [Eq. (5.1.12)], and the output noise fluctuation spectrum of cavity 1, all as functions of frequency in units of $\Gamma_{\mathrm{m},1}$, for cooperativities $\mathcal{C}_1 = \{1, 3, 10, 30\}$, $\mathcal{C}_2 = \mathcal{C}_1 - 0.1\sqrt{\mathcal{C}_1}$ (yellow to black, or light to dark). Parameters are $\kappa_2/\kappa_1 = 0.7, \Gamma_{\mathrm{m},1}/\kappa_1 = 10^{-2}, \Gamma_{\mathrm{m},2}/\Gamma_{\mathrm{m},1} = 0.8$, thermal occupation of the mechanical resonators $n_{\mathrm{m},1} = n_{\mathrm{m},2} = 100$, and cavities $n_{\mathrm{c},1} = n_{\mathrm{c},2} = 0$. Depending on parameters, external sideband cooling with an auxiliary mode can achieve $n_{\mathrm{m},j} \approx 0$, without negatively affecting amplification properties, as discussed below. The red (dashed) curve in each plot illustrates this case, with $\mathcal{C}_1 = 30$ and effective parameters $n_{\mathrm{eff},i} = n_{\mathrm{m},i}(\Gamma_{\mathrm{m},i}/\Gamma_{\mathrm{eff},i}), \Gamma_{\mathrm{eff},i} = 50\Gamma_{\mathrm{m},i}$.

chosen the cooperativities in both arms to be equal $\mathcal{C}_1 \equiv \mathcal{C}_{1i}, \mathcal{C}_2 \equiv \mathcal{C}_{2i}$.

We have chosen the couplings [Eq. (5.1.2)] due to the following reasons. First, an even number of blue and red tones ensures equivalent arms of the circuit. Second, amplification requires blue tones. Third, a directional amplifier with four blue tones cannot be impedance matched to the signal source, as shown in Sec. 5.1.2. Last, interchanging the hopping and amplifier interactions in one arm of the circuit (e.g., $J_{21} \leftrightarrow J_{11}$ and $G_{11} \leftrightarrow G_{21}$) cannot lead to directional amplification[†].

In Sec. 4.1 we derived the Langevin equations and scattering matrix corresponding to this Hamiltonian. Isolation is achieved when $\mathsf{T}_{12} = 0$, i.e., when the first cavity is decoupled from the second, but $\mathsf{T}_{21} \neq 0$, i.e., the second cavity *is* coupled to the first. For the DPPA, these conditions are on resonance

$$[i\mathsf{T}_{12}]_{12} = \chi_{\mathrm{m},1}(0)G_{11}J_{12} + \chi_{\mathrm{m},2}(0)G_{21}J_{22} = 0, \tag{5.1.3a}$$

$$[i\mathsf{T}_{21}]_{12} = \chi^*_{\mathrm{m},1}(0)G_{11}J_{12} + \chi^*_{\mathrm{m},2}(0)G_{21}J_{22} \neq 0. \tag{5.1.3b}$$

Isolation occurs for certain phases of the coupling amplitudes $\theta_{1i} \equiv \arg(G_{1i})$ and $\theta_{2i} \equiv$

[†]Private communication with Anja Metelmann. Note that choosing $G_{21} = J_{22} = 0, G_{11} = J_{12}, \delta = 0$, yields reciprocal amplifier with unlimited gain-bandwidth product [209].

$\arg(J_{2i})$. However, only the overall relative *plaquette phase*, $\Phi \equiv \theta_{11} + \theta_{21} - \theta_{12} - \theta_{22}$, is relevant, which explains the parameterization in Eq. (5.1.2). For this choice of driving strengths, we find that Eqs. (5.1.3a) and (5.1.3b) become

$$0 = i\Gamma_{\mathrm{m},1}\Gamma_{\mathrm{m},2} + 2\delta_1\Gamma_{\mathrm{m},2} + e^{i\Phi}(i\Gamma_{\mathrm{m},1}\Gamma_{\mathrm{m},2} + 2\delta_2\Gamma_{\mathrm{m},1}), \tag{5.1.4a}$$

$$0 \neq i\Gamma_{\mathrm{m},1}\Gamma_{\mathrm{m},2} + 2\delta_1\Gamma_{\mathrm{m},2} + e^{-i\Phi}(i\Gamma_{\mathrm{m},1}\Gamma_{\mathrm{m},2} + 2\delta_2\Gamma_{\mathrm{m},1}). \tag{5.1.4b}$$

Taking the modulus in Eq. (5.1.4a), we find that isolation requires

$$\frac{\delta_1^2}{\Gamma_{\mathrm{m},1}^2} = \frac{\delta_2^2}{\Gamma_{\mathrm{m},2}^2}. \tag{5.1.5}$$

Note that sending $\Phi \to -\Phi$ interchanges Eqs. (5.1.4a) and (5.1.4b), which means that isolation occurs in the opposite direction. In order to avoid *double isolation*, where forward and backward transmission vanish at the same plaquette phase (as per the previous sentence, this occurs for $\Phi = 0$ or $\Phi = \pi$), we need $\delta_1/\Gamma_{\mathrm{m},1} \neq \delta_2/\Gamma_{\mathrm{m},2}$. We therefore parametrize the detunings by a single dimensionless variable $\delta_1 = \delta\Gamma_{\mathrm{m},1}/2$, $\delta_2 = -\delta\Gamma_{\mathrm{m},2}/2$.

For these choices, the scattering amplitude from $a_{1,\mathrm{in}}$ to $a_{1,\mathrm{out}}$ (reflection) is given by

$$S_{a_1 \to a_1}(0) = \frac{4\mathcal{C}_1}{\delta^2 + 2\mathcal{C}_1 + 1} - 1. \tag{5.1.6}$$

Like in the isolator, we demand zero reflection at the input, which is attained for

$$\delta = \sqrt{2\mathcal{C}_1 - 1}, \tag{5.1.7}$$

the same as in Eq. (4.2.6) and Ref. 53. Then the plaquette phase at which isolation occurs is

$$\Phi = i \log\left(\frac{\delta - i}{\delta + i}\right) = 2\cos^{-1}\sqrt{1 - 1/(2\mathcal{C}_1)}. \tag{5.1.8}$$

Inverting the plaquette phase $-\Phi$ leads to isolation in the opposite direction.

The condition $\mathcal{C}_2 < \mathcal{C}_1$ ensures that the system does not exceed the parametric instability threshold. In the limit of large gain, we obtain our first main result, the scattering matrix

$$\begin{pmatrix} \hat{a}_{1,\mathrm{out}}(0) \\ \hat{a}^\dagger_{2,\mathrm{out}}(0) \end{pmatrix} = \begin{pmatrix} \frac{1}{\sqrt{2}} & -\frac{1}{\sqrt{2}} & 0 & 0 \\ \frac{i\sqrt{\mathcal{G}}}{\sqrt{4\mathcal{C}_1}} & \frac{i\sqrt{\mathcal{G}}}{\sqrt{4\mathcal{C}_1}} & -\sqrt{\mathcal{G}} & \frac{\mathcal{C}_1+\mathcal{C}_2}{\mathcal{C}_2-\mathcal{C}_1} \end{pmatrix} \begin{pmatrix} \hat{b}_{1,\mathrm{in}}(0) \\ \hat{b}_{2,\mathrm{in}}(0) \\ \hat{a}_{1,\mathrm{in}}(0) \\ \hat{a}^\dagger_{2,\mathrm{in}}(0) \end{pmatrix}, \tag{5.1.9}$$

with vanishing reverse gain $|S_{a_2\to a_1}(0)|^2$, but forward gain

$$|S_{a_1\to a_2}(0)|^2 \equiv \mathcal{G} = \frac{4\mathcal{C}_1\mathcal{C}_2}{(\mathcal{C}_1-\mathcal{C}_2)^2}, \tag{5.1.10}$$

which can in principle be arbitrarily large, as long as the RWA is valid (discussed further in Sec. 5.A).

At the same time, thermal noise from the mechanical resonators is suppressed by increasing $\mathcal{C}_1$, as is demonstrated in Fig. 5.1(e), where we plot the noise added to the signal [63, 66, 210],

$$\mathcal{N}(\omega) = \mathcal{G}^{-1}\sum_{i\neq a_1}(n_i+1/2)|S_{i\to a_2}(\omega)|^2 \tag{5.1.11}$$

where we sum over all modes, with associated thermal occupation n_i, and scattering amplitude to the second cavity $S_{i\to a_2}$. Using Eq. (5.1.9), and denoting thermal cavity (mechanical) occupations by $n_{\mathrm{c},i}$ ($n_{\mathrm{m},i}$), the noise on resonance

$$\mathcal{N}_{\mathrm{DPPA}} = \frac{1}{4\mathcal{C}_1}\left(n_{\mathrm{m},1}+n_{\mathrm{m},2}+1\right) + \frac{(\mathcal{C}_1+\mathcal{C}_2)^2}{4\mathcal{C}_1\mathcal{C}_2}\left(n_{\mathrm{c},2}+\frac{1}{2}\right). \tag{5.1.12}$$

As a result, for large $\mathcal{C}_1 \gtrsim \mathcal{C}_2$, and vanishing thermal occupation of the cavity input, we reach the quantum limit of half a quantum of added noise, $\mathcal{N}_{\mathrm{DPPA}} \to 1/2$ (cf. Sec. 1.8 and Refs 63 and 66).

Another important figure of merit is noise emerging from cavity 1, characterized by the normal-ordered output noise spectral density, $S^N_{a_{1,\mathrm{out}}}(\omega) \equiv \int \frac{\mathrm{d}\omega'}{2\pi}\langle \hat{a}^\dagger_{1,\mathrm{out}}(\omega)\hat{a}_{1,\mathrm{out}}(\omega')\rangle$, which we plot in Fig. 5.1(f). Ultimately, the reason for building directional amplifiers is to reduce this figure. On resonance, $S^N_{1,\mathrm{out}}(0) = (n_{\mathrm{m},1}+n_{\mathrm{m},2})/2$. Strategies to reduce this figure are discussed below.

The off-resonance behaviour of the DPPA is remarkably rich and depends on the dimensionless quantities $\kappa_i/\Gamma_{\mathrm{m},j}, \mathcal{C}_1, \mathcal{C}_2$. We plot forward gain, reverse gain, added noise, and the noise spectrum at cavity 1 as functions of frequency at cooperativities $\mathcal{C}_1 = \{1,3,10,30\}, \mathcal{C}_2 = \mathcal{C}_1 - 0.1\sqrt{\mathcal{C}_1}$ in Fig. 5.1(c-f). $\mathcal{C}_2$ is chosen such that when increasing $\mathcal{C}_1$ both gain and bandwidth are enhanced.

We show in the Sec. 5.1.1 that for $\Gamma_{\mathrm{m},j} = \Gamma_{\mathrm{m}}$ and $\kappa_i = \kappa$ and in the regime where $\kappa/\Gamma_{\mathrm{m}} \gg \{1, \mathcal{C}_1, \mathcal{C}_2\}$ the gain bandwidth is $\Gamma = 2(\mathcal{C}_1-\mathcal{C}_2)\Gamma_{\mathrm{m}}$, giving a gain-bandwidth product $P \equiv \sqrt{\mathcal{G}}\Gamma = 4\sqrt{\mathcal{C}_1\mathcal{C}_2}\Gamma_{\mathrm{m}}$ [cf. Fig. 5.1(c)]. As the gain gets large and $\mathcal{C}_1, \mathcal{C}_2$ dominate all other dimensionless parameters, the bandwidth approaches $\Gamma = \kappa(\mathcal{C}_1-\mathcal{C}_2)/\mathcal{C}_1$, leading to the gain-bandwidth product limit $P \equiv \Gamma\sqrt{\mathcal{G}} \to 2\kappa$, independent of $\kappa/\Gamma_{\mathrm{m}}$. Close to resonance, the reverse scattering amplitude $S_{a_2\to a_1}(\omega) \approx -i\omega\sqrt{\mathcal{G}}/\Gamma_{\mathrm{m}}$ such that the

product of isolation bandwidth and gain is $\Gamma_{\rm m}$. Since the gain bandwidth is larger than the isolation bandwidth, there is large reverse gain off resonance [cf. Fig. 5.1(d)], and noise from cavity 2 dominates the noise spectral density at cavity 1 [cf. Fig. 5.1(f)]. With increasing effective mechanical linewidth $\Gamma_{\rm m}$ (through additional sideband cooling), the isolation bandwidth grows, suppressing reverse gain off resonance (cf. red, dashed curve in Fig. 5.1 and Ref. 191). In Sec. 5.A we calculate how off-resonant terms renormalize the parameters of the DPPA.

5.1.1 Bandwidth and gain-bandwidth product of DPPA

In this section we given further details on the calculation of the isolation and gain bandwidths in various parameter regimes.

For $\Gamma_{\rm m,1}=\Gamma_{\rm m,2}=\Gamma_{\rm m}$ and $\kappa_1=\kappa_2=\kappa$, the scattering amplitudes are

$$S_{a_2^\dagger\to a_1}(\omega)=(-i\omega)\sqrt{2\mathcal{C}_2(2\mathcal{C}_1-1)}/\mathcal{A}(\omega), \tag{5.1.13a}$$

$$S_{a_1\to a_2^\dagger}(\omega)=\sqrt{2\mathcal{C}_2(2\mathcal{C}_1-1)}(i\omega-\Gamma_{\rm m})/\mathcal{A}(\omega), \tag{5.1.13b}$$

with

$$\begin{aligned}\mathcal{A}(\omega)=(\Gamma_{\rm m}\kappa^2)^{-1}\{&i\omega(\Gamma_{\rm m}-i\omega)(\kappa-2i\omega)^2+\mathcal{C}_1\Gamma_{\rm m}(\kappa-2i\omega)[\Gamma_{\rm m}\kappa-i(\Gamma_{\rm m}+\kappa)\omega]\\&+\mathcal{C}_2\Gamma_{\rm m}\kappa[2\omega^2+i(\Gamma_{\rm m}+\kappa)\omega-\Gamma_{\rm m}\kappa]\}.\end{aligned} \tag{5.1.14}$$

For the gain-bandwidth product, we are most interested in the limit of large gain, $\mathcal{G}\gg 1$. This implies $(\mathcal{C}_1-\mathcal{C}_2)^2\ll 4\mathcal{C}_1\mathcal{C}_2<2(\mathcal{C}_1+\mathcal{C}_2)^2$. We further assume $\mathcal{C}_1\gg\{1,\Gamma_{\rm m}/\kappa,\kappa/\Gamma_{\rm m}\}$, in which case the first term in the curly brackets in Eq. (5.1.14) can be neglected. In this approximation,

$$\mathcal{A}(\omega)=\kappa^{-2}\left\{(\mathcal{C}_1+\mathcal{C}_2)\left[-i\omega\Gamma_{\rm m}(\kappa-i\omega)\right]+(\mathcal{C}_1-\mathcal{C}_2)\left[\Gamma_{\rm m}(\kappa-i\omega)^2-i\kappa\omega(\kappa-2i\omega)\right]\right\}. \tag{5.1.15}$$

The bandwidth is approximated by the smallest $|\omega|$ at which $2|\mathcal{A}(0)|^2=|\mathcal{A}(\omega)|^2$. Expanding both square brackets to first order in ω, we find that the amplitude bandwidth is approximately

$$\Gamma=\frac{2\Gamma_{\rm m}(\mathcal{C}_1-\mathcal{C}_2)}{2\mathcal{C}_1\frac{\Gamma_{\rm m}}{\kappa}+\left(1+\frac{\Gamma_{\rm m}}{\kappa}\right)(\mathcal{C}_1-\mathcal{C}_2)}. \tag{5.1.16}$$

The gain-bandwidth product $P\equiv\Gamma\sqrt{\mathcal{G}}$ is

$$P=\frac{2\Gamma_{\rm m}\sqrt{4\mathcal{C}_1\mathcal{C}_2}}{2\mathcal{C}_1\frac{\Gamma_{\rm m}}{\kappa}+\left(1+\frac{\Gamma_{\rm m}}{\kappa}\right)(\mathcal{C}_1-\mathcal{C}_2)}. \tag{5.1.17}$$

In the limit of large gain, with $\mathcal{C}_2 \to \mathcal{C}_1$ and $2\mathcal{C}_1 \gg \mathcal{C}_1 - \mathcal{C}_2$, P tends to 2κ.

We will now analyze the limits $\kappa \gg \Gamma_\mathrm{m}$ and $\kappa \ll \Gamma_\mathrm{m}$, but note that they are only valid as long as $\mathcal{C}_1$ is smaller than the ratio κ/Γ_m and Γ_m/κ, respectively. In the limit $\kappa/\Gamma_\mathrm{m} \gg \{1, \mathcal{C}_1, \mathcal{C}_2\}$, we obtain

$$\mathcal{A}(\omega) \approx (\Gamma_\mathrm{m} - i\omega)\Gamma_\mathrm{m}^{-1}[\Gamma_\mathrm{m}(\mathcal{C}_1 - \mathcal{C}_2) + i\omega], \tag{5.1.18}$$

which yields an amplitude gain bandwidth

$$\Gamma = 2(\mathcal{C}_1 - \mathcal{C}_2)\Gamma_\mathrm{m} \tag{5.1.19}$$

and intensity bandwidth $\Gamma/2$. The gain-bandwidth product, defined as $P \equiv \Gamma\sqrt{\mathcal{G}}$ evaluates to

$$P = 2\sqrt{4\mathcal{C}_1\mathcal{C}_2}\Gamma_\mathrm{m}. \tag{5.1.20}$$

This implies that the gain-bandwidth product P increases with gain. When $\mathcal{C}_1\Gamma_\mathrm{m} \sim \kappa$ the approximation above breaks down, and as we have shown just above, the gain bandwidth product saturates to 2κ.

In the opposite limit, $\kappa \ll \Gamma_\mathrm{m}$, we instead have

$$\mathcal{A}(\omega) \approx \kappa^{-2}\Gamma_\mathrm{m}(\kappa - i\omega)\mathcal{C}_1^2[\kappa(\mathcal{C}_1 - \mathcal{C}_2)/(2\mathcal{C}_1) - i\omega], \tag{5.1.21}$$

which implies that the bandwidth is close to $\kappa(\mathcal{C}_1 - \mathcal{C}_2)/\mathcal{C}_1$ and thus $P \approx \kappa\sqrt{4\mathcal{C}_2/\mathcal{C}_1}$. For large gain, $P \approx 2\kappa$, as before.

The isolation bandwidth must be calculated separately. It is the range of frequencies over which sufficient isolation is attained. What sufficient means quantitatively has to be decided with a specific application in mind. Close to $\omega = 0$, to lowest order in ω, the reverse gain departs linearly from zero, namely

$$S_{a_2^\dagger \to a_1}(\omega) = -i\omega\frac{\sqrt{2\mathcal{C}_2(2\mathcal{C}_1 - 1)}}{\Gamma_\mathrm{m}(\mathcal{C}_1 - \mathcal{C}_2)} + \mathcal{O}(\omega^2) = -i\omega\sqrt{\mathcal{G}}/\Gamma_\mathrm{m} + \mathcal{O}(\omega^2). \tag{5.1.22}$$

Thus, the isolation bandwidth is of order $\Gamma_\mathrm{m}/\sqrt{\mathcal{G}}$, independent of κ.

5.1.2 Directional phase-preserving amplifier with only blue tones

Here we analyze the optomechanical plaquette with only pumps on the upper motional sidebands. While directional phase-preserving amplification is still possible, the signal

cannot be impedance matched. We choose coupling amplitudes as follows

$$\mathsf{G} = 0, \qquad \mathsf{J} = \frac{1}{2}\begin{pmatrix} e^{\frac{i\Phi}{2}}\sqrt{\mathcal{C}_1\Gamma_{\mathrm{m},1}\kappa_1} & e^{-\frac{i\Phi}{2}}\sqrt{\mathcal{C}_1\Gamma_{\mathrm{m},2}\kappa_1} \\ \sqrt{\mathcal{C}_2\Gamma_{\mathrm{m},1}\kappa_2} & \sqrt{\mathcal{C}_2\Gamma_{\mathrm{m},2}\kappa_2} \end{pmatrix}. \tag{5.1.23}$$

The analysis proceeds similarly to the DPPA, where Φ is again the plaquette phase. We choose the same detuning parameterization as before $\delta_1 = \delta\Gamma_{\mathrm{m},1}$ and $\delta_2 = -\delta\Gamma_{\mathrm{m},2}$, in which case the plaquette phase takes the same form as before [Eq. (6)]. However, if we look at the optical scattering matrix, we find

$$\begin{pmatrix} \hat{a}_{1,\mathrm{out}} \\ \hat{a}_{2,\mathrm{out}} \end{pmatrix} = \begin{pmatrix} -1 - \frac{4\mathcal{C}_1}{4\delta^2+1-2\mathcal{C}_1} & 0 \\ \frac{-16\delta\sqrt{\mathcal{C}_1\mathcal{C}_2(4\delta^2+1)}}{(4\delta^2-2\mathcal{C}_1+1)(4\delta^2-2\mathcal{C}_2+1)} & -1 - \frac{4\mathcal{C}_2}{4\delta^2-2\mathcal{C}_2+1} \end{pmatrix} \begin{pmatrix} \hat{a}_{1,\mathrm{in}} \\ \hat{a}_{2,\mathrm{in}} \end{pmatrix} + \text{mechanical noise}. \tag{5.1.24}$$

The cooperativities must obey $4\delta^2 + 1 > \mathcal{C}_i > 0$, where the first condition is required for stability and the second arises by definition, such that impedance matching is not possible. As a result, the input will be reflected and amplified. This property is already highly undesirable in a directional amplifier, since the main goal in designing a directional amplifier is protection of the system that emits the signal.

Amplification is obtained if either or both of the cooperativities approach $2\delta^2 + 1/2$. $\mathcal{C}_1 \to 2\delta^2 + 1/2$ leads to a lot of noise being emitted from cavity 1, both due to the reflection and due to amplified mechanical noise (not shown above). Hence, we consider $\mathcal{C}_2 = 2\delta^2 + 1/2 - \varepsilon$, for some small $\varepsilon > 0$, and $\mathcal{C}_1 = 1/2$. For $\delta^2 \gg \varepsilon$, we can then write

$$\begin{pmatrix} \hat{a}_{1,\mathrm{out}} \\ \hat{a}_{2,\mathrm{out}} \end{pmatrix} = \frac{\sqrt{4\delta^2+1}}{\sqrt{2}\delta} \begin{pmatrix} -\frac{1}{2\delta} & \frac{1}{2\delta} \\ -\frac{\delta(2\delta+i)+1}{\varepsilon} & \frac{\delta(2\delta-i)+1}{\varepsilon} \end{pmatrix} \begin{pmatrix} \hat{b}_{1,\mathrm{in}} \\ \hat{b}_{2,\mathrm{in}} \end{pmatrix} - \begin{pmatrix} 1+\frac{1}{2\delta^2} & 0 \\ \frac{4\delta^2+1}{\delta\varepsilon} & \frac{4\delta^2+1}{\varepsilon} \end{pmatrix} \begin{pmatrix} \hat{a}_{1,\mathrm{in}} \\ \hat{a}_{2,\mathrm{in}} \end{pmatrix}. \tag{5.1.25}$$

For large δ, the signal source is only subject to the reflected signal and noise at cavity 1, leading to the approximate scattering matrix

$$\begin{pmatrix} \hat{a}_{1,\mathrm{out}} \\ \hat{a}_{2,\mathrm{out}} \end{pmatrix} = \frac{\delta^2}{\varepsilon} \begin{pmatrix} 0 & 0 \\ -1 & 1 \end{pmatrix} \begin{pmatrix} \hat{b}_{1,\mathrm{in}} \\ \hat{b}_{2,\mathrm{in}} \end{pmatrix} + \begin{pmatrix} -1 & 0 \\ \frac{4\delta}{\varepsilon} & \frac{4\delta^2}{\varepsilon} \end{pmatrix} \begin{pmatrix} \hat{a}_{1,\mathrm{in}} \\ \hat{a}_{2,\mathrm{in}} \end{pmatrix}. \tag{5.1.26}$$

The suppression of mechanical noise works well for cavity 1, but cavity 2, where the signal emerges, is subject to amplified mechanical noise. As a consequence, the amplification is not quantum-limited, in addition to the lack of impedance matching. Interchanging $\mathcal{C}_1 \leftrightarrow \mathcal{C}_2$ leads to

$$\begin{pmatrix} \hat{a}_{1,\mathrm{out}} \\ \hat{a}_{2,\mathrm{out}} \end{pmatrix} = \frac{4\delta}{\sqrt{2}\varepsilon} \begin{pmatrix} -1 & 1 \\ -1 & 1 \end{pmatrix} \begin{pmatrix} \hat{b}_{1,\mathrm{in}} \\ \hat{b}_{2,\mathrm{in}} \end{pmatrix} + \begin{pmatrix} -\frac{4\delta^2}{\varepsilon} & 0 \\ -\frac{4\delta}{\varepsilon} & -1 \end{pmatrix} \begin{pmatrix} \hat{a}_{1,\mathrm{in}} \\ \hat{a}_{2,\mathrm{in}} \end{pmatrix}, \tag{5.1.27}$$

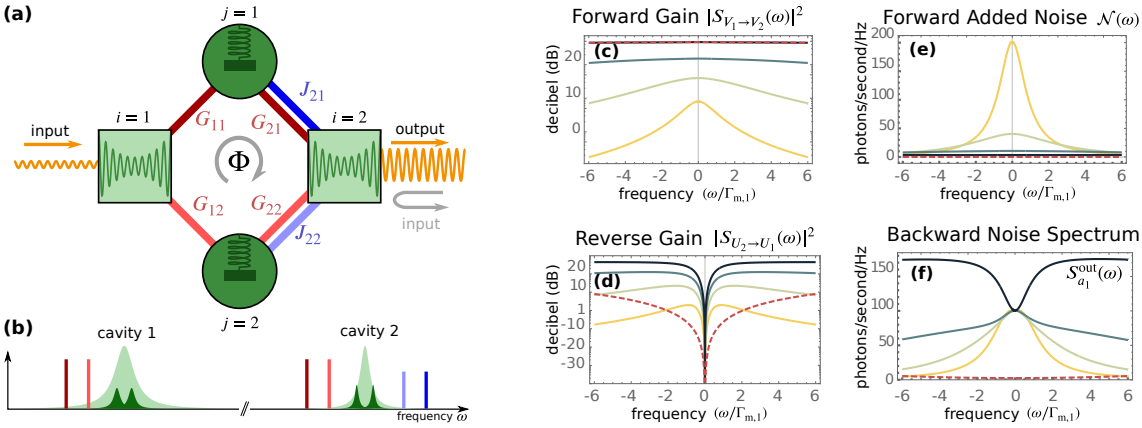

Figure 5.2: The directional phase-sensitive amplifier (DPSA). (a) Model. Single red hopping interactions are impedance matched, double red-blue provide the phase-sensitive amplification. **(b)** Pump setup. Cavity 1 is pumped on the red sidebands of the mechanical resonators, whereas cavity 2 has pumps on the red and blue sidebands. In **(c-f)** we plot forward gain, reverse gain [cf. Eq. (5.1.9)], added noise [Eq. (5.1.12)], and the output noise fluctuation spectrum of cavity 1, all as functions of frequency in units of $\Gamma_{\mathrm{m},1}$, for cooperativities $\mathcal{C}_1 = \{1, 3, 10, 30\}$, $\mathcal{C}_2 = \mathcal{C}_1^2$ (yellow to black, or light to dark). The parameters are the same as in Fig. 5.1. Depending on parameters, external sideband cooling with an auxiliary mode can achieve $n_{\mathrm{m},j} \approx 0$, without negatively affecting amplification properties, as described below. The red (dashed) curve in each plot illustrates this case, with $\mathcal{C}_1 = 30$ and effective parameters $n_{\mathrm{eff},i} = n_{\mathrm{m},i}(\Gamma_{\mathrm{m},i}/\Gamma_{\mathrm{eff},i}), \Gamma_{\mathrm{eff},i} = 50\Gamma_{\mathrm{m},i}$.

i.e., the amplification is quantum-limited, but the signal source is subject to amplified mechanical and optical noise. Thus, we conclude that an impedance-matched, quantum-limited DPPA with only blue tones is not feasible.

5.2 Directional phase-sensitive amplifier (DPSA)

We now turn to an implementation of a DPSA, which necessitates six tones. Essentially, we replace the amplifier interaction in the DPPA by a phase-sensitive quantum non-demolition (QND) interaction that couples one quadrature of cavity 2 to only one quadrature of the mechanical resonator [137, 139]. This is done by choosing

$$\mathsf{G} = \frac{1}{2}\begin{pmatrix} e^{i\Phi/2}\sqrt{\mathcal{C}_1\Gamma_{\mathrm{m},1}\kappa_1} & e^{-i\Phi/2}\sqrt{\mathcal{C}_1\Gamma_{\mathrm{m},2}\kappa_1} \\ \sqrt{\mathcal{C}_2\Gamma_{\mathrm{m},1}\kappa_2} & \sqrt{\mathcal{C}_2\Gamma_{\mathrm{m},2}\kappa_2} \end{pmatrix}, \tag{5.2.1}$$

and the same J as for the DPPA [Eq. (5.1.2)], illustrated in Fig. 5.2(a,b). Since the QND interaction requires $|G_{i2}| = |J_{i2}|$, and we require symmetric amplifier arms, two cooperativities suffice to characterize the six tones. Of the six phases in G, J, two are fixed

by requiring that the same input quadrature scatters to the two mechanical resonators, $\mu = \arg(G_{11}\chi_{\mathrm{m},1}(0)G_{21}/J_{21}) = \arg(\pm G_{12}\chi_{\mathrm{m},2}(0)G_{22}/J_{22})$, and another two by requiring that the quadratures on the resonators that contain the information both emerge in the same cavity quadrature, $\nu = \arg(G_{21}J_{21}) = \arg(\pm G_{22}J_{22})$. The two phases μ and ν thus determine the quadratures involved in amplification. The two remaining phases are an arbitrary mechanical phase, and the plaquette phase.

While there is no parametric instability of the kind that limits back-action evading measurements [140, 143], we show in the Sec. 5.C that counterrotating terms induce an instability threshold for finite sideband parameter (similar to Ref. 211), and the RWA is only valid for sideband parameters that are bigger than the cooperativities. This is not out of reach [93], but needs to be taken into account in experimental design.

The isolation, detuning, and impedance-matching conditions coincide with those of the DPPA, and we obtain another central result, the scattering matrix

$$\begin{pmatrix} \hat{U}_{1,\mathrm{out}} \\ \hat{V}_{1,\mathrm{out}} \\ \hat{U}_{2,\mathrm{out}} \\ \hat{V}_{2,\mathrm{out}} \end{pmatrix} = \begin{pmatrix} 0 & 0 & 0 & 0 \\ 0 & 0 & 0 & 0 \\ 0 & 0 & -1 & 0 \\ 0 & \sqrt{\mathcal{G}} & 0 & -1 \end{pmatrix} \begin{pmatrix} \hat{U}_{1,\mathrm{in}} \\ \hat{V}_{1,\mathrm{in}} \\ \hat{U}_{2,\mathrm{in}} \\ \hat{V}_{2,\mathrm{in}} \end{pmatrix} + \frac{1}{\sqrt{2}} \begin{pmatrix} 1 & 0 & -1 & 0 \\ 0 & 1 & 0 & -1 \\ 0 & 0 & 0 & 0 \\ \sqrt{2\mathcal{F}} & 0 & \sqrt{2\mathcal{F}} & 0 \end{pmatrix} \begin{pmatrix} \hat{X}_{1,\mathrm{in}} \\ \hat{P}_{1,\mathrm{in}} \\ \hat{X}_{2,\mathrm{in}} \\ \hat{P}_{2,\mathrm{in}} \end{pmatrix}, \tag{5.2.2}$$

where we defined noise scattering intensity $\mathcal{F} \equiv 4\mathcal{C}_2/\mathcal{C}_1^2$, gain

$$\mathcal{G} = \frac{8\mathcal{C}_2(2\mathcal{C}_1 - 1)}{\mathcal{C}_1^2}, \tag{5.2.3}$$

mechanical quadratures $\hat{X}_i = (b_i + b_i^\dagger)/\sqrt{2}$, $\hat{P}_i = i(b_i^\dagger - b_i)/\sqrt{2}$, and optical quadratures $\hat{U}_i = (\hat{a}_i + \hat{a}_i^\dagger)/\sqrt{2}$, $\hat{V}_i = i(\hat{a}_i^\dagger - \hat{a}_i)/\sqrt{2}$.

The amplifier is phase-sensitive and directional, as only the phase quadrature of the second cavity, $\hat{V}_2$, inherits the amplified signal from the phase quadrature of the first cavity, $\hat{V}_1$. We calculate the noise added to the signal as before

$$\mathcal{N}_{\mathrm{DPSA}} = \frac{n_{\mathrm{m},1} + n_{\mathrm{m},2} + 1}{2(2\mathcal{C}_1 - 1)} + \frac{\mathcal{C}_1}{8\mathcal{C}_2}\frac{\mathcal{C}_1}{2\mathcal{C}_1 - 1}\left(n_{\mathrm{c},2} + \frac{1}{2}\right). \tag{5.2.4}$$

The crucial difference to the DPPA is that the noise stemming from reflection of fluctuations at cavity 2 can *also* be suppressed, such that in the limit $\mathcal{C}_2 \gg \mathcal{C}_1 \gg 1$ added noise vanishes.

To investigate the off-resonant behaviour of the DPSA, we plot forward gain, reverse gain, added noise, and spectral noise density at cavity 1 in Fig. 5.2(c-f) at cooperativities $\mathcal{C}_1 = \{1, 3, 10, 30\}, \mathcal{C}_2 = \mathcal{C}_1^2$. Increasing $\mathcal{C}_1$ enhances bandwidth and gain [cf. Fig. 5.2(c)].

At the same time, the mechanical noise is suppressed [cf. Fig. 5.2(e)]. As calculated in more detail in Sec. 5.2.1 below, close to resonance, the reverse scattering behaves the same as for the DPPA $S_{a_2\to a_1}(\omega) \approx -i\omega\sqrt{\mathcal{G}}/\Gamma_\mathrm{m}$, and the same conclusions apply [cf. Fig. 5.2(d,f)]. The gain-isolation-bandwidth product is Γ_m. Forward and reverse gain are proportional to $\sqrt{\mathcal{C}_2}$, implying an unlimited gain-bandwidth product (cf. Sec. 5.2.1). For equivalent mechanical resonators $\Gamma_{\mathrm{m},1} = \Gamma_{\mathrm{m},2} = \Gamma_\mathrm{m}$ and in the limit $\kappa/\Gamma_\mathrm{m} \gg \{1, \mathcal{C}_1\}$, the amplitude gain bandwidth of the DPSA is well approximated by $\Gamma_\text{gain} = 2\mathcal{C}_1\Gamma_\mathrm{m}$.

5.2.1 Bandwidth and gain-bandwidth product of DPSA

For the DPSA, we find the scattering amplitudes

$$S_{a_1\to a_2^\dagger}(\omega) = \sqrt{2\mathcal{C}_2(2\mathcal{C}_1-1)}(i\omega-\Gamma_\mathrm{m})/\mathcal{B}(\omega), \tag{5.2.5a}$$

$$S_{a_2^\dagger\to a_1}(\omega) = \sqrt{2\mathcal{C}_2(2\mathcal{C}_1-1)}(-i\omega)/\mathcal{B}(\omega), \quad \text{with} \tag{5.2.5b}$$

$$\mathcal{B}(\omega) = (\Gamma_\mathrm{m}\kappa^2)^{-1}(\kappa-i\omega)\{\mathcal{C}_1\Gamma_\mathrm{m}[\Gamma_\mathrm{m}\kappa - i\omega(\Gamma_\mathrm{m}+\kappa)] - (\kappa-2i\omega)i\omega(\Gamma_\mathrm{m}-i\omega)\}. \tag{5.2.5c}$$

Since both $S_{2\to1} \propto \sqrt{\mathcal{C}_2}$ and $S_{1\to2} \propto \sqrt{\mathcal{C}_2}$, we can immediately conclude that the bandwidth is independent of the gain, and the gain-bandwidth product therefore unlimited. Ultimately, the reason for this is that the amplified quadratures are QND variables, such that there is no dynamical backaction, similar to the BAE measurement (Fig. 3.7).

For $\{\mathcal{C}_1\omega, \mathcal{C}_1\Gamma_\mathrm{m}\} \ll \kappa$, we find

$$\mathcal{B}(\omega) \approx (\Gamma_\mathrm{m}-i\omega)\Gamma_\mathrm{m}^{-1}(\mathcal{C}_1\Gamma_\mathrm{m}-i\omega), \tag{5.2.6}$$

and therefore

$$S_{1\to2}(\omega) \approx \frac{\sqrt{2\mathcal{C}_2(2\mathcal{C}_1-1)}\Gamma_\mathrm{m}}{-(\mathcal{C}_1\Gamma_\mathrm{m}-i\omega)}, \qquad S_{2\to1}(\omega) \approx \frac{\sqrt{2\mathcal{C}_2(2\mathcal{C}_1-1)}i\omega\Gamma_\mathrm{m}}{-(\Gamma_\mathrm{m}-i\omega)(\mathcal{C}_1\Gamma_\mathrm{m}-i\omega)}, \tag{5.2.7}$$

such that the gain bandwidth $\Gamma_{1\to2} = 2\mathcal{C}_1\Gamma_\mathrm{m}$.

To study the departure from isolation, we expand the reverse gain around $\omega = 0$. To first order (note that we do *not* assume $\{\mathcal{C}_1\omega, \mathcal{C}_1\Gamma_\mathrm{m}\} \ll \kappa$ here)

$$S_{2\to1}(\omega) = -i\omega\frac{\sqrt{2\mathcal{C}_2(2\mathcal{C}_1-1)}}{\mathcal{C}_1\Gamma_\mathrm{m}} + \mathcal{O}(\omega^2) = -i\omega\sqrt{\mathcal{G}}/\Gamma_\mathrm{m} + \mathcal{O}(\omega^2). \tag{5.2.8}$$

Thus, the isolation bandwidth is again of order $\Gamma_\mathrm{m}/\sqrt{\mathcal{G}}$ (but note that $\mathcal{G}$ takes different forms for DPSA and DPPA), independent of κ.

5.3 Backward propagating noise and sideband cooling

The noise emitted in the reverse direction is of central importance for directional amplifiers. For both DPPA and DPSA, the output noise spectral density of cavity 1 on resonance is $S^N_{1,\mathrm{DPSA}}(0) = S^N_{1,\mathrm{DPPA}}(0) = (n_{\mathrm{m},1} + n_{\mathrm{m},2})/2$. Due to vanishing reflection and directionality, fluctuations incident on the in input port of either cavities do not appear in $a_{1,\mathrm{out}}$ [cf. Eqs. (5.1.9) and (5.2.2)]. The commutation relations of $a_{1,\mathrm{out}}$ then imply $\sum_{j=1}^{2}(|S_{b_i\to a_1}(0)|^2 - |S_{b_i^\dagger\to a_1}(0)|^2) = 1$, i.e, mechanical fluctuations have to appear in the output instead. The lowest possible value for $S_{1,\mathrm{out}}$ is 0, attainable for zero thermal noise quanta in the mechanical resonators.

However, even in state-of-the-art dilution refrigerators, the temperatures required for ground state cooling of the mechanical modes are out of reach, due to their low frequencies. One way to mitigate backward noise emission is to add another microwave mode to the setup that can replace the fluctuations in the output of cavity 1, essentially realizing a circulator. Without modifying the theory above, one can either increase the resonance frequency of the mechanical modes, which is mainly a technological challenge, or one could resort to external sideband cooling with an auxiliary mode. The latter can achieve $n_{\mathrm{m}} \to 0$ [42, 43, 212], and has the added benefit of enhancing mechanical linewidths [cf. red (dashed) curve in Figs. 5.1 and 5.2 and Sec. 5.B], though note that for the DPSA there is an additional stringent requirement on the sideband parameter. Whilst this could be done with an additional cavity mode for each resonator, implementing a circuit with four cavity modes coupled to two mechanical resonators is a formidable technical challenge. A problem arises when cooling with only one additional mode, since it can lead to a coupling of the mechanical resonators via the extra cooling mode, thereby changing the topology of the system thus spoiling directionality. As we show in Sec. 5.B, this can be mitigated by detuning each pump by several mechanical linewidths, making cooling with only one additional mode feasible.

5.4 Connection to Metelmann-Clerk recipe for directionality

In this section we relate the calculations above to the method for constructing nonreciprocal interactions presented in Ref. 191, which can be understood in terms of reservoir engineering. Clearly, both conditions in Eq. (5.1.3) can only be fulfilled for complex susceptibilities, underscoring the importance of dissipation. In order to distinguish coherent and dissipative parts of the coupling, we compare Eq. (3) with the equations of motion for a nondegenerate

parametric amplifier with interaction Hamiltonian

$$\hat{H}_{\text{int}} = \lambda \hat{a}_1^\dagger \hat{a}_2^\dagger + \text{H.c.}, \tag{5.4.1}$$

namely

$$\left(\frac{\kappa_1}{2} + \partial_t\right)\langle \hat{\mathbf{A}}_1\rangle = i\begin{pmatrix} 0 & -\lambda \\ \lambda^* & 0 \end{pmatrix}\langle \hat{\mathbf{A}}_2\rangle, \qquad \left(\frac{\kappa_2}{2} + \partial_t\right)\langle \hat{\mathbf{A}}_2\rangle = i\begin{pmatrix} 0 & -\lambda \\ \lambda^* & 0 \end{pmatrix}\langle \hat{\mathbf{A}}_1\rangle, \tag{5.4.2}$$

where $\hat{\mathbf{A}}_i \equiv (\hat{a}_i, \hat{a}_i^\dagger)^T$. The phase of λ is arbitrary, as it is determined by the origin of time when going into the rotating frame. Equation (5.4.2) suggests that coherent and dissipative interaction mediated by the mechanical resonators are the sum and difference of $i\mathsf{T}_{12}$ and $i\mathsf{T}_{21}$. Thus, the coherent part is

$$\lambda = \sum_i \text{Re}[\chi_{\text{m},i}(0)]G_{i1}J_{i2} = \sum_i \frac{2\Gamma_{\text{m},i}G_{i1}J_{i2}}{\Gamma_{\text{m},i}^2 + 4\delta_i^2}, \tag{5.4.3}$$

whereas the dissipative part of the interaction is

$$i\sigma = \sum_i i\,\text{Im}[\chi_{\text{m},i}(0)]G_{i1}J_{i2} = i\sum_i \frac{4\delta_i G_{i1}J_{i2}}{\Gamma_{\text{m},i}^2 + 4\delta_i^2}. \tag{5.4.4}$$

Directionality is attained for $\lambda + i\sigma = 0$, but $\lambda, \sigma \neq 0$, such that $\lambda - i\sigma \neq 0$, a condition that the driving strengths in Eq. (5.1.2) fulfil. For the DPPA, with Eq. (5), and $\mathcal{C}_1 = 1$ for simplicity, the equations of motion are

$$(\kappa_1 + \partial_t)\langle \hat{\mathbf{A}}_1\rangle = i\begin{pmatrix} 0 & -\lambda - i\sigma \\ \lambda^* - i\sigma^* & 0 \end{pmatrix}\langle \hat{\mathbf{A}}_2\rangle = 0, \tag{5.4.5a}$$

$$\left[\frac{\kappa_2}{2}(1-\mathcal{C}_2) + \partial_t\right]\langle \hat{\mathbf{A}}_2\rangle = i\begin{pmatrix} 0 & -\lambda + i\sigma \\ \lambda^* + i\sigma^* & 0 \end{pmatrix}\langle \hat{\mathbf{A}}_1\rangle = 2i\begin{pmatrix} 0 & \lambda \\ -\lambda^* & 0 \end{pmatrix}\langle \hat{\mathbf{A}}_1\rangle, \tag{5.4.5b}$$

with

$$\lambda = i\mathsf{T}_{12}(0)/2. \tag{5.4.6}$$

Now that we have discerned which part of the interaction is dissipative and which is coherent, we can map onto a quantum master equation. Following Ref. 191, the way to make a coherent interaction $H = J\hat{a}_1^\dagger \hat{a}_2^\dagger + \text{H.c.}$ directional is by introducing a dissipative

term in the QME of the form $\Gamma\mathcal{L}[\hat{z}]\hat{\rho}$, with

$$\hat{z} = \sqrt{2}(\cos\theta\hat{a}_1 + e^{i\varphi}\sin\theta\hat{a}_2^\dagger). \tag{5.4.7}$$

Directionality is obtained for the appropriate choice of θ and φ. Indeed, we have

$$\langle\dot{\hat{a}}_1\rangle = -\left(\kappa_1/2 + \Gamma\cos^2\theta\right)\langle\hat{a}_1\rangle + \left(iJ - \Gamma\sin\theta\cos\theta e^{i\varphi}\right)\langle\hat{a}_2^\dagger\rangle, \tag{5.4.8a}$$
$$\langle\dot{a}_2^\dagger\rangle = -\left(\kappa_2/2 - \Gamma\sin^2\theta\right)\langle\hat{a}_2^\dagger\rangle - \left(iJ^* - \Gamma\sin\theta\cos\theta e^{-i\varphi}\right)\langle\hat{a}_1\rangle. \tag{5.4.8b}$$

Setting Γ and θ such that $\Gamma\sin\theta\cos\theta e^{i\varphi} = iJ$,

$$\left(\frac{\kappa_1}{2} + |J\cot\theta| + \partial_t\right)\langle\hat{a}_1\rangle = 0, \tag{5.4.9a}$$
$$\left(\frac{\kappa_2}{2} - |J\tan\theta| + \partial_t\right)\langle\hat{a}_2^\dagger\rangle = -2iJ^*\langle a_1\rangle. \tag{5.4.9b}$$

With $J = \lambda$, the RHS of Eq. (5.4.9) matches Eq. (5.4.5).

In order to appropriately map the Langevin equations onto a master equation, we have to take into account that there are *two* coherent interactions and *two* baths. Therefore, we have to repeat this procedure twice, making the two parts of the coherent interaction

$$i\lambda_1 = \mathrm{Re}[\chi_{\mathrm{m},1}(0)]G_{11}J_{12} = \frac{\sqrt{\kappa_1\kappa_2\mathcal{C}_2}}{4}e^{i\Phi/2}, \tag{5.4.10a}$$
$$i\lambda_2 = \mathrm{Re}[\chi_{\mathrm{m},2}(0)]G_{21}J_{22} = \frac{\sqrt{\kappa_1\kappa_2\mathcal{C}_2}}{4}e^{-i\Phi/2} \tag{5.4.10b}$$

individually directional. This yields

$$\left(\frac{\kappa_1}{2} + \sum_i |\lambda_i\cot\theta_i| + \partial_t\right)\langle\hat{a}_1\rangle = 0, \tag{5.4.11a}$$
$$\left(\frac{\kappa_2}{2} - \sum_i |\lambda_i\tan\theta_i| + \partial_t\right)\langle\hat{a}_2^\dagger\rangle = -2(i\lambda_1^* + i\lambda_2^*)\langle\hat{a}_1\rangle. \tag{5.4.11b}$$

Impedance matching gives $\tan\theta_i = 4|\lambda_1|/\kappa_1$, and we recover Eq. (5.4.5).

To illustrate why two baths are necessary, consider again Eq. (5.4.9), which only has one bath. Choosing θ such that $|\cot\theta| = \kappa_1/(2|J|)$ (impedance matching), we do not quite recover Eq. (5.4.5), but instead find

$$\frac{\kappa_2}{2}(1 - \mathcal{C}_2/2)\langle\hat{a}_2^\dagger\rangle = -2i\lambda^*\langle\hat{a}_1\rangle. \tag{5.4.12}$$

Whilst this leads to the same interaction (RHS), the self-energies on the LHS differ.

Therefore, we need to theoretically include both baths in order to obtain an accurate representation of our system. The reason for the factor of 2 difference lies in the fact that the coherent interactions differ by $\pi/2$ in phase, such that $|\lambda| = (|\lambda_1| + |\lambda_2|)/\sqrt{2}$ [cf. Eq. (5.4.6)].

5.5 Conclusion

We have presented quantum-limited, nonreciprocal amplifiers using an optomechanical plaquette comprising two cavities and intermediate mechanical resonators [3, 53]. Such devices carry great promise, as they can be integrated into superconducting circuits and amplify near or at the quantum limit, whilst protecting the signal source from noise. Upon reaching maturity they may become a central component of superconducting circuit quantum computers.

Appendix

5.A Off-resonant terms

In most of this chapter, we have neglect all time-dependent terms in the Hamiltonian. When calibrating pumps and phases, their effect will have to be included. Below, we answer three questions about counterrotating terms. First, do they change the topology of the circuit and therefore make directionality impossible? We find that to a good approximation this is not the case, as we analyze in Sec. 5.A. Second, do off-resonant terms change the effective parameters of the circuit? As in previous studies the answer is yes, detailed in Sections 5.A and 5.C. Third, can off-resonant terms lead to an instability? Again the answer is yes, for sufficiently strong driving or sufficiently low sideband parameter, as described in Sec. 5.C. We also find that the RWA theory is valid for large but finite sideband parameter, after taking into account the effective parameters.

There are two kinds of off-resonant terms contained in Eq. (4.1.4). One, which we term *counterrotating terms*, which have a time-dependence $\mathcal{O}(2\omega_{\mathrm{m},i})$, which are usually negligible. The other are much slower *off-resonant terms* rotating at frequency $\Omega = \omega_{\mathrm{m},2} + \delta_2 - \omega_{\mathrm{m},1} - \delta_1$, which can have an appreciable effect [3, 53]. For a related study see Ref. 143. The Hamiltonian describing the off-resonant terms is

$$\begin{aligned}\hat{H}_{\text{off-resonant}}(t) = &-\sum_i \hat{a}_i^\dagger \Big[g_{0,i2}\alpha_{i1+}\hat{b}_2^\dagger e^{i\Omega t} + g_{0,i2}\alpha_{i1+}\hat{b}_2 e^{-i\Omega t} + g_{0,i1}\alpha_{i2+}\hat{b}_1^\dagger e^{-i\Omega t} \\ &+ g_{0,i1}\alpha_{i2+}\hat{b}_1 e^{i\Omega t}\Big] + \text{H.c.} \\ = &-\sum_i \hat{a}_i^\dagger \left[e^{i\Omega t}\left(\tilde{J}_{i2}\hat{b}_2^\dagger + \tilde{G}_{i1}\hat{b}_1\right) + e^{-i\Omega t}\left(\tilde{G}_{i2}\hat{b}_2 + \tilde{J}_{i1}\hat{b}_1^\dagger\right)\right] + \text{H.c},\end{aligned} \tag{5.A.1}$$

where $\tilde{G}_{i1} = G_{i2}g_{0,i1}/g_{0,i2}$ (and the same for $G \leftrightarrow J$ and $1 \leftrightarrow 2$). Including $H_{\text{off-resonant}}$, the Hamiltonian is no longer time-independent, but rather periodic, with period $2\pi/\Omega$. The resulting explicitly time-dependent Langevin equations can be mapped to stationary ones by use of the Floquet formalism from Part I. Writing system operators in terms of Fourier components, for instance $\hat{b}(t) = \sum_n \exp(in\Omega t)\hat{b}^{(n)}(t)$, we obtain Langevin equations

without explicit time-dependence, which are thus diagonal in frequency space

$$\chi_{\mathrm{m},j}^{-1}(\omega - n\Omega)\hat{b}_j^{(n)}(\omega) = i\sum_{i=1}^{2}\left(\hat{a}_i^{(n)}G_{ij}^{*} + \hat{a}_i^{(n)\dagger}J_{ij}\right) + \delta_{n,0}\sqrt{\Gamma_{\mathrm{m},j}}\hat{b}_{j,\mathrm{in}} + i\sum_{i=1}^{2}\left(\hat{a}_i^{(n\pm1)}\tilde{G}_{ij}^{*} + \hat{a}_i^{(n\pm1)\dagger}\tilde{J}_{ij}\right), \tag{5.A.2a}$$

$$\chi_{\mathrm{c},i}^{-1}(\omega - n\Omega)\hat{a}_i^{(n)}(\omega) = i\sum_{j=1}^{2}\left(G_{ij}\hat{b}_j^{(n)} + J_{ij}\hat{b}_j^{(n)\dagger}\right) + \delta_{n,0}\sqrt{\kappa_i}\hat{a}_{i,\mathrm{in}} + i\left(\tilde{J}_{i2}\hat{b}_2^{(n-1)\dagger} + \tilde{G}_{i1}\hat{b}_1^{(n-1)} + \tilde{G}_{i2}\hat{b}_2^{(n+1)} + \tilde{J}_{i1}\hat{b}_1^{(n+1)\dagger}\right), \tag{5.A.2b}$$

where in Eq. (5.A.2)(a), $j = 1$ corresponds to the $+$-sign and $j = 2$ to the $-$-sign. Note that in our conventions $[\hat{b}^{(n)}(\omega)]^\dagger = \hat{b}^{(-n)}(-\omega)$. In principle, Eqs. (5.A.2) constitute an infinitely large set of coupled linear equations (equivalently, an infinitely large matrix to invert). However, the coupling between different Fourier modes is suppressed by the mechanical and optical susceptibilities. In particular, the mechanical susceptibilities are strongly peaked ($\Gamma_{\mathrm{m},i} \ll \Omega$), such that it is a good approximation to let $\hat{b}_j^{(n\neq 0)} = 0$. Since in this approximation $\hat{b}_j = \hat{b}_j^{(0)}$, we will omit the superscript (0) for $\hat{b}$ in the following. Another consequence of the approximation is $\hat{a}_i^{(n)} = 0$ for $|n| > 1$.

We can think of $\hat{a}_i^{(\pm1)}$ as four extra, "virtual modes", as is done in Ref. 53. They are given by

$$\hat{a}_i^{(1)}(\omega) = i\chi_{\mathrm{c},i}(\omega - \Omega)\left[\tilde{J}_{i2}\hat{b}_2^{\dagger}(\omega) + \tilde{G}_{i1}\hat{b}_1(\omega)\right], \tag{5.A.3a}$$

$$\hat{a}_i^{(-1)}(\omega) = i\chi_{\mathrm{c},i}(\omega + \Omega)\left[\tilde{J}_{i1}\hat{b}_1^{\dagger}(\omega) + \tilde{G}_{i2}\hat{b}_2(\omega)\right], \tag{5.A.3b}$$

whence we write down the new equation of motion for $\hat{b}$ in Fourier space, e.g.,

$$\chi_{\mathrm{m},1}^{-1}(\omega)\hat{b}_1(\omega) = i\sum_i\left[G_{i1}^{*}\hat{a}_i^{(0)} + J_{i1}\hat{a}_i^{(0)\dagger}\right] + \sqrt{\Gamma_{\mathrm{m},1}}\hat{b}_{1,\mathrm{in}} - \sum_i \chi_{\mathrm{c},i}(\omega - \Omega)\left[(|\tilde{G}_{i1}|^2 - |\tilde{J}_{i1}|^2)\hat{b}_1 + (\tilde{G}_{i1}^{*}\tilde{J}_{i2} - \tilde{J}_{i1}\tilde{G}_{i2}^{*})\hat{b}_2^{\dagger}\right]. \tag{5.A.4}$$

The two types of terms that appear due to the off-resonant terms is one proportional to b_1 that describes off-resonant cooling or heating, which can be incorporated into the susceptibility of the mechanical resonator, but also one that couples the first mechanical resonator to the second. The latter process only occurs when there is a drive on the red sideband of one resonator and one on the blue sideband of the other resonator. This is most easily understood when looking for example at the process underlying the term

$\chi_{\mathrm{m},1}(\omega-\Omega)\hat{b}_2^\dagger\tilde{G}_{11}^*\tilde{J}_{12}$. $\tilde{J}_{12}$ is an interaction that creates a phonon in resonator 2 and a photon in cavity 1, but the process is off-resonant, meaning that the frequency of the photon created is approximately $\omega_{\mathrm{c},1}-\Omega$. $\tilde{G}_{11}$ shifts the frequencies the other way, such that this term mediates a resonant interaction between the mechanical resonators, with an off-resonant intermediate state. In contrast, $\tilde{J}_{11}$ would create a phonon in resonator 1 and a photon in cavity at frequency $\omega_{\mathrm{c},1}+\Omega$. Thus the term $\tilde{J}_{11}\tilde{J}_{12}$ would produce a phonon with frequency $\omega_{\mathrm{m},1}-2\Omega$, a process that is strongly suppressed.

The spurious coupling between the resonators trivially vanishes in four-tone schemes, where one of G_{ij} or J_{ij} is zero for all i,j. For more tones, we have to find $\tilde{G}_{i1}^*\tilde{J}_{i2}-\tilde{J}_{i1}\tilde{G}_{i2}^* = G_{i1}^*J_{i2}-J_{i1}G_{i2}^*$. This vanishes for the DPSA, since in the case $i=1$, there are only red drives, and for $i=2$, the coupling strengths are the same $J_{2j}=G_{2j}$ [see Eq. (5.2.1)]. Thus we can eliminate the off-resonant Fourier modes and write their effect as a self energy that modifies the susceptibility $\chi_{\mathrm{m},i}^{-1}(\omega)\to\chi_{\mathrm{m},i}^{-1}(\omega)+\Sigma_1(\omega)$, with

$$\Sigma_1(\omega)=\sum_i\left(\frac{g_{0,i1}}{g_{0,i2}}\right)^2\chi_{\mathrm{c},i}(\omega-\Omega)\left(|G_{i2}|^2-|J_{i2}|^2\right) \tag{5.A.5}$$

(for b_2, we do $1\leftrightarrow 2$). For the DPPA, we obtain

$$\begin{aligned}\Sigma_1^{\mathrm{DPPA}}&=\left(\frac{g_{0,11}}{g_{0,12}}\right)^2\chi_{\mathrm{c},1}(\omega-\Omega)\frac{\mathcal{C}_1\Gamma_{\mathrm{m},2}\kappa_1}{4}-\left(\frac{g_{0,21}}{g_{0,22}}\right)^2\chi_{\mathrm{c},2}(\omega-\Omega)\frac{\mathcal{C}_2\Gamma_{\mathrm{m},2}\kappa_2}{4},\\ \Sigma_2^{\mathrm{DPPA}}&=\left(\frac{g_{0,12}}{g_{0,11}}\right)^2\chi_{\mathrm{c},1}(\omega-\Omega)\frac{\mathcal{C}_1\Gamma_{\mathrm{m},1}\kappa_1}{4}-\left(\frac{g_{0,22}}{g_{0,21}}\right)^2\chi_{\mathrm{c},2}(\omega-\Omega)\frac{\mathcal{C}_2\Gamma_{\mathrm{m},1}\kappa_2}{4},\end{aligned} \tag{5.A.6}$$

whereas for the DPSA, the self-energies read

$$\begin{aligned}\Sigma_1^{\mathrm{DPSA}}&=\left(\frac{g_{0,11}}{g_{0,12}}\right)^2\chi_{\mathrm{c},1}(\omega-\Omega)\frac{\mathcal{C}_1\Gamma_{\mathrm{m},2}\kappa_1}{4},\\ \Sigma_2^{\mathrm{DPSA}}&=\left(\frac{g_{0,12}}{g_{0,11}}\right)^2\chi_{\mathrm{c},1}(\omega-\Omega)\frac{\mathcal{C}_1\Gamma_{\mathrm{m},1}\kappa_1}{4}.\end{aligned} \tag{5.A.7}$$

Eqs. (5.A.7) do not have a contribution from the drives on the second cavity, because the blue and red drives are balanced, such that the dynamical backaction cancels.

In the end, in an approximation where we neglect the frequency dependence of the self energies [i.e., $\chi_{\mathrm{c},i}\approx(\kappa_i/2+i\Omega)^{-1}$], which is valid for small frequencies around resonance $\omega\ll\Omega,\kappa_i$, the effect of the complex self-energies can be subsumed as a change of damping and detuning parameters.

We stress again that the other important conclusion from this analysis is that the off-resonant terms do not change the topology of the circuit, neither in the DPPA nor in the

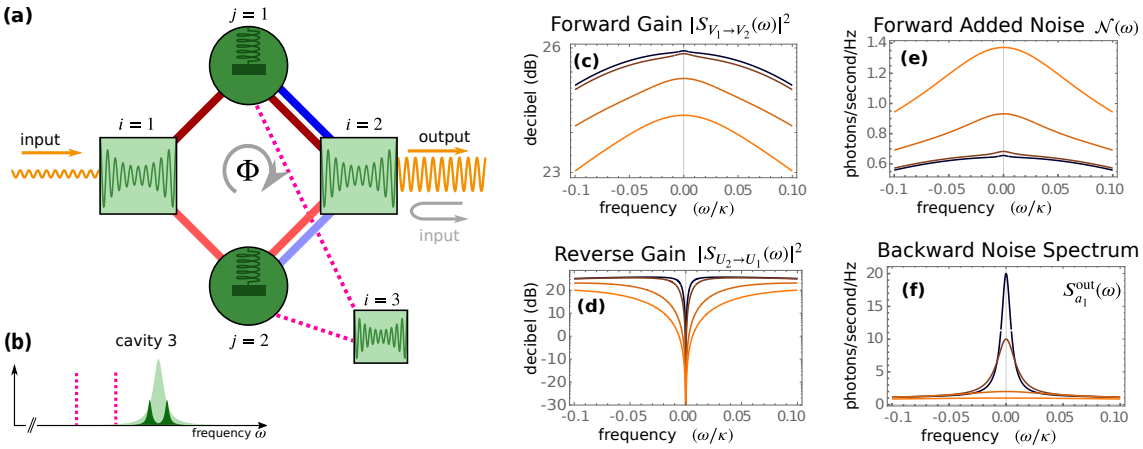

Figure 5.3: Off-resonant cooling with one extra mode. (a) The plaquette is extended with another cavity mode. It is clear from this figure that coupling this cavity mode to both mechanical resonators changes the topology of the plaquette. This is why we go into some length to show that detuning the extra mode by a sufficient amount mitigates this problem. (b) The third cavity mode is pumped with two tones close to the red sidebands of mechanical oscillators, at frequencies $\omega_{\mathrm{c},3} - \omega_{\mathrm{m},j} + \Delta_j$, with detunings $\Delta_1 = -\Delta_2 = \Delta \gg \Gamma_{\mathrm{m},j}$. The detuning ensures that phonons are prevented from hopping from one resonator to the other. (c-f) We plot forward gain, reverse gain, forward added noise, and backward noise spectrum for *fixed coupling strengths* (i.e., not fixed cooperativities), but with increasingly large off-resonant cooling. Parameters are $\kappa_2 = \kappa_1 = \kappa$, $\Gamma_{\mathrm{m},1} = \Gamma_{\mathrm{m},2} = \Gamma = 10^{-4}\kappa \times \Lambda$, $\delta_1 = \Gamma\delta, \delta_2 = -\Gamma\delta, \delta = \sqrt{2\mathcal{C}_1 - 1}$, $\mathcal{C}_1 = 4G_{11}^2/(\kappa\gamma)$, $G_{11} = \exp(i\Phi/2)0.2\kappa, G_{21}\exp(-i\Phi/2)0.2\kappa$, $G_{12} = G_{22} = J_{12} = J_{22} = 2\kappa, J_{11} = J_{21} = 0$, $n_{\mathrm{c},1} = n_{\mathrm{c}_2} = 0$, $n_{\mathrm{m},1} = n_{\mathrm{m},2} = 1000/\Lambda$. Cooling parameter takes the values $\Lambda = \{50, 100, 500, 1000\}$ as the colour of the curve varies from black to orange. Note that we plot these curves as functions of frequency in units of κ, unlike Figs. 5.1 and 5.2.

DPSA, such that the theory presented above applies to a very good approximation. The embedding into a Floquet ansatz explains how the extra modes and their properties arise in the description of Ref. 53.

5.B Off-resonant cooling with auxiliary mode

The above calculation can be repeated for the proposed off-resonant cooling with a third cavity mode. This involves two drives detuned from the sidebands of the mechanical resonator (or one drive roughly in the middle of the two sidebands). For instance, consider pumps at frequencies $\omega_{\mathrm{c},3} - \omega_{\mathrm{m},j} + \Delta_j$, where $\omega_{\mathrm{c},3}$ is the frequency of the third cavity mode, $\Delta_1 = \Delta$, $\Delta_2 = -\Delta$, and $\Delta \gg \Gamma_{\mathrm{m},j}$. This leads to similar off-resonant terms as above, namely,

$$\hat{H}_{\mathrm{cool}} = -\hat{a}_3^\dagger \left(e^{-i\Delta t} G_{31} \hat{b}_1 + e^{i\Delta t} G_{32} \hat{b}_2 \right) + \mathrm{H.c.} \tag{5.B.1}$$

This adds another contribution to the self-energy, similar to above

$$\Sigma_j^{\text{cool}}(\omega) = \chi_{\text{c},3}(\omega)|G_{3j}|^2 \approx \frac{2}{\kappa_3}|G_{3j}|^2. \tag{5.B.2}$$

The detuning choice ensures that phonons cannot hop from one resonator to the other via the auxiliary mode. The final result of this treatment is a new, enhanced damping rate Γ_{eff}. However, the noise strength in the Langevin equations is unchanged. We can write

$$\dot{\hat{b}} = \ldots + \sqrt{\Gamma_{\text{m}}}\hat{b}_{\text{in}} = \ldots + \sqrt{\Gamma_{\text{eff}}}\tilde{b}_{\text{in}}, \tag{5.B.3}$$

where the new effective noise has correlators $\langle \tilde{b}_{\text{in}}(t)\tilde{b}_{\text{in}}(t')\rangle = n_{\text{th}}\delta(t-t') \times (\Gamma_{\text{m}}/\Gamma_{\text{eff}}) = n_{\text{th}}\delta(t-t')/\Lambda$, where we have introduced a cooling parameter $\Lambda = \Gamma_{\text{eff}}/\Gamma_{\text{m}}$. In effect, we have modified parameters $\Gamma_{\text{eff}} = \Lambda\Gamma_{\text{m}}$ and $n_{\text{eff}} = n_{\text{th}}/\Lambda$, parametrize by Λ, with the remainder of the Langevin equations unchanged.

The effect of cooling with an additional drive is illustrated for the DPSA in Fig. 5.3. In this figure, we show the plaquette with the extra cooling mode, and plot the gain and noise in both directions for *fixed coupling constants*, but for varying levels of cooling Λ. The reason for keeping the coupling rates rather than the cooperativities unchanged is that high cooperativities become unattainable for strongly broadened mechanical resonators. We observe that the auxiliary cooling negatively affects gain, and forward added noise, which is due to the effective decrease in cooperativity. On the other hand, the isolation bandwidth is increased, since it depends on the mechanical linewidth. Most importantly though, the backward noise can be strongly reduced.

5.C Stability

5.C.1 Theory

It is important to know in which regimes the rotating-wave approximation (RWA) is valid. In order to numerically analyze the system beyond the RWA, we use the Hamiltonian Eq. (4.1.4), but now keep all of the terms. In the resulting Hamiltonian, there are two frequencies present, $\omega_{\text{m},2} + \delta_1$ and $\omega_{\text{m},2} + \delta_2$. Our approach is taken from Ref. 1, but now extended to incorporate two frequencies. Note that other approaches are possible [211]. In fact, we will choose the two frequencies to be $\tilde{\Omega}_1 = \omega_{\text{m},1} + \delta_1 + \omega_{\text{m},2} + \delta_2$ and $\tilde{\Omega}_2 = \omega_{\text{m},1} + \delta_1 - \omega_{\text{m},2} - \delta_2$, since it will lead to a more compact Floquet matrix. If we restrict the theory to only the second Fourier frequency $\tilde{\Omega}_2$ we recover the theory from the two sections above. While this does capture changes in effective parameters, it does not

show instabilities that are present in the full description. Collecting all system variables into a vector $\hat{\mathbf{x}} = (\hat{b}_1, \hat{b}_1^\dagger, \hat{b}_2, \hat{b}_2^\dagger, \hat{a}_1, \hat{a}_1^\dagger, \hat{a}_2, \hat{a}_2^\dagger)^T$, we can write the equations of motion as

$$\dot{\hat{\mathbf{x}}} = \mathsf{A}(t)\hat{\mathbf{x}} + \mathsf{L}\hat{\mathbf{x}}_{\text{in}}, \tag{5.C.1}$$

where the dynamical matrix $A(t)$ is sometimes called Langevin matrix and

$$\mathsf{L} = \text{diag}(\sqrt{\Gamma_{\text{m},1}}, \sqrt{\Gamma_{\text{m},1}}, \sqrt{\Gamma_{\text{m},2}}, \sqrt{\Gamma_{\text{m},2}}, \sqrt{\kappa_1}, \sqrt{\kappa_1}, \sqrt{\kappa_2}, \sqrt{\kappa_2}). \tag{5.C.2}$$

Since the Hamiltonian has two Fourier frequencies, we can write the Langevin matrix in terms of its Fourier components as well

$$\mathsf{A}(t) = \sum_{m,n} e^{im\tilde{\Omega}_1 t + in\tilde{\Omega}_2 t} \mathsf{A}^{(m,n)}. \tag{5.C.3}$$

For the Hamiltonian we consider, the non-zero Fourier components $\mathsf{A}^{(m,n)}$ are those with $|m|, |n| \leq 1$. We can do the same to $\mathbf{x}$, which defines $\mathbf{x}^{(m,n)}(t)$. However the Fourier components of $\mathbf{x}$ will still contain fluctuations, so they are not time-independent. We additionally perform a Fourier transform of all Fourier components of $\mathbf{x}$, so that we can finally write the original equation of motion (5.C.1) as ($\forall m, n$)

$$i(\omega - \tilde{\Omega}_1 m - \tilde{\Omega}_2 n)\mathbf{x}^{(m,n)}(\omega) + \sum_{k=-1}^{1}\sum_{l=-1}^{1} \mathsf{A}^{(k,l)}\mathbf{x}^{(m-k,n-l)}(\omega) = -\delta_{m,0}\delta_{n,0}\mathsf{L}\mathbf{x}_{\text{in}}(\omega). \tag{5.C.4}$$

While in principle there are infinitely many coupled equations (one for each combination of $m, n \in \mathbb{Z}$), we have to truncate at a certain number to make the problem tractable. From the truncated matrix we calculate the scattering matrix between the Fourier modes. Of particular interest here is the scattering between the zeroth Fourier modes, for we are interested in a signal on resonance. Forward and reverse gain are defined in the same way as above, except that they now refer to the equivalent elements in relation to the scattering matrix between the zeroth Fourier modes.

In general, we can distinguish four different regimes. For sideband parameters $\omega_{\text{m},i}/\kappa$, $(\omega_{\text{m},1} - \omega_{\text{m},2})/\kappa$ that are very large in comparison to the cooperativities $\mathcal{C}_{ij} = G_{ij}/(\kappa_i\omega_{\text{m},j})$, the RWA theory is fully valid. As the sideband parameters decrease, there is a regime where the effective parameters of the systems start to change. Since isolation relies on fine-tuning parameters, it is very sensitive to such a change of parameters. The RWA theory can be restored when working with renormalized parameters or when numerically optimizing the plaquette phase, as we demonstrate below. As the nonresonant terms become even stronger, i.e., through increasing cooperativities or a lower sideband parameter, the system

has a qualitatively different response. Finally, there is a regime where the system invariably becomes unstable (cf. also Ref. 211).

In the whole section we take $\kappa_1 = \kappa_2 = \kappa$ and $\Gamma_{\mathrm{m},1} = \Gamma_{\mathrm{m},2} = \Gamma_{\mathrm{m}} = 10^{-2}\kappa$ and choose units such that $\kappa = 1$ for simplicity. Our proposed additional sideband cooling can increase Γ_{m} beyond that value. We note that a mechanical damping rate $\Gamma_{\mathrm{m}} = \kappa$ quantitatively changes our conclusions below, since it enhances the detrimental effect of the counterrotating terms, but that the results are qualitatively the same.

5.C.2 Optimizing coupling rates at finite sideband parameters

Here we show by example (cf. Fig. 5.4) that for moderate sideband parameters and cooperativities, optimizing the plaquette phase leads to near ideal behaviour.

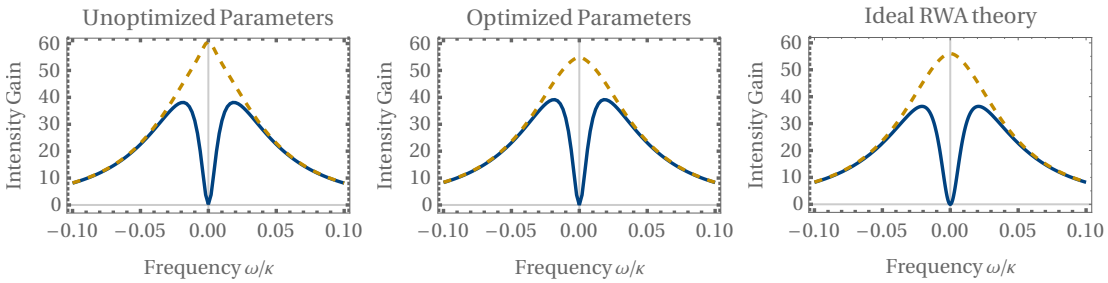

Figure 5.4: Optimizing coupling parameters for weak off-resonant terms. For finite sideband parameters, the RWA is not fully valid. The left panel shows forward and backward gain of the DPSA when using the coupling parameters of the ideal RWA theory. In the middle panel we have numerically optimized the plaquette phase. As comparison, the right panel shows the ideal theory. Parameters are $\mathcal{C}_1 = 4, \mathcal{C}_2 = 16, \omega_{\mathrm{m},1}/\kappa = 5, \omega_{\mathrm{m},2}/\kappa = 20$. Although the differences may appear subtle, we can quantify them (all on resonance): For unoptimized parameters, reverse gain is 0.23, whereas forward gain is 61. After optimizing, we have reverse gain of the order of 2×10^{-17}, which is essentially 0 within numerical errors, and forward gain 55. The ideal theory predicts 0 and 56.

5.C.3 Qualitative and quantitative deviations from ideal theory

For larger coupling rates we enter the regime where qualitative differences appear and the quantitative difference increase further. This is illustrated in Fig. 5.5. Optimizing the plaquette phase still recovers isolation, as before, but forward gain takes a qualitatively different form and is considerably reduced in comparison with ideal theory.

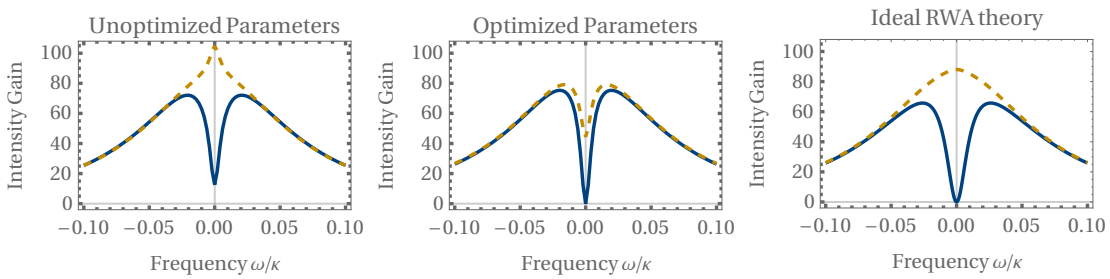

Figure 5.5: Optimizing coupling parameters for strong off-resonant terms. Increasing the coupling strength further, we enter the regime where qualitative differences appear. The left panel shows forward and backward gain of the DPSA when using the coupling parameters of the ideal RWA theory. In the middle panel we have numerically optimized the plaquette phase. As comparison, the right panel shows the ideal theory. Parameters are $\mathcal{C}_1 = 6, \mathcal{C}_2 = 36, \omega_{\mathrm{m},1}/\kappa = 5, \omega_{\mathrm{m},2}/\kappa = 20$. While in Fig. 5.4 the differences were only quantitative, here the forward gain in the middle panel shows a strong deviation from ideal theory (right panel). Again we list forward and reverse gain on resonance: unoptimized parameters, reverse/forward gain of 12.7 and 105, after optimizing, reverse/forward gain are $\sim 8 \times 10^{-17}$ and 44.2. As a comparison, the ideal theory predicts 0 and 88.

5.C.4 Instability threshold

In this subsection we demonstrate a method to find the instability threshold. We find that for a sideband parameter $\Omega/\kappa \gg 1$ the eigenvectors are centred around a specific Fourier frequency and only mix with adjacent frequencies, due to the fact that the coupling is highly off-resonant. In the converse case, the eigenvectors are spread out over many Fourier frequencies. Thus, in the resolved sideband regime, we have to include only few Fourier frequencies. Furthermore, due to the truncation at a certain Fourier index, there are eigenvectors that are concentrated at the edges of the Fourier domain that are not eigenvectors of the infinitely big matrix. After solving the eigenvalue problem, we therefore select only those eigenvectors that have an appreciable support at the zeroth Fourier component. We then look for the instability in this restricted set of modes. We observe that there is an instability that occurs for certain cooperativities. For an analysis in a related system, see Ref. 211.

We plot the instability threshold (in units of κ) as a function of resonator frequency in Fig. 5.6. Note however that the plots in this section have been obtained for driving parameters given by the ideal theory. We can make some progress through optimizing the driving parameters in the presence of the off-resonant terms, as discussed in the previous subsections.

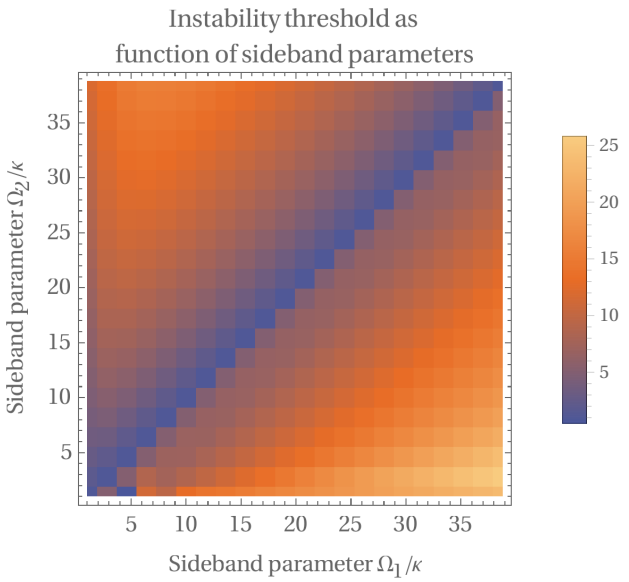

Figure 5.6: Instability threshold. We plot the cooperativity at which the instability occurs as a function of the two sideband parameters, $\omega_{\mathrm{m},1}/\kappa$ and $\omega_{\mathrm{m},2}/\kappa$. The onset of stability is defined as the cooperativity $\mathcal{C}_1$ (note $\mathcal{C}_2 = \mathcal{C}_1^2$) at the real part of one of the eigenvalues becomes positive. The set of eigenvalues is restricted to those belonging to eigenvectors with support at the zeroth Fourier component.

6 | Nonreciprocity for fermions from reservoir engineering

6.1 Introduction

Transport through nanoelectronic structures has been a thriving research field for many years, with quantum dots (QDs) being a prime example [213]. Goals of this effort include high precision currents from single-electron pumps [214–218] and quantum devices encoding information with single electrons or electron spins [219–221]. One important aspect of transport is current rectification. It can be achieved through the Pauli spin blockade in double quantum dots (DQDs) [222–225] or through Coulomb blockade in triple quantum dots [226, 227]. In both cases, rectification is a result of many-body effects with an electron trapped permanently in one of the QDs.

Reservoir engineering promises robust generation of quantum states through designed environments [12]. It has been applied to trapped atoms [228], trapped ions [229–231], circuit quantum electrodynamics [232–234], and cavity optomechanics [44–46, 51, 121, 235]. Recently, it has been exploited for promising magnetic-field-free directional devices for photons [3, 52–54, 189, 191]. Surprisingly, fermionic reservoir engineering is virtually unexplored, except for situations where the system couples to spin [236] or bosonic degrees of freedom [237] of the reservoir.

In this chapter, we present a novel mechanism for rectification in a DQD that works on the single-particle level and relies on dissipation in a reservoir shared between both dots, which has been published as Ref. 5. In contrast to Refs 236 and 237, the engineered reservoir exchanges fermions with the system. The mechanism is based on a directional interaction that arises due to interference of *coherent* (from a Hamiltonian) and *dissipative* coupling (from a shared reservoir). It mirrors the mechanism for bosonic directionality in Chapters 4 and 5, but this chapter shows that the mechanism is independent of particle statistics [191]. The relative phase of coherent and dissipative coupling is controlled by an externally applied magnetic field and can be tuned to yield forward directionality, backward

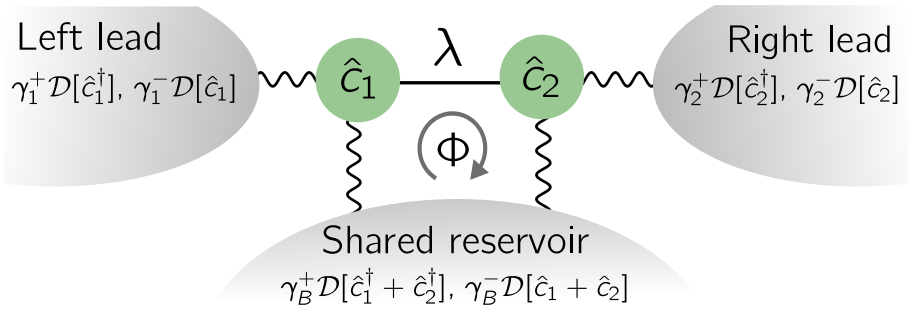

Figure 6.1: Double quantum dot (DQD) in contact with three reservoirs. We consider a single energy level in each dot, with annihilation operator $\hat{c}_1, \hat{c}_2$. Electrons can tunnel between the two sites with complex amplitude λ. Each dot is tunnel-coupled to a reservoir (denoted left and right lead, playing the role of source and drain) whose chemical potential can be controlled by externally applied voltages. The crucial feature of our proposal is that both sites are additionally tunnel-coupled to a shared reservoir that induces non-local electron loss.

directionality, or reciprocal transport. It is therefore a form of passive coherent control, in contrast to active feedback control [238, 239], with potentially interesting consequences for quantum thermodynamics [240].

We unearth the directionality mechanism using a simple weak-coupling quantum master equation (QME) and corroborate our analysis with the exact solution obtained from the Laplace transform of the equations of motion, which shows that the current-voltage characteristics are smoothed out over the width of the energy levels. Finally, we discuss experimental implementation, and the impact of other physical effects on directionality, including non-Markovianity of the reservoir. Our work introduces fermionic reservoir engineering, paving the way to a new class of nanoelectronic devices, with applications in electronic quantum information technology and precision current generation.

This chapter was published in essentially the same form as Ref. 5.

6.2 Model

We consider a serial double quantum dot (DQD) in a magnetic field, where each site is tunnel-coupled to a lead, and both are connected to a shared electronic reservoir (see Fig. 6.1). We assume that the energy level spacing in each dot is large compared to other parameters in the problem and that the chemical potentials are sufficiently low such that we only need to consider one level per dot. If the applied magnetic field induces a large energy splitting between the spin states, such that only one spin state is relevant, we can

drop the spin index. Under these assumptions, the Hamiltonian of the system is ($\hbar = 1$)

$$\hat{H} = \hat{H}_{\text{sys}} + \hat{H}_{\text{res}} + \hat{H}_{\text{sys-res}}, \tag{6.2.1a}$$

$$\hat{H}_{\text{sys}} = \sum_{i=1}^{2} \varepsilon_i \hat{n}_i + \lambda \hat{c}_1^\dagger \hat{c}_2 + \lambda^* \hat{c}_2^\dagger \hat{c}_1, \tag{6.2.1b}$$

$$\hat{H}_{\text{res}} = \sum_{\alpha=1,2,B} \sum_k \varepsilon_{k,\alpha} \hat{b}_{k,\alpha}^\dagger \hat{b}_{k,\alpha}, \tag{6.2.1c}$$

$$\hat{H}_{\text{sys-res}} = -\sum_k \sum_{i=1}^{2} \hat{c}_i^\dagger \left(G_{k,i} \hat{b}_{k,B} + J_{k,i} \hat{b}_{k,i} \right) + \text{H.c.} \tag{6.2.1d}$$

Here, $\hat{n}_i = \hat{c}_i^\dagger \hat{c}_i$ is the fermionic number operator for site i, λ the complex tunnelling amplitude between the dots, $\hat{b}_{k,\alpha}$ are the annihilation operators for fermions in the reservoirs, and $G_{k,i}$, $J_{k,i}$ are real couplings of the sites to the reservoir modes.

In presence of a magnetic field, electrons moving in a closed loop pick up a phase proportional to the flux through the loop. In our system, the only closed loop is formed by the two dots with the shared reservoir (cf. Fig. 6.1). In Eq. (6.2.1) we have chosen a gauge in which the resulting Peierls phase Φ is associated with the inter-dot coupling $\lambda = |\lambda| \exp(i\Phi)$. This phase is the crucial ingredient to obtain destructive interference between coherent and dissipative interaction. While time-reversal symmetry is broken by dissipation, the applied magnetic field breaks the symmetry under exchange of 1 and 2.

Without the shared reservoir, Eq. (6.2.1) is the standard Hamiltonian for a serial DQD [241–244]. In contrast to previous work, we include a third, shared reservoir, which can be realized experimentally by tunnel-coupling both sites to a wire or a 2D electron gas parallel to the structure. We propose a specific experiment below (Fig. 6.5).

Let us first explore the mechanism for directionality within the quantum master equation (QME). It is derived assuming the system is weakly coupled to its reservoirs and the Born-Markov approximation is valid [245]. The QME takes the Lindblad form (derivation in Appendix 6.A)

$$\dot{\hat{\rho}}_S = -i[\tilde{H}_{\text{sys}}, \hat{\rho}_S] + \sum_j [\gamma_j^- \mathcal{D}(\hat{c}_j) + \gamma_j^+ \mathcal{D}(\hat{c}_j^\dagger)]\hat{\rho}_S + [\gamma_B^+ \mathcal{D}(\hat{c}_1^\dagger + \hat{c}_2^\dagger) + \gamma_B^- \mathcal{D}(\hat{c}_1 + \hat{c}_2)]\hat{\rho}_S, \tag{6.2.2}$$

with

$$\tilde{H}_{\text{sys}} = \tilde{\varepsilon}(\hat{n}_1 + \hat{n}_2) + \tfrac{\tilde{\delta}}{2}(\hat{n}_1 - \hat{n}_2) + (\tilde{\lambda} \hat{c}_1^\dagger \hat{c}_2 + \text{H.c.}), \tag{6.2.3a}$$

$$\gamma_\alpha^+ = \Gamma_\alpha f(\varepsilon - \mu_\alpha), \qquad \gamma_\alpha^- = \Gamma_\alpha [1 - f(\varepsilon - \mu_\alpha)], \tag{6.2.3b}$$

where the tilde denotes that the parameters have been renormalized by the self-energy

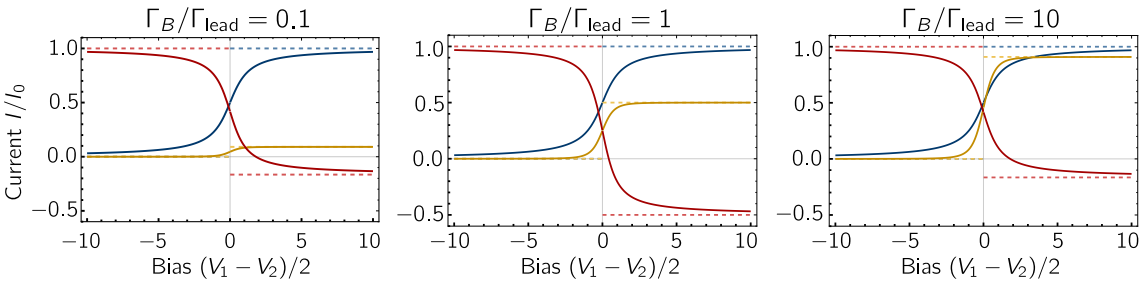

Figure 6.2: Current-voltage characteristics. We plot the currents $\langle \hat{I}_1 \rangle$ (blue), $\langle \hat{I}_{12} \rangle$ (yellow), $\langle \hat{I}_2 \rangle$ (red) for strong coupling [Eq. (6.4.2), in solid, dark] and weak coupling (dotted, light), at zero temperature, as a function of the bias, where $V_1 \equiv 2(\mu_1 - \varepsilon)/(\Gamma_B + \Gamma_{\text{lead}}) = -V_2$, for weak (left), intermediate (middle) and strong (right) inter-dot coupling relative to the coupling to the leads. The currents are plotted in units of $I_0 = \Gamma_B \Gamma_{\text{lead}}/(\Gamma_B + \Gamma_{\text{lead}})$. In reverse bias, current from lead 2 flows into the shared reservoir, but current never flows into lead 1 and both $\langle \hat{I}_1 \rangle$ and $\langle \hat{I}_{12} \rangle$ go to zero. In forward (positive) bias, current flows from lead 1 to 2, but the current into lead 2 is at most half of the current leaving lead 1, which happens in the "impedance-matched" case where the inter-dot coupling rate $2|\lambda| = \Gamma_B$ equals the lead coupling rate Γ_{lead}. As the asymmetry in $\Gamma_B/\Gamma_{\text{lead}}$ grows, more electrons get directed into the shared reservoir [cf. Eq. (6.4.2)].

due to the reservoirs, and $\tilde{\varepsilon} \equiv (\tilde{\varepsilon}_1 + \tilde{\varepsilon}_2)/2$, $\tilde{\delta} \equiv \tilde{\varepsilon}_1 - \tilde{\varepsilon}_2$. In the remainder of this chapter we will drop the tilde again. The index α runs over $(1, 2, B)$. The dissipation rates depend on the reservoir density of states at energy ε and the coupling amplitudes, which has been combined into the overall rate Γ_α, as detailed in Appendix 6.A. $f(\varepsilon) = \{\exp[\varepsilon/(k_B T)] + 1\}^{-1}$ is the Fermi-Dirac distribution. We assume all reservoirs to be at the same temperature, but allow the chemical potential to vary between the reservoirs, as they will be set by the applied voltages.

There is extensive literature about whether the QME should be derived with respect to local degrees of freedom or with respect to global energy eigenstates of the system [246–248]. In thermodynamic equilibrium, global dissipators tend to be more accurate, but in out-of-equilibrium situations, it has been shown that local dissipators model transport behaviour more accurately [248], which is why we have employed local dissipators here. In order to show that they do indeed capture the appropriate physics, we compare to the exact solution for reservoirs with infinite bandwidth below.

6.3 Directionality

Consider the equation of motion for the expectation value of the number of electrons on site 1, $\hat{n}_1$, derived from Eq. (6.2.2)

$$\begin{aligned}\frac{d}{dt}\langle\hat{n}_1\rangle = &-(\Gamma_1+\Gamma_B)\langle\hat{n}_1\rangle - i\langle\lambda\hat{c}_1^\dagger\hat{c}_2 - \lambda^*\hat{c}_2^\dagger\hat{c}_1\rangle \\ &- \frac{\Gamma_B}{2}\langle\hat{c}_1^\dagger\hat{c}_2 + \hat{c}_2^\dagger\hat{c}_1\rangle + (\gamma_B^+ + \gamma_1^+).\end{aligned} \tag{6.3.1}$$

The terms in this equation describe (in order): loss of electrons into two reservoirs, *coherent* tunnelling of electrons between the two sites, *dissipative* coupling arising from the non-local dissipator, and a constant rate of fermions added from the reservoirs. The term $-i\langle\lambda\hat{c}_1^\dagger\hat{c}_2 - \lambda^*\hat{c}_2^\dagger\hat{c}_1\rangle$ is the current between the two sites. It is cancelled by the succeeding term in Eq. (6.3.1) if

$$\lambda = i\Gamma_B/2 \tag{6.3.2}$$

which causes destructive interference between the coherent and the dissipative process [191]. This choice for λ, which we adopt for the rest of the chapter, makes $\langle\hat{n}_1\rangle$ independent of site 2, which is the essence of isolation. Crucially, the same is not true for site 2, as we have

$$\begin{aligned}\frac{d}{dt}\langle\hat{n}_2\rangle = &-(\Gamma_2+\Gamma_B)\langle\hat{n}_1\rangle + i\langle\lambda\hat{c}_1^\dagger\hat{c}_2 - \lambda^*\hat{c}_2^\dagger\hat{c}_1\rangle \\ &- \frac{\Gamma_B}{2}\langle\hat{c}_1^\dagger\hat{c}_2 + \text{H.c.}\rangle + (\gamma_B^+ + \gamma_2^+),\end{aligned} \tag{6.3.3}$$

such that for our choice [Eq. (6.3.2)] the current from site 1 to site 2 is *enhanced*. Mathematically, this happens because the phase in the coherent interaction is conjugated ($\lambda^*\hat{c}_2^\dagger\hat{c}_1$) when exchanging 1 and 2, whereas the dissipator [$\mathcal{D}(\hat{c}_1+\hat{c}_2)$] is symmetric.

While the QME enables a simple analysis, we gain confidence in our result by deriving the exact solution directly from the equations of motion, which is also valid for strong coupling. Using the Laplace transform $\tilde{c}(z) \equiv \int_0^\infty \exp(-zt)c(t)dt$ allows us to write the equations of motion as algebraic ones

$$\begin{aligned}&\begin{pmatrix} z+i\varepsilon_1+i\Sigma_1(z) & i\lambda+\sum_k \frac{G_{k,1}G_{k,2}}{z+i\varepsilon_{k,B}} \\ i\lambda^*+\sum_k \frac{G_{k,2}G_{k,1}}{z+i\varepsilon_{k,B}} & z+i\varepsilon_2+i\Sigma_2(z)\end{pmatrix}\begin{pmatrix}\tilde{c}_1(z)\\ \tilde{c}_2(z)\end{pmatrix} \\ &= \begin{pmatrix}\hat{c}_1(0)+\sum_k \frac{iG_{k,1}}{z+i\varepsilon_{k,B}}\hat{b}_{k,B}(0)+\sum_k \frac{iJ_{k,1}}{z+i\varepsilon_{k,1}}\hat{b}_{k,1}(0)\\ \hat{c}_2(0)+\sum_k \frac{iG_{k,2}}{z+i\varepsilon_{k,B}}\hat{b}_{k,B}(0)+\sum_k \frac{iJ_{k,2}}{z+i\varepsilon_{k,2}}\hat{b}_{k,2}(0)\end{pmatrix}\end{aligned} \tag{6.3.4}$$

with

$$i\Sigma_j(z) = \sum_k \left(\frac{G_{k,j}^2}{z + i\varepsilon_{k,B}} + \frac{J_{k,j}^2}{z + i\varepsilon_{k,j}} \right) \to \int \frac{d\omega}{2\pi} \left(\frac{\Gamma_{j,B}(\omega)}{z + i\omega} + \frac{\Gamma_j(\omega)}{z + i\omega} \right). \tag{6.3.5}$$

The matrix on the left-hand side of Eq. (6.3.4) describes similar physical effects as the QME. $\Sigma_i(z)$ is a complex self-energy induced by the coupling to the two reservoirs, which describes loss (imaginary part) and renormalization of the energy (real part). The inter-dot coupling λ is also modified by an equivalent term, which captures the interference of coherent and dissipative coupling. Finally, the right-hand side of Eq. (6.3.4) contains the initial state of the system. The correlators between the reservoir modes contain information about chemical potential and temperature of the reservoir.

For a dense set of reservoir modes, we can replace the sums over energy eigenstates (denoted symbolically by $\sum_k$), as done in Eq. (6.3.5). In order to match the exact solution to the QME, we choose the reservoir spectral density to be flat, i.e., $\Gamma_\alpha(\omega) = \Gamma_\alpha$. Assuming for simplicity that $\Gamma_{1,B} = \Gamma_{2,B} \equiv \Gamma_B$ (full solution in Appendix 6.D), directionality is attained again for $\lambda = i\Gamma_B/2$, in agreement with Eq. (6.3.2). Furthermore, the fact that this effect occurs in the equations of motion for the operators c_1, c_2 [Eq. (6.3.4)] is clear evidence that directionality arises due to interference.

6.4 Currents

Ultimately, the relevant quantities in experiment are the currents between the sites and through the leads. We derive them below for both the QME and the exact solution.

Together with the equation of motion for the expectation value of the inter-dot current operator $\hat{I}_{12} = -\Gamma_B(\hat{c}_1^\dagger \hat{c}_2 + \hat{c}_2^\dagger \hat{c}_1)/2$ the QME yields a closed system of equations which is solved to obtain the steady-state expectation value (cf. Appendix 6.B)

$$\langle \hat{I}_{12} \rangle = \frac{\Gamma_B^2 \Gamma_{\text{lead}} [f(\varepsilon - \mu_1) - f(\varepsilon - \mu_B)]}{(\Gamma_B + \Gamma_{\text{lead}})^2 + \delta^2}, \tag{6.4.1}$$

where we have set $\Gamma_i \equiv \Gamma_{\text{lead}}$ for simplicity. Equation (6.4.1) is a key result of our analysis. In order to obtain fully directional transport we need $\gamma_B^+ = 0$, attained for $\varepsilon - \mu_B \gg k_B T$, such that electrons from the shared reservoir do not enter the system. In this case, the current is always non-negative, the hallmark of directional transport. This is the regime we consider in the rest of the chapter.

In Eq. (6.4.1), δ is the energy difference between the two sites. If it is large compared to the dissipation rates, the two fermionic modes do not overlap, and current is suppressed.

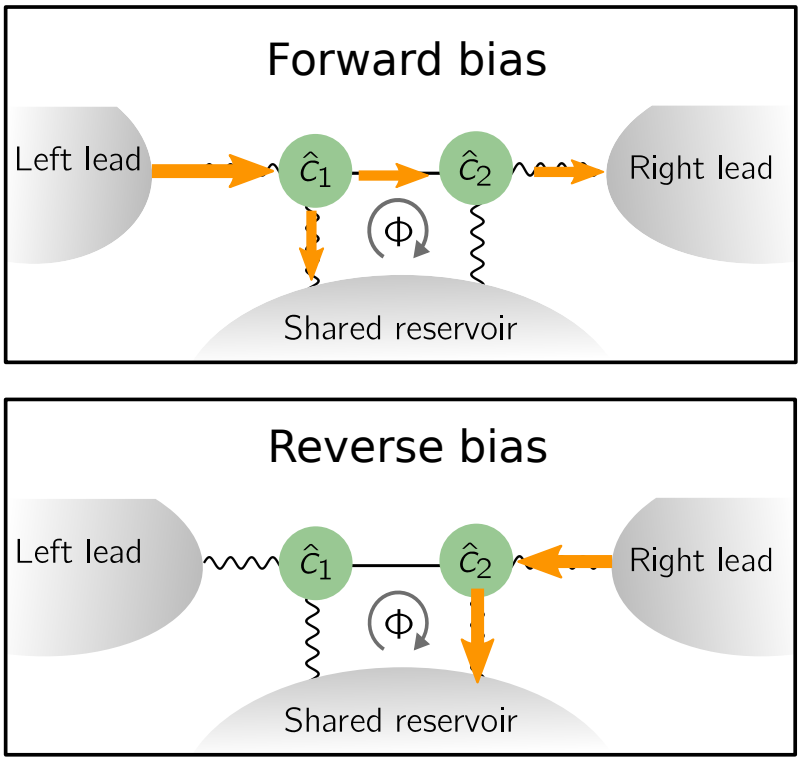

Figure 6.3: Current flow in forward and reverse bias. We show how currents flow in a DQD with impedance-matched inter-dot and dot-lead coupling rates $\Gamma_B = \Gamma_{\text{lead}}$, and in the directional regime $\lambda = i\Gamma_B/2$. In reverse bias, the whole current from the lead is absorbed in the shared reservoir, and no current arrives in the left lead. On the other hand, in forward bias, half of the current is absorbed by the shared reservoir, and the other half is transmitted, which can be seen in Eq. (6.4.2).

If δ is negligible, and for strong bias ($\mu_1 - \varepsilon \gg k_B T$, such that $\gamma_1^+ = \Gamma_{\text{lead}}$), we have $\langle \hat{I}_{12} \rangle \approx \Gamma_B^2 \Gamma_{\text{lead}}/(\Gamma_B + \Gamma_{\text{lead}})^2$, and we identify two limits. If $\Gamma_B \gg \Gamma_{\text{lead}}$, inter-dot coupling is large compared to dot-lead coupling, and the current is dominated by the rate at which electrons are added: $\langle \hat{I}_{12} \rangle \approx \Gamma_{\text{lead}}$. Conversely, if $\Gamma_B \ll \Gamma_{\text{lead}}$, the current is dominated by the rate at which electrons are shuttled from site 1 to 2: $\langle \hat{I}_{12} \rangle \approx \Gamma_B^2/\Gamma_{\text{lead}}$.

Intriguingly, current from the shared reservoir reduces $\langle \hat{I}_{12} \rangle$. While it could seem surprising or worrying that electrons seemingly flow against directionality, it is a natural consequence of the fact that the directionality originates from interference. Electrons on site 2 have zero amplitude of travelling to site 1, but this is not true for electrons from the shared reservoir, which are added in a superposition on sites 1 and 2. Despite this, our system is not a circulator, as can be seen from the asymmetry between the currents from the three terminals (cf. Appendix 6.B).

To verify Eq. (6.4.1), we present the exact solution obtained from Eq. (6.3.4), and compare it to the QME in Fig. 6.2. Inverting the Laplace transform yields the real-time solution for all operators, whose correlators converge to stationary values in the long-time

limit, which are generically expressed as integrals over all energies. At zero temperature, the inter-dot current $\langle\hat{\mathcal{I}}_{12}\rangle$ and the current leaving lead $i = 1, 2$, $\langle\hat{\mathcal{I}}_i\rangle$, become

$$\langle\hat{\mathcal{I}}_1\rangle = I_0\mathcal{I}_s(V_1), \quad \langle\hat{\mathcal{I}}_{12}\rangle = \frac{I_0\Gamma_{\text{lead}}}{\Gamma_B + \Gamma_{\text{lead}}}\mathcal{I}_d(V_1), \tag{6.4.2a}$$

$$\langle\hat{\mathcal{I}}_2\rangle = I_0\mathcal{I}_s(V_2) - \frac{2\Gamma_B}{\Gamma_B + \Gamma_{\text{lead}}}\langle\hat{\mathcal{I}}_{12}\rangle. \tag{6.4.2b}$$

where the scaled chemical potential $V_\alpha \equiv 2(\mu_\alpha - \varepsilon)/(\Gamma_B + \Gamma_{\text{lead}})$, and we have defined $I_0 \equiv (\Gamma_B\Gamma_{\text{lead}})/(\Gamma_B + \Gamma_{\text{lead}})$ and the currents through a single (s) and double (d) dot

$$\mathcal{I}_s(V) = \frac{1}{2} + \frac{\tan^{-1}(V)}{\pi}, \qquad \mathcal{I}_d(V) = \mathcal{I}_s(V) + \frac{V}{\pi(1+V^2)}, \tag{6.4.3}$$

which are the integral over a Lorentzian and the square of a Lorentzian, respectively (illustrated in Fig. 6.4). Alternatively, V can be considered a voltage scaled to the energy of the site ε.

It is known that I_0 is the maximum current through a mode (per spin) [249] and that current through a mode is proportional to the area under the lineshape up to the chemical potential [249]. At finite temperature, $\mathcal{I}_{s,d}$ are modified, but Eq. (6.4.2) remains unchanged. We distinguish expectation values in the exact solution by using a calligraphic $\mathcal{I}$, even though the current operator is the same in both cases. The QME result (at $\delta = 0$) can be obtained from Eq. (6.4.2) by replacing

$$\mathcal{I}_{s,d}(V) \quad \to \quad f(\mu - \varepsilon). \tag{6.4.4}$$

Essentially, the weak-coupling QME neglects the finite width of the modes.

We plot the current-voltage characteristics for symmetric bias, $V_2 = -V_1$, zero temperature, and $V_B \to -\infty$ for both solutions in Fig. 6.2. The current leaving the first lead coincides with current through a single dot [244], reflected in $\mathcal{I}_s$. The second lead additionally receives current from the first lead, which passes through both dots and hence has a characteristic given by $\mathcal{I}_d$.

The current is clearly directional, in the sense that current never enters the first lead, even in reverse bias. However, some current is directed into the shared reservoir. In the ideal case, where inter-dot coupling and dot-lead coupling rates are matched, $\Gamma_B = \Gamma_{\text{lead}}$, and for $V_1 \gg 1$, $\langle\hat{\mathcal{I}}_1\rangle \to I_0$, whereas $\langle\hat{\mathcal{I}}_2\rangle \to -I_0/2$ and half of the current flows into the shared reservoir, as shown in Fig. 6.3. Away from that point the amount of current lost increases steadily [cf. Eq. (6.4.2) and Fig. 6.2].

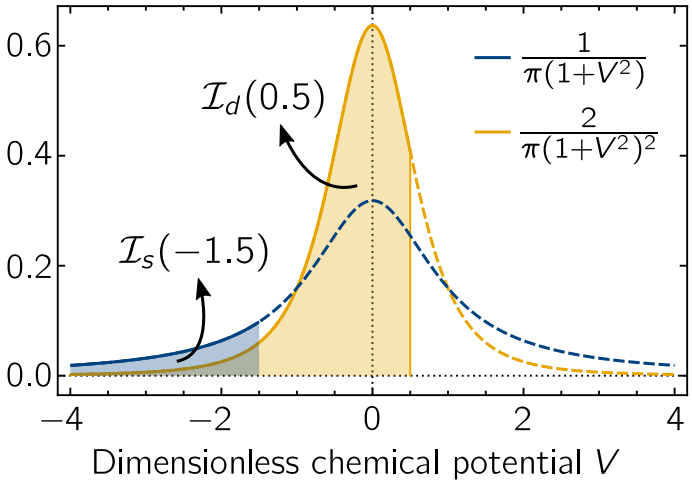

Figure 6.4: Form of characteristic functions. $\mathcal{I}_s$ ($\mathcal{I}_d$) is the integral over a normalized Lorentzian (squared) from $-\infty$ to the normalized chemical potential V.

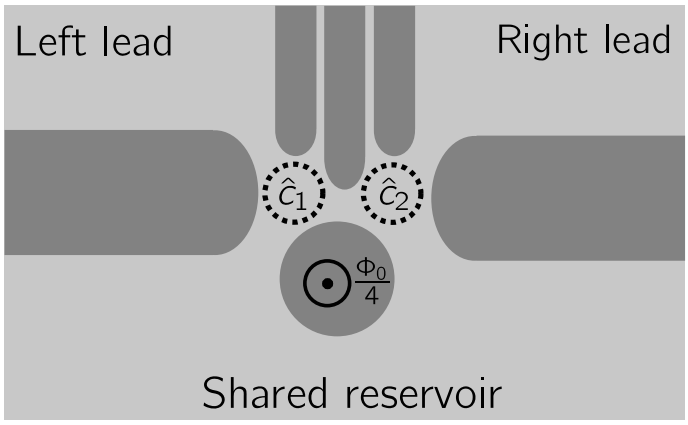

Figure 6.5: Potential experimental implementation with a gated GaAs/AlGaAs heterostructure. Gates that expel the 2D electron gas are drawn in dark grey.

6.5 Experimental implementation

Our proposal can be realized in gated GaAs/AlGaAs heterostructures, a well-established platform for QDs [213, 250], where related systems are a reality [251–253]. Directionality requires finely tuned coupling rates, which are achievable in current experiments [254–256]. Island gates with magnetic flux have been implemented before [251, 253]. A magnetic flux of $\Phi_0/4$ threading an area of $0.01\,\mu\text{m}^2$—a typical scale for experiments [250–253, 257]—requires a magnetic field of approximately $50\,\text{mT}$, which is routinely achieved. If not confined to the island, this magnetic field simultaneously serves to spin-polarize the dots.

6.6 Discussion

One important open question concerns the effects of structure in the various reservoirs on the directionality properties. In Eq. (6.3.4) we see that isolation occurs when $i\lambda = -\int(d\omega/2\pi)\Gamma_B(\omega)/(z+i\omega)$, independent of the leads, such that we can confidently conclude that structure in the leads does not impact directionality—though clearly a finite bandwidth of the shared reservoir does. We expect isolation to work well when the characteristic frequency range $\Delta\Gamma$ over which the reservoir density of states changes is large compared to the width of the system modes, $\Delta\Gamma \gg \Gamma_B, \Gamma_{\text{lead}}$. If this condition is not fulfilled, one would have to resort to one of the several numerical approaches that have been developed to tackle non-Markovian reservoirs [258]. Approaches that extend the mode space of the quantum system [259] might be particularly suitable.

Decoherence processes that couple to the number operator, such as the phonon reservoir or the Coulomb interaction, do not affect the mechanism for directionality, since the equation of motion for $\hat{n}_i$ does not change when dissipators such as $\mathcal{D}(\hat{n}_1)$ or $\mathcal{D}(\hat{n}_1 \pm \hat{n}_2)$ are added. The current between the dots, however, is reduced as the coherence between the sites is lost, akin to a quantum Zeno effect.

A more realistic double quantum dot model might include a non-linear Coulomb-repulsion term $\xi\hat{c}_1^\dagger\hat{c}_1\hat{c}_2^\dagger\hat{c}_2$ in Eq. (6.2.1). It is not immediately clear how such a term modifies directionality. While it precludes the straightforward solution via equations of motion, it commutes with $\hat{n}_1, \hat{n}_2, \hat{I}_{12}$, and thus does not alter the QME result, but the QME derived here might cease to be applicable.

Finally, since the equations are linear, the QME result can easily be generalized to $\lambda \neq i\Gamma_B/2$, which could become relevant for experiment.

6.7 Conclusion

We have introduced fermionic reservoir engineering in DQDs and shown that a third reservoir shared between both sites of a serial DQD leads to current rectification. The effect is robust to various sources of decoherence and is observable with current quantum dot technology.

Appendix

6.A Dissipators in quantum master equation

In the Born-Markov approximation, the equation of motion for the density matrix is given by the QME [245]

$$\frac{d}{dt}\hat{\rho}_S(t) = -\int_0^\infty ds\ \mathrm{tr}_B\left[\hat{H}_I(t), \left[\hat{H}_I(t-s), \hat{\rho}_S(t)\otimes\hat{\rho}_B\right]\right], \tag{6.A.1}$$

where $\hat{H}_I(t)$ is the interaction-picture Hamiltonian for the interaction with the reservoirs. Here we take the bare Hamiltonian $\hat{H}_0 = \varepsilon(\hat{n}_1+\hat{n}_2) + \hat{H}_{\text{res}}$ and leave out the energy splitting $\hat{H}_\delta = (\delta/2)(\hat{n}_1-\hat{n}_2)$ as well as inter-dot coupling $\hat{H}_\lambda = \lambda\hat{c}_1^\dagger\hat{c}_2 + \lambda^*\hat{c}_2^\dagger\hat{c}_1$, such that the interaction-picture Hamiltonian for the system-reservoir coupling becomes

$$\hat{H}_I(t) = -\sum_k\sum_{j=1}^{2}\hat{c}_j^\dagger e^{i\varepsilon t}\left(G_{k,j}\hat{b}_{k,B}e^{ikx_i - i\varepsilon_{k,B}t} + J_{k,j}\hat{b}_{k,j}e^{-i\varepsilon_{k,j}t}\right) + \text{H.c.} \tag{6.A.2}$$

The reservoir density matrix $\hat{\rho}_B$ remains unchanged over time (Born approximation). Here, we will assume it to be thermal, with a fixed chemical potential, such that the occupation of each mode is given by the Fermi-Dirac distribution. If there are no correlations between the reservoirs, we can treat them separately.

The part that couples site j to lead j

$$\hat{H}_{I,j}(t) = -\sum_k \hat{c}_j^\dagger e^{i\varepsilon t}J_{k,j}\hat{b}_{k,j}e^{-i\varepsilon_k t} + \text{H.c.} \tag{6.A.3}$$

leads to a contribution to the QME

$$\dot{\hat{\rho}}_S = |J_{k_0,j}|^2 2\pi\nu_j(\varepsilon)\left[(1-f_j(\varepsilon))\mathcal{D}(\hat{c}_j) + f_j(\varepsilon)\mathcal{D}(\hat{c}_j^\dagger)\right]\hat{\rho}_S - i\,\mathrm{Re}[\Sigma_j][\hat{c}_j^\dagger\hat{c}_j, \hat{\rho}_S] + \cdots, \tag{6.A.4}$$

where k_0 is the wavevector at which $\varepsilon_{k_0} = \varepsilon$, $f_j(\varepsilon) = \{1+\exp[(\varepsilon-\mu_j)/(k_BT_j)]\}^{-1}$, and the dots denote that this is only part of the equation of motion for $\hat{\rho}_S$. The first

term corresponds to incoherent particle loss or gain, depending on temperature, chemical potential, and the energy of the site. The second term renormalizes the energy of the site by the self-energy $\mathrm{Re}[\Sigma_j] \equiv \sum_k |J_{k,j}|^2 \mathrm{P}(1/(\varepsilon_k - \varepsilon))$, where P denotes the principal part.

We repeat the analysis for the shared reservoir

$$\hat{H}_{I,B}(t) = -\sum_j \hat{c}_j^\dagger G_{k,j} \hat{b}_{k,B} e^{i\varepsilon t + ikx_j - i\varepsilon_{k,B} t} + \text{H.c.} \tag{6.A.5}$$

Going through the same procedure as before, we arrive at

$$\begin{aligned}\dot{\hat{\rho}}_S = -\sum_{k,i,j} \Big\{ &(1 - f_B(\varepsilon_k)) \left[G_{ij}(k,t)(\hat{c}_i^\dagger \hat{c}_j \hat{\rho} - \hat{c}_j \hat{\rho} \hat{c}_i^\dagger) + G_{ij}^*(k,t)(-\hat{c}_i \hat{\rho} \hat{c}_j^\dagger + \hat{\rho} \hat{c}_j^\dagger \hat{c}_i) \right] \\ &+ f_B(\varepsilon_k) \left[G_{ij}(k,t)(-\hat{c}_i^\dagger \hat{\rho} \hat{c}_j + \hat{\rho} \hat{c}_j \hat{c}_i^\dagger)\; G_{ij}^*(k,t)(\hat{c}_i \hat{c}_j^\dagger \hat{\rho} - \hat{c}_j^\dagger \hat{\rho} \hat{c}_i) \right] \Big\} + \cdots ,\end{aligned} \tag{6.A.6}$$

with

$$G_{ij}(k,t) = G_{k,i} G_{k,j}^* e^{ik(x_i - x_j)} \left(\mathrm{P} \frac{-1}{i(\varepsilon_k - \varepsilon)} + \pi \delta(\varepsilon_k - \varepsilon) \right). \tag{6.A.7}$$

Rearranging yields

$$\begin{aligned}\dot{\hat{\rho}}_S = &\sum_k 2\pi \delta(\varepsilon_k - \varepsilon) \left[(1 - f_B(\varepsilon_k)) \mathcal{D}(\hat{z}_k) \hat{\rho}_S + f_B(\varepsilon_k) \mathcal{D}(\hat{z}_k^\dagger) \hat{\rho}_S \right] \\ &+ \mathrm{P} \frac{1}{i(\varepsilon_k - \varepsilon)} [\hat{z}_k^\dagger \hat{z}_k, \hat{\rho}_S] + \cdots ,\end{aligned} \tag{6.A.8}$$

with

$$\hat{z}_k \equiv G_{k,1}^* e^{-ikx_1} \hat{c}_1 + G_{k,2}^* e^{-ikx_2} \hat{c}_2. \tag{6.A.9}$$

The first term can be evaluated, due to the presence of the delta function, and the second can be written as an effective Hamiltonian. We further assume

- that the reservoir dispersion relation is symmetric at the energy ε, i.e., that $\varepsilon_{-k_0} = \varepsilon_{k_0}$. This can be tuned with a current through the reservoir, which may be another way to obtain a complex phase, and directionality without a magnetic field. Note that the factor of 2 disappears because the density of states includes the states at positive and negative wavevector, which we have to write out explicitly.
- symmetric coupling $G_{k,i} = G_k$ with $G_{k_0} \in \mathbb{R}$ without loss of generality.

Including the two individual leads, we arrive at the QME in Lindblad form

$$\dot{\hat{\rho}}_S = -i[\tilde{H}_{\text{sys}}, \hat{\rho}_S] + \sum_j [\gamma_j^- \mathcal{D}(\hat{c}_j) + \gamma_j^+ \mathcal{D}(\hat{c}_j^\dagger)] \hat{\rho}_S + [\gamma_B^+ \mathcal{D}(\hat{c}_1^\dagger + \hat{c}_2^\dagger) + \gamma_B^- \mathcal{D}(\hat{c}_1 + \hat{c}_2)] \hat{\rho}_S, \tag{6.A.10}$$

with

$$\tilde{H}_{\text{sys}} = \hat{H}_0 + \hat{H}_\delta + \hat{H}_\lambda + \hat{H}_{\text{self-energies}}, \tag{6.A.11a}$$

$$\gamma_B^+ = 2\pi G_{k_0}^2 \nu_B(\varepsilon) f_B(\varepsilon) \cos[k_0(x_1 - x_2)], \tag{6.A.11b}$$

$$\gamma_B^- = 2\pi G_{k_0}^2 \nu_B(\varepsilon)[1 - f_B(\varepsilon)] \cos[k_0(x_1 - x_2)], \tag{6.A.11c}$$

$$\gamma_j^+ = 2\pi J_{k_0,j} \nu_j(\varepsilon) f_j(\varepsilon) + 2\pi \nu_B(\varepsilon) G_{k_0}^2 f_B(\varepsilon)\{1 - \cos[k_0(x_1 - x_2)]\}, \tag{6.A.11d}$$

$$\gamma_j^- = 2\pi J_{k_0,j} \nu_j(\varepsilon)[1 - f_j(\varepsilon)] + 2\pi \nu_B(\varepsilon) G_{k_0}^2 [1 - f_B(\varepsilon)]\{1 - \cos[k_0(x_1 - x_2)]\}, \tag{6.A.11e}$$

and where $H_{\text{self-energies}}$ is the sum of the terms in Eqs. (6.A.4) and (6.A.8). In order to derive the exact form of the dissipation rates, we started by assuming the coupling rates to the shared reservoir take the form $G_k e^{i\varepsilon_{k,i}x}$. This specific form is unlikely to be present in a realistic system. However, the resulting $\cos(\phi)$ term can be used to parametrize the imbalance between the reservoir couplings, with ϕ varying from $-\pi/2$ to $\pi/2$. This will modify the precise form of the rates, but not change the physics fundamentally. These are subtleties that we do not wish to address in this chapter, and hence we set $\cos[k_0(x_1 - x_2)] = 1$.

With this choice, we arrive at the expressions in the main text

$$\gamma_\alpha^+ = \Gamma_\alpha f_\alpha(\varepsilon), \qquad \gamma_\alpha^- = \Gamma_\alpha[1 - f_\alpha(\varepsilon)], \tag{6.A.12a}$$

where $\alpha \in \{1, 2, B\}$, and $\Gamma_\alpha \equiv \gamma_\alpha^+ + \gamma_\alpha^-$. Note that if the temperature is equal across all reservoirs, we can write $f_\alpha(\varepsilon) = f(\varepsilon - \mu_\alpha)$, with $f(\varepsilon) = \{1 + \exp[\varepsilon/(k_B T)]\}^{-1}$, as is done in the main text.

6.B Solution of equations of motion

From the master equation, we derive the equations of motion for the site occupation

$$\frac{d}{dt}\langle \hat{n}_1 \rangle = -(\Gamma_1 + \Gamma_B)\langle \hat{n}_1 \rangle - i\langle \lambda \hat{c}_1^\dagger \hat{c}_2 - \lambda^* \hat{c}_2^\dagger \hat{c}_1 \rangle - \frac{\Gamma_B}{2}\langle \hat{c}_1^\dagger \hat{c}_2 + \text{H.c.} \rangle + (\gamma_B^+ + \gamma_1^+), \tag{6.B.1a}$$

$$\frac{d}{dt}\langle \hat{n}_2 \rangle = -(\Gamma_2 + \Gamma_B)\langle \hat{n}_2 \rangle + i\langle \lambda \hat{c}_1^\dagger \hat{c}_2 - \lambda^* \hat{c}_2^\dagger \hat{c}_1 \rangle - \frac{\Gamma_B}{2}\langle \hat{c}_1^\dagger \hat{c}_2 + \text{H.c.} \rangle + (\gamma_B^+ + \gamma_2^+), \tag{6.B.1b}$$

$$\frac{d}{dt}\langle \hat{c}_1^\dagger \hat{c}_2 \rangle = (i\delta - \Gamma_y)\langle \hat{c}_1^\dagger \hat{c}_2 \rangle + i\lambda^* \langle \hat{n}_2 - \hat{n}_1 \rangle - \frac{\Gamma_B}{2}\langle \hat{n}_1 + \hat{n}_2 \rangle + \gamma_B^+, \tag{6.B.1c}$$

having defined $\Gamma_B \equiv \gamma_B^+ + \gamma^-$, $\Gamma_j = \gamma_j^+ + \gamma_j^-$, and $\Gamma_y \equiv \Gamma_B + (\Gamma_1 + \Gamma_2)/2$. Setting $\lambda = i\Gamma_B/2$, we arrive at

$$\frac{d\langle\hat{n}_1\rangle}{dt} = -(\Gamma_1 + \Gamma_B)\langle\hat{n}_1\rangle + \gamma_1^+ + \gamma_B^+, \tag{6.B.2a}$$

$$\frac{d\langle\hat{n}_2\rangle}{dt} = -(\Gamma_2 + \Gamma_B)\langle\hat{n}_2\rangle + \gamma_2^+ + \gamma_B^+ - \Gamma_B\langle\hat{c}_1^\dagger\hat{c}_2 + \hat{c}_2^\dagger\hat{c}_1\rangle, \tag{6.B.2b}$$

$$\frac{d}{dt}\langle\hat{c}_1^\dagger\hat{c}_2\rangle = (i\delta - \Gamma_y)\langle\hat{c}_1^\dagger\hat{c}_2\rangle - \Gamma_B\langle\hat{n}_1\rangle + \gamma_B^+. \tag{6.B.2c}$$

The steady-state solution is obtained by setting Eqs. (6.B.2) to zero

$$\langle\hat{n}_1\rangle = \frac{\gamma_1^+ + \gamma_B^+}{\Gamma_1 + \Gamma_B}, \tag{6.B.3a}$$

$$\langle\hat{c}_1^\dagger\hat{c}_2\rangle = \frac{\Gamma_1\gamma_B^+ - \Gamma_B\gamma_1^+}{(\Gamma_1 + \Gamma_B)(\Gamma_y - i\delta)}, \tag{6.B.3b}$$

$$\langle\hat{n}_2\rangle = \frac{\gamma_2^+ + \gamma_B^+}{\Gamma_2 + \Gamma_B} + \frac{2\Gamma_y\Gamma_B(\Gamma_B\gamma_1^+ - \Gamma_1\gamma_B^+)}{(\Gamma_1 + \Gamma_B)(\Gamma_2 + \Gamma_B)(\Gamma_y^2 + \delta^2)}. \tag{6.B.3c}$$

In the limit considered in the main text, $\Gamma_i = \Gamma_{\text{lead}}, \Gamma_{i,B} = \Gamma_B, \delta = 0$, and zero temperature, these turn into

$$\langle\hat{n}_1\rangle = \frac{\Gamma_{\text{lead}}\Theta(V_1) + \Gamma_B\Theta(V_B)}{\Gamma_{\text{lead}} + \Gamma_B}, \tag{6.B.4a}$$

$$\langle\hat{c}_1^\dagger\hat{c}_2\rangle = \frac{\Gamma_{\text{lead}}\Gamma_B}{(\Gamma_{\text{lead}} + \Gamma_B)^2}\left[\Theta(V_B) - \Theta(V_1)\right], \tag{6.B.4b}$$

$$\langle\hat{n}_2\rangle = \frac{\Gamma_{\text{lead}}\Theta(V_2) + \Gamma_B\Theta(V_B)}{\Gamma_{\text{lead}} + \Gamma_B} + \frac{2\Gamma_B^2\Gamma_{\text{lead}}}{(\Gamma_{\text{lead}} + \Gamma_B)^3}\left[\Theta(V_1) - \Theta(V_B)\right], \tag{6.B.4c}$$

where Θ is the Heaviside step function.

6.C Lead currents and inter-dot current operator

In order to find the current flowing from one site 1 to site 2, we consider the Heisenberg equation of motion for the number of particles at site 1 (in the absence of reservoirs)

$$\dot{\hat{n}}_1 = i[\hat{H}_S, \hat{n}_2] = -i(\lambda\hat{c}_1^\dagger\hat{c}_2 - \lambda^*\hat{c}_2^\dagger\hat{c}_1) = \frac{\Gamma_B}{2}(\hat{c}_1^\dagger\hat{c}_2 + \hat{c}_2^\dagger\hat{c}_1). \tag{6.C.1}$$

We can interpret the RHS as the current from site 2 to 1 or as minus the current from site 1 to 2. Its expectation value in the steady-state of the full model is

$$\begin{aligned}\langle \hat{I}_{12} \rangle &= -\frac{\Gamma_B}{2}\langle \hat{c}_1^\dagger \hat{c}_2 + \hat{c}_2^\dagger \hat{c}_1 \rangle = \frac{\Gamma_B \Gamma_y}{\Gamma_y^2 + \delta^2} \frac{\Gamma_B \gamma_1^+ - \Gamma_1 \gamma_B^+}{\Gamma_1 + \Gamma_B} \\ &\xrightarrow{\Gamma_i = \Gamma_{\text{lead}}} \Gamma_B^2 \frac{\Gamma_B \gamma_1^+ - \Gamma_{\text{lead}} \gamma_B^+}{(\Gamma_{\text{lead}} + \Gamma_B)^2 + \delta^2}.\end{aligned} \tag{6.C.2}$$

The currents between the sites and the reservoirs have to be found in a slightly roundabout way. Considering again the equations of motion for the number of particles on site 1, we can write it as

$$\frac{d}{dt}\langle \hat{n}_1 \rangle = \gamma_1^+ (1 - \langle \hat{n}_1 \rangle) - \gamma_1^- \langle \hat{n}_1 \rangle - \Gamma_B \langle \hat{n}_1 \rangle + \gamma_B^+. \tag{6.C.3}$$

This form makes it clear that the current from the left lead to the first site is given by

$$\langle \hat{I}_1 \rangle = \gamma_1^+ (1 - \langle \hat{n}_1 \rangle) - \gamma_1^- \langle \hat{n}_1 \rangle. \tag{6.C.4}$$

Analogously we can find the current from the right lead onto site 2, $\langle \hat{I}_2 \rangle$. Plugging in the solution above,

$$\langle \hat{I}_1 \rangle = \frac{\Gamma_B \gamma_1^+ - \Gamma_1 \gamma_B^+}{\Gamma_1 + \Gamma_B}, \tag{6.C.5a}$$

$$\langle \hat{I}_2 \rangle = \frac{\Gamma_B \gamma_2^+ - \Gamma_2 \gamma_B^+}{\Gamma_2 + \Gamma_B} - \frac{2\Gamma_y \Gamma_2 \Gamma_B (\Gamma_B \gamma_1^+ - \Gamma_1 \gamma_B^+)}{(\Gamma_1 + \Gamma_B)(\Gamma_2 + \Gamma_B)(\Gamma_y^2 + \delta^2)}. \tag{6.C.5b}$$

6.D Exact solution through Laplace transform

We derive the following equations of motion from the Hamiltonian in the main text

$$\dot{\hat{c}}_1 = -i\varepsilon_1 \hat{c}_1 - i\lambda \hat{c}_2 + i \sum_k \left(G_{k,1} \hat{b}_{k,B} + J_{k,1} \hat{b}_{k,1} \right), \tag{6.D.1a}$$

$$\dot{\hat{c}}_2 = -i\varepsilon_2 \hat{c}_2 - i\lambda^* \hat{c}_1 + i \sum_k \left(G_{k,2} \hat{b}_{k,B} + J_{k,2} \hat{b}_{k,2} \right), \tag{6.D.1b}$$

$$\dot{\hat{b}}_{k,B} = -i\varepsilon_{k,B} \hat{b}_{k,B} + iG_{k,1} \hat{c}_1 + iG_{k,2} \hat{c}_2, \tag{6.D.1c}$$

$$\dot{\hat{b}}_{k,i} = -i\varepsilon_{k,i} \hat{b}_{k,i} + iJ_{k,i} \hat{c}_i. \tag{6.D.1d}$$

Through a Laplace transform $\tilde{c}_1(z) = \int_0^\infty dt\ \exp(-zt)\hat{c}_1(t)$, these equations can be turned into algebraic ones. Eliminating the reservoir modes

$$\tilde{b}_{k,B}(z) = \frac{1}{z + i\varepsilon_{k,B}} \left(\hat{b}_{k,B}(0) + iG_{k,1}\tilde{c}_1(z) + iG_{k,2}\tilde{c}_2(z) \right), \tag{6.D.2a}$$

$$\tilde{b}_{k,i}(z) = \frac{1}{z + i\varepsilon_{k,i}} \left(\hat{b}_{k,i}(0) + iJ_{k,i}\tilde{c}_i(z) \right), \tag{6.D.2b}$$

we arrive at

$$\begin{aligned} &\begin{pmatrix} z + i\tilde{\varepsilon}_1 & i\lambda + \sum_k \frac{G_{k,1}G_{k,2}}{z+i\varepsilon_{k,B}} \\ i\lambda^* + \sum_k \frac{G_{k,2}G_{k,1}}{z+i\varepsilon_{k,B}} & z + i\tilde{\varepsilon}_2 \end{pmatrix} \begin{pmatrix} \tilde{c}_1(z) \\ \tilde{c}_2(z) \end{pmatrix} \\ &= \begin{pmatrix} \hat{c}_1(0) + \sum_k \frac{iG_{k,1}}{z+i\varepsilon_{k,B}} \hat{b}_{k,B}(0) + \sum_k \frac{iJ_{k,1}}{z+i\varepsilon_{k,1}} \hat{b}_{k,1}(0) \\ \hat{c}_2(0) + \sum_k \frac{iG_{k,2}}{z+i\varepsilon_{k,B}} \hat{b}_{k,B}(0) + \sum_k \frac{iJ_{k,2}}{z+i\varepsilon_{k,2}} \hat{b}_{k,2}(0) \end{pmatrix} \equiv \begin{pmatrix} \tilde{c}_{1,\text{in}}(z) \\ \tilde{c}_{2,\text{in}}(z) \end{pmatrix}, \end{aligned} \tag{6.D.3}$$

where the energy of the modes has been modified

$$\tilde{\varepsilon}_i \equiv \varepsilon_i - i \sum_k \frac{G_{k,i}^2}{z + i\varepsilon_{k,B}} - i \sum_k \frac{J_{k,i}^2}{z + i\varepsilon_{k,i}}. \tag{6.D.4}$$

In order to make progress, we will have to make assumptions about the spectrum of reservoir modes. Here, we assume them to be dense (such that we have proper dissipation) and write

$$\sum_k \frac{G_{k,i}^2}{z + i\varepsilon_{k,B}} = \int \frac{d\omega}{2\pi} \frac{\Gamma_{i,B}(\omega)}{z + i\omega}, \tag{6.D.5}$$

and

$$\sum_k \frac{J_{k,i}^2}{z + i\varepsilon_{k,i}} = \int \frac{d\omega}{2\pi} \frac{\Gamma_i(\omega)}{z + i\omega}. \tag{6.D.6}$$

We will further assume the tunnelling rates to be Lorentzians $\Gamma(\omega) = \Gamma\delta^2/(\omega^2 + \delta^2)$, and let the bandwidth $\delta \to \infty$. Non-Markovian effects can be included by keeping δ finite. Together, these choices simplify Eq. (6.D.3) to

$$\begin{pmatrix} z + i\tilde{\varepsilon}_1 & i\lambda + \frac{\sqrt{\Gamma_{1,B}\Gamma_{2,B}}}{2} \\ i\lambda^* + \frac{\sqrt{\Gamma_{1,B}\Gamma_{2,B}}}{2} & z + i\tilde{\varepsilon}_2 \end{pmatrix} \begin{pmatrix} \tilde{c}_1(z) \\ \tilde{c}_2(z) \end{pmatrix} = \begin{pmatrix} \tilde{c}_{1,\text{in}}(z) \\ \tilde{c}_{2,\text{in}}(z) \end{pmatrix}, \tag{6.D.7}$$

where now

$$\tilde{\varepsilon}_i = \varepsilon_i - i\frac{\Gamma_1 + \Gamma_{1,B}}{2} \tag{6.D.8}$$

We see that $2\lambda = i\sqrt{\Gamma_{1,B}\Gamma_{2,B}}$ leads to directional interaction (and that that the direction is flipped for the opposite phase). This choice makes the problem easier to solve as well.

Here, isolation can be perfect due to the infinite bandwidth reservoirs. In a realistic setting, the bandwidth of the reservoir will limit the bandwidth of isolation.

We can express $\tilde{c}_i(z)$ in terms of the input operators by inverting the matrix

$$\begin{pmatrix}\tilde{c}_1(z)\\ \tilde{c}_2(z)\end{pmatrix} = \begin{pmatrix}(z+i\tilde{\varepsilon}_1)^{-1} & 0\\ \frac{-\sqrt{\Gamma_{1,B}\Gamma_{2,B}}}{(z+i\tilde{\varepsilon}_1)(z+i\tilde{\varepsilon}_2)} & (z+i\tilde{\varepsilon}_2)^{-1}\end{pmatrix}\begin{pmatrix}\tilde{c}_{1,\text{in}}(z)\\ \tilde{c}_{2,\text{in}}(z)\end{pmatrix}. \tag{6.D.9}$$

Due to the wide-band limit and directionality, the inverse Laplace transform can be found easily

$$\tilde{\chi}_i(z) \equiv (z+i\tilde{\varepsilon}_i)^{-1} \quad \rightarrow \quad \chi_i(t) = \exp(-i\tilde{\varepsilon}_i t), \tag{6.D.10a}$$

$$\tilde{G}_{k,i}(z) \equiv \tilde{\chi}_i(z)\frac{iG_{k,i}}{z+i\varepsilon_{k,B}} \quad \rightarrow \quad \frac{G_{k,i}}{\tilde{\varepsilon}_i-\varepsilon_{k,B}}\left(e^{-i\varepsilon_{k,B}t}-e^{-i\tilde{\varepsilon}_i t}\right), \tag{6.D.10b}$$

$$\tilde{J}_{k,i}(z) \equiv \tilde{\chi}_i(z)\frac{iJ_{k,i}}{z+i\varepsilon_{k,i}} \quad \rightarrow \quad \frac{J_{k,i}}{\tilde{\varepsilon}_i-\varepsilon_{k,i}}\left(e^{-i\varepsilon_{k,i}t}-e^{-i\tilde{\varepsilon}_i t}\right), \tag{6.D.10c}$$

$$\tilde{\chi}_{12}(z) \equiv \frac{-\sqrt{\Gamma_{1,B}\Gamma_{2,B}}}{(z+i\tilde{\varepsilon}_1)(z+i\tilde{\varepsilon}_2)} \quad \rightarrow \quad \chi_{12}(t) = \frac{\sqrt{\Gamma_{1,B}\Gamma_{2,B}}}{i(\tilde{\varepsilon}_1-\tilde{\varepsilon}_2)}\left(e^{-i\tilde{\varepsilon}_1 t}-e^{-i\tilde{\varepsilon}_2 t}\right), \tag{6.D.10d}$$

$$\tilde{\alpha}_{k,i}(z) \equiv \tilde{\chi}_{12}(z)\frac{iG_{k,i}}{z+i\varepsilon_{k,B}} \quad \rightarrow \tag{6.D.10e}$$

$$-iG_{k,i}\sqrt{\Gamma_{1,B}\Gamma_{2,B}}\frac{(\tilde{\varepsilon}_1-\varepsilon_{k,B})e^{-i\tilde{\varepsilon}_2 t}+(\varepsilon_{k,B}-\tilde{\varepsilon}_2)e^{-i\tilde{\varepsilon}_1 t}+(\tilde{\varepsilon}_2-\tilde{\varepsilon}_1)e^{-i\varepsilon_{k,B}t}}{(\tilde{\varepsilon}_1-\varepsilon_{k,B})(\varepsilon_{k,B}-\tilde{\varepsilon}_2)(\tilde{\varepsilon}_2-\tilde{\varepsilon}_1)},$$

$$\tilde{\beta}_{k,i}(z) \equiv \tilde{\chi}_{12}(z)\frac{iJ_{k,i}}{z+i\varepsilon_{k,i}} \quad \rightarrow \tag{6.D.10f}$$

$$-iJ_{k,i}\sqrt{\Gamma_{1,B}\Gamma_{2,B}}\frac{(\tilde{\varepsilon}_1-\varepsilon_{k,i})e^{-i\tilde{\varepsilon}_2 t}+(\varepsilon_{k,i}-\tilde{\varepsilon}_2)e^{-i\tilde{\varepsilon}_1 t}+(\tilde{\varepsilon}_2-\tilde{\varepsilon}_1)e^{-i\varepsilon_{k,i}t}}{(\tilde{\varepsilon}_1-\varepsilon_{k,i})(\varepsilon_{k,i}-\tilde{\varepsilon}_2)(\tilde{\varepsilon}_2-\tilde{\varepsilon}_1)}.$$

6.D.1 Inter-dot current

Let us first evaluate the expectation value of the current operator from site 1 to site 2, $\hat{I}_{12} = -\sqrt{\Gamma_{1,B}\Gamma_{2,B}}(\hat{c}_1^\dagger\hat{c}_2+\hat{c}_2^\dagger\hat{c}_1)/2$

$$\langle\hat{\mathcal{I}}_{12}\rangle = -\sqrt{\Gamma_{1,B}\Gamma_{2,B}}\,\mathrm{Re}\Big[\chi_1^*(t)\chi_{12}(t)\langle\hat{c}_1^\dagger(0)\hat{c}_1(0)\rangle + \sum_k\Big\{G_{k,1}^*(t)\left[G_{k,2}(t)+\alpha_{k,1}(t)\right]\langle\hat{b}_{k,B}^\dagger(0)\hat{b}_{k,B}(0)\rangle + J_{k,1}^*(t)\beta_{k,1}(t)\langle\hat{b}_{k,1}^\dagger(0)\hat{b}_{k,1}(0)\rangle\Big\}\Big]. \tag{6.D.11}$$

Like in the main text, we distinguish the exact result from the QME solution by using a calligraphic $\mathcal{I}$. At late times, only a few terms remain

$$\langle\hat{\mathcal{I}}_{12}\rangle = \sum_k \mathrm{Re}\left\{\Gamma_{1,B}\Gamma_{2,B}\left[\frac{iG_{k,1}^2 f_B(\varepsilon_{k,B})}{|\tilde{\varepsilon}_1-\varepsilon_{k,B}|^2(\varepsilon_{k,B}-\tilde{\varepsilon}_2)}+\frac{iJ_{k,1}^2 f_1(\varepsilon_{k,1})}{|\tilde{\varepsilon}_1-\varepsilon_{k,1}|^2(\varepsilon_{k,1}-\tilde{\varepsilon}_2)}\right]\right.$$
$$\left.-\frac{\sqrt{\Gamma_{1,B}\Gamma_{2,B}}G_{k,1}G_{k,2}f_B(\varepsilon_{k,B})}{(\tilde{\varepsilon}_1^*-\varepsilon_{k,B})(\tilde{\varepsilon}_2-\varepsilon_{k,B})}\right\}. \tag{6.D.12}$$

We turn the sum into an integral, noting that we are in the wide-band limit for the reservoir, such that

$$\begin{aligned}\langle\hat{\mathcal{I}}_{12}\rangle &= \Gamma_{1,B}\Gamma_{2,B}\int\frac{d\omega}{2\pi}\,\mathrm{Re}\left\{\frac{i\Gamma_{1,B}f_B(\omega)}{|\omega-\tilde{\varepsilon}_1|^2(\omega-\tilde{\varepsilon}_2)}+\frac{i\Gamma_1 f_1(\omega)}{|\omega-\tilde{\varepsilon}_1|^2(\omega-\tilde{\varepsilon}_2)}-\frac{f_B(\omega)}{(\tilde{\varepsilon}_1^*-\omega)(\tilde{\varepsilon}_2-\omega)}\right\}\\ &= \Gamma_{1,B}\Gamma_{2,B}\int\frac{d\omega}{2\pi}\left\{\frac{(\Gamma_2+\Gamma_{2,B})\Gamma_{1,B}f_B(\omega)}{2|\omega-\tilde{\varepsilon}_1|^2|\omega-\tilde{\varepsilon}_2|^2}+\frac{(\Gamma_2+\Gamma_{2,B})\Gamma_1 f_1(\omega)}{2|\omega-\tilde{\varepsilon}_1|^2|\omega-\tilde{\varepsilon}_2|^2}-\frac{f_B(\omega)}{(\tilde{\varepsilon}_1^*-\omega)(\tilde{\varepsilon}_2-\omega)}\right\}\end{aligned} \tag{6.D.13}$$

This current has three parts. The first describes fermions from the joint reservoir entering the double dot on the first site and being transported to the second site, and the second part is due to electrons entering the system from the first lead (connected to the first site). Finally, the third term reduces the current $\langle\hat{\mathcal{I}}_{12}\rangle$ and can even make it negative. It arises as a result of fermions added to both sites through the shared reservoir. Their amplitudes add destructively on the second site, but constructively on the first site. The first and third terms can be made small if the chemical potential of the shared reservoir is lowered. The second term encodes the desired part of the current. All parts are also present in Eq. (6.C.2), where they are encoded as γ_1^+ and γ_B^+, which are the rate of electrons being added from the first lead and from the joint reservoir, respectively.

The integral in Eq. (6.D.13) can be performed numerically for $T\neq 0$ and analytically for generic values of the parameters at $T=0$, but the result is cumbersome. Assuming $\Gamma_i=\Gamma_{\text{lead}}$, $\Gamma_{i,B}=\Gamma_B$, $\delta=\varepsilon_2-\varepsilon_1=0$ and setting temperature $T=0$, we find

$$\langle\hat{\mathcal{I}}_{12}\rangle = I_0\left\{\frac{\Gamma_{\text{lead}}\mathcal{I}_d(V_1)+\Gamma_B\mathcal{I}_d(V_B)}{\Gamma_B+\Gamma_{\text{lead}}}-\mathcal{I}_s(V_B)\right\}, \tag{6.D.14}$$

where $V_\alpha\equiv 2(\mu_\alpha-\varepsilon)/(\Gamma_{\text{lead}}+\Gamma_B)$, $I_0=(\Gamma_B\Gamma_{\text{lead}})/(\Gamma_B+\Gamma_{\text{lead}})$, and we define the currents through a single (s) and double (d) dot (shown in Fig. 6.6)

$$\mathcal{I}_s(V)=\frac{1}{2}+\frac{\tan^{-1}(V)}{\pi},\qquad \mathcal{I}_d(V)=\mathcal{I}_s(V)+\frac{V}{\pi(1+V^2)}. \tag{6.D.15}$$

Taking the chemical potential for the shared reservoir $\mu_B\to-\infty$, we are left with the

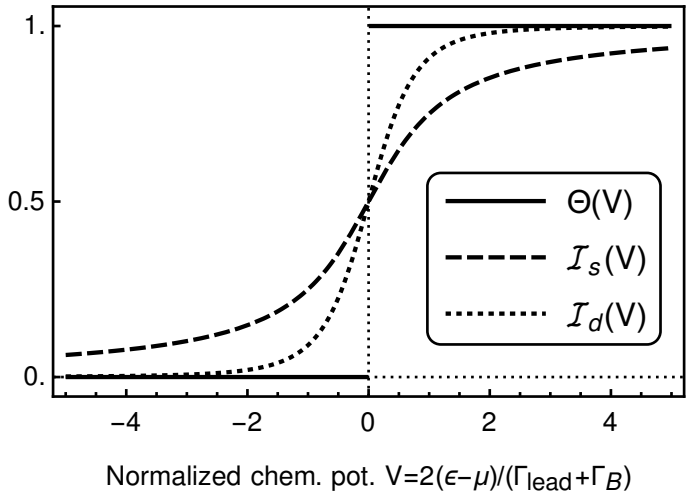

Figure 6.6: Current characteristic functions. A comparison of the three underlying functions in the current characteristics: $\Theta(V)$ (Heaviside step function), $\mathcal{I}_s(V)$, and $\mathcal{I}_d(V)$ as defined in Eq. (6.D.15). As is discussed in the main text, the Heaviside step function $\Theta(V)$ appears in the QME solution, which does not take the finite width of the modes into account, whereas $\mathcal{I}_s(V)$ and $\mathcal{I}_d(V)$ can be identified as the current through a single mode and two modes.

first term, as in the main text. Finally, here and below, it can be checked that the QME result (at $\delta = 0$) can be obtained by replacing

$$\mathcal{I}_{s,d}(V) \;\rightarrow\; f(\mu - \varepsilon), \tag{6.D.16}$$

which also works for finite μ_B.

6.D.2 Current leaving lead 1

To find the current leaving leads 1 and 2, we consider [244]

$$\langle \hat{\mathcal{I}}_i \rangle = -\lim_{t\to\infty} \frac{d}{dt} \sum_k \langle \hat{b}^\dagger_{k,i}(t) \hat{b}_{k,i}(t) \rangle. \tag{6.D.17}$$

Given the Laplace transform of the system operators Eq. (6.D.9), we can find the Laplace transform of the reservoir operators Eq. (6.D.2). Keeping only terms that survive at late

times, we obtain

$$\hat{b}_{k,1}(t) \to e^{-i\varepsilon_{k,1}t}\hat{b}_{k,1}(0) + \frac{J_{k,1}e^{-i\varepsilon_{k,1}t}}{\tilde{\varepsilon}_1 - \varepsilon_{k,1}}\hat{c}_1(0) + \sum_q \frac{J_{k,1}G_{q,1}}{\varepsilon_{k,1} - \varepsilon_{q,B}}\left(\frac{e^{-i\varepsilon_{q,B}t}}{\tilde{\varepsilon}_1 - \varepsilon_{q,B}} + \frac{e^{-i\varepsilon_{k,1}t}}{\varepsilon_{k,1} - \tilde{\varepsilon}_1}\right)\hat{b}_{q,B}(0) + \sum_q \frac{J_{k,1}J_{q,1}}{\varepsilon_{k,1} - \varepsilon_{q,1}}\left(\frac{e^{-i\varepsilon_{q,1}t}}{\tilde{\varepsilon}_1 - \varepsilon_{q,1}} + \frac{e^{-i\varepsilon_{k,1}t}}{\varepsilon_{k,1} - \tilde{\varepsilon}_1}\right)\hat{b}_{q,1}(0), \tag{6.D.18}$$

which gives rise to the reservoir occupation at late times

$$\begin{aligned}\sum_k \langle \hat{b}^\dagger_{k,1}(t)\hat{b}_{k,1}(t)\rangle \to{}& \sum_k f_1(\varepsilon_{k,1}) + \sum_k \frac{J^2_{k,1}}{|\varepsilon_{k,1} - \tilde{\varepsilon}_1|^2}\langle \hat{c}^\dagger_1(0)\hat{c}_1(0)\rangle \\ &- 2\,\mathrm{Re}\sum_{k,q}\frac{J_{k,1}J_{q,1}}{\varepsilon_{k,1} - \varepsilon_{q,1}}e^{i\varepsilon_{k,1}t}\left(\frac{e^{-i\varepsilon_{q,1}t}}{\varepsilon_{q,1} - \tilde{\varepsilon}_1} - \frac{e^{-i\varepsilon_{k,1}t}}{\varepsilon_{k,1} - \tilde{\varepsilon}_1}\right)\langle \hat{b}^\dagger_{k,1}(0)\hat{b}_{q,1}(0)\rangle \\ &+ \int \frac{d\omega\, d\omega'}{4\pi^2}\frac{\Gamma_1\Gamma_{1,B}}{(\omega - \omega')^2}\left|\frac{e^{-i\omega' t}}{\omega' - \tilde{\varepsilon}_1} - \frac{e^{-i\omega t}}{\omega - \tilde{\varepsilon}_1}\right|^2 f_B(\omega') \\ &+ \int \frac{d\omega\, d\omega'}{4\pi^2}\frac{\Gamma_1^2}{(\omega - \omega')^2}\left|\frac{e^{-i\omega' t}}{\omega' - \tilde{\varepsilon}_1} - \frac{e^{-i\omega t}}{\omega - \tilde{\varepsilon}_1}\right|^2 f_1(\omega').\end{aligned} \tag{6.D.19}$$

The first row is time-independent, so it does not contribute to the current. In the second row, both the nominator and denominator go to zero as $q \to k$. Applying l'Hôpital's rule, we find a term linear in t, leading to a constant current.

$$\begin{aligned}&- 2\,\mathrm{Re}\sum_{k,q}\frac{J_{k,1}J_{q,1}}{\varepsilon_{k,1} - \varepsilon_{q,1}}e^{i\varepsilon_{k,1}t}\left(\frac{e^{-i\varepsilon_{q,1}t}}{\varepsilon_{q,1} - \tilde{\varepsilon}_1} - \frac{e^{-i\varepsilon_{k,1}t}}{\varepsilon_{k,1} - \tilde{\varepsilon}_1}\right)\langle \hat{b}^\dagger_{k,1}(0)\hat{b}_{q,1}(0)\rangle \\ &\qquad \to -2\,\mathrm{Re}\int \frac{d\omega}{2\pi}\frac{\Gamma_1 f_1(\omega)}{(\omega - \tilde{\varepsilon}_1)^2}\left[1 + it(\omega - \tilde{\varepsilon}_1)\right].\end{aligned} \tag{6.D.20}$$

Finally, for the last two rows we need to use [244]

$$\lim_{t\to\infty}\frac{d}{dt}\int\frac{d\omega}{2\pi}\frac{1}{(\omega - \omega')^2}\left|\frac{e^{-i\omega' t}}{\omega' - \tilde{\varepsilon}_1} - \frac{e^{-i\omega t}}{\omega - \tilde{\varepsilon}_1}\right|^2 = \frac{1}{|\omega' - \tilde{\varepsilon}_1|^2}, \tag{6.D.21}$$

which can be derived from $\lim_{t\to\infty} f(t) = \lim_{z\to 0} z\int_0^\infty dt\, e^{-zt} f(t)$ [244].

Hence the current at late times is given by

$$\begin{aligned}\langle \hat{\mathcal{I}}_1\rangle \to{}& \int\frac{d\omega}{2\pi}\frac{\Gamma_1(\Gamma_1 + \Gamma_{1,B})f_1(\omega)}{|\omega - \tilde{\varepsilon}_1|^2} - \int\frac{d\omega}{2\pi}\frac{\Gamma_1\left[\Gamma_1 f_1(\omega) + \Gamma_{1,B}f_B(\omega)\right]}{|\omega - \tilde{\varepsilon}_1|^2} \\ ={}& \int\frac{d\omega}{2\pi}\frac{\Gamma_1\Gamma_{1,B}[f_1(\omega) - f_B(\omega)]}{|\omega - \tilde{\varepsilon}_1|^2}.\end{aligned} \tag{6.D.22}$$

Again, any reference to lead 2 is absent, because of isolation. In fact, the form of Eq. (6.D.22) exactly coincides with the current through a single quantum dot connected to two leads, which in this case are the first lead and the shared reservoir.

At zero temperature, we can evaluate the integral straightforwardly to yield

$$\langle \hat{\mathcal{I}}_1 \rangle = \frac{\Gamma_{1,B}\Gamma_1}{\Gamma_{1,B}+\Gamma_1}\left[\mathcal{I}_s(V_1) - \mathcal{I}_s(V_B)\right] \xrightarrow{\mu_B \to -\infty} \frac{\Gamma_{1,B}\Gamma_1}{\Gamma_{1,B}+\Gamma_1}\mathcal{I}_s(V_1). \tag{6.D.23}$$

$\mathcal{I}_s(V)$ is defined as in the main text [also cf. Eq. (6.D.15)]. For a plot see Fig. 6.6. Note that the last expression is always positive, so there is no reverse current in the limit $\mu_B \to -\infty$, independent of μ_2.

6.D.3 Current leaving lead 2

We repeat this procedure for the second lead. We have

$$\begin{aligned}\tilde{b}_{k,2}(z) = \frac{\hat{b}_{k,2}(0)}{z+i\varepsilon_{k,2}} + \frac{iJ_{k,2}}{(z+i\tilde{\varepsilon}_2)(z+i\varepsilon_{k,2})}\left[\hat{c}_2(0) + \sum_q \frac{iG_{q,2}\hat{b}_{q,B}(0)}{z+i\varepsilon_{q,B}} + \sum_q \frac{iJ_{q,2}\hat{b}_{q,2}(0)}{z+i\varepsilon_{q,2}}\right] \\ - \frac{iJ_{k,2}\sqrt{\Gamma_{1,B}\Gamma_{2,B}}}{(z+i\tilde{\varepsilon}_2)(z+i\tilde{\varepsilon}_1)(z+i\varepsilon_{k,2})}\left[\hat{c}_1(0) + \sum_q \frac{iG_{q,1}\hat{b}_{q,B}(0)}{z+i\varepsilon_{q,B}} + \sum_q \frac{iJ_{q,1}\hat{b}_{q,1}(0)}{z+i\varepsilon_{q,1}}\right].\end{aligned} \tag{6.D.24}$$

At late times, this is

$$\begin{aligned}\hat{b}_{k,2}(t) \to e^{-i\varepsilon_{k,2}t}\hat{b}_{k,2}(0) + \frac{J_{k,2}e^{-i\varepsilon_{k,2}t}}{\tilde{\varepsilon}_2-\varepsilon_{k,2}}\hat{c}_2(0) + \sum_q \frac{J_{k,2}G_{q,2}\hat{b}_{q,B}(0)}{\varepsilon_{k,2}-\varepsilon_{q,B}}\left(\frac{e^{-i\varepsilon_{q,B}t}}{\tilde{\varepsilon}_2-\varepsilon_{q,B}} + \frac{e^{-i\varepsilon_{k,2}t}}{\varepsilon_{k,2}-\tilde{\varepsilon}_2}\right) \\ + \sum_q \frac{J_{k,2}J_{q,2}\hat{b}_{q,2}(0)}{\varepsilon_{k,2}-\varepsilon_{q,2}}\left(\frac{e^{-i\varepsilon_{q,2}t}}{\tilde{\varepsilon}_2-\varepsilon_{q,2}} + \frac{e^{-i\varepsilon_{k,2}t}}{\varepsilon_{k,2}-\tilde{\varepsilon}_2}\right) + iJ_{k,2}\sqrt{\Gamma_{1,B}\Gamma_{2,B}}\left\{\frac{\hat{c}_1(0)e^{-i\varepsilon_{k,2}t}}{(\tilde{\varepsilon}_1-\varepsilon_{k,2})(\tilde{\varepsilon}_2-\varepsilon_{k,2})}\right. \\ + \sum_q \frac{G_{q,1}\hat{b}_{q,B}(0)}{\varepsilon_{k,2}-\varepsilon_{q,B}}\left[\frac{e^{-i\varepsilon_{q,B}t}}{(\tilde{\varepsilon}_1-\varepsilon_{q,B})(\tilde{\varepsilon}_2-\varepsilon_{q,B})} - \frac{e^{-i\varepsilon_{k,2}t}}{(\tilde{\varepsilon}_1-\varepsilon_{k,2})(\tilde{\varepsilon}_2-\varepsilon_{k,2})}\right] \\ \left. + \sum_q \frac{J_{q,1}\hat{b}_{q,1}(0)}{\varepsilon_{k,2}-\varepsilon_{q,1}}\left[\frac{e^{-i\varepsilon_{q,1}t}}{(\tilde{\varepsilon}_1-\varepsilon_{q,1})(\tilde{\varepsilon}_2-\varepsilon_{q,1})} - \frac{e^{-i\varepsilon_{k,2}t}}{(\tilde{\varepsilon}_1-\varepsilon_{k,2})(\tilde{\varepsilon}_2-\varepsilon_{k,2})}\right]\right\}.\end{aligned} \tag{6.D.25}$$

The first four terms are the same as for lead 1, except with $1 \leftrightarrow 2$. The rest of the expression originates from coupling to site 1. The reservoir occupation at late times contains the same

terms as Eq. (6.D.19) (except with $1 \leftrightarrow 2$), in addition to the terms

$$2\,\mathrm{Re}\int \frac{d\omega\,d\omega'}{4\pi^2}\frac{i\Gamma_{1,B}\Gamma_{2,B}\Gamma_2 f_B(\omega')}{(\omega-\omega')^2}\left(\frac{e^{i\omega' t}}{\tilde{\varepsilon}_2^*-\omega'}-\frac{e^{i\omega t}}{\tilde{\varepsilon}_2^*-\omega}\right)\left(\frac{e^{-i\omega' t}}{(\tilde{\varepsilon}_1-\omega')(\tilde{\varepsilon}_2-\omega')}-\frac{e^{-i\omega t}}{(\tilde{\varepsilon}_1-\omega)(\tilde{\varepsilon}_2-\omega)}\right)$$
$$+\int \frac{d\omega\,d\omega'}{4\pi^2}\frac{\Gamma_{1,B}^2\Gamma_{2,B}\Gamma_2 f_B(\omega')}{(\omega-\omega')^2}\left|\frac{e^{-i\omega' t}}{(\tilde{\varepsilon}_1-\omega')(\tilde{\varepsilon}_2-\omega')}-\frac{e^{-i\omega t}}{(\tilde{\varepsilon}_1-\omega)(\tilde{\varepsilon}_2-\omega)}\right|^2$$
$$+\int \frac{d\omega\,d\omega'}{4\pi^2}\frac{\Gamma_1\Gamma_2\Gamma_{1,B}\Gamma_{2,B} f_1(\omega')}{(\omega-\omega')^2}\left|\frac{e^{-i\omega' t}}{(\tilde{\varepsilon}_1-\omega')(\tilde{\varepsilon}_2-\omega')}-\frac{e^{-i\omega t}}{(\tilde{\varepsilon}_1-\omega)(\tilde{\varepsilon}_2-\omega)}\right|^2. \tag{6.D.26}$$

The first line originates from the correlator of line 1 and 3 in Eq. (6.D.25), whereas the latter two lines stem from the last two lines in Eq. (6.D.25). The time derivative of the first line can be shown to be

$$-\frac{d}{dt}\int \frac{d\omega\,d\omega'}{4\pi^2}\Gamma_{1,B}\Gamma_{2,B}\Gamma_2 f_B(\omega')\frac{\Gamma_1+\Gamma_{1,B}}{(\omega-\omega')^2}\left|\frac{e^{-i\omega' t}}{(\tilde{\varepsilon}_1-\omega')(\tilde{\varepsilon}_2-\omega')}-\frac{e^{-i\omega t}}{(\tilde{\varepsilon}_1-\omega)(\tilde{\varepsilon}_2-\omega)}\right|^2. \tag{6.D.27}$$

Similarly to above,

$$\lim_{t\to\infty}\frac{d}{dt}\int\frac{d\omega}{2\pi}\frac{1}{(\omega-\omega')^2}\left|\frac{e^{-i\omega' t}}{(\omega'-\tilde{\varepsilon}_1)(\omega'-\tilde{\varepsilon}_2)}-\frac{e^{-i\omega t}}{(\omega-\tilde{\varepsilon}_1)(\omega-\tilde{\varepsilon}_2)}\right|^2=\frac{1}{|\omega'-\tilde{\varepsilon}_1|^2|\omega'-\tilde{\varepsilon}_2|^2}. \tag{6.D.28}$$

Applying the same method as above we derive the current at late times

$$\langle\hat{\mathcal{I}}_2\rangle=-\int\frac{d\omega}{2\pi}\frac{\Gamma_2\Gamma_{2,B}[f_B(\omega)-f_2(\omega)]}{|\omega-\tilde{\varepsilon}_2|^2}-\int\frac{d\omega}{2\pi}\frac{\Gamma_{1,B}\Gamma_{2,B}\Gamma_1\Gamma_2}{|\omega-\tilde{\varepsilon}_1|^2|\omega-\tilde{\varepsilon}_2|^2}\left[f_1(\omega)-f_B(\omega)\right], \tag{6.D.29}$$

where the first term is the same as for the first lead, except with $1 \leftrightarrow 2$, whereas the second term is an additional contribution due to the coupling to lead 1. In the limit of zero-temperature reservoirs, we perform the integral (again setting $\Gamma_{i,B}=\Gamma_B$, $\Gamma_i=\Gamma_{\text{lead}}$ and $\delta=0$)

$$\langle\hat{\mathcal{I}}_2\rangle=I_0\left[\mathcal{I}_s(V_2)-\mathcal{I}_s(V_B)\right]+\frac{2I_0\Gamma_B\Gamma_{\text{lead}}}{(\Gamma_B+\Gamma_{\text{lead}})^2}\left[\mathcal{I}_d(V_B)-\mathcal{I}_d(V_1)\right]. \tag{6.D.30}$$

6.D.4 Comparison between QME and exact result

For reference, we collect the expressions for all currents here.

$$\langle\hat{\mathcal{I}}_1\rangle = I_0[\mathcal{I}_s(V_1) - \mathcal{I}_s(V_B)], \tag{6.D.31a}$$

$$\langle\hat{\mathcal{I}}_{12}\rangle = I_0\left[\frac{\Gamma_{\text{lead}}\mathcal{I}_d(V_1) + \Gamma_B\mathcal{I}_d(V_B)}{\Gamma_B + \Gamma_{\text{lead}}} - \mathcal{I}_s(V_B)\right], \tag{6.D.31b}$$

$$\langle\hat{\mathcal{I}}_2\rangle = I_0\left\{\mathcal{I}_s(V_2) - \mathcal{I}_s(V_B) + \frac{2\Gamma_B\Gamma_{\text{lead}}[\mathcal{I}_d(V_B) - \mathcal{I}_d(V_1)]}{(\Gamma_B + \Gamma_{\text{lead}})^2}\right\}. \tag{6.D.31c}$$

We can compare this with the currents in the weak-coupling limit for the same parameters

$$\langle\hat{I}_1\rangle_{\text{weak}} = I_0\left[f(\varepsilon - \mu_1) - f(\varepsilon - \mu_B)\right], \tag{6.D.32a}$$

$$\langle\hat{I}_{12}\rangle_{\text{weak}} = \frac{\Gamma_{\text{lead}}\Gamma_B^2}{(\Gamma_{\text{lead}} + \Gamma_B)^2 + \delta^2}\left[f(\varepsilon - \mu_1) - f(\varepsilon - \mu_B)\right], \tag{6.D.32b}$$

$$\langle\hat{I}_2\rangle_{\text{weak}} = I_0\left[f(\varepsilon - \mu_2) - f(\varepsilon - \mu_B)\right] + \frac{2I_0\Gamma_B\Gamma_{\text{lead}}}{(\Gamma_{\text{lead}} + \Gamma_B)^2 + \delta^2}\left[f(\varepsilon - \mu_B) - f(\varepsilon - \mu_1)\right]. \tag{6.D.32c}$$

It is straightforward to verify the replacement in the main text even for finite μ_B (but still $\delta = 0$).

The current leaving lead 1 that does not enter lead 2 flows into the shared reservoir $\langle\hat{\mathcal{I}}_{\text{B}}\rangle = -\langle\hat{\mathcal{I}}_1\rangle - \langle\hat{\mathcal{I}}_2\rangle$.

7 | Conclusion

In the introduction of this thesis, we have highlighted some of the technological applications of cavity optomechanics. Featuring precise control about the motional state of massive oscillators with very high quality factors, optomechanics enables excellent charge sensors [25], force sensors [26, 28], mass sensors (mass spectrometers) [27], thermometers [260], and acceleration sensors [261], the latter enabling applications in navigation, bio-tracking, ballistocardiology [116], and detection of gravitational waves [29] and micro-g gravitational fields for gradiometry [116]. With sensors based on levitated optomechanics already outperforming commercially available devices [116], and being deployable in the field [262], it would be no surprise to see commercially available optomechanical sensors in the near future. Within physics research, optomechanical sensing has already been used successfully to detect physical phenomena, such as gravitational waves [29], or excitations in superfluid helium [80].

Why is optomechanics so well-suited for these tasks, and why does this development happen today? First, advances in nanofabrication for solid state devices and perfecting laser trapping techniques for levitated objects have led to mechanical resonators with very high quality factors [78, 83, 85, 86]. Once sufficiently isolated from their environment, optical cooling and squeezing techniques such as those studied in Part I allow the preparation of motional states that are highly susceptible to external forces, while further affording control of resonant frequency (via the optomechanical spring effect [102]) and bandwidth (via optical damping [100]). Finally the tight connection to the optical field enables efficient readout, such that optomechanical sensors can attain very high sensitivities [25–28, 261].

Long coherence time and ground state cooling are steps toward mechanical quantum memory. Protocols for swapping optical with mechanical states have already been analyzed theoretically [263] and demonstrated experimentally [32, 264]. In general this requires a strong coupling regime, in which swapping rates exceed decoherence times. In this regime, coherent manipulation of quantum information is feasible, forming a cornerstone of mechanical devices that amplify or rectify quantum signals, as studied in Part II of this thesis.

Isolators and amplifiers ought to be linear for a large range of input powers. The weak optomechanical nonlinearity, often seen as an obstacle to the production of nonclassical motional states, becomes a boon in this case. Due to the weak nonlinearity, large coherent states are required to coherently enhance the optomechanical coupling into the strong coupling regime, setting the scale over which the resulting devices are linear. As we have already concluded in Sec. 4.5, the two main obstacles on the way toward optomechanical isolators and directional amplifiers are their low bandwidth, a result of the narrow mechanical resonances, and the (current) necessity for four tones that pump the optomechanical interaction. Future research can build on the concepts studied in the optomechanical plaquette and hopefully improve on these important constraints, and we have highlighted some examples of work in this direction in Sec. 4.5.

Recent proposals have seen the generalization of optomechanical systems to arrays in one or two dimensions [184, 185, 265, 266], which could be implemented for example with snowflake phononic and photonic crystals [267]. While currently fabrication disorder in these crystals is prohibitive, future improvements might turn this into a viable platform. Arrays of optomechanical systems might provide large quantum memories, play an important role in phononic quantum networks [268], allow the simulation of (classical) dynamical gauge fields for photons [184, 269], exhibit topological bandstructures for photons and phonons [185], with resulting one-dimensional chiral optomechanical waveguides, and display synchronization [265], extending recent research into the synchronization of (two) oscillators [270–275].

Finally, while technologically immensely useful, the linearized regime of optomechanics has significant drawbacks in the quest to produce, stabilize, and exploit non-classical states in mechanical oscillators. Linear dynamics and dissipation on their own do not naturally lead to non-Gaussian states. Experimentally, single-photon strong coupling [71, 72] is still out of reach, which means that other nonlinearities have to be introduced. There have been efforts to produce heralded or conditional non-Gaussian states in mechanical resonators [110–113, 115, 116, 276] and entanglement [117, 277] through nonlinear detection (photon counting), and theoretical proposals exist for non-classical steady states afforded by a quadratic optomechanical coupling [278]. Another approach is to couple optomechanical system to manifestly nonlinear quantum systems, in particular qubits. Using strain coupling, mechanical resonators have been coupled to NV-centres in diamonds [279–281], and to qubits in superconducting circuits [36, 97, 98]. Apart from the generation of non-classical motional states, this approach can also be employed to increase qubit coherence times by swapping it into the mechanical resonator for storage.

With this brief outlook we have put the work in this thesis into the greater context of the ongoing development of quantum technologies.

Bibliography

[1] D. Malz and A. Nunnenkamp, "Floquet approach to bichromatically driven cavity-optomechanical systems," Physical Review A **94**, 023803 (2016).

[2] D. Malz and A. Nunnenkamp, "Optomechanical dual-beam backaction-evading measurement beyond the rotating-wave approximation," Physical Review A **94**, 053820 (2016).

[3] N. R. Bernier, L. D. Tóth, A. Koottandavida, M. A. Ioannou, D. Malz, A. Nunnenkamp, A. K. Feofanov, and T. J. Kippenberg, "Nonreciprocal reconfigurable microwave optomechanical circuit," Nature Communications **8**, 604 (2017).

[4] D. Malz, L. D. Tóth, N. R. Bernier, A. K. Feofanov, T. J. Kippenberg, and A. Nunnenkamp, "Quantum-Limited Directional Amplifiers with Optomechanics," Physical Review Letters **120**, 023601 (2018).

[5] D. Malz and A. Nunnenkamp, "Current rectification in a double quantum dot through fermionic reservoir engineering," Physical Review B **97**, 165308 (2018).

[6] M. Planck, "Zur Theorie des Gesetzes der Energieverteilung im Normalspectrum," Verhandlungen der Deutschen Physikalischen Gesellschaft **2**, 237–245 (1900).

[7] E. Schrödinger, "Die gegenwärtige Situation in der Quantenmechanik," Die Naturwissenschaften **23**, 807–812 (1935).

[8] H. D. Zeh, "On the interpretation of measurement in quantum theory," Foundations of Physics **1**, 8 (1970).

[9] W. H. Zurek, "Decoherence and the transition from quantum to classical – REVISITED," Los Alamos Science **27** (2003).

[10] M. Schlosshauer, "Decoherence, the measurement problem, and interpretations of quantum mechanics," Reviews of Modern Physics **76**, 1267–1305 (2005).

[11] W. H. Zurek, "Pointer basis of quantum apparatus: Into what mixture does the wave packet collapse?" Physical Review D **24**, 1516–1525 (1981).

[12] J. F. Poyatos, J. I. Cirac, and P. Zoller, "Quantum Reservoir Engineering with Laser Cooled Trapped Ions," Physical Review Letters **77**, 4728–4731 (1996).

[13] P. Lebedew, "Untersuchungen über die Druckkräfte des Lichtes," Annalen der Physik **311**, 433–458 (1901).

[14] E. F. Nichols and G. F. Hull, "A Preliminary Communication on the Pressure of Heat and Light Radiation," Physical Review (Series I) **13**, 307–320 (1901).

[15] A. Ashkin, "Acceleration and Trapping of Particles by Radiation Pressure," Physical Review Letters **24**, 156–159 (1970).

[16] S. Chu, J. E. Bjorkholm, A. Ashkin, and A. Cable, "Experimental Observation of Optically Trapped Atoms," Physical Review Letters **57**, 314–317 (1986).

[17] W. D. Phillips, "Nobel Lecture: Laser cooling and trapping of neutral atoms," Reviews of Modern Physics **70**, 721–741 (1998).

[18] J. Dalibard and C. Cohen-Tannoudji, "Laser cooling below the Doppler limit by polarization gradients: simple theoretical models," Journal of the Optical Society of America B **6**, 2023 (1989).

[19] M. H. Anderson, J. R. Ensher, M. R. Matthews, C. E. Wieman, and E. A. Cornell, "Observation of Bose-Einstein Condensation in a Dilute Atomic Vapor," Science **269**, 198–201 (1995).

[20] K. B. Davis, M. O. Mewes, M. R. Andrews, N. J. Van Druten, D. S. Durfee, D. M. Kurn, and W. Ketterle, "Bose-Einstein condensation in a gas of sodium atoms," Physical Review Letters **75**, 3969–3973 (1995).

[21] F. Marquardt and S. Girvin, "Optomechanics," Physics **2**, 40 (2009).

[22] G. Milburn and M. Woolley, "An Introduction to Quantum Optomechanics," Acta Physica Slovaca. Reviews and Tutorials **61**, 483–601 (2011).

[23] P. Meystre, "A short walk through quantum optomechanics," Annalen der Physik **525**, 215–233 (2013).

[24] M. Aspelmeyer, T. J. Kippenberg, and F. Marquardt, "Cavity optomechanics," Reviews of Modern Physics **86**, 1391–1452 (2014).

[25] A. N. Cleland and M. L. Roukes, "A nanometre-scale mechanical electrometer," Nature **392**, 160–162 (1998).

[26] H. J. Mamin and D. Rugar, "Sub-attonewton force detection at millikelvin temperatures," Applied Physics Letters **79**, 3358–3360 (2001).

[27] K. Jensen, K. Kim, and A. Zettl, "An atomic-resolution nanomechanical mass sensor," Nature Nanotechnology **3**, 533–537 (2008).

[28] E. Gavartin, P. Verlot, and T. J. Kippenberg, "A hybrid on-chip optomechanical transducer for ultrasensitive force measurements," Nature Nanotechnology **7**, 509–514 (2012).

[29] The LIGO Scientific Collaboration and Virgo Collaboration, "Observation of Gravitational Waves from a Binary Black Hole Merger," Physical Review Letters **116**, 061102 (2016).

[30] K. Stannigel, P. Rabl, A. S. Sørensen, P. Zoller, and M. D. Lukin, "Optomechanical Transducers for Long-Distance Quantum Communication," Physical Review Letters **105**, 220501 (2010).

[31] K. Stannigel, P. Rabl, A. S. Sørensen, M. D. Lukin, and P. Zoller, "Optomechanical transducers for quantum-information processing," Physical Review A **84**, 042341 (2011).

[32] A. P. Reed, K. H. Mayer, J. D. Teufel, L. D. Burkhart, W. Pfaff, M. Reagor, L. Sletten, X. Ma, R. J. Schoelkopf, E. Knill, and K. W. Lehnert, "Faithful conversion of propagating quantum information to mechanical motion," Nature Physics **13**, 1163–1167 (2017).

[33] J. I. Cirac, P. Zoller, H. J. Kimble, and H. Mabuchi, "Quantum State Transfer and Entanglement Distribution among Distant Nodes in a Quantum Network," Physical Review Letters **78**, 3221–3224 (1997).

[34] H. J. Kimble, "The quantum internet," Nature **453**, 1023–1030 (2008).

[35] B. Rogers, N. Lo Gullo, G. De Chiara, G. M. Palma, and M. Paternostro, "Hybrid optomechanics for Quantum Technologies," Quantum Measurements and Quantum Metrology **2**, 11–43 (2014).

[36] Y. Chu, P. Kharel, W. H. Renninger, L. D. Burkhart, L. Frunzio, P. T. Rakich, and R. J. Schoelkopf, "Quantum acoustics with superconducting qubits," Science **358**, 199–202 (2017).

[37] D. Stamper-Kurn, "Cavity Optomechanics with cold atoms," in *Cavity Optomechanics*, edited by M. Aspelmeyer, T. J. Kippenberg, and F. Marquardt (Springer Berlin Heidelberg, Berlin, Heidelberg, 2014) pp. 283–325.

[38] M. Gertsenshtein, "Wave Resonance of Light and Gravitational Waves," Journal of Experimental and Theoretical Physics **14**, 113 (1960).

[39] C. M. Caves, "Quantum-mechanical noise in an interferometer," Physical Review D **23**, 1693–1708 (1981).

[40] The LIGO Scientific Collaboration, "A gravitational wave observatory operating beyond the quantum shot-noise limit: Squeezed light in application," Nature Physics **7**, 962–965 (2011).

[41] The LIGO Scientific Collaboration, "Enhancing the sensitivity of the LIGO gravitational wave detector by using squeezed states of light," Nature Photonics **7**, 613–619 (2013).

[42] J. D. Teufel, T. Donner, D. Li, J. W. Harlow, M. S. Allman, K. Cicak, A. J. Sirois, J. D. Whittaker, K. W. Lehnert, and R. W. Simmonds, "Sideband cooling of micromechanical motion to the quantum ground state," Nature **475**, 359–363 (2011).

[43] J. Chan, T. P. M. Alegre, A. H. Safavi-Naeini, J. T. Hill, A. Krause, S. Gröblacher, M. Aspelmeyer, and O. Painter, "Laser cooling of a nanomechanical oscillator into its quantum ground state," Nature **478**, 89–92 (2011).

[44] E. E. Wollman, C. U. Lei, A. J. Weinstein, J. Suh, A. Kronwald, F. Marquardt, A. A. Clerk, and K. C. Schwab, "Quantum squeezing of motion in a mechanical resonator," Science **349**, 952–955 (2015).

[45] J.-M. Pirkkalainen, E. Damskägg, M. Brandt, F. Massel, and M. A. Sillanpää, "Squeezing of Quantum Noise of Motion in a Micromechanical Resonator," Physical Review Letters **115**, 243601 (2015).

[46] F. Lecocq, J. B. Clark, R. W. Simmonds, J. Aumentado, and J. D. Teufel, "Quantum Nondemolition Measurement of a Nonclassical State of a Massive Object," Physical Review X **5**, 041037 (2015).

[47] C. F. Ockeloen-Korppi, E. Damskägg, J.-M. Pirkkalainen, M. Asjad, A. A. Clerk, F. Massel, M. J. Woolley, and M. A. Sillanpää, "Stabilized entanglement of massive mechanical oscillators," Nature **556**, 478–482 (2018).

[48] J. T. Hill, A. H. Safavi-Naeini, J. Chan, and O. Painter, "Coherent optical wavelength conversion via cavity optomechanics," Nature Communications **3**, 1196 (2012).

[49] F. Massel, T. T. Heikkilä, J.-M. Pirkkalainen, S. U. Cho, H. Saloniemi, P. J. Hakonen, and M. A. Sillanpää, "Microwave amplification with nanomechanical resonators," Nature **480**, 351–354 (2011).

[50] J. Suh, A. J. Weinstein, C. U. Lei, E. E. Wollman, S. K. Steinke, P. Meystre, A. A. Clerk, and K. C. Schwab, "Mechanically detecting and avoiding the quantum fluctuations of a microwave field." Science **344**, 1262–1265 (2014).

[51] L. D. Tóth, N. R. Bernier, A. Nunnenkamp, A. K. Feofanov, and T. J. Kippenberg, "A dissipative quantum reservoir for microwave light using a mechanical oscillator," Nature Physics **13**, 787–793 (2017).

[52] K. Fang, J. Luo, A. Metelmann, M. H. Matheny, F. Marquardt, A. A. Clerk, and O. Painter, "Generalized non-reciprocity in an optomechanical circuit via synthetic magnetism and reservoir engineering," Nature Physics **13**, 465–471 (2017).

[53] G. A. Peterson, F. Lecocq, K. Cicak, R. W. Simmonds, J. Aumentado, and J. D. Teufel, "Demonstration of Efficient Nonreciprocity in a Microwave Optomechanical Circuit," Physical Review X **7**, 031001 (2017).

[54] S. Barzanjeh, M. Wulf, M. Peruzzo, M. Kalaee, P. B. Dieterle, O. Painter, and J. M. Fink, "Mechanical on-chip microwave circulator," Nature Communications **8**, 953 (2017).

[55] A. A. Geraci, S. J. Smullin, D. M. Weld, J. Chiaverini, and A. Kapitulnik, "Improved constraints on non-Newtonian forces at 10 microns," Physical Review D **78**, 022002 (2008).

[56] J. Schmöle, M. Dragosits, H. Hepach, and M. Aspelmeyer, "A micromechanical proof-of-principle experiment for measuring the gravitational force of milligram masses," Classical and Quantum Gravity **33**, 125031 (2016).

[57] K. F. Riley, M. P. Hobson, and S. J. Bence, *Mathematical methods for Physics and Engineering* (Cambridge University Press, Cambridge, 2006).

[58] R. Kubo, "The fluctuation-dissipation theorem," Reports on Progress in Physics **29**, 306 (1966).

[59] P. A. M. Dirac, *The Principles of Quantum Mechanics*, International series of monographs on physics (Clarendon Press, 1981).

[60] A. O. Caldeira and A. J. Leggett, "Influence of Dissipation on Quantum Tunneling in Macroscopic Systems," Physical Review Letters **46**, 211–214 (1981).

[61] R. Feynman and F. Vernon, "The theory of a general quantum system interacting with a linear dissipative system," Annals of Physics **24**, 118–173 (1963).

[62] G. W. Ford, M. Kac, and P. Mazur, "Statistical Mechanics of Assemblies of Coupled Oscillators," Journal of Mathematical Physics **6**, 504–515 (1965).

[63] C. M. Caves, "Quantum limits on noise in linear amplifiers," Physical Review D **26**, 1817–1839 (1982).

[64] B. Yurke and J. S. Denker, "Quantum network theory," Physical Review A **29**, 1419–1437 (1984).

[65] C. W. Gardiner and M. J. Collett, "Input and output in damped quantum systems: Quantum stochastic differential equations and the master equation," Physical Review A **31**, 3761–3774 (1985).

[66] A. A. Clerk, M. H. Devoret, S. M. Girvin, F. Marquardt, and R. J. Schoelkopf, "Introduction to quantum noise, measurement, and amplification," Reviews of Modern Physics **82**, 1155–1208 (2010).

[67] C. Gardiner and P. Zoller, *Quantum Noise: A Handbook of Markovian and Non-Markovian Quantum Stochastic Methods with Applications to Quantum Optics*, Springer Series in Synergetics (Springer, 2004).

[68] D. Walls and G. J. Milburn, *Quantum Optics*, edited by D. Walls and G. J. Milburn (Springer Berlin Heidelberg, Berlin, Heidelberg, 2008).

[69] W. P. Bowen and G. J. Milburn, *Quantum Optomechanics* (Taylor & Francis, Boca Raton, 2015).

[70] P. Bocchieri and A. Loinger, "Quantum Recurrence Theorem," Physical Review **107**, 337–338 (1957).

[71] P. Rabl, "Photon Blockade Effect in Optomechanical Systems," Physical Review Letters **107**, 063601 (2011).

[72] A. Nunnenkamp, K. Børkje, and S. M. Girvin, "Single-Photon Optomechanics," Physical Review Letters **107**, 063602 (2011).

[73] C. K. Law, "Interaction between a moving mirror and radiation pressure: A Hamiltonian formulation," Physical Review A **51**, 2537–2541 (1995).

[74] S. Gröblacher, J. B. Hertzberg, M. R. Vanner, G. D. Cole, S. Gigan, K. C. Schwab, and M. Aspelmeyer, "Demonstration of an ultracold micro-optomechanical oscillator in a cryogenic cavity," Nature Physics **5**, 485–488 (2009).

[75] D. Kleckner, B. Pepper, E. Jeffrey, P. Sonin, S. M. Thon, and D. Bouwmeester, "Optomechanical trampoline resonators," Optics Express **19**, 19708 (2011).

[76] J. D. Thompson, B. M. Zwickl, A. M. Jayich, F. Marquardt, S. M. Girvin, and J. G. E. Harris, "Strong dispersive coupling of a high-finesse cavity to a micromechanical membrane." Nature **452**, 72–5 (2008).

[77] E. Verhagen, S. Deléglise, S. Weis, A. Schliesser, and T. J. Kippenberg, "Quantum-coherent coupling of a mechanical oscillator to an optical cavity mode," Nature **482**, 63–67 (2012).

[78] M. Bhattacharya, A. N. Vamivakas, and P. Barker, "Levitated optomechanics: introduction," Journal of the Optical Society of America B **34**, LO1 (2017).

[79] L. A. D. Lorenzo and K. C. Schwab, "Superfluid optomechanics: coupling of a superfluid to a superconducting condensate," New Journal of Physics **16**, 113020 (2014).

[80] G. I. Harris, D. L. McAuslan, E. Sheridan, Y. Sachkou, C. Baker, and W. P. Bowen, "Laser cooling and control of excitations in superfluid helium," Nature Physics **12**, 788–793 (2016).

[81] L. Childress, M. P. Schmidt, A. D. Kashkanova, C. D. Brown, G. I. Harris, A. Aiello, F. Marquardt, and J. G. E. Harris, "Cavity optomechanics in a levitated helium drop," Physical Review A **96**, 063842 (2017).

[82] G. Bahl, K. H. Kim, W. Lee, J. Liu, X. Fan, and T. Carmon, "Brillouin cavity optomechanics with microfluidic devices," Nature Communications **4**, 1994 (2013).

[83] Y. Tsaturyan, A. Barg, A. Simonsen, L. G. Villanueva, S. Schmid, A. Schliesser, and E. S. Polzik, "Demonstration of suppressed phonon tunneling losses in phononic

bandgap shielded membrane resonators for high-Q optomechanics," Optics Express **22**, 6810 (2014).

[84] Y. Tsaturyan, A. Barg, E. S. Polzik, and A. Schliesser, "Ultracoherent nanomechanical resonators via soft clamping and dissipation dilution," Nature Nanotechnology **12**, 776–783 (2017).

[85] S. S. Verbridge, D. F. Shapiro, H. G. Craighead, and J. M. Parpia, "Macroscopic Tuning of Nanomechanics: Substrate Bending for Reversible Control of Frequency and Quality Factor of Nanostring Resonators," Nano Letters **7**, 1728–1735 (2007).

[86] A. H. Ghadimi, S. A. Fedorov, N. J. Engelsen, M. J. Bereyhi, R. Schilling, D. J. Wilson, and T. J. Kippenberg, "Elastic strain engineering for ultralow mechanical dissipation," Science **360**, 764–768 (2018).

[87] H. Walther, B. T. H. Varcoe, B.-G. Englert, and T. Becker, "Cavity quantum electrodynamics," Reports on Progress in Physics **69**, 1325–1382 (2006).

[88] J. I. Cirac and P. Zoller, "Quantum Computations with Cold Trapped Ions," Physical Review Letters **74**, 4091–4094 (1995).

[89] R. Blatt and D. Wineland, "Entangled states of trapped atomic ions," Nature **453**, 1008–1015 (2008).

[90] D. Jaksch, C. Bruder, J. I. Cirac, C. W. Gardiner, and P. Zoller, "Cold Bosonic Atoms in Optical Lattices," Physical Review Letters **81**, 3108–3111 (1998).

[91] C. Gross and I. Bloch, "Quantum simulations with ultracold atoms in optical lattices," Science **357**, 995–1001 (2017).

[92] U. Vool and M. Devoret, "Introduction to quantum electromagnetic circuits," International Journal of Circuit Theory and Applications **45**, 897–934 (2017).

[93] J. D. Teufel, D. Li, M. S. Allman, K. Cicak, A. J. Sirois, J. D. Whittaker, and R. W. Simmonds, "Circuit cavity electromechanics in the strong-coupling regime," Nature **471**, 204–208 (2011).

[94] A. Blais, R.-S. Huang, A. Wallraff, S. M. Girvin, and R. J. Schoelkopf, "Cavity quantum electrodynamics for superconducting electrical circuits: An architecture for quantum computation," Physical Review A **69**, 062320 (2004).

[95] A. D. Armour, M. P. Blencowe, and K. C. Schwab, "Entanglement and Decoherence of a Micromechanical Resonator via Coupling to a Cooper-Pair Box," Physical Review Letters **88**, 148301 (2002).

[96] E. K. Irish and K. Schwab, "Quantum measurement of a coupled nanomechanical resonator–Cooper-pair box system," Physical Review B **68**, 155311 (2003).

[97] Y. Chu, P. Kharel, T. Yoon, L. Frunzio, P. T. Rakich, and R. J. Schoelkopf, "Climbing the phonon Fock state ladder," arXiv:1804.07426 (2018).

[98] K. J. Satzinger, Y. P. Zhong, H. S. Chang, G. A. Peairs, A. Bienfait, M.-H. Chou, A. Y. Cleland, C. R. Conner, E. Dumur, J. Grebel, I. Gutierrez, B. H. November, R. G. Povey, S. J. Whiteley, D. D. Awschalom, D. I. Schuster, and A. N. Cleland, "Quantum control of surface acoustic wave phonons," arXiv:1804.07308 (2018).

[99] R. Leijssen, G. R. La Gala, L. Freisem, J. T. Muhonen, and E. Verhagen, "Nonlinear cavity optomechanics with nanomechanical thermal fluctuations," Nature Communications **8**, 16024 (2017).

[100] F. Marquardt, J. P. Chen, A. A. Clerk, and S. M. Girvin, "Quantum Theory of Cavity-Assisted Sideband Cooling of Mechanical Motion," Physical Review Letters **99**, 093902 (2007).

[101] I. Wilson-Rae, N. Nooshi, W. Zwerger, and T. J. Kippenberg, "Theory of Ground State Cooling of a Mechanical Oscillator Using Dynamical Backaction," Physical Review Letters **99**, 093901 (2007).

[102] T. Corbitt, Y. Chen, E. Innerhofer, H. Müller-Ebhardt, D. Ottaway, H. Rehbein, D. Sigg, S. Whitcomb, C. Wipf, and N. Mavalvala, "An All-Optical Trap for a Gram-Scale Mirror," Physical Review Letters **98**, 150802 (2007).

[103] V. B. Braginskii and Manukin Anatolii Borisovich, *Measurement of weak forces in physics experiments*, edited by D. H. Douglass (University of Chicago Press, Chicago, 1977).

[104] T. J. Kippenberg and K. J. Vahala, "Cavity Optomechanics: Back-Action at the Mesoscale," Science **321**, 1172–1176 (2008).

[105] S. Bose, K. Jacobs, and P. L. Knight, "Preparation of nonclassical states in cavities with a moving mirror," Physical Review A **56**, 4175–4186 (1997).

[106] S. Mancini, V. I. Man'ko, and P. Tombesi, "Ponderomotive control of quantum macroscopic coherence," Physical Review A **55**, 3042–3050 (1997).

[107] D. Vitali, S. Gigan, A. Ferreira, H. R. Böhm, P. Tombesi, A. Guerreiro, V. Vedral, A. Zeilinger, and M. Aspelmeyer, "Optomechanical Entanglement between a Movable Mirror and a Cavity Field," Physical Review Letters **98**, 030405 (2007).

[108] D. Vitali, P. Tombesi, M. J. Woolley, A. C. Doherty, and G. J. Milburn, "Entangling a nanomechanical resonator and a superconducting microwave cavity," Physical Review A **76**, 042336 (2007).

[109] C. Genes, A. Mari, P. Tombesi, and D. Vitali, "Robust entanglement of a micromechanical resonator with output optical fields," Physical Review A **78**, 032316 (2008).

[110] M. R. Vanner, M. Aspelmeyer, and M. S. Kim, "Quantum State Orthogonalization and a Toolset for Quantum Optomechanical Phonon Control," Physical Review Letters **110**, 010504 (2013).

[111] C. Galland, N. Sangouard, N. Piro, N. Gisin, and T. J. Kippenberg, "Heralded Single-Phonon Preparation, Storage, and Readout in Cavity Optomechanics," Physical Review Letters **112**, 143602 (2014).

[112] J. D. Cohen, S. M. Meenehan, G. S. MacCabe, S. Gröblacher, A. H. Safavi-Naeini, F. Marsili, M. D. Shaw, and O. Painter, "Phonon counting and intensity interferometry of a nanomechanical resonator," Nature **520**, 522–525 (2015).

[113] T. J. Milburn, M. S. Kim, and M. R. Vanner, "Nonclassical-state generation in macroscopic systems via hybrid discrete-continuous quantum measurements," Physical Review A **93**, 053818 (2016).

[114] M. Ringbauer, T. J. Weinhold, L. A. Howard, A. G. White, and M. R. Vanner, "Generation of mechanical interference fringes by multi-photon counting," New Journal of Physics **20**, 053042 (2018).

[115] S. Hong, R. Riedinger, I. Marinković, A. Wallucks, S. G. Hofer, R. A. Norte, M. Aspelmeyer, and S. Gröblacher, "Hanbury Brown and Twiss interferometry of single phonons from an optomechanical resonator," Science **358**, 203–206 (2017).

[116] J. Li, S. Gröblacher, S.-Y. Zhu, and G. S. Agarwal, "Generation and detection of non-Gaussian phonon-added coherent states in optomechanical systems," Physical Review A **98**, 011801 (2018).

[117] R. Riedinger, A. Wallucks, I. Marinković, C. Löschnauer, M. Aspelmeyer, S. Hong, and S. Gröblacher, "Remote quantum entanglement between two micromechanical oscillators," Nature **556**, 473–477 (2018).

[118] M. Collett, R. Loudon, and C. Gardiner, "Quantum Theory of Optical Homodyne and Heterodyne Detection," Journal of Modern Optics **34**, 881–902 (1987).

[119] G. J. Milburn, "Quantum measurement theory of optical heterodyne detection," Physical Review A **36**, 5271–5279 (1987).

[120] H. A. Haus and J. A. Mullen, "Quantum Noise in Linear Amplifiers," Physical Review **128**, 2407–2413 (1962).

[121] A. Kronwald, F. Marquardt, and A. A. Clerk, "Arbitrarily large steady-state bosonic squeezing via dissipation," Physical Review A **88**, 063833 (2013).

[122] C. U. Lei, A. J. Weinstein, J. Suh, E. E. Wollman, A. Kronwald, F. Marquardt, A. A. Clerk, and K. C. Schwab, "Quantum Nondemolition Measurement of a Quantum Squeezed State Beyond the 3 dB Limit," Physical Review Letters **117**, 100801 (2016).

[123] B. A. Levitan, A. Metelmann, and A. A. Clerk, "Optomechanics with two-phonon driving," New Journal of Physics **18**, 093014 (2016).

[124] A. Mari and J. Eisert, "Gently Modulating Optomechanical Systems," Physical Review Letters **103**, 213603 (2009).

[125] A. Papageorge, A. Majumdar, E. D. Kim, and J. Vučković, "Bichromatic driving of a solid-state cavity quantum electrodynamics system," New Journal of Physics **14**, 013028 (2012).

[126] N. Wereley and S. Hall, "Frequency response of linear time periodic systems," in *29th IEEE Conference on Decision and Control* (IEEE, 1990) pp. 3650–3655 vol.6.

[127] W.-T. Wu, J. Wickert, and H. Griffin, "Modal analysis of the steady state response of a driven periodic linear system," Journal of Sound and Vibration **183**, 297–308 (1995).

[128] J. A. Ball, I. Gohberg, and M. A. Kaashoek, "A frequency response function for linear, time-varying systems," Mathematics of Control, Signals, and Systems **8**, 334–351 (1995).

[129] P. Vanassche, G. Gielen, and W. Sansen, "Symbolic modeling of periodically time-varying systems using harmonic transfer matrices," IEEE Transactions on Computer-Aided Design of Integrated Circuits and Systems **21**, 1011–1024 (2002).

[130] H. Sandberg, E. Mollerstedt, and Bernhardsson, "Frequency-domain analysis of linear time-periodic systems," IEEE Transactions on Automatic Control **50**, 1971–1983 (2005).

[131] P. Z. G. Fonseca, E. B. Aranas, J. Millen, T. S. Monteiro, and P. F. Barker, "Nonlinear Dynamics and Strong Cavity Cooling of Levitated Nanoparticles," Physical Review Letters **117**, 173602 (2016).

[132] E. B. Aranas, P. Z. G. Fonseca, P. F. Barker, and T. S. Monteiro, "Split-sideband spectroscopy in slowly modulated optomechanics," New Journal of Physics **18**, 113021 (2016).

[133] E. B. Aranas, M. J. Akram, D. Malz, and T. S. Monteiro, "Quantum noise spectra for periodically driven cavity optomechanics," Physical Review A **96**, 063836 (2017).

[134] L. Qiu, I. Shomroni, M. A. Ioannou, D. Malz, A. Nunnenkamp, and T. Kippenberg, "Motional Sideband Asymmetry in Quantum Optomechanics in the Presence of Kerr-type Nonlinearities," arXiv:1805.12364 (2018).

[135] L. Ranzani and J. Aumentado, "Graph-based analysis of nonreciprocity in coupled-mode systems," New Journal of Physics **17**, 023024 (2015).

[136] C. M. Caves, K. S. Thorne, R. W. P. Drever, V. D. Sandberg, and M. Zimmermann, "On the measurement of a weak classical force coupled to a quantum-mechanical oscillator. I. Issues of principle," Reviews of Modern Physics **52**, 341–392 (1980).

[137] V. B. Braginsky, Y. I. Vorontsov, and K. S. Thorne, "Quantum Nondemolition Measurements," Science **209**, 547–557 (1980).

[138] M. F. Bocko and R. Onofrio, "On the measurement of a weak classical force coupled to a harmonic oscillator: experimental progress," Reviews of Modern Physics **68**, 755–799 (1996).

[139] A. A. Clerk, F. Marquardt, and K. Jacobs, "Back-action evasion and squeezing of a mechanical resonator using a cavity detector," New Journal of Physics **10**, 095010 (2008).

[140] J. B. Hertzberg, T. Rocheleau, T. Ndukum, M. Savva, A. A. Clerk, and K. C. Schwab, "Back-action-evading measurements of nanomechanical motion," Nature Physics **6**, 213–217 (2010).

[141] E. S. Polzik and K. Hammerer, "Trajectories without quantum uncertainties," Annalen der Physik **527**, A15–A20 (2015).

[142] G. Vasilakis, H. Shen, K. Jensen, M. Balabas, D. Salart, B. Chen, and E. S. Polzik, "Generation of a squeezed state of an oscillator by stroboscopic back-action-evading measurement," Nature Physics **11**, 389–392 (2015).

[143] M. J. Woolley and A. A. Clerk, "Two-mode back-action-evading measurements in cavity optomechanics," Physical Review A **87**, 063846 (2013).

[144] C. F. Ockeloen-Korppi, E. Damskägg, J.-M. Pirkkalainen, T. T. Heikkilä, F. Massel, and M. A. Sillanpää, "Low-Noise Amplification and Frequency Conversion with a Multiport Microwave Optomechanical Device," Physical Review X **6**, 041024 (2016).

[145] J. Millen, P. Z. G. Fonseca, T. Mavrogordatos, T. S. Monteiro, and P. F. Barker, "Cavity Cooling a Single Charged Levitated Nanosphere," Physical Review Letters **114**, 123602 (2015).

[146] A. E. Fomin, M. L. Gorodetsky, I. S. Grudinin, and V. S. Ilchenko, "Nonstationary nonlinear effects in optical microspheres," Journal of the Optical Society of America B **22**, 459 (2005).

[147] H. Rokhsari and K. J. Vahala, "Observation of Kerr nonlinearity in microcavities at room temperature," Optics Letters **30**, 427 (2005).

[148] P. E. Barclay, K. Srinivasan, and O. Painter, "Nonlinear response of silicon photonic crystal micresonators excited via an integrated waveguide and fiber taper," Optics Express **13**, 801 (2005).

[149] M. Tsang and C. M. Caves, "Evading Quantum Mechanics: Engineering a Classical Subsystem within a Quantum Environment," Physical Review X **2**, 031016 (2012).

[150] D. M. Pozar, *Microwave Engineering*, 4th ed. (Wiley, 2011).

[151] B. A. Auld and B. A. Auld, "The Synthesis of Symmetrical Waveguide Circulators," IRE Transactions on Microwave Theory and Techniques **7**, 238–246 (1959).

[152] U. Milano, J. H. Saunders, and L. Davis, "A Y-Junction Strip-Line Circulator," IEEE Transactions on Microwave Theory and Techniques **8**, 346–351 (1960).

[153] C. Fay and R. Comstock, "Operation of the Ferrite Junction Circulator," IEEE Transactions on Microwave Theory and Techniques **13**, 15–27 (1965).

[154] L. J. Aplet and J. W. Carson, "A Faraday Effect Optical Isolator," Applied Optics **3**, 544 (1964).

[155] M. Shirasaki and K. Asama, "Compact optical isolator for fibers using birefringent wedges," Applied Optics **21**, 4296 (1982).

[156] T. Sato, J. Sun, R. Kasahara, and S. Kawakami, "Lens-free in-line optical isolators," Optics Letters **24**, 1337 (1999).

[157] L. Bi, J. Hu, P. Jiang, D. H. Kim, G. F. Dionne, L. C. Kimerling, and C. A. Ross, "On-chip optical isolation in monolithically integrated non-reciprocal optical resonators," Nature Photonics **5**, 758–762 (2011).

[158] S. Manipatruni, J. T. Robinson, and M. Lipson, "Optical Nonreciprocity in Optomechanical Structures," Physical Review Letters **102**, 213903 (2009).

[159] L. Fan, J. Wang, L. T. Varghese, H. Shen, B. Niu, Y. Xuan, A. M. Weiner, and M. Qi, "An all-silicon passive optical diode," Science **335**, 447–450 (2012).

[160] X. Guo, C.-L. Zou, H. Jung, and H. X. Tang, "On-Chip Strong Coupling and Efficient Frequency Conversion between Telecom and Visible Optical Modes," Physical Review Letters **117**, 123902 (2016).

[161] B. Anderson and R. Newcomb, "On reciprocity and time-variable networks," Proceedings of the IEEE **53**, 1674–1674 (1965).

[162] Z. Yu and S. Fan, "Complete optical isolation created by indirect interband photonic transitions," Nature Photonics **3**, 91–94 (2009).

[163] H. Lira, Z. Yu, S. Fan, and M. Lipson, "Electrically Driven Nonreciprocity Induced by Interband Photonic Transition on a Silicon Chip," Physical Review Letters **109**, 033901 (2012).

[164] M. S. Kang, A. Butsch, and P. S. J. Russell, "Reconfigurable light-driven opto-acoustic isolators in photonic crystal fibre," Nature Photonics **5**, 549–553 (2011).

[165] N. A. Estep, D. L. Sounas, J. Soric, and A. Alù, "Magnetic-free non-reciprocity and isolation based on parametrically modulated coupled-resonator loops," Nature Physics **10**, 923–927 (2014).

[166] B. Peng, S. K. Özdemir, F. Lei, F. Monifi, M. Gianfreda, G. L. Long, S. Fan, F. Nori, C. M. Bender, and L. Yang, "Parity–time-symmetric whispering-gallery microcavities," Nature Physics **10**, 394–398 (2014).

[167] C.-H. Dong, Z. Shen, C.-L. Zou, Y.-L. Zhang, W. Fu, and G.-C. Guo, "Brillouin-scattering-induced transparency and non-reciprocal light storage," Nature Communications **6**, 6193 (2015).

[168] J. Kim, M. C. Kuzyk, K. Han, H. Wang, and G. Bahl, "Non-reciprocal Brillouin scattering induced transparency," Nature Physics **11**, 275–280 (2015).

[169] M. Scheucher, A. Hilico, E. Will, J. Volz, and A. Rauschenbeutel, "Quantum optical circulator controlled by a single chirally coupled atom," Science **354**, 1577–1580 (2016).

[170] D. Jalas, A. Petrov, M. Eich, W. Freude, S. Fan, Z. Yu, R. Baets, M. Popović, A. Melloni, J. D. Joannopoulos, M. Vanwolleghem, C. R. Doerr, and H. Renner, "What is — and what is not — an optical isolator," Nature Photonics **7**, 579–582 (2013).

[171] M. H. Devoret and R. J. Schoelkopf, "Superconducting Circuits for Quantum Information: An Outlook," Science **339**, 1169–1174 (2013).

[172] K. Gallo, G. Assanto, K. R. Parameswaran, and M. M. Fejer, "All-optical diode in a periodically poled lithium niobate waveguide," Applied Physics Letters **79**, 314–316 (2001).

[173] J. Koch, A. A. Houck, K. L. Hur, and S. M. Girvin, "Time-reversal-symmetry breaking in circuit-QED-based photon lattices," Physical Review A **82**, 043811 (2010).

[174] A. Kamal, J. Clarke, and M. H. Devoret, "Noiseless non-reciprocity in a parametric active device," Nature Physics **7**, 311–315 (2011).

[175] K. Fang, Z. Yu, and S. Fan, "Realizing effective magnetic field for photons by controlling the phase of dynamic modulation," Nature Photonics **6**, 782–787 (2012).

[176] D. L. Sounas, C. Caloz, and A. Alù, "Giant non-reciprocity at the subwavelength scale using angular momentum-biased metamaterials," Nature Communications **4**, 2407 (2013).

[177] M. Hafezi and P. Rabl, "Optomechanically induced non-reciprocity in microring resonators," Optics Express **20**, 7672 (2012).

[178] C. G. Poulton, R. Pant, A. Byrnes, S. Fan, M. J. Steel, and B. J. Eggleton, "Design for broadband on-chip isolator using stimulated Brillouin scattering in dispersion-engineered chalcogenide waveguides," Optics Express **20**, 21235 (2012).

[179] S. Longhi, "Effective magnetic fields for photons in waveguide and coupled resonator lattices," Optics Letters **38**, 3570 (2013).

[180] K. Fang, Z. Yu, and S. Fan, "Experimental demonstration of a photonic Aharonov-Bohm effect at radio frequencies," Physical Review B **87**, 060301 (2013).

[181] D.-W. Wang, H.-T. Zhou, M.-J. Guo, J.-X. Zhang, J. Evers, and S.-Y. Zhu, "Optical Diode Made from a Moving Photonic Crystal," Physical Review Letters **110**, 093901 (2013).

[182] B. Abdo, K. Sliwa, S. Shankar, M. Hatridge, L. Frunzio, R. Schoelkopf, and M. Devoret, "Josephson Directional Amplifier for Quantum Measurement of Superconducting Circuits," Physical Review Letters **112**, 167701 (2014).

[183] K. M. Sliwa, M. Hatridge, A. Narla, S. Shankar, L. Frunzio, R. J. Schoelkopf, and M. H. Devoret, "Reconfigurable Josephson Circulator/Directional Amplifier," Physical Review X **5**, 041020 (2015).

[184] M. Schmidt, S. Kessler, V. Peano, O. Painter, and F. Marquardt, "Optomechanical creation of magnetic fields for photons on a lattice," Optica **2**, 635 (2015).

[185] V. Peano, C. Brendel, M. Schmidt, and F. Marquardt, "Topological Phases of Sound and Light," Physical Review X **5**, 031011 (2015).

[186] V. Peano, M. Houde, F. Marquardt, and A. A. Clerk, "Topological Quantum Fluctuations and Traveling Wave Amplifiers," Physical Review X **6**, 041026 (2016).

[187] C. Brendel, V. Peano, O. J. Painter, and F. Marquardt, "Pseudomagnetic fields for sound at the nanoscale," Proceedings of the National Academy of Sciences **114**, E3390–E3395 (2017).

[188] C. Brendel, V. Peano, O. Painter, and F. Marquardt, "Snowflake phononic topological insulator at the nanoscale," Physical Review B **97**, 020102 (2018).

[189] L. Ranzani and J. Aumentado, "A geometric description of nonreciprocity in coupled two-mode systems," New Journal of Physics **16**, 103027 (2014).

[190] F. Lecocq, L. Ranzani, G. A. Peterson, K. Cicak, R. W. Simmonds, J. D. Teufel, and J. Aumentado, "Nonreciprocal Microwave Signal Processing with a Field-Programmable Josephson Amplifier," Physical Review Applied **7**, 024028 (2017).

[191] A. Metelmann and A. A. Clerk, "Nonreciprocal Photon Transmission and Amplification via Reservoir Engineering," Physical Review X **5**, 021025 (2015).

[192] A. Kamal and A. Metelmann, "Minimal Models for Nonreciprocal Amplification Using Biharmonic Drives," Physical Review Applied **7**, 034031 (2017).

[193] L. Tian and Z. Li, "Nonreciprocal quantum-state conversion between microwave and optical photons," Physical Review A **96**, 013808 (2017).

[194] N. R. Bernier, L. D. Tóth, A. K. Feofanov, and T. J. Kippenberg, "Nonreciprocity in microwave optomechanical circuits," arXiv:1804.09599 (2018).

[195] B. J. Chapman, E. I. Rosenthal, J. Kerckhoff, B. A. Moores, L. R. Vale, J. A. B. Mates, G. C. Hilton, K. Lalumière, A. Blais, and K. W. Lehnert, "Widely Tunable On-Chip Microwave Circulator for Superconducting Quantum Circuits," Physical Review X **7**, 041043 (2017).

[196] F. Ruesink, J. P. Mathew, M.-A. Miri, A. Alù, and E. Verhagen, "Optical circulation in a multimode optomechanical resonator," Nature Communications **9**, 1798 (2018).

[197] Z. Shen, Y.-L. Zhang, Y. Chen, F.-W. Sun, X.-B. Zou, G.-C. Guo, C.-L. Zou, and C.-H. Dong, "Reconfigurable optomechanical circulator and directional amplifier," Nature Communications **9**, 1797 (2018).

[198] D. B. Sohn, S. Kim, and G. Bahl, "Time-reversal symmetry breaking with acoustic pumping of nanophotonic circuits," Nature Photonics **12**, 91–97 (2018).

[199] D. L. Sounas and A. Alù, "Non-reciprocal photonics based on time modulation," Nature Photonics **11**, 774–783 (2017).

[200] E. Verhagen and A. Alù, "Optomechanical nonreciprocity," Nature Physics **13**, 922–924 (2017).

[201] C. Müller, S. Guan, N. Vogt, J. H. Cole, and T. M. Stace, "Passive On-Chip Superconducting Circulator Using a Ring of Tunnel Junctions," Physical Review Letters **120**, 213602 (2018).

[202] B. Abdo, K. Sliwa, L. Frunzio, and M. Devoret, "Directional Amplification with a Josephson Circuit," Physical Review X **3**, 031001 (2013).

[203] A. Metelmann and A. A. Clerk, "Nonreciprocal quantum interactions and devices via autonomous feedforward," Physical Review A **95**, 013837 (2017).

[204] Z. Shen, Y.-L. Zhang, Y. Chen, C.-L. Zou, Y.-F. Xiao, X.-B. Zou, F.-W. Sun, G.-C. Guo, and C.-H. Dong, "Experimental realization of optomechanically induced non-reciprocity," Nature Photonics **10**, 657–661 (2016).

[205] F. Ruesink, M.-A. Miri, A. Alù, and E. Verhagen, "Nonreciprocity and magnetic-free isolation based on optomechanical interactions," Nature Communications **7**, 13662 (2016).

[206] X.-W. Xu, Y. Li, A.-X. Chen, and Y.-X. Liu, "Nonreciprocal conversion between microwave and optical photons in electro-optomechanical systems," Physical Review A **93**, 023827 (2016).

[207] C. Macklin, K. O'Brien, D. Hover, M. E. Schwartz, V. Bolkhovsky, X. Zhang, W. D. Oliver, and I. Siddiqi, "A near-quantum-limited Josephson traveling-wave parametric amplifier," Science **350**, 307–310 (2015).

[208] A. Roy and M. Devoret, "Quantum-limited parametric amplification with Josephson circuits in the regime of pump depletion," Physical Review B **98**, 045405 (2018).

[209] A. Metelmann and A. A. Clerk, "Quantum-Limited Amplification via Reservoir Engineering," Physical Review Letters **112**, 133904 (2014).

[210] A. Nunnenkamp, V. Sudhir, A. K. Feofanov, A. Roulet, and T. J. Kippenberg, "Quantum-Limited Amplification and Parametric Instability in the Reversed Dissipation Regime of Cavity Optomechanics," Physical Review Letters **113**, 023604 (2014).

[211] J. Li, I. M. Haghighi, N. Malossi, S. Zippilli, and D. Vitali, "Generation and detection of large and robust entanglement between two different mechanical resonators in cavity optomechanics," New Journal of Physics **17**, 103037 (2015).

[212] R. Rivière, S. Deléglise, S. Weis, E. Gavartin, O. Arcizet, A. Schliesser, and T. J. Kippenberg, "Optomechanical sideband cooling of a micromechanical oscillator close to the quantum ground state," Physical Review A **83**, 063835 (2011).

[213] W. G. van der Wiel, S. De Franceschi, J. M. Elzerman, T. Fujisawa, S. Tarucha, and L. P. Kouwenhoven, "Electron transport through double quantum dots," Reviews of Modern Physics **75**, 1–22 (2002).

[214] J. M. Martinis, M. Nahum, and H. D. Jensen, "Metrological accuracy of the electron pump," Physical Review Letters **72**, 904–907 (1994).

[215] S. J. Chorley, J. Frake, C. G. Smith, G. A. C. Jones, and M. R. Buitelaar, "Quantized charge pumping through a carbon nanotube double quantum dot," Applied Physics Letters **100**, 143104 (2012).

[216] M. R. Connolly, K. L. Chiu, S. P. Giblin, M. Kataoka, J. D. Fletcher, C. Chua, J. P. Griffiths, G. A. C. Jones, V. I. Fal'ko, C. G. Smith, and T. J. B. M. Janssen, "Gigahertz quantized charge pumping in graphene quantum dots," Nature Nanotechnology **8**, 417–420 (2013).

[217] J. P. Pekola, O.-P. Saira, V. F. Maisi, A. Kemppinen, M. Möttönen, Y. A. Pashkin, and D. V. Averin, "Single-electron current sources: Toward a refined definition of the ampere," Reviews of Modern Physics **85**, 1421–1472 (2013).

[218] D. M. T. van Zanten, D. M. Basko, I. M. Khaymovich, J. P. Pekola, H. Courtois, and C. B. Winkelmann, "Single Quantum Level Electron Turnstile," Physical Review Letters **116**, 166801 (2016).

[219] D. Loss and D. P. DiVincenzo, "Quantum computation with quantum dots," Physical Review A **57**, 120–126 (1998).

[220] M. H. Devoret and H. Grabert, "Introduction to Single Charge Tunneling," in *Single Charge Tunneling*, edited by H. Garbert and M. H. Devoret (Springer Berlin Heidelberg, 1992) Chap. 1, pp. 1–19.

[221] P. D. Tougaw and C. S. Lent, "Logical devices implemented using quantum cellular automata," Journal of Applied Physics **75**, 1818–1825 (1994).

[222] K. Ono, "Current Rectification by Pauli Exclusion in a Weakly Coupled Double Quantum Dot System," Science **297**, 1313–1317 (2002).

[223] J. Fransson and M. Råsander, "Pauli spin blockade in weakly coupled double quantum dots," Physical Review B **73**, 205333 (2006).

[224] B. Muralidharan and S. Datta, "Generic model for current collapse in spin-blockaded transport," Physical Review B **76**, 035432 (2007).

[225] M. R. Buitelaar, J. Fransson, A. L. Cantone, C. G. Smith, D. Anderson, G. A. C. Jones, A. Ardavan, A. N. Khlobystov, A. A. R. Watt, K. Porfyrakis, and G. A. D. Briggs, "Pauli spin blockade in carbon nanotube double quantum dots," Physical Review B **77**, 245439 (2008).

[226] M. Stopa, "Rectifying Behavior in Coulomb Blockades: Charging Rectifiers," Physical Review Letters **88**, 146802 (2002).

[227] A. Vidan, R. M. Westervelt, M. Stopa, M. Hanson, and A. C. Gossard, "Triple quantum dot charging rectifier," Applied Physics Letters **85**, 3602–3604 (2004).

[228] H. Krauter, C. A. Muschik, K. Jensen, W. Wasilewski, J. M. Petersen, J. I. Cirac, and E. S. Polzik, "Entanglement Generated by Dissipation and Steady State Entanglement of Two Macroscopic Objects," Physical Review Letters **107**, 080503 (2011).

[229] J. T. Barreiro, M. Müller, P. Schindler, D. Nigg, T. Monz, M. Chwalla, M. Hennrich, C. F. Roos, P. Zoller, and R. Blatt, "An open-system quantum simulator with trapped ions," Nature **470**, 486–491 (2011).

[230] Y. Lin, J. P. Gaebler, F. Reiter, T. R. Tan, R. Bowler, A. S. Sørensen, D. Leibfried, and D. J. Wineland, "Dissipative production of a maximally entangled steady state of two quantum bits," Nature **504**, 415–418 (2013).

[231] D. Kienzler, H.-Y. Lo, B. Keitch, L. de Clercq, F. Leupold, F. Lindenfelser, M. Marinelli, V. Negnevitsky, and J. P. Home, "Quantum harmonic oscillator state synthesis by reservoir engineering," Science **347**, 53–56 (2015).

[232] K. W. Murch, U. Vool, D. Zhou, S. J. Weber, S. M. Girvin, and I. Siddiqi, "Cavity-Assisted Quantum Bath Engineering," Physical Review Letters **109**, 183602 (2012).

[233] S. Shankar, M. Hatridge, Z. Leghtas, K. M. Sliwa, A. Narla, U. Vool, S. M. Girvin, L. Frunzio, M. Mirrahimi, and M. H. Devoret, "Autonomously stabilized entanglement between two superconducting quantum bits," Nature **504**, 419–422 (2013).

[234] Z. Leghtas, S. Touzard, I. M. Pop, A. Kou, B. Vlastakis, A. Petrenko, K. M. Sliwa, A. Narla, S. Shankar, M. J. Hatridge, M. Reagor, L. Frunzio, R. J. Schoelkopf, M. Mirrahimi, and M. H. Devoret, "Confining the state of light to a quantum manifold by engineered two-photon loss," Science **347**, 853–857 (2015).

[235] M. J. Woolley and A. A. Clerk, "Two-mode squeezed states in cavity optomechanics via engineering of a single reservoir," Physical Review A **89**, 063805 (2014).

[236] M. J. A. Schuetz, E. M. Kessler, L. M. K. Vandersypen, J. I. Cirac, and G. Giedke, "Nuclear spin dynamics in double quantum dots: Multistability, dynamical polarization, criticality, and entanglement," Physical Review B **89**, 195310 (2014).

[237] A. L. Grimsmo, F. Qassemi, B. Reulet, and A. Blais, "Quantum Optics Theory of Electronic Noise in Coherent Conductors," Physical Review Letters **116**, 043602 (2016).

[238] T. Brandes, "Feedback Control of Quantum Transport," Physical Review Letters **105**, 060602 (2010).

[239] C. Emary, "Feedback Control in Quantum Transport," in *Control of Self-Organizing Nonlinear Systems*, edited by E. Schöll, S. H. L. Klapp, and P. Hövel (Springer International Publishing, Cham, 2016) pp. 275–287.

[240] J. P. Pekola, "Towards quantum thermodynamics in electronic circuits," Nature Physics **11**, 118–123 (2015).

[241] C. A. Stafford and N. S. Wingreen, "Resonant Photon-Assisted Tunneling through a Double Quantum Dot: An Electron Pump from Spatial Rabi Oscillations," Physical Review Letters **76**, 1916–1919 (1996).

[242] B. Wunsch, M. Braun, J. König, and D. Pfannkuche, "Probing level renormalization by sequential transport through double quantum dots," Physical Review B **72**, 205319 (2005).

[243] M. W. Y. Tu and W.-M. Zhang, "Non-Markovian decoherence theory for a double-dot charge qubit," Physical Review B **78**, 235311 (2008).

[244] G. Schaller, *Open Quantum Systems Far from Equilibrium*, Lecture Notes in Physics, Vol. 881 (Springer International Publishing, Cham, 2014).

[245] H.-P. Breuer and F. F. Petruccione, *The theory of open quantum systems* (Oxford University Press, 2002).

[246] A. Levy and R. Kosloff, "The local approach to quantum transport may violate the second law of thermodynamics," EPL (Europhysics Letters) **107**, 20004 (2014).

[247] M. T. Mitchison and M. B. Plenio, "Non-additive dissipation in open quantum networks out of equilibrium," New Journal of Physics **20**, 033005 (2018).

[248] P. P. Hofer, M. Perarnau-Llobet, L. D. M. Miranda, G. Haack, R. Silva, J. B. Brask, and N. Brunner, "Markovian master equations for quantum thermal machines: local versus global approach," New Journal of Physics **19**, 123037 (2017).

[249] S. Datta, *Electronic Transport in Mesoscopic Systems*, Cambridge Studies in Semiconductor Physics and Microelectronic Engineering (Cambridge University Press, 1997).

[250] R. Hanson, L. P. Kouwenhoven, J. R. Petta, S. Tarucha, and L. M. K. Vandersypen, "Spins in few-electron quantum dots," Reviews of Modern Physics **79**, 1217–1265 (2007).

[251] R. Schuster, E. Buks, M. Heiblum, D. Mahalu, V. Umansky, and H. Shtrikman, "Phase measurement in a quantum dot via a double-slit interference experiment," Nature **385**, 417–420 (1997).

[252] A. W. Holleitner, C. R. Decker, H. Qin, K. Eberl, and R. H. Blick, "Coherent Coupling of Two Quantum Dots Embedded in an Aharonov-Bohm Interferometer," Physical Review Letters **87**, 256802 (2001).

[253] M. Avinun-Kalish, M. Heiblum, O. Zarchin, D. Mahalu, and V. Umansky, "Crossover from 'mesoscopic' to 'universal' phase for electron transmission in quantum dots," Nature **436**, 529–533 (2005).

[254] J. M. Elzerman, R. Hanson, J. S. Greidanus, L. H. Willems van Beveren, S. De Franceschi, L. M. K. Vandersypen, S. Tarucha, and L. P. Kouwenhoven, "Few-electron quantum dot circuit with integrated charge read out," Physical Review B **67**, 161308 (2003).

[255] F. H. L. Koppens, C. Buizert, K. J. Tielrooij, I. T. Vink, K. C. Nowack, T. Meunier, L. P. Kouwenhoven, and L. M. K. Vandersypen, "Driven coherent oscillations of a single electron spin in a quantum dot," Nature **442**, 766–771 (2006).

[256] T. A. Baart, M. Shafiei, T. Fujita, C. Reichl, W. Wegscheider, and L. M. K. Vandersypen, "Single-spin CCD," Nature Nanotechnology **11**, 330–334 (2016).

[257] F. R. Braakman, P. Barthelemy, C. Reichl, W. Wegscheider, and L. M. K. Vandersypen, "Long-distance coherent coupling in a quantum dot array," Nature Nanotechnology **8**, 432–437 (2013).

[258] I. de Vega and D. Alonso, "Dynamics of non-Markovian open quantum systems," Reviews of Modern Physics **89**, 015001 (2017).

[259] P. Strasberg, G. Schaller, T. L. Schmidt, and M. Esposito, "Fermionic reaction coordinates and their application to an autonomous Maxwell demon in the strong-coupling regime," Physical Review B **97**, 205405 (2018).

[260] T. P. Purdy, K. E. Grutter, K. Srinivasan, and J. M. Taylor, "Quantum correlations from a room-temperature optomechanical cavity," Science **356**, 1265–1268 (2017).

[261] A. G. Krause, M. Winger, T. D. Blasius, Q. Lin, and O. Painter, "A high-resolution microchip optomechanical accelerometer," Nature Photonics **6**, 768–772 (2012).

[262] Y. L. Li, "Don't hesitate, innovate," Nature Nanotechnology **11**, 652–652 (2016).

[263] Y.-D. Wang and A. A. Clerk, "Using Interference for High Fidelity Quantum State Transfer in Optomechanics," Physical Review Letters **108**, 153603 (2012).

[264] T. A. Palomaki, J. W. Harlow, J. D. Teufel, R. W. Simmonds, and K. W. Lehnert, "Coherent state transfer between itinerant microwave fields and a mechanical oscillator," Nature **495**, 210–214 (2013).

[265] G. Heinrich, M. Ludwig, J. Qian, B. Kubala, and F. Marquardt, "Collective Dynamics in Optomechanical Arrays," Physical Review Letters **107**, 043603 (2011).

[266] M. Ludwig and F. Marquardt, "Quantum Many-Body Dynamics in Optomechanical Arrays," Physical Review Letters **111**, 073603 (2013).

[267] A. H. Safavi-Naeini, J. T. Hill, S. Meenehan, J. Chan, S. Gröblacher, and O. Painter, "Two-Dimensional Phononic-Photonic Band Gap Optomechanical Crystal Cavity," Physical Review Letters **112**, 153603 (2014).

[268] S. J. M. Habraken, K. Stannigel, M. D. Lukin, P. Zoller, and P. Rabl, "Continuous mode cooling and phonon routers for phononic quantum networks," New Journal of Physics **14**, 115004 (2012).

[269] P. Zapletal, S. Walter, and F. Marquardt, "Dynamically Generated Synthetic Electric Fields for Photons," arXiv:1806.08191 (2018).

[270] S. Walter, A. Nunnenkamp, and C. Bruder, "Quantum Synchronization of a Driven Self-Sustained Oscillator," Physical Review Letters **112**, 094102 (2014).

[271] S. Walter, A. Nunnenkamp, and C. Bruder, "Quantum synchronization of two Van der Pol oscillators," Annalen der Physik **527**, 131–138 (2015).

[272] N. Lörch, E. Amitai, A. Nunnenkamp, and C. Bruder, "Genuine Quantum Signatures in Synchronization of Anharmonic Self-Oscillators," Physical Review Letters **117**, 073601 (2016).

[273] N. Lörch, S. E. Nigg, A. Nunnenkamp, R. P. Tiwari, and C. Bruder, "Quantum Synchronization Blockade: Energy Quantization Hinders Synchronization of Identical Oscillators," Physical Review Letters **118**, 243602 (2017).

[274] E. Amitai, N. Lörch, A. Nunnenkamp, S. Walter, and C. Bruder, "Synchronization of an optomechanical system to an external drive," Physical Review A **95**, 053858 (2017).

[275] T. Weiss, S. Walter, and F. Marquardt, "Quantum-coherent phase oscillations in synchronization," Physical Review A **95**, 041802 (2017).

[276] U. B. Hoff, J. Kollath-Bönig, J. S. Neergaard-Nielsen, and U. L. Andersen, "Measurement-Induced Macroscopic Superposition States in Cavity Optomechanics," Physical Review Letters **117**, 143601 (2016).

[277] K. Børkje, A. Nunnenkamp, and S. M. Girvin, "Proposal for Entangling Remote Micromechanical Oscillators via Optical Measurements," Physical Review Letters **107**, 123601 (2011).

[278] M. Brunelli, O. Houhou, D. W. Moore, A. Nunnenkamp, M. Paternostro, and A. Ferraro, "Unconditional preparation of nonclassical states via linear-and-quadratic optomechanics," arXiv:1804.00014 (2018).

[279] J. Teissier, A. Barfuss, P. Appel, E. Neu, and P. Maletinsky, "Strain Coupling of a Nitrogen-Vacancy Center Spin to a Diamond Mechanical Oscillator," Physical Review Letters **113**, 020503 (2014).

[280] A. Barfuss, J. Teissier, E. Neu, A. Nunnenkamp, and P. Maletinsky, "Strong mechanical driving of a single electron spin," Nature Physics **11**, 820–824 (2015).

[281] E. R. MacQuarrie, M. Otten, S. K. Gray, and G. D. Fuchs, "Cooling a mechanical resonator with nitrogen-vacancy centres using a room temperature excited state spin–strain interaction," Nature Communications **8**, 14358 (2017).